

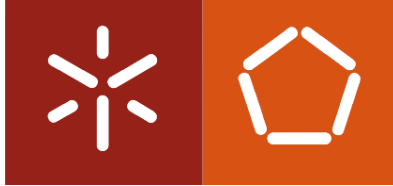


Eva Carolina Ferreira da Silva

Additive manufacturing components for thermal management using reactive materials

Universidade do Minho
Escola de Engenharia





Universidade do Minho
Escola de Engenharia

Eva Carolina Ferreira da Silva

Additive manufacturing components for thermal management using reactive materials

Tese de Doutoramento

Programa Doutoral em
Ciência e Engenharia de Polímeros e Compósitos

Trabalho efetuado sob a orientação do

Professor Doutor António José Vilela Pontes

Professor Doutor Álvaro Miguel do Céu Gramaxo Oliveira
Sampaio

março de 2024

DIREITOS DE AUTOR E CONDIÇÕES DE UTILIZAÇÃO DO TRABALHO POR TERCEIROS

Este é um trabalho académico que pode ser utilizado por terceiros desde que respeitadas as regras e boas práticas internacionalmente aceites, no que concerne aos direitos de autor e direitos conexos.

Assim, o presente trabalho pode ser utilizado nos termos previstos na licença abaixo indicada.

Caso o utilizador necessite de permissão para poder fazer um uso do trabalho em condições não previstas no licenciamento indicado, deverá contactar o autor, através do RepositóriUM da Universidade do Minho.

Licença concedida aos utilizadores deste trabalho



Atribuição
CC BY

<https://creativecommons.org/licenses/by/4.0/>

ACKNOWLEDGEMENTS

Many people directly or indirectly contributed to the development of this work in different ways and moments. I must express my gratitude to:

My supervisors, Professor António J. Pontes and Professor Álvaro M. Sampaio, for their support, guidance and availability. Without them, this work would not have been possible.

DONE Lab, where I had the possibility to carry out this work, and to all the people there for the constant furtherance. A special thanks to Carina Lopes, my “partner in crime”, to Sérgio Rodrigues, for his readiness and untiring help with machining operations, to Hugo Rodrigues for his support in numerical simulations, and to Rita Gonçalves, for many of the photographs presented in this work.

Portuguese Foundation for Science and Technology for the financial support under the PhD scholarship SFRH/BD/144590/2019.

Department of Polymer Engineering (DEP), for the facilities and equipment provided, and all the technicians, teachers and colleagues who helped me in some way.

Department of Mechanical Engineering (DEM) and to PIEP (Innovation in Polymer Engineering), for the thermal and mechanical tests performed.

Bosch Car Multimedia, in the person of Aníbal Portinha, for providing the original heat sink model evaluated in this work.

My boy-best-friend, Luís Martins, my parents, my sister and my brother, the most important people of my life and with whom I recharge all my strength and energies.

My grandparents and my uncles in heaven, my protective and caring angels.

To all of you, a huge thank you.

DECLARAÇÃO DE INTEGRIDADE

Declaro ter atuado com integridade na elaboração do presente trabalho académico e confirmo que não recorri à prática de plágio nem a qualquer outra forma de utilização indevida ou falsificação de informações ou resultados em nenhuma das etapas conducente à sua elaboração.

Mais declaro que conheço e respeitei o Código de Conduta Ética da Universidade do Minho.

Universidade do Minho, ___/___/_____

Nome completo: Eva Carolina Ferreira da Silva

Assinatura: _____

RESUMO

Componentes para gestão térmica obtidos por fabrico aditivo com materiais reativos

Para além das boas propriedades térmicas, o fabrico aditivo metálico permite uma grande liberdade geométrica na conceção de componentes para gestão térmica. Assim, o principal objetivo deste projeto doutoral é o estudo de componentes para gestão térmica produzidos por fusão de pó, com materiais reativos e termicamente condutores, como o alumínio, respondendo à pergunta de investigação “Em que medida o fabrico aditivo contribui para melhorar o desempenho de componentes para gestão térmica?”.

Inicialmente, como o principal objetivo inclui obter peças conforme a custos mais baixos, é abordado o tópico do fabrico híbrido, que combina tecnologias aditivas e subtrativas. Para tal, são testados provetes produzidos por fabrico aditivo com a liga de alumínio AlSi10Mg, por maquinaria convencional com a liga de alumínio AW-6082 e por fabrico híbrido, combinando ambos os materiais. Nas amostras com AlSi10Mg, é descrita a influência do tratamento térmico de alívio de tensões, recomendado pelo fornecedor. Em cada caso, as propriedades físicas, mecânicas e térmicas são avaliadas para corroborar a eventual perda de propriedades causada pelo fabrico híbrido.

De seguida, aplicam-se os dados e conhecimentos obtidos no desenvolvimento de dissipadores de calor ativos, através de simulações numéricas, considerando diferentes tipos de arrefecimento. Os melhores dissipadores de calor foram validados experimentalmente num sistema de teste, de modo a validar o acordo numérico-experimental. No final, numa estratégia de investigação-ação, foi otimizado um dissipador de calor real, que é parte de um computador central automóvel, de modo a reduzir a sua massa e as emissões de calor.

No final, todo o conhecimento previamente adquirido, é aplicado na conceção de insertos moldantes com canais de arrefecimento conformados. Considerando a melhor geometria de canais, produziram-se os insertos moldantes em AlSi10Mg (posteriormente concluídos via maquinaria) para avaliar experimentalmente o seu desempenho na injeção de peças amorfas e semi-cristalinas. No final, considerando a abordagem híbrida estudada ao longo deste trabalho, o melhor de ambos os métodos de fabrico pode ser combinado, para uma produção mais rápida e com menos desperdício de material.

Palavras-chave: Fabrico aditivo; Fabrico híbrido; Fusão de pó; AlSi10Mg; Gestão térmica; Canais conformados; Dissipador de calor; Moldação por injeção.

ABSTRACT

Additive manufacturing components for thermal management using reactive materials

Besides the good thermal properties, metallic additive manufacturing (AM) allows a great geometric freedom in the design of components for thermal management. Thus, the main goal of this philosophy doctor (PhD) thesis is the study of components for thermal management produced by powder bed fusion (PBF), with reactive materials, such as aluminium, answering the research question " How much additive manufacturing contributes to improve the performance of thermal management components?".

First, as the main goal includes obtaining compliant parts at lower costs, the topic of hybrid manufacturing (HM), which combines additive and subtractive technologies, is addressed. For this purpose, specimens produced by AM with AlSi10Mg aluminium alloy, by conventional machining with AW-6082 aluminium alloy and by HM, combining both materials, are tested. In the samples with AlSi10Mg, the influence of the stress relief heat treatment, recommended by the supplier, is described. In each case, physical, mechanical and thermal properties are evaluated to corroborate the eventual loss of properties caused by HM.

Next, the data and knowledge obtained are applied to the development of active heat sinks (HS), through numerical simulations, considering different types of cooling. The best HS were experimentally validated using an apparatus, in order to validate the numerical-experimental agreement. At the end, in an action-research strategy, a real HS, which is part of an automotive central computer, was optimised in order to reduce its mass and heat emissions to air.

At the end, all the knowledge previously acquired is applied to design moulding inserts with conformal cooling channels (CCC). Considering the best channel geometry, AlSi10Mg moulding inserts were produced (later finished via machining) to experimentally evaluate their performance in the injection moulding (IM) of amorphous and semi-crystalline parts. In the end, considering the hybrid approach studied throughout this work, the best of both manufacturing methods can be combined, for faster production and with less material waste.

Keywords: Additive Manufacturing; Laser Cusing; Reactive material; Thermal management; Conformal cooling; Heat sink; Hybrid manufacturing; Coating; Injection moulding.

CONTENTS

Acknowledgements	iii
Resumo	v
Abstract	vi
Contents	vii
List of figures.....	xi
List of tables.....	xvi
List of equations	xviii
List of abbreviations and symbols.....	xix
List of publications from this work	xxi
1. Introduction.....	1
1.1. Contextualization and motivation	2
1.2. Objectives	3
1.3. Thesis outline.....	4
1.4. References.....	7
2. Material characterization	8
2.1. Introduction	9
2.2. Research status of aluminium hybrid parts	10
2.3. Materials and experimental methodology	12
2.3.1. Materials	12
2.3.2. Methodology	12
2.3.3. Production of specimens.....	13
AlSi10Mg additively manufactured specimens.....	13
AW-6082 conventional manufactured specimens	14
AlSi10Mg+AW-6082 hybrid specimens	14
2.4. Characterization of additive, subtractive and hybrid aluminium parts	15
2.4.1. Physical properties.....	16
2.4.2. Thermal properties.....	17

Specific heat capacity.....	17
Thermal expansion.....	18
Thermal conductivity.....	19
Thermal diffusivity.....	21
2.4.3. Mechanical properties.....	22
Tensile properties	22
Mode-I fracture properties	25
Compressive properties.....	28
Case study.....	30
2.4.4. Dimensional and geometrical properties.....	31
2.5. Final remarks of this chapter.....	35
2.6. References.....	37
3. Heat Sinks.....	40
3.1. Introduction	41
3.2. Basic theoretical framework	41
3.3. Brief review on heat sinks designs and topology.....	42
3.3.1. Conventional heat sinks	42
3.3.2. Additively manufactured heat sinks	45
3.3.3. Microchannels heat sinks.....	46
3.4. Overall heat sinks performance	48
3.4.1. Air-cooled heat sinks	48
Fins heat sinks.....	53
Pins heat sinks	57
Lattice heat sinks.....	61
Fins vs Pins vs Lattice heat sink	61
Experimental validation	62
Air-cooled heat sinks – brief summary	64
3.4.2. Water-cooled heat sinks	64
Air vs water-cooled heat sinks.....	69
3.4.3. Hybrid-cooled heat sinks	69
3.5. Case study.....	70
3.5.1. Numerical simulations	71

3.5.2. Experimental validation	74
3.6. Final remarks of this chapter	78
3.7. References.....	79
4. Injection Moulding inserts	83
4.1. Introduction	84
4.2. Brief review on metallic injection moulding inserts	85
4.2.1. Conformal cooling channels	85
Basic theoretical background.....	86
Design notes.....	86
4.2.2. Quality of mouldings.....	87
4.2.3. Economic evaluation and the emerging of hybrid manufacturing.....	88
4.3. Moulding inserts development.....	89
4.3.1. Part and mould structure.....	89
4.3.2. Numerical procedure.....	91
Materials properties	92
Conformal cooling system design	93
4.3.3. Evaluation of thermal behaviour.....	94
4.3.4. Mechanical simulations	97
4.3.5. Injection moulding process simulations.....	101
4.3.6. Production of moulding inserts.....	104
4.4. Injection moulding.....	107
4.5. Parts analysis.....	108
4.5.1. Warpage.....	109
4.5.2. Relative crystallinity	110
4.5.3. Haze	111
4.6. Final remarks of this chapter.....	113
4.7. References	115
5. Concluding remarks	118
5.1. Main conclusions	119
5.2. Future research directions.....	120
Appendixes.....	121

Appendix 1 – AlSi10Mg datasheet	122
Appendix 2 – AW-6082 datasheet.....	123
Appendix 3 – Specific heat capacity (raw data)	124
Appendix 4 – Pressure transmitter BFT10-110	126
Appendix 5 – Styrolution PS 165N/L.....	127
Appendix 6 – SABIC PP 579S.....	128
Appendix 7 – Tailoring the mechanical properties of lattices fabricated by powder bed fusion by changing the deposition layer thickness	129
Appendix 8 – Temperature vs time evolution during injection moulding	142
Appendix 9 – Average tab angle of injection moulded specimens	143

LIST OF FIGURES

Figure 1-1. Infographic summarizing the doctoral project.....	6
Figure 2-1. Schematics of powder bed fusion technology.	10
Figure 2-2. SEM micrograph showing the morphology of AlSi10Mg powder for additive manufacturing (left) and powder size distribution (right) (adapted from [7]).	10
Figure 2-3. Schematic of the strategy used in the production of components by additive manufacturing [30].	14
Figure 2-4. Schematic of the strategy used in the production of components by hybrid manufacturing.	15
Figure 2-5. Production of hybrid specimens.	15
Figure 2-6. Representative curves of specific heat capacity vs temperature recorded for conventionally, additively and hybrid manufactured specimens.	18
Figure 2-7. Representative curves of CTE vs temperature recorded for conventionally, additively and hybrid manufactured specimens.	19
Figure 2-8. Mounting the sample and centering the sensor in hot disk thermal constants analyzer (adapted from [47]).	20
Figure 2-9. Representative tensile stress-strain curves recorded for conventionally, additively and hybrid manufactured specimens.	24
Figure 2-10. Low-magnification microscope images of AlSi10Mg specimens before (left) and after (right) heat treatment.	25
Figure 2-11. Microscopic observation of additive (left) and conventional (right) parts of an as-built AW-6082+AlSi10Mg specimen, after the tensile test.	25
Figure 2-12. Representative load-displacement curves recorded for conventionally, additively and hybrid manufactured specimens on mode-I fracture testes.	27
Figure 2-13. Crack propagation on a hybrid specimen without (left) and with heat treatment (right), after the mode I fracture test.	28
Figure 2-14. Representative compressive stress-strain curves recorded for conventionally, additively and hybrid manufactured specimens.	29
Figure 2-15. Crankset at the beginning (left) and at the end (right) of the three-point flexural test.	30
Figure 2-16. Evaluation of undamaged crankset.	30
Figure 2-17. Load-displacement curves for AW-6082 and hybrid cranks (left) and the damaged hybrid crankset (right) after the three-point flexural test.	31

Figure 2-18. Test artifact and measured dimensional and geometric elements.	32
Figure 2-19. Analysis of holes (left) and pins (right).	34
Figure 2-20. Analysis of positive (left) and negative (right) thin walls.	34
Figure 2-21. Parallelism of thin walls as a function of thickness.	34
Figure 3-1. Streamline surfaces on fin heat sink [37].	43
Figure 3-2. Horizontal and vertical finned heat sinks (adapted from [39])	43
Figure 3-3. Schematics of heat sink with oblique fins (front view) (adapted from [40]).	44
Figure 3-4. Multiple cross-section pins heat sink (left) (adapted from [53]) and an example of a knurled pins heat sink (right) (adapted from [52]).	44
Figure 3-5. Pins heat sinks with (left) and without (right) wings in staggered arrangement [55].	45
Figure 3-6. Geometry of optimized heat sink (left) (adapted from [56]), heat sink based on brain coral (center) (adapted from [57]) and lattice heat sink (right) [89].	45
Figure 3-7. Schematic view of a microfin array heat sink (left) (adapted from [60]) and heat sink structure with louvers (adapted from [61]).	46
Figure 3-8. Microchannels channels with misaligned inlet and outlet points (adapted from [63] and [66]).	46
Figure 3-9. Close view of single layer honeycomb plate (left), close view of two layers of honeycomb plates bonded together (centre) [67] and sectional oblique fins in a microchannel heat sink [68].	47
Figure 3-10. Configurations of alternating elliptical channels (left) and alternating rectangular channels (right) (adapted from [70]).	47
Figure 3-11. Different microchannels with reentrant cavities (adapted from [71-73]).	47
Figure 3-12. Permeable membrane heat sink design (adapted from [81]).	48
Figure 3-13. Computational domain for studying air-cooled heat sinks.	49
Figure 3-14. Lattice heat sink mesh.	50
Figure 3-15. Temperature contours vs time for each type of heat sink.	51
Figure 3-16. Different fins heat sink models.	52
Figure 3-17. Different pins shapes under study.	53
Figure 3-18. Different lattice heat sinks models.	53
Figure 3-19. Main effects for fins heat sinks minimum temperature.	54
Figure 3-20. Main effects for fins heat sinks pressure drop.	54
Figure 3-21. Model B variants.	56
Figure 3-22. Model C variants.	56

Figure 3-23. Model E variants.	57
Figure 3-24. Best fin heat sink (among those studied).	57
Figure 3-25. Possible pin heat sinks arrangements and orientatios.	58
Figure 3-26. Main effects for heat sink temperature (top) and pressure drop (bottom) for pins heat sinks.	59
Figure 3-27. Comparison between circular pins (A) and circular pins outwards (A1).	60
Figure 3-28. Pins heat sinks with frontal (H2) and side (H3) holes and radial pins heat sink with frontal holes (H4).	60
Figure 3-29. Best pin heat sink (among those studied).	61
Figure 3-30. Fins, pins, and lattice heat sinks, respectively.	62
Figure 3-31. Air-cooled heat sinks produced by PBF.	62
Figure 3-32. Experimental testing apparatus to evaluate heat sinks performance.	63
Figure 3-33. Computational domain for studying water-cooled heat sinks.	65
Figure 3-34. Influence of pins diameter or fins thickness on HS temperature after 15 seconds and on pressure drop.	66
Figure 3-35. Influence of pins/fins spacing on HS temperature after 15 seconds and on pressure drop.	67
Figure 3-36. Water-cooled heat sinks based on the best air-cooled ones.	68
Figure 3-37. Lattice air-cooled heat sink temperature for different heights.	69
Figure 3-38. Hybrid-cooled fins heat sink.	70
Figure 3-39. Hybrid-cooled pins heat sink.	70
Figure 3-40. Central computer considered as case study.	71
Figure 3-41. Heat sink under study.	71
Figure 3-42. Computational domain considered for the case study.	72
Figure 3-43. Example of a heat sink mesh considered for the case study.	72
Figure 3-44. Heat sink designs considered for the case study.	73
Figure 3-45. Surface temperature contours of original (left) and lattice sink (right) (reported at approximately 10 seconds).	74
Figure 3-46. Temperature evolution recorded on the highlighted points in Figure 3-44, along 60 seconds.	74
Figure 3-47. Conventional heat sink produced by machining (left), AM heat sink produced by PBF (middle) and HM heat sink produced by machining and PBF (right).	75

Figure 3-48. Flowchart of the production of hybrid heat sink and other hybrid parts.	75
Figure 3-49. Electronic enclosure used to experimental validate the heat sinks.	76
Figure 3-50. Temperature evolution on the electronic enclosure, considering each heat sink.	76
Figure 4-1. Hybrid mould concept and technologies used.	84
Figure 4-2. The injection moulding process.	85
Figure 4-3. a) Straight-drilled vs b) conformal cooling channels [15].	86
Figure 4-4. Rougher passages of cooling channels (left) and conformal cooling channels (CCC) with internal supports (adapted from [24]).	87
Figure 4-5. Technical drawing of the test part.	89
Figure 4-6. Mould structure.	90
Figure 4-7. Original moulding inserts (left) and moulding inserts reduced to half (right).	90
Figure 4-8. Conventional temperature control system on cavity (left) and core (right).	90
Figure 4-9. Ejection system.	91
Figure 4-10. Procedure to select the best injection moulding inserts.	91
Figure 4-11. Relative coverage of the part with each conformal cooling channels designed.	94
Figure 4-12. Number of mesh elements in the part as a function of melt from temperature and computation time for conventional moulding inserts.	95
Figure 4-13. FEM model of the part and designed cooling channels with inlets and outlets for simulation in Moldex3D.	95
Figure 4-14. Multistep setting of the packing pressure profile.	97
Figure 4-15. Average temperature after packing for each cooling channels.	97
Figure 4-16. Filling pressure curves obtained in Moldex3D.	98
Figure 4-17. Pressure applied on the injection moulding inserts (left) and fixed faces (right).	98
Figure 4-18. Stress and displacement of core (top) and cavity (bottom) with conformal cooling channels.	99
Figure 4-19. Unitary periodic auxetic cell with printing direction highlighted by red arrow, used to mass and volume optimizations [59].	100
Figure 4-20. Injection moulding inserts with conformal cooling channels and auxetic structures.	100
Figure 4-21. Stress and deformation of optimized core (top) and cavity (bottom) with conformal cooling channels.	101
Figure 4-22. Frozen layer ratio and average temperature considering the defined cooling time.	102
Figure 4-23. Numerical simulation results of part surface temperature at the end of the cooling.	103

Figure 4-24. Cavity surface average temperature moulding PP 579S and GPPS 165H.	103
Figure 4-25. Numerical simulation of volumetric shrinkage at the end of the injection cycle.	104
Figure 4-26. Numerical simulation of total displacements at the end of the injection cycle.	104
Figure 4-27. Injection moulding inserts produced by subtractive manufacturing with straight-drilled cooling channels.	105
Figure 4-28. Schematic images of oversized moulding inserts to be produced by additive manufacturing.	105
Figure 4-29. Injection moulding inserts produced by additive manufacturing before (left) and after (right) surface finishing (via machining).	105
Figure 4-30. Detailed view of porous surface on the cavity produced by PBF, after machining.	106
Figure 4-31. Location of pressure and temperature sensors on the surface of the part.	107
Figure 4-32. Cavity pressure curves for PP (up) and PS (bottom).	108
Figure 4-33. Surface appearance of the GPPS 165H mouldings, produced with the additive (top) and conventional (bottom) moulding inserts.	108
Figure 4-34. Warpage of the mouldings (predicted – top; actual – bottom).	110
Figure 4-35. DSC curve for PP 579S parts moulded with AlSi10Mg (conformal cooled) and AW-6082 (straight-drilled cooled) moulding inserts.	111
Figure 4-36. Hypothesis of hybrid manufacturing to produce injection moulding inserts.	113

LIST OF TABLES

Table 2-1. Chemical composition of the aluminium alloys studied by Chan <i>et al.</i> [17].	11
Table 2-2. Chemical composition of the aluminium alloys considered in this study [3, 23].	12
Table 2-3. Experimental tests, specimens and standards.	13
Table 2-4. Density measurements for conventionally, additively and hybrid manufactured specimens.	16
Table 2-5. Averaged coefficient of thermal expansion (between 20 °C and 200 °C) for conventionally, additively and hybrid manufactured specimens.	19
Table 2-6. Literature thermal conductivity values for different orientations.	20
Table 2-7. Thermal conductivity reported for conventionally, additively and hybrid manufactured specimens.	21
Table 2-8. Averaged thermal diffusivity for conventionally, additively and hybrid manufactured specimens, at room temperature.	22
Table 2-9. Reference studies regarding the influence of heat treatment on tensile properties.	23
Table 2-10. Hybrid specimens' tensile properties reported by Chan et al. [17, 22].	23
Table 2-11. Tensile properties of conventionally, additively and hybrid manufactured specimens.	24
Table 2-12. Mode-I fracture properties of conventionally, additively and hybrid manufactured specimens.	27
Table 2-13. Compressive properties for conventionally, additively and hybrid manufactured specimens.	29
Table 2-14. Dimensional and geometric properties of the test artifact produced by additive manufacturing in AlSi10Mg, without stress relief heat treatment.	33
Table 3-1. Main properties of the materials considered for each component on air-cooled heat sinks.	49
Table 3-2. Levels and factors for DOE matrix for fins heat sinks.	51
Table 3-3. Levels and factors for DOE matrix for pins heat sinks.	51
Table 3-4. Correlation between heat sink temperature and geometrical parameters.	55
Table 3-5. Correlation between pressure drop and DOE factors.	55
Table 3-6. Temperature and pressure drop for each fin heat sink model.	55
Table 3-7. Correlation between pressure drop and geometrical parameters for an inlet air velocity of 3.51 m/s.	58
Table 3-8. Temperature and pressure drop for each pin heat sink model.	59
Table 3-9. Temperature and pressure drop for each pin heat sink model.	61

Table 3-10. Temperature and pressure drop for each pin heat sink model.	61
Table 3-11. Direct comparison between heat sinks with fins, pins, and blades ($Re = 12500$).	62
Table 3-12. Heat sink temperature and pressure drop for pins heat sink with holes (diameter 2.5 mm).	63
Table 3-13. Air-cooled heat sinks performance: simulation vs experimental.	64
Table 3-14. Main properties of the materials considered for each component on water-cooled heat sinks.	65
Table 3-15. Influence of fins/pins thickness/diameter and spacing inside the microchannel HS.	67
Table 3-16. Performance of different microchannel lattice HS.	68
Table 3-17. Geometric characteristics of the heat sink designs considered for the case study.	74
Table 3-18. Mass and time to produce each heat sink.	75
Table 3-19. Thermal resistance of each heat sink.	77
Table 4-1. Injection materials main properties.	92
Table 4-2. Moulding inserts materials main properties.	92
Table 4-3. Conformal cooling channels studied.	93
Table 4-4. Basic process parameters used in the injection analysis.	96
Table 4-5. Results of weight/volume optimization of moulding inserts with conformal cooling channels.	101
Table 4-6. Summary of material and time consuming in the production of conventional moulding inserts (by subtractive manufacturing) and with conformal cooling channels (by additive manufacturing).	106
Table 4-7. Recorded average temperature for each moulding inserts and polymers, considering 10 shots.	107
Table 4-8. Average tab angle of injection moulded specimens, considering five measurements on the side of the core, and comparison with the predicted tab angle predicted by the simulations.	109
Table 4-9. DSC characterization of PP 579S samples.	111
Table 4-10. Forecast of material and time consuming, if a hybrid production of the moulding inserts was considered.	114

LIST OF EQUATIONS

Equation 2-1. Specific density using Archimedes' principle.	16
Equation 2-2. Heat capacity using DSC signal	17
Equation 2-3. Heating power required for the calculation of thermal conductivity [47].	21
Equation 2-4. Thermal diffusivity.	21
Equation 2-5. Fracture toughness.	26
Equation 2-6. Coefficient crack-size/specimen-width.	26
Equation 2-7. Conditions to deem when calculating fracture toughness.....	26
Equation 3-1. Fourier's Law of Conduction.	42
Equation 3-2. Newton's Law of Cooling.	42
Equation 3-3. Thermal resistance.....	42
Equation 3-4. Reynolds number.	51
Equation 4-1. Heat transfer balance in injection moulding process.....	86
Equation 4-2. Heat transfer balance in injection moulding process (simplified).....	86
Equation 4-3. Apparent viscosity according to Modified Cross Model.	96
Equation 4-4. Lower Newtonian viscosity for PP 579S, according to Modified Cross Model.	96
Equation 4-5. Lower Newtonian viscosity for GPPS 165H, according to Modified Cross Model.	96
Equation 4-6. Calculation of material constants for GPPS 165H.....	96

LIST OF ABBREVIATIONS AND SYMBOLS

Abbreviation	Meaning	Abbreviation	Meaning
	Density	D	Diameter
	DSC signal	D_H	Hydraulic diameter
	Theoretical thermal conductivity	DC	Direct current
	Thermal diffusivity	DOE	Design of experiments
$\sigma_{0.2\%}$	0.2 % offset yield strength	DSC	Differential scanning calorimeter
σ_{MAX}	Maximum stress	Fe	Iron
	Thermal resistance	FEM	Finite element method
	Viscosity	h	Convective coefficient
	Lower newtonian viscosity	HM	Hybrid manufacturing
	Shear rate	HS	Heat sink
3PB	Three-point bending	HT	Heat treatment
a	Crack size	IM	Injection moulding
Al	Aluminium	k	Experimental thermal conductivity
AM	Additive manufacturing	K_{Ic}	Fracture toughness
ANOVA	Analysis of variance	m	Mass
ASTM	American Society for Testing and Materials	Mg	Magnesium
B	Specimen thickness	Mn	Manganese
BCC	Body-centered cubic	NIST	National Institute of Standards and Technology
CAD	Computer-aided design	P	Pressure
CAE	Computer-aided engineering	PBF	Powder bed fusion
CCC	Conformal cooling channels	PCB	Printed circuit board
CFD	Computational fluid dynamics	PP	Polypropylene
CNC	Computer numerical control	PS	Polystyrene
c_p	Specific heat capacity	Q	Heat transfer
CT	Computed tomography	r	Radius
CTE	Coefficient of thermal expansion	Re	Reynolds number
Cu	Copper		

Abbreviation	Meaning
SEM	Scanning Electron Microscope
Si	Silicon
SLA	Stereolithography
STEP	Standard for the Exchange of Product Data
T	Temperature
Ti	Titanium
TIP	Thermally induced porosity
UTS	Ultimate tensile strength.
v	Velocity
W	Specimen width
Zn	Zinc

LIST OF PUBLICATIONS FROM THIS WORK

International Journal Publications

Silva, E.C.; Sampaio, Á.M.; Pontes, A.J. Evaluation of Active Heat Sinks Design under Forced Convection—Effect of Geometric and Boundary Parameters. *Materials* 2021, 14, 2041. <https://doi.org/10.3390/ma14082041>

Silva, E.C.; Candiango, J.A.; Rodrigues, S.J.; Sampaio, Á.M.; Pontes, A.J. Hybrid Manufacturing of Aluminium Parts Combining Additive and Conventional Technologies—Mechanical and Thermal Properties. *J. Manuf. Mater. Process.* 2022, 6, 40. <https://doi.org/10.3390/jmmp6020040>

Carneiro, V.H., **Silva, E.C.**, Gomes, I., Duarte, I., Puga, H.; Sampaio, Á.M., Pontes, A.J. Tailoring the mechanical properties of lattices fabricated by powder bed fusion by changing the deposition layer thickness. *Metals and Materials International*. 2023. (submitted)

Magazine publications

Pereira A.B., Pontes A.J., Silva C.S., **Silva E.C.** et al. Comparação de tempo e custo entre moldes convencionais e híbridos para injeção de dissipadores de calor. *O Molde*, 137, 2023, pp. 66–71. <https://www.cefamol.pt/index.php?id=85&idn=658>

Oral communications

Silva, E.C.; Sampaio, Á.M.; Pontes, A.J., “Additive manufacturing for repairing aluminium parts – a case study”, International Polymer Process Innovation Conference (PPI), Virtual Event, 14-15 December 2021.

Lopes A.C., **Silva, E.C.**; Sampaio, Á.M.; Pontes, A.J., “Understanding dimensional and geometrical tolerances of metal, polymer and composite powder bed fusion additive manufacturing technologies”, *Materiais 2022*, Marinha Grande, Portugal, 10-13 April 2022.

Silva, E.C.; Sampaio, Á.M.; Pontes, A.J., “Computational evaluation of sustainable water-cooled heat sinks manufactured by powder bed fusion”, *RESIM 2022*, Virtual Event, 2-3 June 2022.

Silva, E.C.; Sampaio, Á.M.; Pontes, A.J., “Thermal optimization of electronic enclosures developing new additively manufactured heat sinks”, International Polymer Process Innovation Conference (PPI) 2022, Lavrion, Greece, 15-16 September 2022.

Under preparation

Journal publicarions

Silva, E.C., Lopes, A.C., Sampaio, Á.M., Pontes, A.J. Influence of layer thickness on dimensional and geometrical properties of aluminium parts produced by powder bed fusion.

Silva, E.C., Rodrigues, S.J., Rodrigues, H.L., Fernandes, L.C., Sampaio, Á.M., Pontes, A.J. Evaluation of AlSi10Mg injection moulding inserts with conformal cooling channels

Patent

Silva, E.C.; Sampaio, Á.M.; Pontes, A.J. A method to produce thermal management components using conventional and additive techniques.

1. INTRODUCTION

The major focus of this chapter is to provide a brief overview of the most relevant topics outlined this doctoral thesis, namely additive manufacturing, reactive materials and thermal management components. The relevance of optimising these components is emphasized, evidencing a motivation to the work. The research questions and subsequent objectives are also presented.

1.1. Contextualization and motivation

Powder bed fusion (PBF), an additive manufacturing (AM) technology, is increasingly used to produce end use parts. In this process, most of the used powder (95 – 97 %) is not solidified during it, being reused as it is, which is beneficial for part cost and resource consumption. However, the technology is not commonly used in industrial applications due to quality and safety concerns, especially when reactive powders are used, such as aluminium and titanium alloys [1, 2]. Reactive metal powders are the metal powders whose chemical properties mean that they react spontaneously with oxygen from the atmosphere. This reaction is dependent on the particle size and the distribution or swirling up in the air. Swirled-up dust of these reactive metal powders and soot residues can react in the form of a dust explosion, if flammable swirled-up dust is present in a suitable concentration in a mixture with a gaseous oxidiser and the ignition energy is exceeded. This ignition energy for soot explosions is so low that they are capable of spontaneous ignition if there is turbulence [3]. Furthermore, when processing reactive materials, high chemical purity of such powders is especially important in order to ensure manufacturing of fully dense parts [4].

Moreover, the trend of industrial products demanding miniaturization, flexibility and reduced energy consumption continues growing. This situation is required by industries because the consumers desire more products in less time and at lower cost and, preferably, with differentiation that can be achieved by new functionality, innovative technologies and/or electronics incorporation. In this context, thermal management becomes a more a more important element of electronic product design. Performance reliability and life expectancy of an electronic equipment are inversely related to its temperature, which can be minimized using appropriate heat sinks. Heat sinks are devices that enhance heat dissipation from a hot surface, maintaining the device temperature below the maximum allowable temperature specified by the device manufacturers.

The production of heat sinks by AM considering the use of reactive materials is recent [5]. Geometric freedom and the inclusion of channels for the active temperature control provided by AM are singular and disruptive factors in the current state of knowledge. However, in contrast, AM technology may imply the presence of empty spaces, which translates into a material that is not completely homogeneous in their structure and density and, as such, may compromise the intended performance. This work will go even further by proposing a new method of manufacturing heat sinks, combining the production speed of conventional simple geometries with the geometric freedom of AM, with low waste of raw material. Moreover, to date and the best of my knowledge, there is no studies regarding thermal properties on hybrid-manufactured aluminium parts.

In addition to these thermal management components, the use of AM in the production of moulding inserts with conformal cooling channels (CCC) for injection moulds has been widely studied, although mainly using steel or polymers as mould materials, with scarce studies when it comes to aluminium. This alloy has mainly been studied considering subtractive technologies instead of AM, focusing essentially in the wear of these tools throughout the injection moulding process and the use of coatings to overcome this issue. Therefore, this research intends to explore aluminium moulding inserts obtained by AM, with a disruptive temperature control system, to obtain optimal parts.

According to the described above, the main research question for this study is:

How much additive manufacturing contributes to improve the performance of thermal management components?

To answer this research question, it can be divided in four subordinate questions:

- a. How much hybrid manufacturing, i.e. combining subtractive and additive technologies, contributes to the production of optimal aluminium parts?
- b. How much AM improves the performance of heat sinks? How close are CAE simulations to real measurements in predicting thermal management?
- c. Which is the general behaviour of aluminium moulding inserts for injection moulding with transparent materials?
- d. How much savings these approaches achieve?

1.2. Objectives

In response to the research question, the main purpose of this doctoral project is the study of thermal management components produced by AM in reactive materials, namely aluminium. To this end, two different application will be considered: (i) active heat sinks and (ii) injection moulding inserts with conformal cooling channels for plastic injection moulds.

To this end, it is expected to achieve the following objectives:

- § Characterization and evaluation of the adhesion between aluminium alloys processed by subtractive and additive technologies as well as the feasibility of the reconstruction of components produced by AM in reactive material;
- § Development and production of additively manufactured heat sinks with reactive material AlSi10Mg, using CAD/CAE software and considering different configurations;

- Š Characterization and performance evaluation of heat sinks developed and optimised in a case study, considering a suitable apparatus for evaluation of the thermal behaviour;
- Š Development and production of aluminium moulding inserts, via AM, that allow exceptional thermal management;
- Š Injection moulding with the previously developed moulding inserts, considering amorphous and semi-crystalline polymers.

1.3. Thesis outline

This doctoral thesis is structured in five chapters: (1) Introduction, (2) Material characterization, (3) Heat sinks, (4) Injection moulding inserts, and (5) Conclusions. Chapter 2 has the main objective of acquiring technical and scientific knowledge to be applied in the development of Chapters 3 and 4 (Figure 1-1). Within each of these chapters, brief notes of the current state of the art related to the theme of the chapter are presented.

The contents of each chapter are summarized below.

Chapter 1 | Introduction – includes this introduction and provides a brief overview of the most relevant topics outlined the thesis, namely additive manufacturing, reactive materials and thermal management components. The relevance of optimising these components is emphasized, evidencing a motivation to the work. The research questions and subsequent objectives are also presented.

Chapter 2 | Material characterization – intends to answer the first question “How much hybrid manufacturing, that is, combining subtractive and additive technologies, contributes to the production of sustainable aluminium parts and without significant loss of properties?”. To this, specimens produced by additive manufacturing with AlSi10Mg, by conventional machining with AW-6082 aluminium alloy and by hybrid manufacturing are tested. In AlSi10Mg samples, the influence of the stress relief heat treatment, recommended by the supplier, is reported. In each case, physical, mechanical and thermal properties are evaluated to corroborate the eventual loss of properties caused by hybrid manufacturing. In addition, a flexural test is done on a functional part, previously made in AW-6082 and rebuilt by additive manufacturing, demonstrating the potential of hybrid manufacturing in repairing and building of sustainable components.

Chapter 3 | Heat sinks – intends to answer the research questions (b) and (d). To this, different active heat sinks were evaluated via computational fluid dynamics (CFD) simulations, considering different types of cooling. The best heat sinks designs were experimentally validated on a testing apparatus to

compare with the simulated results. In the end, in an action-research strategy, a case study involving an automotive central computer with a heat sink was optimized through hybrid manufacturing to reduce heat emissions to air and car weight.

Chapter 4 | Injection moulding inserts – intends to answer the research questions (c) and (d). To this, different conformal cooling channels designs were evaluated via numerical simulations. The best design was applied to aluminium moulding inserts to experimentally evaluate their performance moulding amorphous and semi-crystalline parts. In the end, considering the hybrid approach studied throughout this work, it is evidenced the potential in combining the best of both methods for a faster production with less material waste.

Chapter 5 | Conclusions – summarizes a general overview of the work developed and proposals for future research on the subjects covered and beyond.

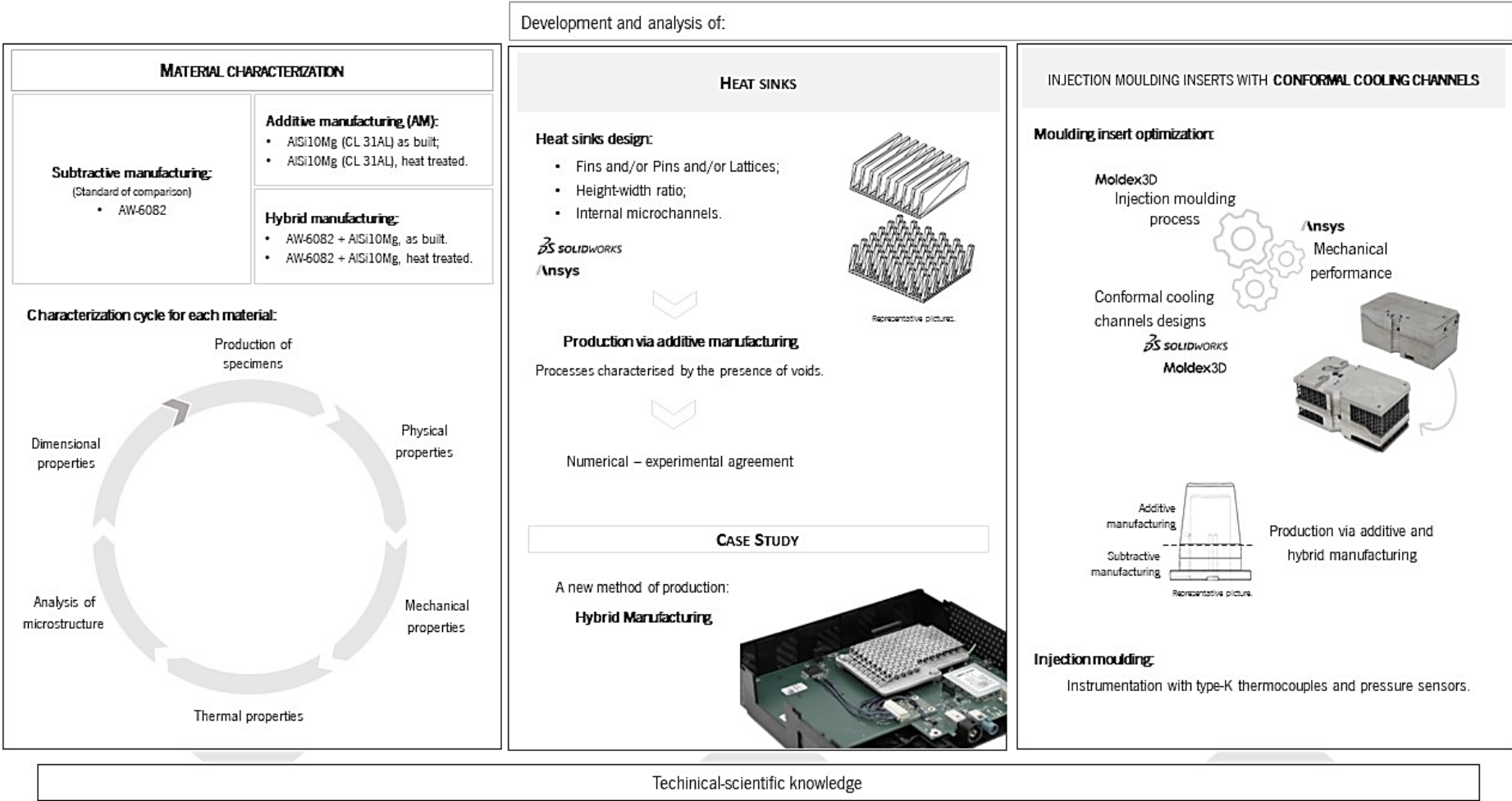


Figure 1-1. Infographic summarizing the doctoral project.

1.4. References

- [1] Wohlers TT, Campbell I, Diegel O, et al. *Wohlers report 2022: 3D printing and additive manufacturing global state of the industry*. 2022.
- [2] Lutter-Günther M, Bröker M, Mayer T, et al. Spatter formation during laser beam melting of AlSi10Mg and effects on powder quality. In: *Procedia CIRP*. Elsevier B.V., 2018, pp. 33–38.
- [3] Concept Laser GmbH. M2 cusing Single-Laser/Dual-Laser | Manual de operação, www.concept-laser.de (2015).
- [4] Moghimian P, Poirié T, Habibnejad-Korayem M, et al. Metal powders in additive manufacturing: A review on reusability and recyclability of common titanium, nickel and aluminum alloys. *Additive Manufacturing*, 43. Epub ahead of print 1 July 2021. DOI: 10.1016/j.addma.2021.102017.
- [5] Wong KK, Ho JY, Leong KC, et al. Fabrication of heat sinks by Selective Laser Melting for convective heat transfer applications. *Virtual Phys Prototyp* 2016; 11: 159–165.

2. MATERIAL CHARACTERIZATION

This chapter intends to answer the question “How much hybrid manufacturing, that is, combining subtractive and additive technologies, contributes to the production of sustainable aluminium parts and without significant loss of properties?” To this, specimens produced by additive manufacturing with AlSi10Mg, by conventional machining with AW-6082 aluminium alloy and by hybrid manufacturing are tested. In AlSi10Mg samples, the influence of the stress relief heat treatment, recommended by the supplier, is reported. In each case, physical, mechanical and thermal properties are evaluated to corroborate the eventual loss of properties caused by hybrid manufacturing. In addition, a flexural test is done on a functional part, previously made in AW-6082 and rebuilt by additive manufacturing, demonstrating the potential of hybrid manufacturing in the building of sustainable components.

2.1. Introduction

Aluminium is one of the most abundant metals in the earth's crust. Aluminium is available with a purity level of 99 %, with low specific weight, excellent corrosion resistance, high strength and stiffness, good formability, weldability and high electrical and heat conductivity. However, without the presence of other alloy elements, aluminium has a tensile strength of only 90 MPa, making it very ductile. For this reason, to improve mechanical properties or to change the microstructure, it is necessary to add some elements [1]. Among the possible constituents of an aluminium alloy, the following are the most popular [2]:

- § Copper (Cu): improves mechanical strength and hardness but, in specific compositions and material conditions, increases stress-corrosion susceptibility;
- § Iron (Fe): improves strength at high temperatures but also the embrittlement of the microstructure;
- § Magnesium (Mg): widely used in application requiring bright surface finish, excellent response to chemical finishing, corrosion resistance and attractive combinations of strength and ductility;
- § Silicon (Si): improves fluidity, hot tear resistance and feeding characteristics;
- § Titanium (Ti): refines the grain structure and reduces internal stresses.

AlSi10Mg alloy is a series 6 aluminium alloy with silicon content between 9 % and 11 % and magnesium content between 0.2 % and 0.45 %. This aluminium alloy combines good strength and thermal properties with low weight and flexible post processing possibilities. It can be used for production of lightweight components in the field of automotive and aerospace industries with high mechanical and dynamic loads [2–4].

When using this aluminium alloy in additive manufacturing, components are manufactured by means of powder bed fusion (Figure 2.1). Firstly, a layer of powder is laid on a substrate of the same material as the powder that is placed on a z-axis moving platform. The work chamber is filled with argon or nitrogen gas to provide an inert environment. Secondly, a diode pumped Yb-Fibre continuous wave laser scans the cross-section area (xy plan) of the part design, sintering the powder particles which then fuse and solidify to form a solid part. Thirdly, the platform will descend to allow a second layer of powder over the first layer and the laser will then process and fuse again the powder particles. The process repeats itself until the part is fully produced [5, 6].

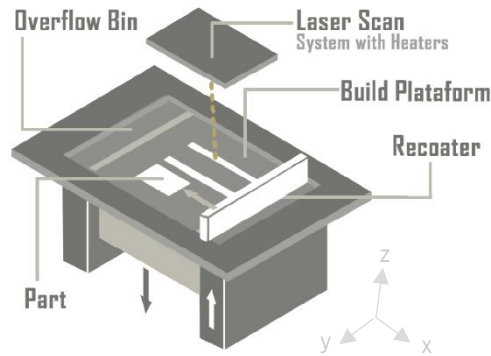


Figure 2-1. Schematics of powder bed fusion technology.

Figure 2.2 (left) shows a Scanning Electron Microscope (SEM) micrograph of AlSi10Mg powder for additive manufacturing. The powder particles can be considered spherical with some small irregular particles attached to the big ones. Figure 2.2 (right) shows the size distribution of the powder, with an average particle size of 35 μm . The unsymmetrical distribution can be caused by the irregular powder morphology mentioned before [5, 7].

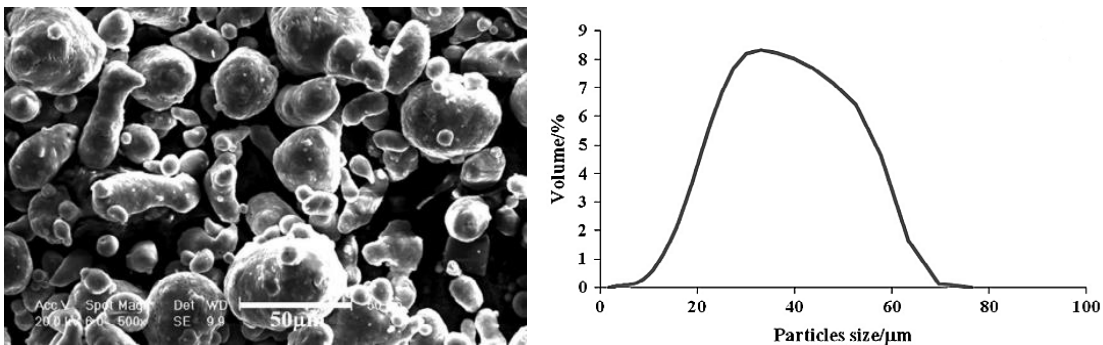


Figure 2-2. SEM micrograph showing the morphology of AlSi10Mg powder for additive manufacturing (left) and powder size distribution (right) (adapted from [7]).

2.2. Research status of aluminium hybrid parts

Metal additive manufacturing technologies enable the production of complex geometries. However, high manufacturing costs hinder these technologies from being employed in some industries. A cost-effective hybrid strategy can be a good solution to achieve the best of additive and subtractive technologies, i.e., complex geometries at a lower cost, with good properties. Therefore, the concept of hybrid manufacturing consists of building a complex portion of a part by additive manufacturing on a simple pre-machined simple base substrate. Behind this, this approach can also be favourable in the restoration of damaged parts, offering significant economic advantages [8].

Hybrid manufacturing was proposed by Boivie *et al.* [9] for application in steel injection moulding inserts with conformal cooling channels and replicated by some other authors [10–12]. The results showed that the production cost using hybrid manufacturing technology can be reduced up to 20 % with

respect to tool inserts made entirely with additive manufacturing [10, 12]. According to the authors, the best cost-benefit can be achieved when 65 % of the part is produced by subtractive manufacturing and the remaining 35 % by additive manufacturing [11].

The interface analysis between both technologies considering steel substrates and powders have been successfully investigated, mainly employing uniaxial tensile tests combined with microstructure observation. Even with a strong fusion bonding at the interface boundary between the additive powder and machined substrate, there is a compromise in tensile strength. Mostly, fracture occurred in the interface although, sometimes, it can occur in the side of the weaker material, away from the interface, depending on the substrate material and the heat treatment applied [12–16]

However, studies with hybrid-built reactive materials such as aluminium are more limited. Chan *et al.* [17] evaluated the interface bonding integrity, in terms of microstructure and mechanical properties, of powder AISi10Mg and three types of substrate aluminium alloys: AW-5083, AW-6061 e Alumecc 89, whose chemical compositions are shown in Table 2-1 [3, 18–20]. Microstructure analysis revealed excellent powder-substrate fusion and tensile specimens ruptured at the side where the material was of lower strength. Optical microscopic examinations revealed good adhesion of deposited powder onto the substrate, mainly with Alumecc 89. Although this was not the aluminium alloy with the most similar chemical composition to the additive manufacturing alloy, the higher amount of zinc lead to higher solubility and provided a solderable surface [21].

Table 2-1. Chemical composition of the aluminium alloys studied by Chan *et al.* [17].

	AISi10Mg	AW-5083	AW-6061	Alumecc 89
Al	Balance	Balance	Balance	Balance
Si	9 % – 11 %	< 0.40 %	0.4 % - 0.8 %	< 1.20 %
Mn	< 0.45 %	0.4 % - 1.0 %	< 0.15 %	< 1.50 %
Fe	< 0.55 %	< 0.40 %	< 0.70 %	< 1.40 %
Mg	0.20 % - 0.45 %	4,0 % - 4,9 %	0.8 % - 1.2 %	< 3.70 %
Zn	< 0.10 %	< 0.25 %	< 0.25 %	< 12.0 %

Later, the same authors fabricated injection-moulding inserts using the hybrid additive–subtractive strategy. 5083-H116 wrought aluminium alloy was selected as the substrate material and a time saving close to 27 % was achieved (compared with fully additively manufactured moulding inserts) [22].

Based on this, to the best of my knowledge, in addition to the fact that there are no studies evaluating AISi10Mg+AW-6082 hybrid parts, there are also no studies assessing the thermal properties of hybrid parts, regardless of constituent alloys. Following this, in the next pages of this chapter, a complete characterization is made, including physical, thermal, mechanical and dimensional properties of

components produced in AlSi10Mg by additive manufacturing, in AW-6082 by subtractive manufacturing and combining both materials and manufacturing methods.

2.3. Materials and experimental methodology

2.3.1. Materials

Considering the powder material used for additive manufacturing - AlSi10Mg -, it was selected a widely used aluminium alloy with similar chemical composition available indoor as substrate: AW-6082. This alloy has excellent mechanical characteristics and good corrosion resistance and it is widely used in construction structural elements, machine elements, home appliances, high precision parts and shipbuilding applications [23]. Chemical composition of both alloys is recorded in Table 2-2 and datasheet of these materials can be found in Appendixes 1 and 2.

Table 2-2. Chemical composition of the aluminium alloys considered in this study [3, 23].

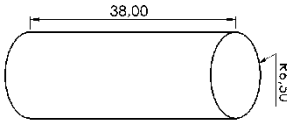
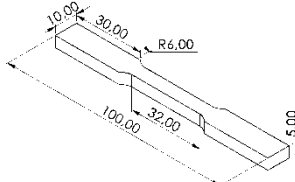
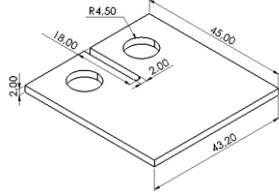
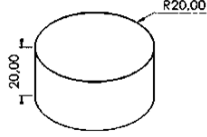
	AlSi10Mg	AW-6082
Al	Balance	Balance
Si	9 % – 11 %	0.7 % - 1.3 %
Mn	< 0.45 %	0.4 % - 1.0 %
Fe	< 0.55 %	< 0.50 %
Mg	0.20 % - 0.45 %	0.60 % - 1.20 %

2.3.2. Methodology

According to the manufacturer, after the production of AlSi10Mg aluminium alloy components in the Concept Laser M2 Cusing equipment, a heat treatment must be carried out to release stresses. For this reason, the properties of this alloy with and without heat treatment are analysed. AW-6082 aluminium alloy is already supplied with T6 heat treatment [3, 23]. So, for the physical, mechanical and thermal characterization, specimens were produced in accordance with Table 2-3 in each of the following stages:

- § AlSi10Mg without heat treatment;
- § AlSi10Mg with heat treatment;
- § AW-6082;
- § AlSi10Mg + AW-6082 without heat treatment;
- § AlSi10Mg + AW-6082 with heat treatment

Table 2-3. Experimental tests, specimens and standards.

Characterization	Property	Specimen	Nr of specimens	Standard
Physical	Density	(compressive specimens)	-	-
Mechanical	Uniaxial compression		5	ASTM E9 [24]
	Uniaxial tension		5	ASTM E8 [25]
	Fracture (mode I)		5	ASTM E399 [26]
Thermal	Thermal conductivity		-	-
	Specific heat	(fractured specimens)	-	ASTM E1269 [27]
	Coefficient of thermal expansion	(fractured specimens)	-	ASTM E831 [28]

2.3.3. Production of specimens

AlSi10Mg additively manufactured specimens

AlSi10Mg additively manufactured specimens were produced in Concept Laser M2 Cusing equipment, vertically oriented to facilitate the subsequent hybrid manufacturing. They were produced in a single batch with layer thickness of 25 μm , as it is known that a smaller layer thickness will improve the tensile strength and strain [29]. The remaining parameters were a laser power of 370 W with a spot size of 190 μm , scanning speed and hatch spacing of 1400 mm/s and 112 μm , in an atmosphere inert with nitrogen to prevent oxidation and reactivity, with a maximum oxygen content of 0.2 %. In each production layer, the sintering area was divided into several islands (Figure 2-3) measuring 5 mm. For

each consecutive layer, the pattern is shifted 1 mm and rotated 90° to reduce discontinuities between the perimeters of the islands [30].

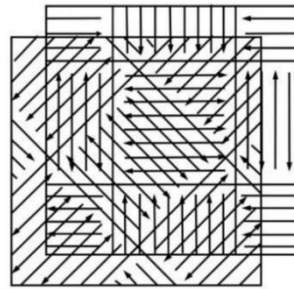


Figure 2-3. Schematic of the strategy used in the production of components by additive manufacturing [30].

After producing the specimens and removing supports, the stress relief heat treatment recommended by the manufacturer was carried out in some samples (i) heating them up to 240 °C (in one hour), (ii) maintaining the temperature for six hours, (iii) cooling, in the oven, to 100 °C and (iv) cooling completely in the ambient atmosphere [3].

AW-6082 conventional manufactured specimens

The production of the AW-6082 aluminium specimens was carried out in the DMG Mori DMU 50 machine, using the appropriate tools and coolant. Each typology was produced according to different batches and programs, using milling cutters with 12 mm of diameter, at 6000 rpm and feed rate of 2000 mm/min, cooled with an emulsion with cutting oil and water.

AlSi10Mg+AW-6082 hybrid specimens

To produce hybrid specimens, three types of solid substrate blocks were designed and manufactured through CNC machining in AW-6082 aluminium alloy: one for tensile and compressive tests, other for fracture tests and other for thermal conductivity tests. All substrate blocks were mounted to the pre-machined building platform for the equipment Concept Laser M2 Cusing (Figure 2-4) and fixed with M3 screws. Before start the production of the additively part, it was ensured that the surfaces of the machined substrates were perfectly aligned to ensure proper calibration of the additive manufacturing process [12].

After a detailed positioning in Magics software, the remaining half specimens were produced by additive manufacturing. Then, all specimens were obtained from the hybrid-built parts by milling (Figure 2-5).

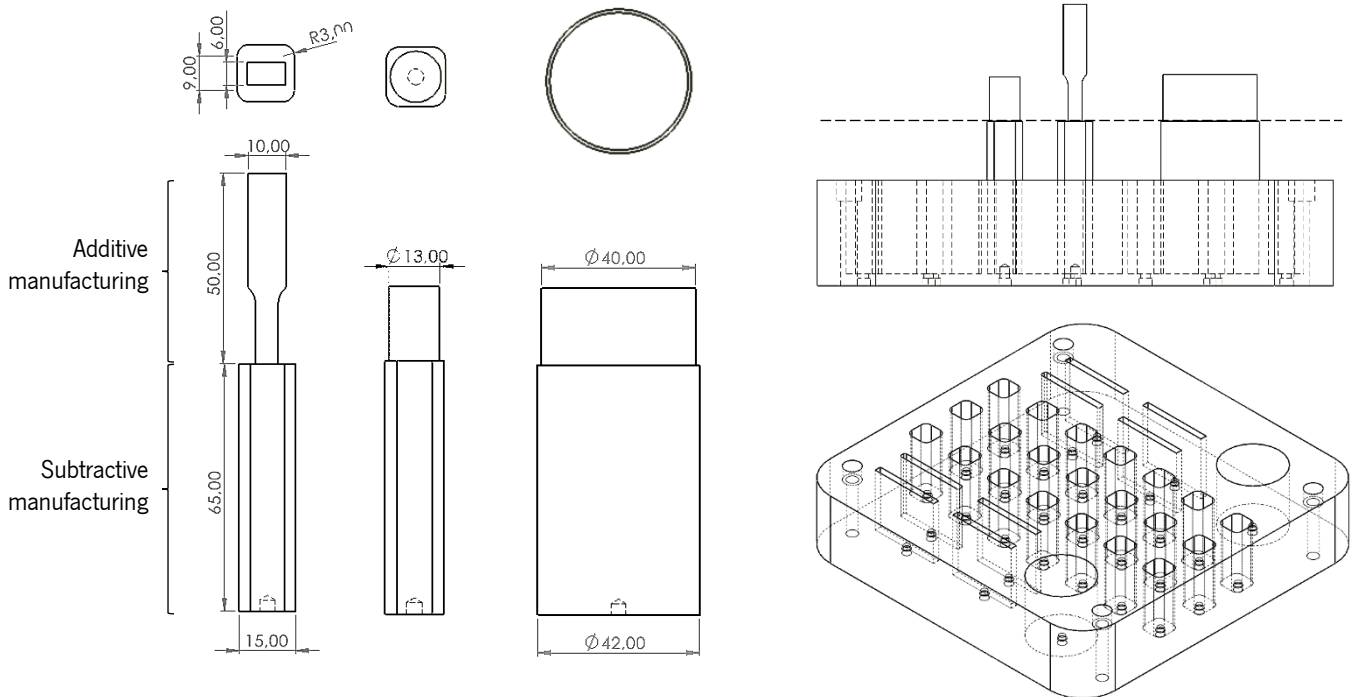


Figure 2-4. Schematic of the strategy used in the production of components by hybrid manufacturing.

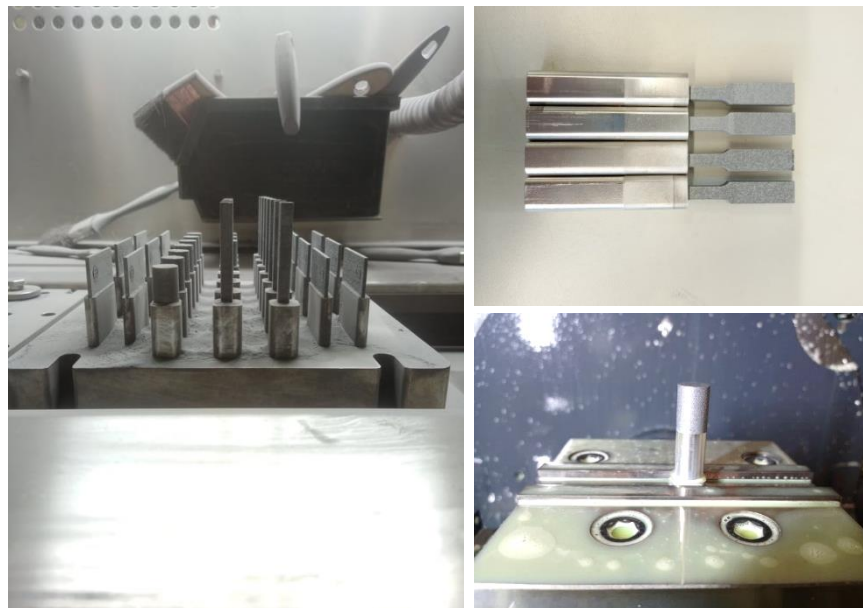


Figure 2-5. Production of hybrid specimens.

2.4. Characterization of additive, subtractive and hybrid aluminium parts

Even hybrid manufacturing is pertinent for a reduction in manufacturing time and costs, the characterization of the parts produced by this strategy must be done to ensure the best performance of

the component to be applied. In this work, some physical, thermal, mechanical and dimensional properties are evaluated.

2.4.1. Physical properties

Powder bed fusion (PBF) technologies show potential for fabricating a vast number of components requiring good mechanical and thermal properties, such as heat sinks and injection moulding inserts, as they can process parts of high relative density. Understanding porosity formation aids in improving parts' quality when applied in industry [31–33]. According to some authors, the application of heat treatment on AlSi10Mg samples may reduce density due to the exposure to high temperatures and, the more is treatment duration and/or temperature, the less can be the density [34, 35].

In this work, the Archimedes principle was used to measure parts' density. According to this principle, the volume of an immersed solid is equal to the volume of the displaced volume. Thus, a solid immersed in a liquid is exposed to the buoyancy force which, in turn, is equal to the weight of the liquid displaced by the volume of the solid. The specific density of the solid is calculated using Equation 2-1, where \bar{U} represents the buoyancy force.

Equation 2-1. Specific density using Archimedes' principle.

$$\frac{\bar{U}}{\bar{U}}$$

The procedure for determination of density was performed on an analytical balance AS 220.R2 from Radwag with density kit. Based on five samples, the average density obtained for conventionally, additively and hybrid manufactured aluminium parts is resumed in Table 2-4.

Table 2-4. Density measurements for conventionally, additively and hybrid manufactured specimens.

AW-6082	AlSi10Mg (as-built)	AlSi10Mg (heat treated)	AW-6082/AlSi10Mg (as-built)	AW-6082/AlSi10Mg (heat-treated)
2.757±0.008 g/cm ³	2.641±0.007 g/cm ³	2.645±0.005 g/cm ³	2.727±0.004 g/cm ³	2.717±0.002 g/cm ³

Regardless of the heat treatment, the density of components produced by additive manufacturing is about 96 % of the density of components produced by subtractive manufacturing. With the hybrid approach, as expected, the density gets close to that of the AW-6082 aluminium alloy. In hybrid samples, the application of heat treatment decreases the density. However, this effect is not the same on the additively manufactured ones, where density was independent on the heat treatment applied.

2.4.2. Thermal properties

Although thermal properties of an equivalent aluminium bulk material may be known, the use of additive manufacturing as processing technique can result in different values. Uncertainties in the thermal properties may induce under or overvalued results in thermal management applications, when predicted by numerical simulations [36]. For this reason, to better understand the material and bring the posterior simulation processes as close as possible to reality, its thermal characterization is an important step.

Specific heat capacity

Specific heat capacity is the quantification of energy required to increment material's temperature in one degree. Literature values of specific heat capacity reported for AlSi10Mg additively manufactured alloy vary from about 0.73 J/kg°C to 1.10 J/kg°C, depending on the test temperature [37–39].

In this work, specific heat capacity under constant pressure was measured using a differential scanning calorimeter (DSC) (Netzsch 200 F3) at the 30 °C – 200 °C temperature range, with a heating rate of 10 °C/min and in isothermal period of two minutes at the beginning and at the end of the test. Heat flow signals for the sample and the sapphire (a calibration standard of known specific heat capacity) are compared, according to ASTM E1269 [27] and heat capacity is given by Equation 2-2, where c_p and $c_{p,s}$ represent the specific heat of the sample and the sapphire, m and m_s represent the masses and \dot{Q} , \dot{Q}_s and \dot{Q}_b represent the signal obtained by DSC (in mW) for the sample, sapphire and baseline, respectively.

Equation 2-2. Heat capacity using DSC signal

Representative curves of specific heat capacity along temperature recorded for conventionally, additively and hybrid manufactured specimens is shown in Figure 2-6 and raw data are available in Appendix 3.

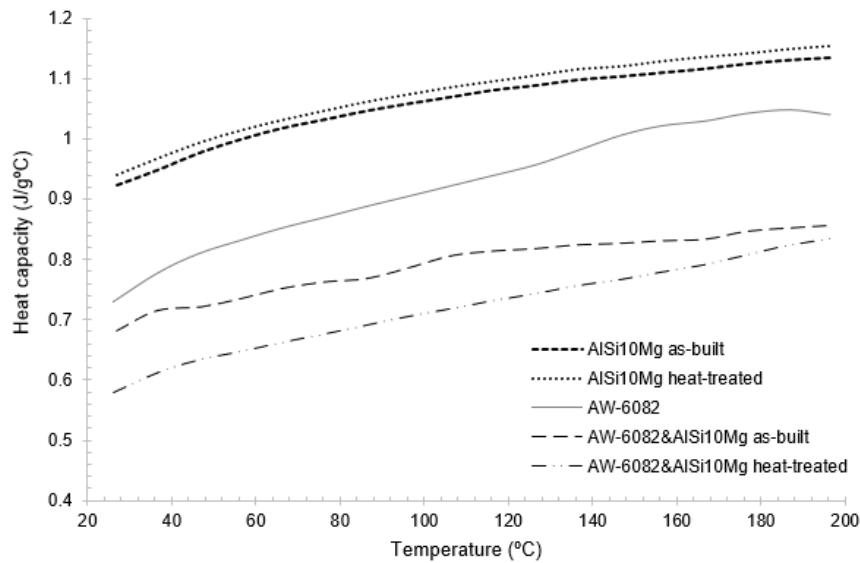


Figure 2-6. Representative curves of specific heat capacity vs temperature recorded for conventionally, additively and hybrid manufactured specimens.

As expected, specific heat capacity increases with temperature for all cases. AISi10Mg aluminium alloys have a higher specific heat capacity, mainly in heat-treated samples. Specific heat capacity of AW-6082 is lower. However, the lowest specific heat capacity is achieved in heat-treated hybrid samples. This means that the joint between the two materials has not so good effects on this property. Generally, a high specific heat capacity is desirable because it means that a material can absorb more energy, which may help to prevent overheating in the electronic components.

Thermal expansion

The thermal expansion describes how the size of an object changes with a change in temperature. Engine parts and heat sinks used in cars are often produced from Al-Si alloys due to their low coefficient of thermal expansion (CTE), high wear resistance and the high strength-to-weight ratio [40, 41].

Gumbleton *et al.* [41] evaluated the coefficient of thermal expansion of additively manufactured AISi10Mg aluminium alloy using microwaves techniques over a temperature range between -267 °C and 177 °C and showed that the material under test exhibits lower thermal expansion when compared with an equivalent bulk aluminium alloy ($\sim 21 \times 10^{-6} \text{ } ^\circ\text{C}^{-1}$). For higher temperatures, Strumza *et al.* [42] demonstrated that, above 400 °C, the samples showed anomalous thermal expansion attributed to thermally induced porosity¹. Based on other studies, CTE increased as the temperature increased and there is no dependence on the polar angle up to approximately 120 °C [34, 38, 43].

¹ Thermally induced porosity (TIP) is a process by which the material swells during heating when pores expand under increasing internal pressure.

In this work, the coefficient of thermal expansion (CTE) was determined through Dynamic Mechanical Analysis (DMA) using the equipment Q800 from TA Instruments. Tests were performed between 30 °C and 200 °C at a frequency of 1 Hz for three samples in each case. The change of the specimen length was electronically recorded as a function of temperature (Figure 2-7) and the calculated coefficient of thermal expansion is resumed in Table 2-5.

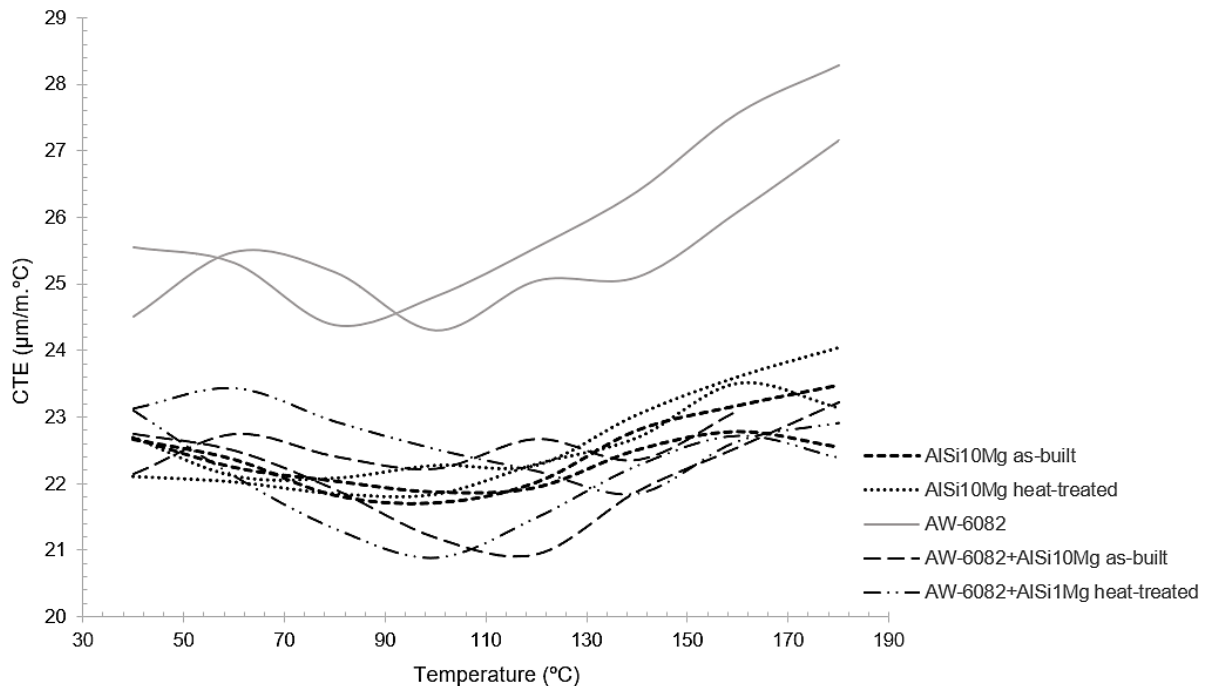


Figure 2-7. Representative curves of CTE vs temperature recorded for conventionally, additively and hybrid manufactured specimens.

Table 2-5. Averaged coefficient of thermal expansion (between 20 °C and 200 °C) for conventionally, additively and hybrid manufactured specimens.

	AW-6082	AlSi10Mg (as-built)	AlSi10Mg (heat treated)	AW-6082/AlSi10Mg (as-built)	AW-6082/AlSi10Mg (heat-treated)
CTE ($\mu\text{m}/\text{m}^\circ\text{C}$)	25.81 ± 0.56	21.92 ± 0.65	21.85 ± 0.53	22.46 ± 0.53	21.69 ± 0.77

According to Figure 2-7 and Table 2-5, AlSi10Mg and hybrid parts exhibit less a thermal expansion coefficient when compared to AW-6082 aluminium alloy, due to the high amount of silicon present [40]. Stress relief heat treatment reduced this coefficient, being this reduction more relevant in hybrid-manufactured samples.

Thermal conductivity

The complex microstructure of geometrically imperfect particles, i.e., irregular shapes and/or the presence of cavities, and eventual temperature variations, significantly influence the thermal conduction behaviour of additively manufactured parts [43, 44]. The higher conductivity of aluminium alloys allows higher thermal diffusivity and results in less heat accumulation in thermal management components [45].

According to some authors, there is a slight difference in thermal conductivity of samples built in-plane or and along build orientation, being around 20 W/m°C lower for the samples of the first case. This anisotropy may be due to several factors and can be decreased through heat treatments [34, 43]. Table 2-6 shows thermal conductivity values obtained by different authors, considering as-built samples, for a reference temperature of 150°C.

Table 2-6. Literature thermal conductivity values for different orientations.

	x-orientated	z-orientated
Yang <i>et al.</i> [34]	110 W/m°C	130 W/m°C
Strumza <i>et al.</i> [43]	160 W/m°C	185 W/m°C

In this study, the thermal conductivity of the samples was measured with a hot disk analyser TPS 2500S. The hot disk method uses a flat sensor element in the shape of a double spiral that is covered on both sides with two layers of electrically insulating film [46]. During the measurements, the hot disk sensor is sandwiched between two sample halves of the material to be investigated, each one with a plane surface (previously polished) facing the sensor, as illustrated in Figure 2-8. Samples and sensor are firmly clamped together, making sure that there is no air gap between the sensor and the sample surfaces.

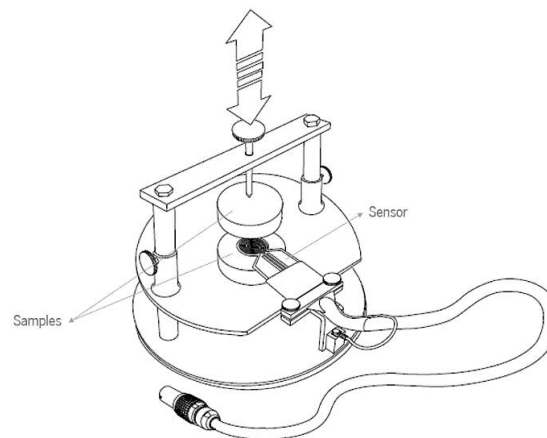


Figure 2-8. Mounting the sample and centering the sensor in hot disk thermal constants analyzer (adapted from [47]).

The sensor acts both as a heat source for increasing the temperature of the sample and as a resistance thermometer for recording the time-dependent temperature increase. During the experiment, constant electric power is supplied to the hot disk sensor. This causes a temperature increase, which is dependent on the thermal transport properties of the material. By monitoring this temperature increase over a short period of time, it is possible to evaluate the thermal conductivity of the material. The solution of the thermal conductivity equation is based on the assumption that the sensor is located in a semi-

infinite material, i.e., the thermal wave generated in an experiment must not reach the outside boundaries of the sample pieces during the transient recording [46].

In this work, considering the sample height of 20 mm, the probing depth was set at 12 mm, with a measurement time of 1 second and a heating power (P) of 1.39 W, calculated based on Equation 2-3, where r is the sensor radius and k the theoretical thermal conductivity of the material (Appendix 1).

Equation 2-3. Heating power required for the calculation of thermal conductivity [47].

Based on three measurements, thermal conductivity of conventionally AW-6082 and additively-manufactured AlSi10Mg samples was calculated and is reported in Table 2-7. In the hybrid samples, the faces in contact with the heat source are in AW-6082, taking into consideration that, in a hybrid heat sink, that will be the face in contact with the printed circuit board (PCB).

Table 2-7. Thermal conductivity reported for conventionally, additively and hybrid manufactured specimens.

	AW-6082	AlSi10Mg (as-built)	AlSi10Mg (heat treated)	AW-6082/AlSi10Mg (as-built)	AW-6082/AlSi10Mg (heat-treated)
k (W/mK)	133.2 ± 1.1	165.0 ± 2.4	165.9 ± 0.2	167.4 ± 1.0	137.4 ± 1.8

Results show that AlSi10Mg aluminium alloys have around 24 % higher thermal conductivity, regardless of the heat treatment, comparing to AW-6082 which showed the lowest thermal conductivity value. Hybrid samples presented values highly influenced by the application of the heat treatment. Moreover, it is important to highlight that stress relief heat treatment also lowered results dispersion in AlSi10Mg samples.

Thermal diffusivity

Thermal diffusivity measures the material's ability to transmit heat relative to its ability to store heat. It can be estimated based on specific heat capacity, on thermal conductivity and on density measurements at room temperature, according to the equation:

Equation 2-4. Thermal diffusivity.

For thermal management appliances, designed to carry the heat out and away from another piece of equipment, high thermal diffusivity is required to enable the quick transport of the heat. That is, part of the heat is stored, and the remaining is conducted in accordance with the thermal diffusivity of the material [48]. Some authors have already reported experimental values for AlSi10Mg thermal diffusivity,

which vary between 0.073 and 0.090, depending on the building orientation and on stress relief heat treatment application [34, 38, 46].

Table 2-8 presents the results obtained for thermal diffusivity () of the additively, conventionally and hybrid manufactured samples, applying the Equation 2-4 and considering the average values of thermal conductivity and specific heat capacity at room temperature (Appendix 3).

Table 2-8. Averaged thermal diffusivity for conventionally, additively and hybrid manufactured specimens, at room temperature.

	AW-6082	AlSi10Mg (as-built)	AlSi10Mg (heat treated)	AW-6082/AlSi10Mg (as-built)	AW-6082/AlSi10Mg (heat-treated)
(mm ² /s)	0.066	0.068	0.067	0.090	0.087

Among the five alloys considered, hybrid manufacturing shows advantages for thermal management applications, once alloys with higher thermal diffusivity can easily dissipate heat. Thermal diffusivity of hybrid samples is up to 34 % higher than thermal diffusivity of AlSi10Mg.

2.4.3. Mechanical properties

AlSi10Mg additively manufactured parts can have mechanical properties comparable to those of conventionally manufactured AlSi10Mg because of the very fine microstructure and fine distribution of the silicon phase [4, 7, 49–56]. Mechanical properties are worse when the largest dimension of the specimens coincides with the building direction, i.e., vertically orientated. This is related to the periodical remelting directions and the separation between weakly bonded layers [4, 57]. As mentioned before, to facilitate the subsequent hybrid manufacturing, this was the orientation considered in this study.

Tensile properties

There is a vast number of studies regarding tensile properties of AlSi10Mg components produced by additive manufacturing. The influence of building orientation and of the heat treatment applied as well as comparison with conventionally cast AlSi10Mg parts are the main topics reported in literature. Table 2-9 resumes some relevant work regarding tensile properties of AlSi10Mg parts vertically oriented, considering the influence of heat treatment. In most cases, the application of some post treatment caused a decrease in the strength with an increase in elongation at break. The higher the time and the temperature of the heat treatment applied, more significant are these variations.

Table 2-9. Reference studies regarding the influence of heat treatment on tensile properties.

Machine	Heat treatment	Test velocity (mm/min)	UTS ² (MPa)	Yield strength 0.2% (MPa)	Elongation at break (%)	Reference
EOS M280	N.A.	1.0	476	220	5.5	[58]
	300°C; 2h		290	175	14.2	
	530°C; 6h		245	139	18.1	
CL M2 Cusing	N.A.	0.5	468±1	-	5.4	[30]
	300°C; 2h		342±5		6.5	
	200°C; 2h		478±1		3.0	
EOS M290	N.A.	1.0	414±3	214±2	4.4±0.1	[59]
	270°C; 1.5h		378±1	215±10	4.2±0.4	
EOS M280	N.A.	2.0	351.9	242.8	2.8	[61]
	300°C; 2h		336.9	212.2	5.7	
	540°C; 2h		259.3	186.1	7.6	
	540°C; 6h		276.1	231.2	4.3	

Terrazas-Najera *et al.* [60] reported the effect that powder bed fusion process interruptions have on simple geometries made of AlSi10Mg. Systematic experiments were carried out with programmed process interruptions lasting one hour and simulating a stop to refill the system with powder, or an unexpected power outage. Mechanical and microstructural properties remained essentially unchanged.

Chan *et al.* [17, 22] studied the interface bonding integrity in terms of mechanical properties of AlSi10Mg hybrid manufactured specimens. Stress-strain curves show that there was no necking or further elongation of the specimen after the maximum tensile stress was reached. Fracture happened instantaneously straight after, at a position well away from the bonded interface. Comparison of mechanical strength of the different combinations of materials evaluated is shown in Table 2-10.

Table 2-10. Hybrid specimens' tensile properties reported by Chan *et al.* [17, 22].

Materials	Yield strength 0.2% (MPa)	UTS (MPa)	Elongation at fracture (%)
AlSi10Mg as-built	-	470 ± 2	6
AlSi10Mg heat-treated	230	350	11
AW-5083	239	312	14
AW-6061	-	311	11
Alumec 89	-	590	-
AlSi10Mg/AW-5083	200	319	7.4
AlSi10Mg/AW-6061	-	319	7.8
AlSi10Mg/Alumec89	-	481	8.2

² Ultimate tensile strength.

In this work, tensile properties of AlSi10Mg as-built and heat treated, AW-6082 and hybrid specimens as-built and heat treated were determined through uniaxial tests carried out in the Instron 5969 Universal Testing System. In each case, five specimens were tested at 1 mm/min with a 50 kN load cell at room temperature. ASTM E8 standard [25] was followed and the results are compiled in Figure 2-9 and Table 2-11.

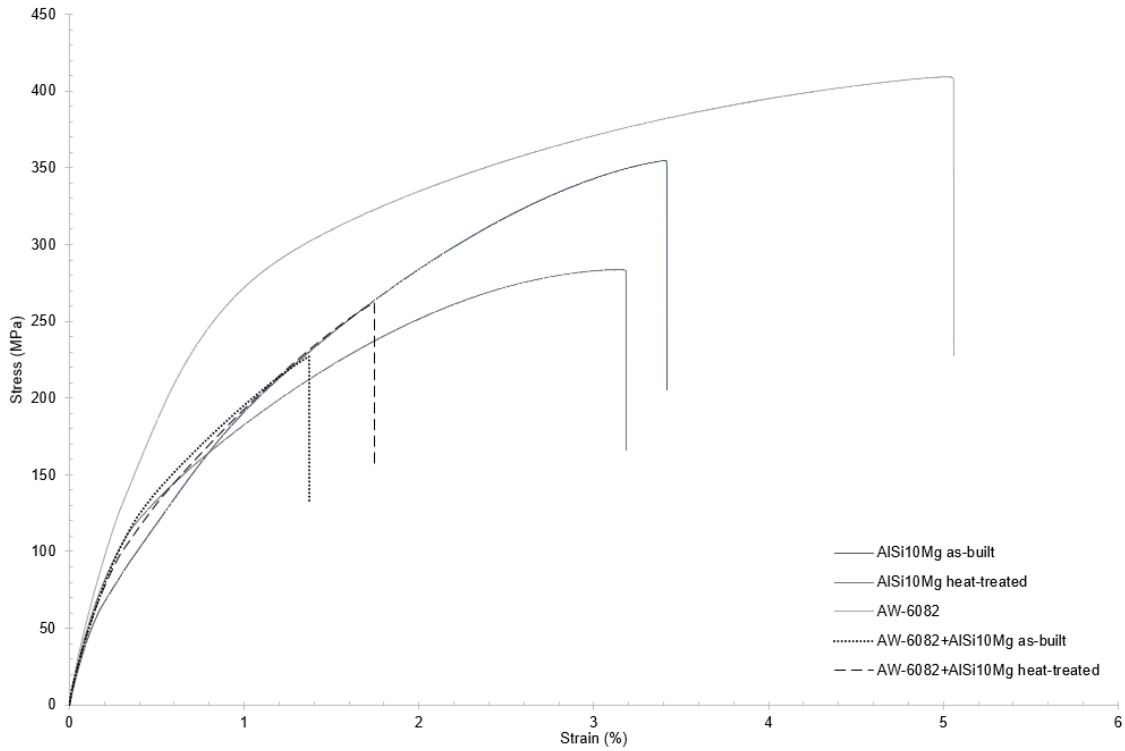


Figure 2-9. Representative tensile stress-strain curves recorded for conventionally, additively and hybrid manufactured specimens.

Table 2-11. Tensile properties of conventionally, additively and hybrid manufactured specimens.

	Young's modulus (GPa)	Yield strength ³ (MPa)	Elongation at yield (%)	Ultimate tensile strength (MPa)	Elongation at break (%)
AlSi10Mg as-built	55.6 ± 1.1	85.6 ± 4.4	0.27 ± 0.02	336.0 ± 12.2	3.56 ± 0.37
AlSi10Mg heat-treated	64.9 ± 0.3	111.5 ± 9.4	0.30 ± 0.06	322.3 ± 26.3	3.29 ± 0.40
Datasheet values ⁴	≈ 75	205 ± 3	-	344 ± 2	6 ± 1
AW-6082	83.7 ± 1.3	182.7 ± 10.7	0.62 ± 0.06	422.0 ± 7.9	4.99 ± 0.79
Datasheet values	≈ 70	110 - 260	-	205 - 310	8 - 12
AW-6082/AlSi10Mg as-built	59.4 ± 0.5	102.5 ± 9.7	0.29 ± 0.07	227.0 ± 19.3	1.32 ± 0.63
AW-6082/AlSi10Mg heat-treated	59.7 ± 1.1	88.4 ± 8.9	0.27 ± 0.05	268.2 ± 12.3	1.76 ± 0.38

³ At 2 % of strain.

⁴ After the recommended stress relief heat treatment.

By analysing the data, the tensile properties of specimens produced by additive manufacturing are improved when heat treatment is applied. Young's modulus and yield strength increase by approximately 17 % and 30 %, respectively. Contrarily, the properties at break suffer a slight decrease of 4 % in ultimate tensile stress and 7% in the respective strain. By images acquired with Leica DMS1000 low-magnification microscope after rupture (Figure 2-10), differences are visible in the specimen shell which, after heat treatment, appears to have less voids.

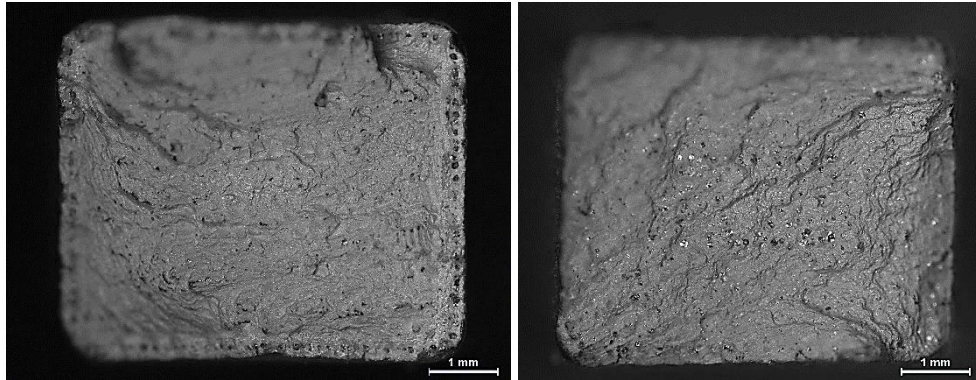


Figure 2-10. Low-magnification microscope images of AISi10Mg specimens before (left) and after (right) heat treatment.

With bare eye, the rupture of the hybrid specimens occurred, in all cases, in the interface between the two manufacturing methods. However, by images acquired with Leica DMS1000 low-magnification microscope after rupture, it is concluded that, in the conventional half, some characteristic details of the additive manufacturing process are visible, which indicates that the rupture occurred in the interface area, after the first additive manufacturing layers (Figure 2-11).

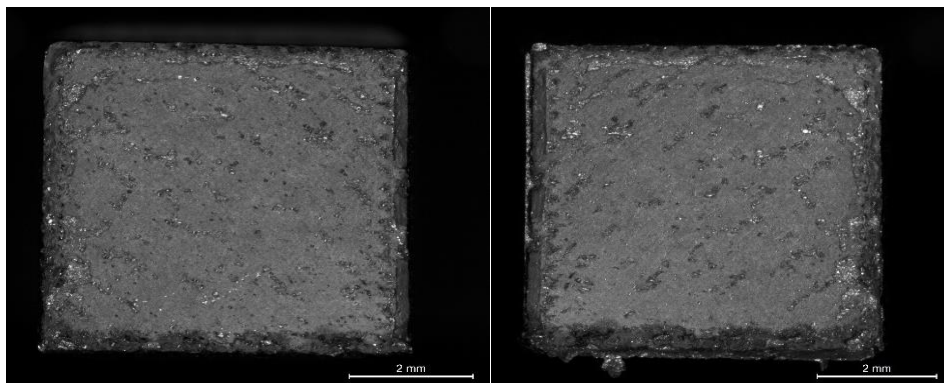


Figure 2-11. Microscopic observation of additive (left) and conventional (right) parts of an as-built AW-6082+AlSi10Mg specimen, after the tensile test.

Mode-I fracture properties

AlSi10Mg PBF samples can revealed similar fracture toughness results as conventional bulk materials, namely toughness (K_{Ic}) values in the range from 36 to 60 $\text{MPa}\sqrt{\text{m}}$ [61, 62]. According to Araújo *et al.* [63], the application of a stress relief heat treatment can improve fracture toughness.

In this work, fracture toughness of AlSi10Mg as-built and heat treated, AW-6082 and hybrid as-built and heat treated specimens was evaluated through samples fabricated according to ASTM E-399 standard [26] and were subject to mode-I fracture toughness tests. The notches were implemented in a subsequent milling procedure and the evaluation was undertaken as outlined in the standard. Instron 5969 Universal Testing System with a maximum load of 50 kN was utilized. The tensile test was carried out with a crosshead speed of 1 mm/min. The crack-mouth opening displacement was measured immediately after the test using a Leica DMS1000 low-magnification microscope and ImageJ software.

According to ASTM-E399 standard [26], the specimens' fracture toughness is calculated according to Equations 2-5 and 2-6, for which P_Q is calculated by evaluating the intersection point between the original load-displacement curve and a 95 % secant line, based on the elastic gradient of the load–displacement curve. P_Q is subsequently used to calculate K_Q . Moreover, B is the specimen thickness, W the specimen width and a the crack size.

Equation 2-5. Fracture toughness.

$$K_Q = \frac{P_Q}{B\sqrt{W-a}}$$

Equation 2-6. Coefficient crack-size/specimen-width.

$$Y = \frac{1.99 - 0.41\left(\frac{a}{W}\right) + 0.72\left(\frac{a}{W}\right)^2 - 0.21\left(\frac{a}{W}\right)^3}{1 - 2\left(\frac{a}{W}\right)}$$

If the conditions of Equation 2-7 were valid, the fracture toughness values are deemed effective and . In this work, both validity requirements were valid in all cases and mode-I fracture results are compiled in Figure 2-12 and Table 2-12.

Equation 2-7. Conditions to deem when calculating fracture toughness.

$$\frac{K_Q}{\sigma_{UTS}} \leq 1 \quad \text{and} \quad \frac{K_Q}{\sigma_{UTS}} \leq 1$$

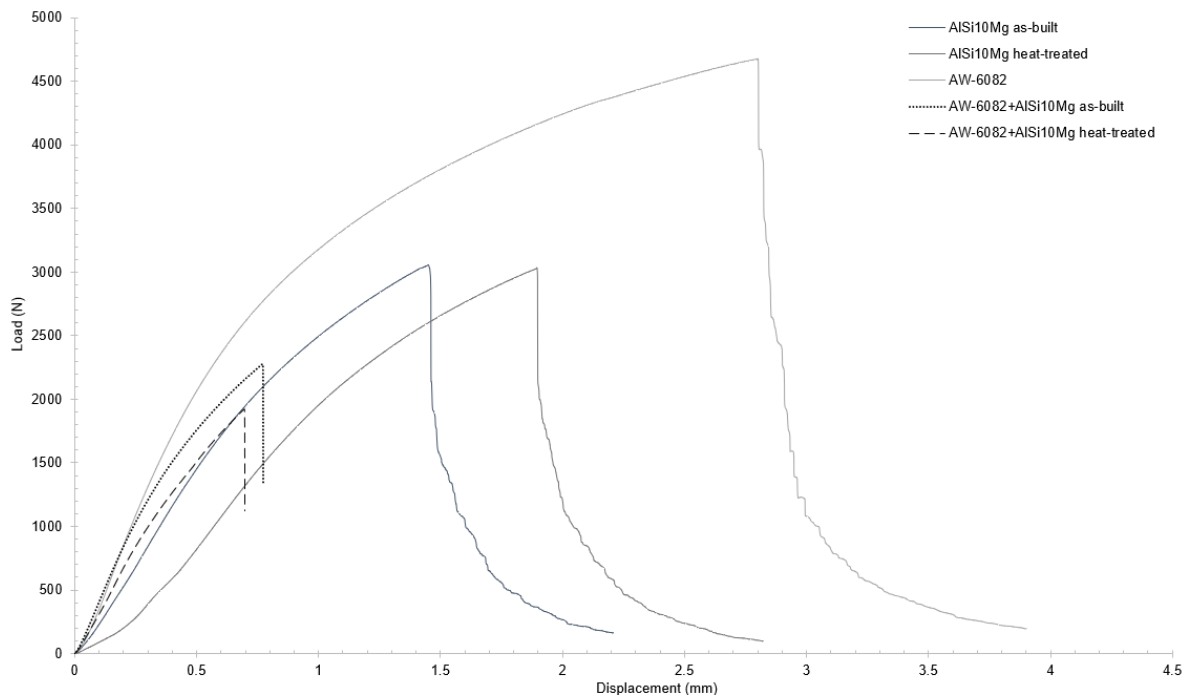


Figure 2-12. Representative load-displacement curves recorded for conventionally, additively and hybrid manufactured specimens on mode-I fracture testes.

Table 2-12. Mode-I fracture properties of conventionally, additively and hybrid manufactured specimens.

	Maximum stress (σ_{max}) (MPa)	Displacement on σ_{max} (mm)	Young's modulus (GPa)	Crack size (mm)	K_{Ic} (MPa \sqrt{m})
AISi10Mg as-built	41.5 ± 2.1	1.43 ± 0.14	1.95 ± 0.30	22.4 ± 0.8	50.3 ± 8.2
AISi10Mg heat-treated	41.6 ± 0.9	1.77 ± 0.19	1.08 ± 0.15	20.8 ± 0.2	43.0 ± 1.9
AW-6082	86.9 ± 4.3	3.00 ± 0.52	3.37 ± 0.53	21.2 ± 1.3	44.8 ± 9.0
AW-6082 + AISi10Mg As-built	24.3 ± 5.1	0.73 ± 0.26	3.23 ± 0.40	21.5 ± 1.9	27.3 ± 6.3
AW-6082 + AISi10Mg Heat-treated	21.9 ± 2.4	0.82 ± 0.24	2.28 ± 0.28	22.5 ± 1.9	25.5 ± 5.2

From the analysis of the results, it was verified that fracture toughness under mode I and the maximum supported stress of the hybrid specimens are lower than those of the specimens produced by a single manufacturing method, even though the crack propagation remains similar. The application of the stress relief heat treatment on the hybrid specimens slightly decreased the maximum stress and fracture toughness.

Through images acquired with Leica DMS1000 low magnification microscope (Figure 2-13), on the hybrid specimens, the crack propagated steadily and uniformly on the additive manufacturing side, regardless of the application of the stress relief heat treatment. These conclusions are in accordance with what was verified in the tensile tests (Figure 2-11).

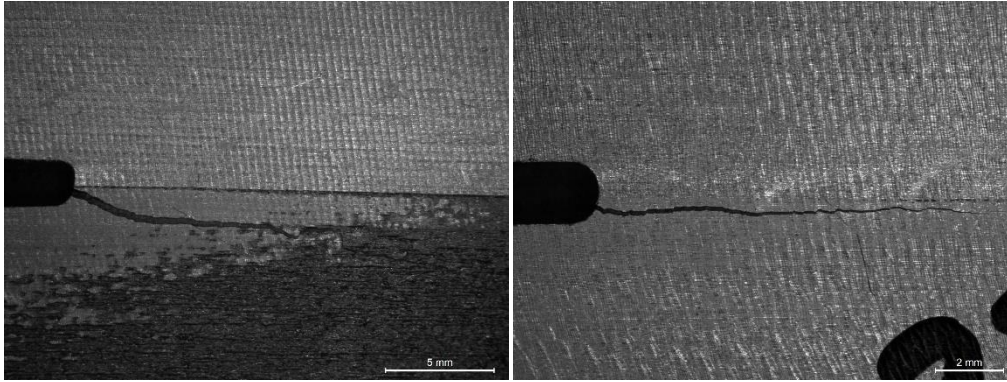


Figure 2-13. Crack propagation on a hybrid specimen without (left) and with heat treatment (right), after the mode I fracture test.

Compressive properties

Most of the compressive studies considering AlSi10Mg aluminium alloy have been directed for cellular lattice structures [64–69] or other similar and lightweight structures that exhibit a relatively high impact energy absorption [70, 71]. One of the first compression studies using solid blocks was done by Hitzler *et al.* [55]. According to their results, the obtained compressive modulus exceeded not only the equivalent tensile modulus but also the compressive modulus of the conventionally fabricated bulk material. Results were similar for yield and fracture strengths. Aboulkhair *et al.* [72] recorded significantly higher compressive yield strength for the as-built material, when compared with heat treated (T6⁵) samples. Nevertheless, both as-built and heat-treated materials demonstrated the ability to withstand high compressive strains as they barrelled and buckled during compression with no evidence of fracture. They also verified that porosity was not critical because the nature of loading tends to close the pores, consolidating the defected regions.

In this work, compressive properties of AlSi10Mg as-built and heat treated, AW-6082 and hybrid specimens as-built and heat treated were determined through uniaxial tests carried out in the Instron 5969 Universal Testing System. In each case, five specimens were tested at 1 mm/min with a 50 kN load cell at room temperature, up to the limit of the load cell. ASTM E9 standard [24] was followed and the results are compiled in Figure 2-14 and Table 2-13.

⁵ T6 heat treatment is a two-phase process which is applied to aluminium alloys to increase the strength of the alloy.

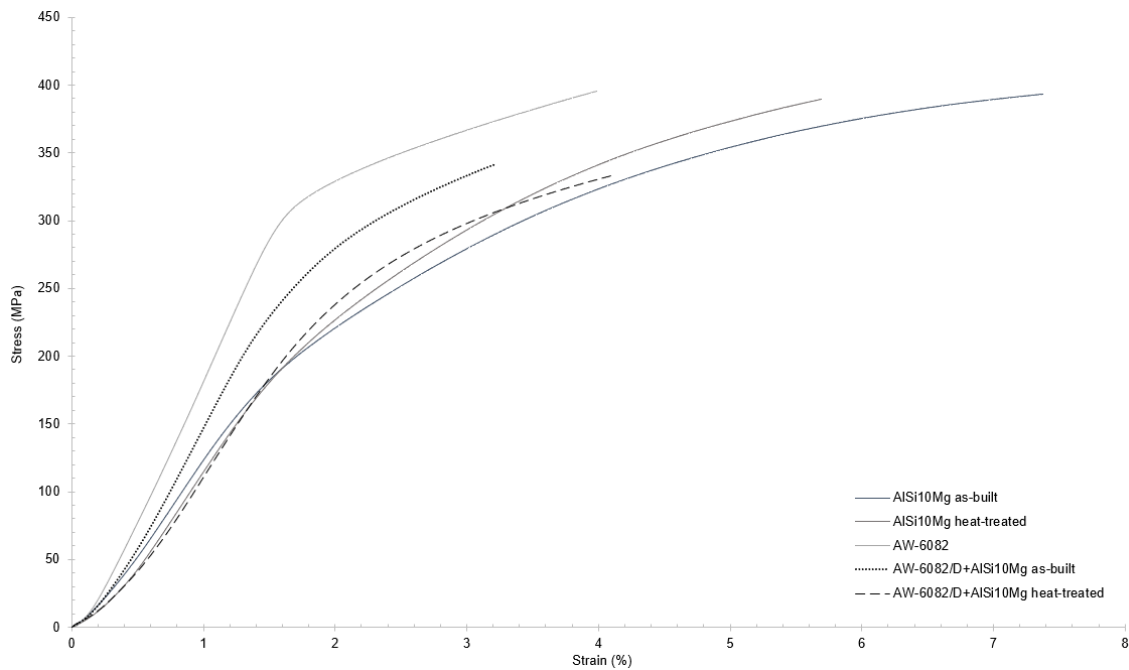


Figure 2-14. Representative compressive stress-strain curves recorded for conventionally, additively and hybrid manufactured specimens.

Table 2-13. Compressive properties for conventionally, additively and hybrid manufactured specimens.

	Compressive modulus (GPa)	Yield strength ⁶ (MPa)	Elongation at yield (%)
AISi10Mg as-built	13.3 ± 1.3	241.2 ± 14.7	2.31 ± 0.25
AISi10Mg heat-treated	14.3 ± 0.4	252.2 ± 9.2	2.43 ± 0.11
AW-6082	19.1 ± 0.6	328.5 ± 7.8	2.06 ± 0.07
AISi10Mg+AW-6082 as-built	16.9 ± 0.5	303.5 ± 10.3	2.37 ± 0.14
AISi10Mg+AW-6082 heat treated	12.9 ± 3.1	298.8 ± 7.0	2.90 ± 0.27

Regarding compressive properties, there are not conclusive differences in the performance of AISi10Mg specimens if the heat treatment is applied. If, on the one hand, there was a slight increase in the yield strength and ductility of the specimen ($\approx 5\%$), on the other, compressive modulus decreased by about 9%. In the case of hybrid specimens, heat treatment caused a decrease in both. Even so, the compressive properties of hybrid specimens are up to 25% higher to those of AISi10Mg. So, it is advantageous to apply hybrid manufacturing techniques in parts that will be subjected to compressive loads. Moreover, in none of the cases the specimen fractured after the end of the test, that is, both materials showed a high capacity to resist compressive stresses, when compared to tensile stimuli. The loading direction tends to close the pores (calculated before as 4%), consolidating the specimen before failure. However, the compression modulus fell short of the tensile modulus.

⁶ At 0.2% of strain.

Case study

Considering these mechanical results, a complex and functional part was developed and produced by hybrid manufacturing to validate the application of additive manufacturing technologies for restoration of parts and the feasibility of hybrid manufacturing. A three-point flexural test (3PB), combining tensile and compressive loads, was done on an AW-6082 aluminium crankset. A Shimadzu AGS-X universal testing machine with a load cell of 50 kN, at a constant crosshead rate of 1 mm/min was used to run the test (Figure 2-15). The fixed supports were located 110 mm to the left and 35 mm to the right of the load application point and the test stopped when the displacement was maximum.



Figure 2-15. Crankset at the beginning (left) and at the end (right) of the three-point flexural test.

At the end of the test, only 40 mm of the initial crankset were undamaged (Figure 2-16). The crankset was grinded until this length, removing the deformed fragment, and rebuilt by additive manufacturing with the silicon aluminium alloy. It was not considered the stress relief heat treatment on the hybrid crankset due to the mechanical results mentioned before.

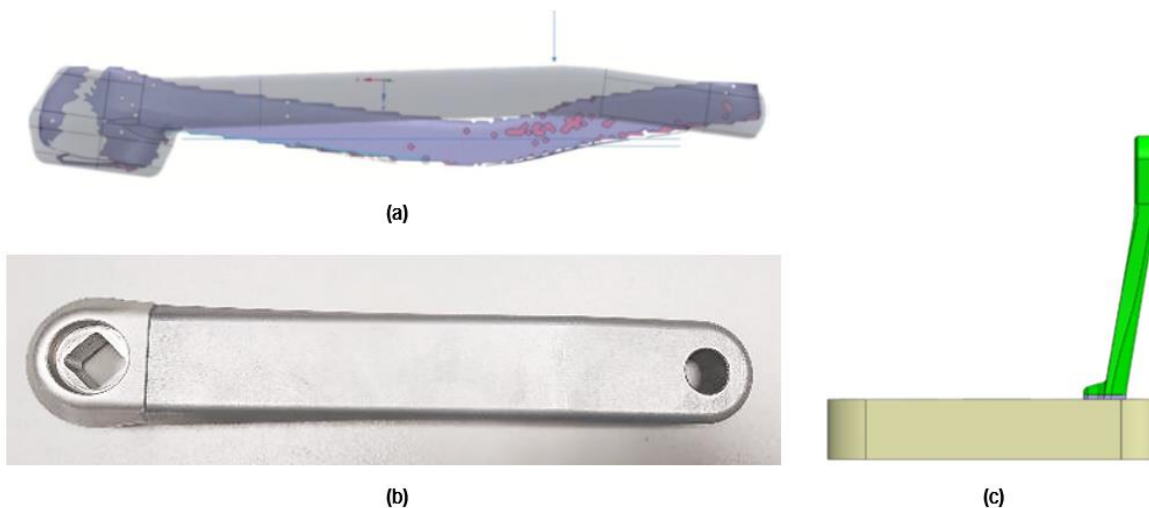


Figure 2-16. Evaluation of undamaged crankset.

According to load-displacement curves (Figure 2-17), AW-6082 crankset presented a higher resistance to bending and a higher ductility. Nevertheless, stiffness was similar in both cases. However, when hybrid crankset was tested, rupture occurred in additive manufacturing area, near the load application point, and not in the join between the original part and the repaired one. So, metallic powder-

bed fusion additive manufacturing technologies could have a significant role in the building of circular economy once the bonding between the two alloys in the interface zone of the repaired crankset was strong enough to withstand the designed loads and the failure occurred outside it.

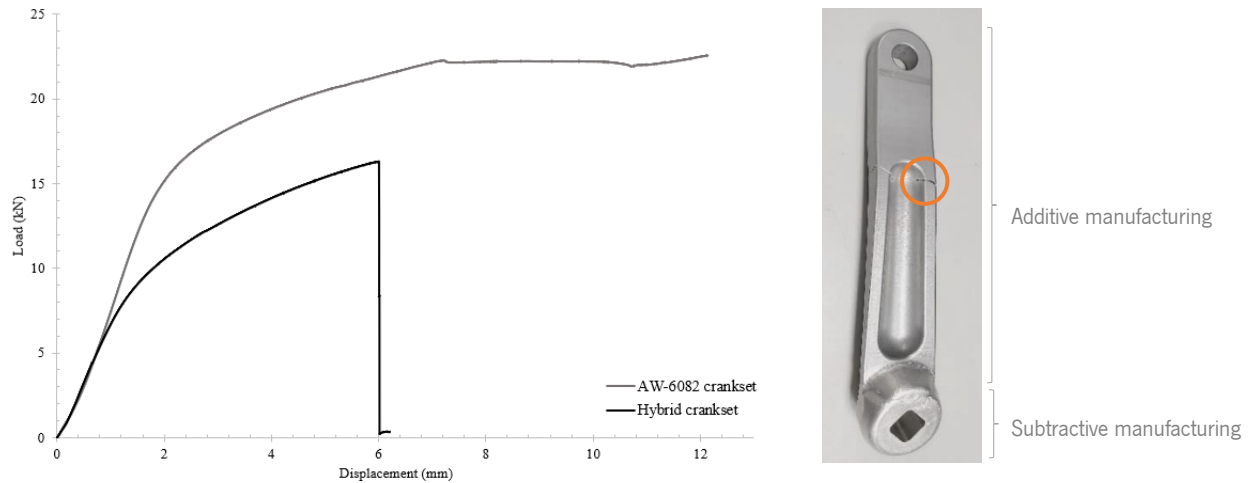


Figure 2-17. Load-displacement curves for AW-6082 and hybrid cranksets (left) and the damaged hybrid crankset (right) after the three-point flexural test.

2.4.4. Dimensional and geometrical properties

To assess the ability of the PBF system to produce parts with dimensional and geometric accuracy, a test artifact developed by the National Institute of Standards and Technology (NIST) and shown in Figure 2-18. Test artifact and measured dimensional and geometric elements. was considered [73]. The test artifact with main dimensions 100×100 mm was produced in the centre of the construction platform of Concept Laser M2 Cusing equipment in AISi10Mg, considering the illustrated xy axis system. After production, the stress relief heat treatment was not applied as it has no influence on dimensional and geometric properties.

The test artifact was analysed by Computed Tomography (CT) in the equipment Zeiss Metrotom 800 225 kV, in measurements at 120 kV and 1000 μ A, considering 2500 projections. The main dimensional and geometric characteristics of the artifact were determined through an average of five measurements per geometric element (Figure 2.18), according to the criteria proposed by the NIST institute, using the INSPECTplus software. The measurements and respective standard deviations for each geometric element are summarized in Table 2-14.

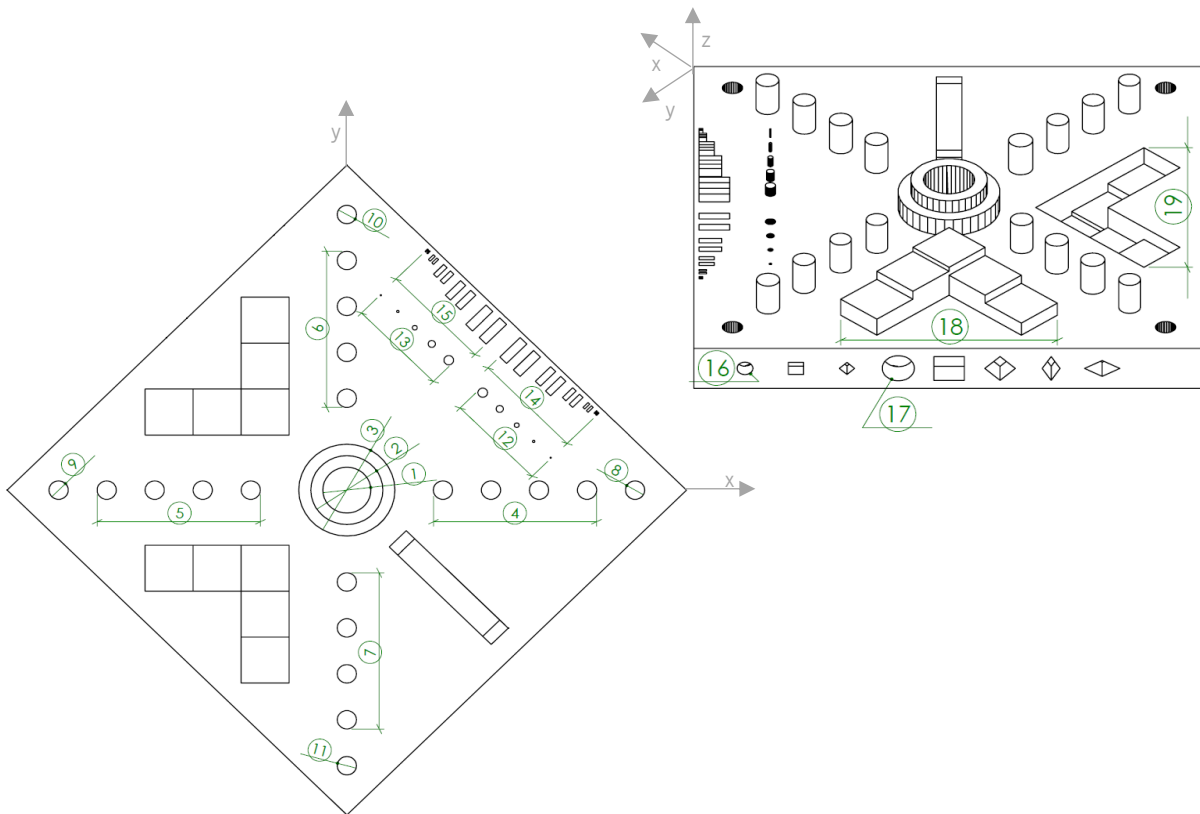


Figure 2-18. Test artifact and measured dimensional and geometric elements.

By analyzing the test artifact (Table 2-14), its main dimensions were 0.6 mm below the nominal (i.e., shortening of 0.6 %). It was found that the holes with better roundness and smaller dimensional deviations are in the third quadrant of the part. The same was not concluded regarding the production of pins, where the best results were verified on the positive side of x-axis. Due to the absence of support, the side holes (16 and 17) are better produced with smaller diameters. Concerning the central shafts, both diameters and roundness were better in the inner cylinder and hole (1 and 2) than in the outer cylinder (3).

Through Figure 2-19, the percentage deviation was minimal in the 1.50 mm holes and 2.00 mm pins. The equipment was not able to produce, in any case, holes and pins with a diameter of 0.25 mm. Holes and pins with a diameter of 0.50 mm were produced, albeit with high dimensional deviations. In general, roundness is better in holes than in pins.

Regarding thin walls, percentage deviation in thickness is smaller for thicker walls (Figure 2-20) and, for minimum thicknesses, percentage deviations are significant. As with the holes and pins, the equipment did not produce walls with thickness of 0.25 mm. The parallelism between thin walls was the geometric parameter with most variation, being worse in positive walls and critical in 0.5 mm thick walls (Figure 2-21).

Table 2-14. Dimensional and geometric properties of the test artifact produced by additive manufacturing in AlSi10Mg, without stress relief heat treatment.

		Main dimensions									
		Nominal dimensions (mm)					100.00 × 100.00				
Actual dimensions	Averaged (mm)	99.44±0.01 × 99.41±0.01									
	Maximum deviation (%)	-0.59									
Average parallelism		0.34 ± 0.06									

		Holes											
		1	8	9	10	11	13				16	17	
Nominal diameter (mm)		10.00	4.00				2.00	1.50	1.00	0.50	0.25	3.00	6.00
Actual diameter	Averaged (mm)	9.98 ±0.00	3.95 ±0.00	4.01 ±0.00	4.04 ±0.00	4.03 ±0.00	1.94 ±0.00	1.49 ±0.01	0.97 ±0.00	0.47 ±0.00		2.99 ±0.01	5.97 ±0.01
	Maximum deviation (%)	-0.19	-1.30	+0.43	+1.00	+0.70	-3.40	-1.00	-3.10	-6.20		-0.50	-0.63
Average circularity		0.10 ±0.01	0.06 ±0.01	0.06 ±0.00	0.05 ±0.01	0.04 ±0.01	0.07 ±0.04	0.07 ±0.02	0.04 ±0.01	0.04 ±0.00		0.12 ±0.02	0.23 ±0.05

		Pins										
		2	3	4	5	6	7	12				
Nominal diameter (mm)		15.00	20.00	4.00				2.00	1.50	1.00	0.50	0.25
Actual diameter	Averaged (mm)	14.90 ±0.01	19.81 ±0.09	3.95 ±0.03	3.93 ±0.03	3.93 ±0.01	3.90 ±0.00	2.01 ±0.01	1.44 ±0.00	0.91 ±0.00	0.58 ±0.00	
	Maximum deviation (%)	-0.70	-1.19	-2.00	-2.40	-2.18	-2.53	+0.75	-4.13	-8.70	+16.4	
Average circularity		0.09 ±0.01	0.11 ±0.01	0.09 ±0.00	0.10 ±0.01	0.11 ±0.00	0.09 ±0.00	0.08 ±0.03	0.07 ±0.02	0.06 ±0.02	0.05 ±0.01	

		Positive thin walls					Negative thin walls				
		14					15				
Nominal thickness (mm)		2.00	1.50	1.00	0.50	0.25	2.00	1.50	1.00	0.50	0.25
Actual thickness	Averaged (mm)	2.00 ±0.01	1.52 ±0.01	1.04 ±0.01	0.65 ±0.01		2.08 ±0.01	1.58 ±0.03	1.08 ±0.00	0.58 ±0.00	
	Maximum deviation (%)	+0.70	+1.93	+5.30	+33.4		+4.30	+6.53	+8.20	+16.8	
Average parallelism between walls		4.54 ±0.70	3.97 ±0.40	3.05 ±0.60	9.82 ±1.32		0.71 ±0.70	1.11 ±0.19	0.38 ±0.20	0.91 ±0.57	

		Positive steps					Negative steps				
		18					19				
Nominal height (mm)		3.00	4.00	5.00	6.00	7.00	3.00	4.00	5.00	6.00	7.00
Actual height	Averaged (mm)	2.96 ±0.07	3.97 ±0.05	4.87 ±0.02	5.88 ±0.03	6.92 ±0.05	3.03 ±0.05	4.08 ±0.07	5.14 ±0.07	6.18 ±0.07	7.22 ±0.02
	Maximum deviation (%)	-3.97	-1.15	-3.08	-2.27	-2.41	+3.17	+4.75	+5.40	+4.48	+3.74
Average flatness		0.05 ±0.01	0.05 ±0.03	0.02 ±0.01	0.03 ±0.01	0.03 ±0.01	0.06 ±0.02	0.10 ±0.02	0.13 ±0.03	0.09 ±0.03	0.09 ±0.03

These dimensional results allowed to conclude that, if an over thickness may be necessary to posterior finishing processes (e.g., machining), 0.60 mm is the minimum that must be considered. This conclusion is based on the highest nominal deviation, obtained for the main dimensions of the test artifact (Table 2-13).

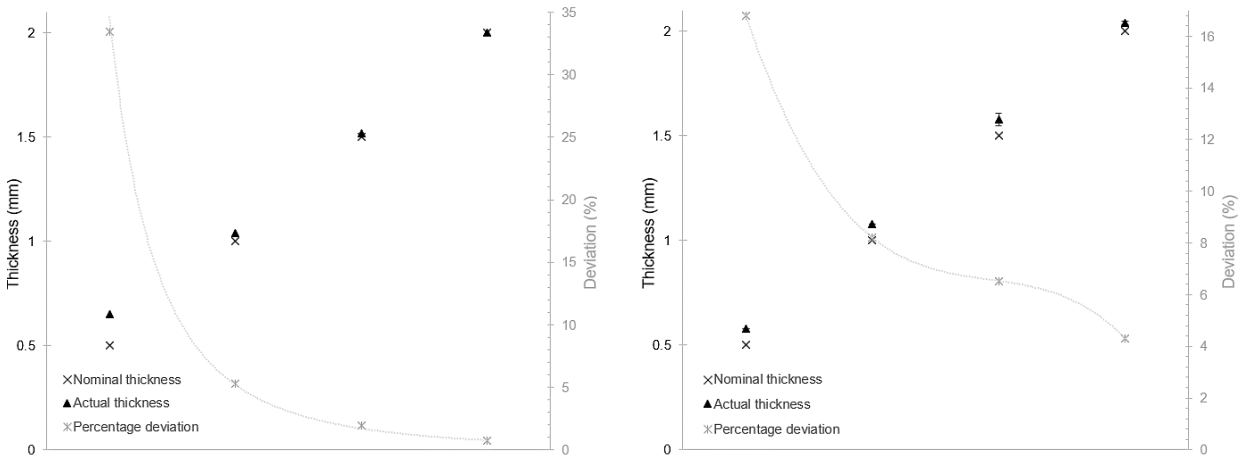


Figure 2-19. Analysis of holes (left) and pins (right).

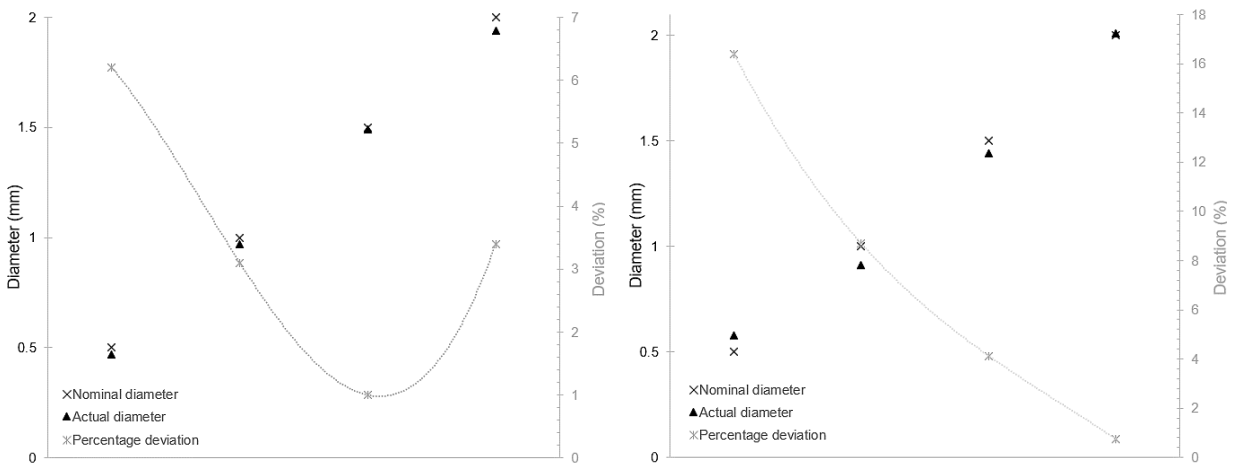


Figure 2-20. Analysis of positive (left) and negative (right) thin walls.

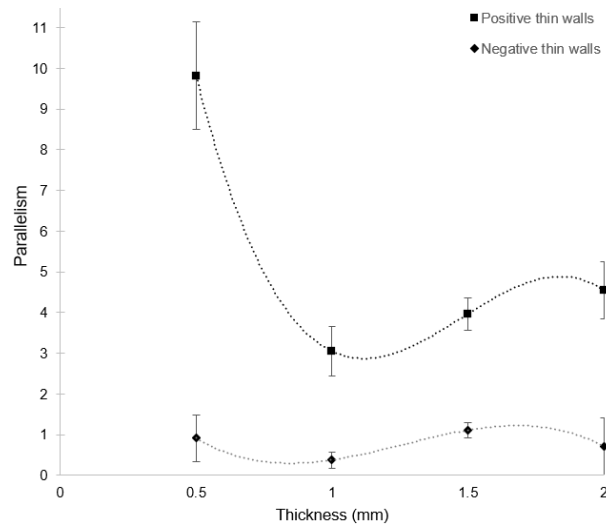


Figure 2-21. Parallelism of thin walls as a function of thickness.

2.5. Final remarks of this chapter

In this chapter, hybrid aluminium parts were successfully additively fabricated by depositing AlSi10Mg on AW-6082 pre-machined substrates. These parts were physically, mechanically and thermally characterised, considering the influence of a stress relief heat treatment on the parts with AlSi10Mg, as recommended by the supplier, and the main conclusions are as follows:

- Š The density of the components produced by additive manufacturing was about 96 % of the density of the components produced by subtractive manufacturing. With the hybrid approach, as expected, the density got close to that of the AW-6082 aluminium alloy. Stress relief heat treatment had no relevant effect.
- Š In thermal properties evaluated (specific heat capacity, CTE, thermal conductivity and thermal diffusivity), the hybrid manufacturing samples provided positive results, i.e., higher thermal conductivity and higher thermal diffusivity, when compared with the simple additive or conventional samples. Stress relief heat treatment had not a relevant effect on these properties.
- Š Regarding mechanical properties, tensile specimens fractured near the interface, after the initial layers of the additive manufacturing process, as reported in previous studies [10,16]. When compressive loads were applied, it was advantageous to apply hybrid manufacturing techniques once compressive properties of as-built hybrid specimens were up to 27 % higher than those of AlSi10Mg. Here, it was not advantageous to apply the stress relief heat treatment.
- Š Applying this knowledge to a case study, the AW-6082 crankset presented a higher resistance to bending and higher ductility. When the hybrid crankset was tested, rupture occurred in the additive manufacturing area and not in the interface between the original part and the repaired one. Nevertheless, stiffness was similar in the two cases.
- Š In terms of dimensional properties, positive features (pins or thin walls) were below the nominal up to 0.20 mm (considering the higher dimensions). With respect to negative features (holes or thin walls), which presented greatest dimensional accuracy, the maximum deviation was of 0.08 mm. In any case, holes, pins or thin walls with diameters or thicknesses less than 0.50 mm were not produced. These dimensional results allowed to conclude that, if an over thickness may be necessary to posterior finishing processes, 0.6 % is the minimum that must be considered.

In this sense, the hybrid manufacturing concept can be successfully applied with affirmative results, mainly in parts for thermal management applications or subjected to compressive stimuli. The application of the stress relief heat treatment did not show advantages in mechanical properties.

Answering the research question: “How much hybrid manufacturing, that is, combining subtractive and additive technologies, contributes to the production of sustainable aluminium parts?”, with hybrid manufacturing we can produce parts with up to 34 % better thermal performance (i.e., higher thermal diffusivity) and 27 % higher than those of AlSi10Mg in terms of compressive response. In addition, according to the case study presented, metallic PBF technologies could have a significant role in the building of a circular economy.

2.6. References

- [1] Kvačakaj T, Bidulský R. *Aluminium Alloys, Theory and Applications*. Rijeka, Croatia: InTech, 2011. Epub ahead of print 2011. DOI: 10.1016/j.ultras.2011.07.008.
- [2] Kaufman JG, Rooy EL. *Aluminium Alloy Castings: Properties, Processes and Applications*. 2009. Epub ahead of print 2009. DOI: 10.1016/j.matdes.2009.05.042.
- [3] Concept Laser. CL 30AL / CL 31AL Aluminium alloys, www.concept-laser.de (2017).
- [4] Wang L, Jiang X, Guo M, et al. Characterisation of structural properties for AlSi10Mg alloys fabricated by selective laser melting. *Materials Science and Technology (United Kingdom)* 2017; 33: 2274–2282.
- [5] Liu A, Chua CK, Leong KF. Properties of test coupons fabricated by selective laser melting. *Key Eng Mater* 2010; 447 448: 780–784.
- [6] Redwood B, Schöffner F, Garret B. *The 3D Printing Handbook - Technologies, design and applications*. 1st ed. Amsterdam: 3D Hubs, 2018.
- [7] Read N, Wang W, Essa K, et al. Selective laser melting of AlSi10Mg alloy: Process optimisation and mechanical properties development. *Mater Des* 2015; 65: 417–424.
- [8] Schroepfer D, Treutler K, Boerner A, et al. Surface finishing of hard-to-machine cladding alloys for highly stressed components. *International Journal of Advanced Manufacturing Technology* 2021; 114: 1427–1442.
- [9] Boivie K, Sørby K, Brøtan V, et al. Development of a hybrid manufacturing cell: Integration of Additive Manufacturing with CNC Machining. *22nd Annual International Solid Freeform Fabrication Symposium - An Additive Manufacturing Conference, SFF 2011* 2011; 153–163.
- [10] Homar D, Čerče L, Kopač J. Cooling simulation of conformal cooling injection mould insert produced by hybrid manufacturing. *Tehnicki vjesnik - Technical Gazette* 2017; 24: 981–986.
- [11] Homar D, Pušavec F. The development of a recognition geometry algorithm for hybrid-Subtractive and additive manufacturing. *Strojnicki Vestnik/Journal of Mechanical Engineering* 2017; 63: 151–160.
- [12] Marin F, de Souza AF, Ahrens CH, et al. A new hybrid process combining machining and selective laser melting to manufacture an advanced concept of conformal cooling channels for plastic injection molds. *International Journal of Advanced Manufacturing Technology* 2021; 113: 1561–1576.
- [13] Azizi H, Ghiaasiaan R, Prager R, et al. Metallurgical and mechanical assessment of hybrid additively-manufactured maraging tool steels via selective laser melting. *Addit Manuf* 2019; 27: 389–397.
- [14] Cyr E, Asgari H, Shamsdini S, et al. Fracture behaviour of additively manufactured MS1-H13 hybrid hard steels. *Mater Lett* 2018; 212: 174–177.
- [15] Santos LMS, de Jesus J, Ferreira JM, et al. Fracture toughness of hybrid components with Selective Laser Melting 18Ni300 steel parts. *Applied Sciences (Switzerland)*; 8. Epub ahead of print 2018. DOI: 10.3390/app8101879.
- [16] Kučerová L, Zetková I, Jeníček Š, et al. Hybrid parts produced by deposition of 18Ni300 maraging steel via selective laser melting on forged and heat treated advanced high strength steel. *Addit Manuf*, 32. Epub ahead of print 2020. DOI: 10.1016/j.addma.2020.101108.
- [17] Chan YL, Diegel O, Xu X. Evaluation of bonding integrity of hybrid-built AlSi10Mg-aluminium alloys parts using the powder bed fusion process. *Mater Today Proc* 2021; 46: 1277–1282.
- [18] Nedal Aluminium. Alloy datasheet EN AW-6061. 2005; 2939512–2939512.
- [19] Universal Afir. Especificações – ALU 5083. 2016; 5083.
- [20] Durbin Metal Industries Ltd. Aluminium Alloy ALUMEC 89. 2017; 1–21.
- [21] Totten GE, MacKenzie DS. *Handbook of Aluminium: Volume 2: Alloy Production and Materials Manufacturing*. 1st ed. New York: CRC Press, 2003.
- [22] Chan YL, Diegel O, Xu X. A machined substrate hybrid additive manufacturing strategy for injection moulding inserts. *International Journal of Advanced Manufacturing Technology* 2021; 112: 577–588.
- [23] Universal Afir. Especificações – ALU 6082.
- [24] ASTM International. Standard test methods of compression testing of metallic materials at room temperature. *Annual Book of ASTM Standards*. Epub ahead of print 1989. DOI: 10.1520/E0009-89AR00.
- [25] ASTM International. ASTM E8/E8M standard test methods for tension testing of metallic materials. *Annual Book of ASTM Standards 4* 2010; 1–27.
- [26] ASTM International. E399: Standard Test Method for Linear-Elastic Plane-Strain Fracture Toughness K_{IC} of Metallic Materials. *Annual Book of ASTM Standards* 2012; 33.
- [27] ASTM International. ASTM E1269-11 Standard Test Method for Determining Specific Heat Capacity by Differential Scanning. *ASTM Standards*. Epub ahead of print 2011. DOI: 10.1520/E1269-11.2.
- [28] ASTM International. Standard Test Method for Linear Thermal Expansion of Solid Materials by Thermomechanical Analysis. *ASTM Standards*. Epub ahead of print 2013. DOI: 10.1520/E0831-13.Copyright.
- [29] Paul MJ, Liu Q, Best JP, et al. Fracture resistance of AlSi10Mg fabricated by laser powder bed fusion. *Acta Mater* 2021; 211: 116869.

- [30] Rosenthal Y, Apelstein Y, Rosenthal I, et al. On laser powder-bed fusion of additively manufactured alsi10mg alloy: Tensile properties and structure characterization. *Annals of 'Dunarea de Jos' University of Galati, Fascicle XII, Welding Equipment and Technology* 2019; 30: 5–12.
- [31] Wong KK, Ho JY, Leong KC, et al. Fabrication of heat sinks by Selective Laser Melting for convective heat transfer applications. *Virtual Phys Prototyp* 2016; 11: 159–165.
- [32] Wits WW, Jafari D, Jeggels Y, et al. Freeform-Optimized Shapes for Natural-Convection Cooling. 2018; 2018: 1–6.
- [33] Taute C, Möller H, Du Plessis A, et al. Characterization of additively manufactured AlSi10Mg cubes with different porosities. *J South Afr Inst Min Metall* 2021; 121: 143–150.
- [34] Yang P, Deibler LA, Bradley DR, et al. Microstructure evolution and thermal properties of an additively manufactured, solution treatable AlSi10Mg part. *J Mater Res* 2018; 33: 4040–4052.
- [35] Girelli L, Giovagnoli M, Tocci M, et al. Evaluation of the impact behaviour of AlSi10Mg alloy produced using laser additive manufacturing. *Materials Science and Engineering A* 2019; 748: 38–51.
- [36] Collins IL, Weibel JA, Pan L, et al. Evaluation of additively manufactured microchannel heat sinks. *IEEE Trans Compon Packaging Manuf Technol* 2019; 9: 446–457.
- [37] Jiang X, Xiong W, Wang L, et al. Heat treatment effects on microstructure-residual stress for selective laser melting AlSi10Mg. *Materials Science and Technology (United Kingdom)* 2020; 36: 168–180.
- [38] Kim MS. Effects of processing parameters of selective laser melting process on thermal conductivity of AlSi10Mg alloy. *Materials*; 14. Epub ahead of print 2021. DOI: 10.3390/ma14092410.
- [39] Wei P, Wei Z, Chen Z, et al. Thermal behavior in single track during selective laser melting of AlSi10Mg powder. *Appl Phys A Mater Sci Process* 2017; 123: 1–13.
- [40] Wang Z, Ummethala R, Singh N, et al. Selective laser melting of aluminum and its alloys. *Materials* 2020; 13: 1–67.
- [41] Gumbleton R, Cuenca JA, Klemencic GM, et al. Evaluating the coefficient of thermal expansion of additive manufactured AlSi10Mg using microwave techniques. *Addit Manuf* 2019; 30: 100841.
- [42] Strumza E, Hayun S, Barzilai S, et al. In situ detection of thermally induced porosity in additively manufactured and sintered objects. *J Mater Sci* 2019; 54: 8665–8674.
- [43] Strumza E, Yeheskel O, Hayun S. The effect of texture on the anisotropy of thermophysical properties of additively manufactured AlSi10Mg. *Addit Manuf* 2019; 29: 100762.
- [44] Wang P, Lei H, Zhu X, et al. Influence of AlSi10Mg particles microstructure on heat conduction during additive manufacturing. *Int J Heat Mass Transf* 2019; 144: 118632.
- [45] Klingaa CG, Zanini F, Mohanty S, et al. Characterization of geometry and surface texture of alsi10mg laser powder bed fusion channels using x-ray computed tomography. *Applied Sciences (Switzerland)*; 11. Epub ahead of print 1 May 2021. DOI: 10.3390/app11094304.
- [46] Diani A, Moro L, Rossetto L. Melting of paraffin waxes embedded in a porous matrix made by additive manufacturing. *Applied Sciences (Switzerland)*; 11. Epub ahead of print 2 June 2021. DOI: 10.3390/app11125396.
- [47] Hot Disk AB. *Hot Disk Thermal Constants Analyser Instruction Manual*. 2019.
- [48] Davis G, Balasubramaniam K, Palanisamy S, et al. Additively manufactured integrated slit mask for laser ultrasonic guided wave inspection. *The International Journal of Advanced Manufacturing Technology* 2020; 110: 1203–1217.
- [49] Kempen K, Thijs L, Van Humbeeck J, et al. Mechanical Properties of AlSi10Mg Produced by Selective Laser Melting. *Phys Procedia* 2012; 39: 439–446.
- [50] Tang M, Pistorius PC. Oxides, porosity and fatigue performance of AlSi10Mg parts produced by selective laser melting. *Int J Fatigue* 2017; 94: 192–201.
- [51] Chen B, Yao Y, Song X, et al. Microstructure and mechanical properties of additive manufacturing AlSi10Mg alloy using direct metal deposition. *Ferroelectrics* 2018; 523: 153–166.
- [52] Rakesh CHS, Priyanka N, Jayaganthan R, et al. Effect of build atmosphere on the mechanical properties of AlSi10Mg produced by selective laser melting. *Mater Today Proc* 2018; 5: 17231–17238.
- [53] Raus AA, Wahab MS, Ibrahim M, et al. Mechanical and Physical Properties of AlSi10Mg Processed through Selective Laser Melting. *International Journal of Engineering and Technology* 2016; 8: 2612–2618.
- [54] Li X, Ni J, Zhu Q, et al. Structure and Mechanical Properties of the AlSi10Mg Alloy Samples Manufactured by Selective Laser Melting. *IOP Conf Ser Mater Sci Eng*; 269. Epub ahead of print 2017. DOI: 10.1088/1757-899X/269/1/012081.
- [55] Hitzler L, Schoch N, Heine B, et al. Compressive behaviour of additively manufactured AlSi10Mg. *Materwiss Werksttech* 2018; 49: 683–688.
- [56] Yan Q, Song B, Shi Y. Comparative study of performance comparison of AlSi10Mg alloy prepared by selective laser melting and casting. *J Mater Sci Technol* 2020; 41: 199–208.
- [57] Rosenthal I, Shneck R, Stern A. AlSi10Mg alloy fabricated by selective laser melting: Impact properties and fractography. *Annals of 'Dunarea de Jos' University of Galati, Fascicle XII, Welding Equipment and Technology* 2018; 2018: 5–10.
- [58] Takata N, Kodaira H, Sekizawa K, et al. Change in microstructure of selectively laser melted AlSi10Mg alloy with heat treatments. *Materials Science and Engineering A* 2017; 704: 218–228.

- [59] Patakham U, Palasay A, Wila P, et al. MPB characteristics and Si morphologies on mechanical properties and fracture behavior of SLM AlSi10Mg. *Materials Science and Engineering A* 2021; 821: 141602.
- [60] Terrazas-Najera CA, Mayoral FL, Garcia OF, et al. Effects of process interruptions on microstructure and mechanical properties of three face centered cubic alloys processed by laser powder bed fusion. *J Manuf Process* 2021; 66: 397–406.
- [61] AlRedha S, Shterenlikht A, Mostafavi M, et al. Effect of build orientation on fracture behaviour of AlSi10Mg produced by selective laser melting. *Rapid Prototyp J* 2021; 27: 112–119.
- [62] Hitzler L, Hirsch J, Schanz J, et al. Fracture toughness of selective laser melted AlSi10Mg. *Proceedings of the Institution of Mechanical Engineers, Part L: Journal of Materials: Design and Applications* 2019; 233: 615–621.
- [63] Araújo LC, Gabriel AHG, Fonseca EB da, et al. Journal Pre-proof. 213. Epub ahead of print 2021. DOI: 10.1016/j.jimecsci.2021.106868.
- [64] Yan C, Hao L, Hussein A, et al. Evaluation of light-weight AlSi10Mg periodic cellular lattice structures fabricated via direct metal laser sintering. *J Mater Process Technol* 2014; 214: 856–864.
- [65] Qiu C, Yue S, Adkins NJE, et al. Influence of processing conditions on strut structure and compressive properties of cellular lattice structures fabricated by selective laser melting. *Materials Science and Engineering A* 2015; 628: 188–197.
- [66] Amani Y, Dancette S, Delroisse P, et al. Compression behavior of lattice structures produced by selective laser melting: X-ray tomography based experimental and finite element approaches. *Acta Mater* 2018; 159: 395–407.
- [67] Liu M, Takata N, Suzuki A, et al. Development of gradient microstructure in the lattice structure of AlSi10Mg alloy fabricated by selective laser melting. *J Mater Sci Technol* 2020; 36: 106–117.
- [68] Li C, Lei H, Liu Y, et al. Crushing behavior of multi-layer metal lattice panel fabricated by selective laser melting. *Int J Mech Sci* 2018; 145: 389–399.
- [69] Suzuki A, Sekizawa K, Liu M, et al. Effects of Heat Treatments on Compressive Deformation Behaviors of Lattice-Structured AlSi10Mg Alloy Fabricated by Selective Laser Melting. *Adv Eng Mater* 2019; 21: 1–9.
- [70] Zhang Y, Liu T, Ren H, et al. Dynamic compressive response of additively manufactured AlSi10Mg alloy hierarchical honeycomb structures. *Compos Struct* 2018; 195: 45–59.
- [71] Ma C, Lei H, Hua J, et al. Experimental and simulation investigation of the reversible bi-directional twisting response of tetra-chiral cylindrical shells. *Compos Struct* 2018; 203: 142–152.
- [72] Aboulkhair NT, Maskery I, Tuck C, et al. The microstructure and mechanical properties of selectively laser melted AlSi10Mg: The effect of a conventional T6-like heat treatment. *Materials Science and Engineering A* 2016; 667: 139–146.
- [73] Moylan SP, Slotwinski J, Cooke A, et al. An Additive Manufacturing Test Artifact. *Bollettino - Societa Paleontologica Italiana* 2014; 33: 289–298.

3. HEAT SINKS

This chapter intends to answer the research questions “How much AM improves the performance of heat sinks?” and “How close are computed-aided engineering (CAE) simulations to real measurements in predicting thermal management?”. To this, different active heat sinks were evaluated via computational fluid dynamics (CFD) simulations, considering different types of cooling. The best heat sinks designs were experimentally validated on a testing apparatus to compare with the simulated results. In the end, in an action-research strategy, a case study involving an automotive central computer with a heat sink was optimized through hybrid manufacturing to reduce heat emissions to air and car weight.

3.1. Introduction

By allowing heat dissipation, heat sinks prevent overheating and play a crucial role in the device's temperature regulation. They make use of extended surfaces to increase heat dissipation from a heat source to the surroundings, providing a low thermal resistance and a low-pressure loss path between them [1]. They can be divided into two main categories: with active and with passive cooling techniques. Use of natural techniques is known as passive thermal management while forced heat dissipation, e.g., by cooling fans, improving heat transfer, is referred to as active thermal management [2–5].

The most common material for heat sinks is aluminium, offering a good balance between cost, weight and thermal conductivity [4, 6–9]. When produced by additive manufacturing (AM), with high geometric freedom and the capability to build complex internal structures, they can outperform the thermal performance of traditional aluminium heat sinks [10]. In most cases, a near fully dense structure is obtained by AM, however, in other cases, depending on the AM process parameters, a porous solid containing voids may result, being important to properly characterize them and consider this characterization in numerical simulations [9, 11–15]. Hybrid heat sinks can also be considered, combining conventional manufacturing and AM technologies [16].

Chinthavali *et al.* [12] produced the first heat sink by AM using a powder bed fusion (PBF) equipment. The strength of the heat sink produced with the AM aluminium alloy was like the strength of the heat sink produced by conventional methods, but the thermal performance was lower for low temperatures, becoming close to equal around 150 °C.

3.2. Basic theoretical framework

In thermal management systems involving heat sinks, there are two basic modes of heat transfer: conduction and convection. Conduction is the internal energy exchange between one body in perfect contact with another or from one part of a body to another part due to a temperature gradient. Convection is the energy exchange between a body and a surrounding fluid.

Conduction heat transfer, along direction n , is defined by Fourier's Law of Conduction (Equation 3-1) where k_n is the material thermal conductivity and $\frac{dT}{dn}$ is the thermal gradient in direction n . Negative sign indicates that heat flows in the opposite direction of the gradient, i.e., heat flows from hot to cold.

Equation 3-1. Fourier's Law of Conduction.

—

Convection heat transfer per unit area between surface and fluid is defined by Newton's Law of Cooling (Equation 3-2), with h the convective film coefficient, T_s the surface temperature and T_b the bulk fluid temperature.

Equation 3-2. Newton's Law of Cooling.

A heat sink works by dispersing heat to the surrounding air, keeping temperatures as low as possible to ensure the reliability and performance of the device. A quantitative measure of heat transfer efficiency can be expressed in terms of thermal resistance (θ), in °C/W, defined in Equation 3-3, where ΔT is the temperature difference between device and air temperatures and Q is the total power or rate of heat dissipation, i.e., the heat dissipated from the device [17, 18].

Equation 3-3. Thermal resistance.

—

3.3. Brief review on heat sinks designs and topology

3.3.1. Conventional heat sinks

Sometimes, choosing the type of a conventional heat sink (pins, fins or blades) is an ambiguous task. Under forced convection, Wong *et al.* [19] defended that fins are the best choice (among fins, blades and circular pins), while Abdelsalam *et al.* [20] compared in-line blades with fins and concluded that the first were better. On its turn, Jonsson and Moshfegh [21] tested different heat sinks models considering Reynolds numbers in a range between 3350 and 13400 and concluded that it is not beneficial to use pin heat sinks at higher Reynolds numbers.

Another aspect is fins, pins or blades spacing. The optimum spacing is dependent on the air velocity, i.e., as the velocity increases, the fin spacing can decrease [3, 22]. However, the dependence of heat transfer with fin or pin spacing is not clear. According to some authors [23–26] the heat transfer increases with increasing fin or pin density, i.e., with reduced spacing. Contrarily, according to other authors, greater heat transfer is obtained for increased spacings [27, 28].

When choosing a fin heat sink, it is typical to choose the conventional rectangular fins. Still, other forms of fins have been tested, such as triangular or trapezoidal fins [29, 30], with fillets [31] or holes [32–36].

Jaffal [36] analysed the thermal performance of different fin heat sinks geometries, via experimental and computational studies, at a certain heat flux interval. It was found that the heat sink with perforated fins showed the best thermal performance. Later, Ibrahim *et al.* [34] investigated the effect of perforation geometry (circular, rectangular and triangular) on the heat transfer of perforated fin heat sinks, under different boundary conditions. In all cases, these perforations increased the heat transfer coefficient and decreased heat sink temperature, regardless of perforation geometry. Tijani and Jaffri [33] also studied the effect of circular perforations on pins or fins heat sinks under forced convection. Inlet velocity and heat flux were constant and perforated pins or fins had the highest heat transfer coefficients, improving thermal efficiency up to 4 % compared to solid pins or fins. In sum, all mentioned studies agreed on the feasibility of considering perforated fins. A stacked fin heat sink (Figure 3-1) was developed by Hsiao and Chang [37], enhancing heat convection and rendering the component cooling more efficiently.

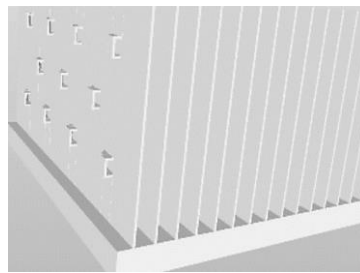


Figure 3-1. Streamline surfaces on fin heat sink [37].

Yeh [38] noticed that considering only the shell of the fins is more advantageous and Teeba *et al.* [39] investigated the thermal parameters of horizontal and vertical finned heat sinks (Figure 3-2). Lower thermal resistance was reported in the vertical position than in horizontal position, due to the thermosiphoning effect in horizontal position which reduced the overall heat dissipation efficiency.

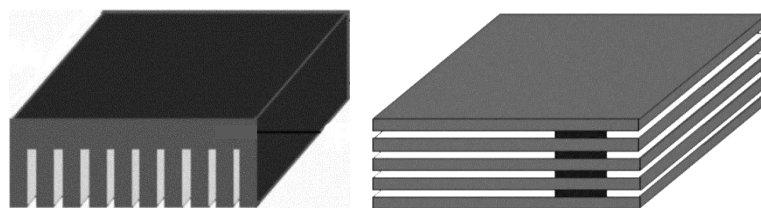


Figure 3-2. Horizontal and vertical finned heat sinks (adapted from [39])

To reduce the undesired blockage on the incoming airflow as the number of fins increases, Lin *et al.* [40] designed a heat sink with oblique planar fins (Figure 3-3) to improve its overall performance.



Figure 3-3. Schematics of heat sink with oblique fins (front view) (adapted from [40]).

When choosing a pin heat sink, several authors agree that square pins are not a good choice [41–43] and that pressure drop is higher when pins arrangement is staggered [21, 24, 27, 44]. However, there is no agreement regarding the best pins shape. Either circular [26, 41, 45], elliptical [23, 41, 45–48], dropform [16, 49] and rhombus [50, 51] can be advantageous, but there are still other unusual shapes that can be a good choice [52, 53].

Gururatana and Li [48] compared elliptic and rectangular staggered pins with the same length-to-thickness ratio but with different hydraulic diameters (D_h). They concluded that elliptic fins produced a higher heat transfer rate when the pressure drop (consequence of pin spacing) was the same. Moreover, Zhou and Catton [54] investigated the thermal and hydraulic performance of different pin heat sinks with various pins shapes including square, circular, elliptic and dropform. The elliptic pins had the best overall performance, regardless of inlet velocity and of the ratio of pin widths to pins spacing.

Ramphueiphad and Bureerat [53] designed and optimized multi-cross-section pins heat sinks (Figure 3-4, left). The results revealed that this type of heat sinks is better than the conventional pins or fins heat sinks (with constant cross-sections) in terms of both thermal efficiency and pumping power.

Maji *et al.* [52] investigated thermal performance of heat sinks with perforated circular pins with different knurled surfaces (Figure 3-4, right). Results were taken for Reynolds numbers from 4700 to 44500. They concluded that the rate of heat transfer for perforated pins up to a particular perforated area was always greater than the solid pins, and with the variation in knurling geometry on fin surface, heat dissipation rate enhanced significantly. Pressure drop around heat sink decreased with the increment of number and size of perforations; with knurling, pressure drop increased.

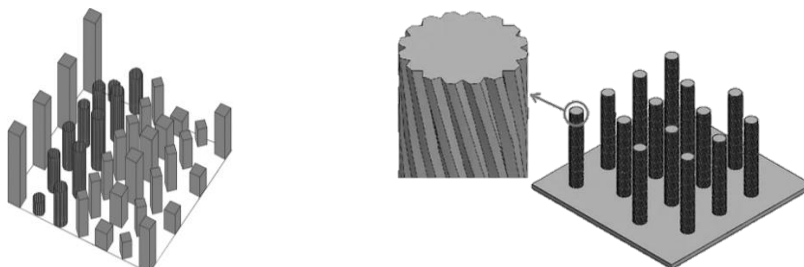


Figure 3-4. Multiple cross-section pins heat sink (left) (adapted from [53]) and an example of a knurled pins heat sink (right) (adapted from [52]).

Choudhary *et al.* [55] researched heat transfer and air flow behaviour of pins heat sinks with and without wings (Figure 3-5) under forced convection. After addition of wings, better results of heat transfer were observed.

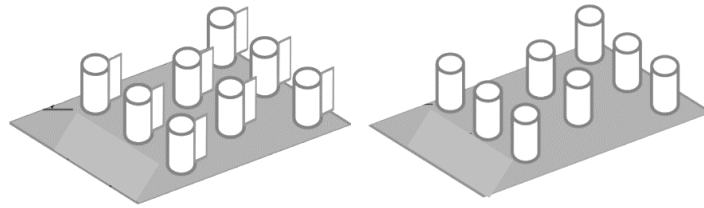


Figure 3-5. Pins heat sinks with (left) and without (right) wings in staggered arrangement [55].

3.3.2. Additively manufactured heat sinks

Since 2014 [12], additive manufacturing has been widely used in the production of heat sinks. Dede *et al.* [56] presented a topology optimization of an air-cooled heat sink. A prototype structure was fabricated using AlSi12 aluminium alloy. Experimental results indicated that the optimized heat sink design (Figure 3-6, left) has a higher coefficient of performance relative to the benchmark heat sink designs. Likewise, Wits *et al.* [57] developed heat sink shapes based on brain coral and used powder bed fused aluminium for experimental testing (Figure 3-6, center).

Another approach widely used is lattice heat sinks (Figure 3-6, right). Lattice structures, due to their good thermomechanical performance have the potential to replace the fins or pins that are traditionally employed in heat sinks. As such, it is important to ensure a cell size and volume fraction that allows enough convection between cells and hence flow of fluid out of the heat sink structure. Each lattice structure presents an optimal beam diameter over unit cell size ratio that maximizes its surface-to-occupancy value, which can be un-uniform [58, 59]. There are numerous unit cells, but among those studied, body-centered cubic (BCC) unit cell showed the maximal surface-to-occupancy ratio.

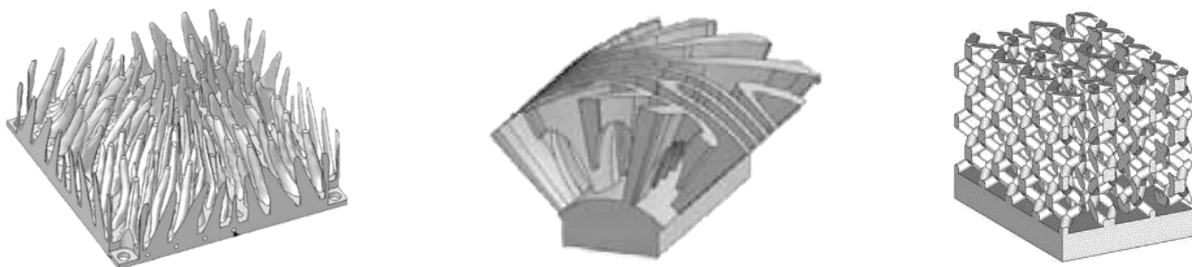


Figure 3-6. Geometry of optimized heat sink (left) (adapted from [56]), heat sink based on brain coral (center) (adapted from [57]) and lattice heat sink (right) [89].

Go *et al.* [60] investigated the feasibility of heat transfer enhancement using the flow-induced vibration of a microfin array (Figure 3-7, left). Through experimental studies, they concluded that the

vibrating deflection plays a key role in enhancing the heat transfer rate. A similar heat sink was proposed by Ikegami *et al.* [61] (Figure 3-7, right).

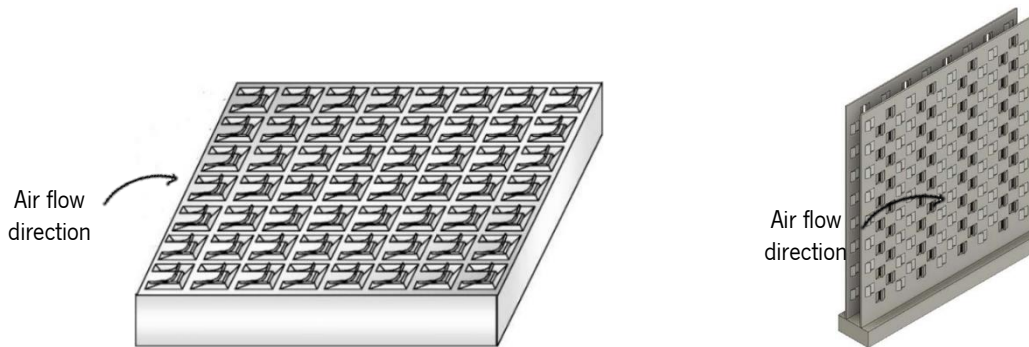


Figure 3-7. Schematic view of a microfin array heat sink (left) (adapted from [60]) and heat sink structure with louvers (adapted from [61]).

According to Bornoff and Parry [11], during the design of a heat sink, an improvement in the thermal performance can be achieved by increasing the surface area at the point of highest temperature, adding a small additional piece of heat sink material on that face. Later, the same authors [62] proposed a method to further improve heat sink performance by the systematic removal of heat sink mass where it is found to make the smallest contribution to increasing the thermal resistance. Therefore, they found an opportunity to reduce the mass without unduly effecting the thermal performance.

3.3.3. Microchannels heat sinks

To improve the thermal performance of heat sinks, cooling channels with numerous possible configurations can be considered. Cho *et al.* [63] investigated inlet/outlet arrangements of microchannel heat sinks for different geometry of the channels (straight or diverging channels with rectangular or trapezoidal headers). Diverging channel with trapezoidal header (Figure 3-8) was the best choice for microchannel heat sink considering the temperature distribution and pressure drop. Similarly, other authors explored the effect of inlet and outlet of the liquid flow within a microchannel heat sink, concluding that, as general rule, the best solution also includes misaligned inlet and outlet points [64–66].

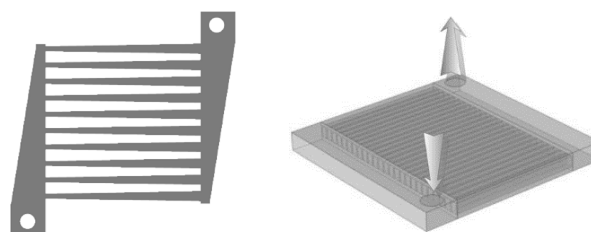


Figure 3-8. Microchannels channels with misaligned inlet and outlet points (adapted from [63] and [66]).

Liu *et al.* [67] stacked multi-layered flat thin rectangular plates (Figure 3-9, left) with a few regular honeycomb cells etched inside, staggered fluid flow channels (Figure 3-9, centre) are formed to enhance heat transfer. Likewise, sectional oblique fins (Figure 3-9, right), imposing also a main and a secondary flow, were employed by Lee *et al.* [68].

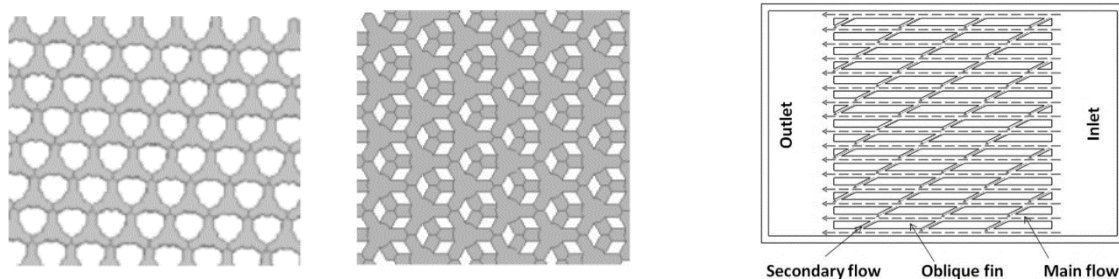


Figure 3-9. Close view of single layer honeycomb plate (left), close view of two layers of honeycomb plates bonded together (centre) [67] and sectional oblique fins in a microchannel heat sink [68].

Regarding the microchannels cross section, a channel with a height- or width-tapered variation was designed by Hung and Yan [69], having the width-tapered channel design a lower and uniform temperature distribution compared to parallel or height-tapered channels, due to the continuous increase in flow. Hu *et al.* [70] investigated two heat transfer enhancing channel shapes: alternating elliptical channel (Figure 3-10, left) and alternating rectangular channel (Figure 3-10, right), comparing with three traditional straight channel shapes (circular, elliptical and rectangular). The results show that alternating channels can improve the performance and should be taken into application to heat sinks.



Figure 3-10. Configurations of alternating elliptical channels (left) and alternating rectangular channels (right) (adapted from [70]).

Xia *et al.* [71, 72] investigated microchannel heat sinks with reentrant cavities (Figure 3-11, left) and found that they enhanced the convective fluid mixing. Similarly, other authors studied a microchannel heat sink with other kind of reentrant cavities (Figure 3-11, right) [73–76]. All results were an improved heat transfer performance with an acceptable pressure drop.

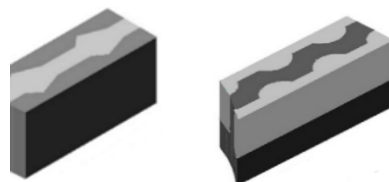


Figure 3-11. Different microchannels with reentrant cavities (adapted from [71-73]).

Some authors introduced the concept of finned microchannel heat sink, with fins/pins along the channels for vortex generation. According to Hosseinpour *et al.* [77], pyramidal-pins owned the best

overall performance among conical, cylindrical and cubical-pins but other unusual shapes can be used [78–80].

Collins *et al.* [81] considered a novel permeable membrane heat sink geometry (**Erro! A origem da referência não foi encontrada.**), possible to be produced by AM, where the cooling fluid is forced through thin and porous walls that act as both conducting fins and membranes that allow flow through their fine internal flow features for efficient heat exchange. This approach resulted in an improvement of the thermal performance.

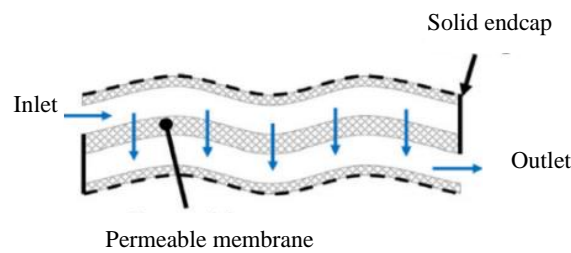


Figure 3-12. Permeable membrane heat sink design (adapted from [81]).

Tseng *et al.* [82] investigated the performance of water-cooled heat sinks with BCC porous structure. The results indicated a much lower thermal resistance and pressure drop; the porous structure forced the working fluid toward the heating surface and resulted in an appreciable increase in heat transfer performance.

3.4. Overall heat sinks performance

3.4.1. Air-cooled heat sinks

This subchapter shows the performance of heat sinks with different designs under air forced convection, varying geometric and boundary parameters, via CFD simulations. Initially, a complete and detailed analysis of the thermal performance of various conventional heat sinks designs is taken. Afterwards, heat sinks designs are modified following some AM approaches.

CFD is the science of predicting fluid flow, heat and mass transfer and related phenomena by solving numerically the set of governing mathematical equations. CFD analysis complements testing and experimentation by reducing total effort and cost required for experimentation and data acquisition. The solvers of the software used in this work - ANSYS - are based on the finite volume method, i.e., domain is discretised into a finite set of control volumes in which general conservation equations for mass, momentum, energy, among others, are solved.

As in other studies involving heat sinks, the main goal of this study is to reach heat sink temperatures as low as possible, minimizing thermal resistance. The computational domain (Figure 3-13) includes a

heat sink (main dimensions $50 \times 50 \times 50 \text{ mm}^3$) and a wind tunnel, designed so that the total flow converges to the heat sink, avoiding the bypass phenomenon [21, 83]. It was considered a fan diameter of 80 mm. The dimensions of the domain are a length of 300 mm and a converging width and height from 80 mm to 52 mm. Heat sink is placed inside the domain, 200 mm away from the inlet and 50 mm from the outlet.

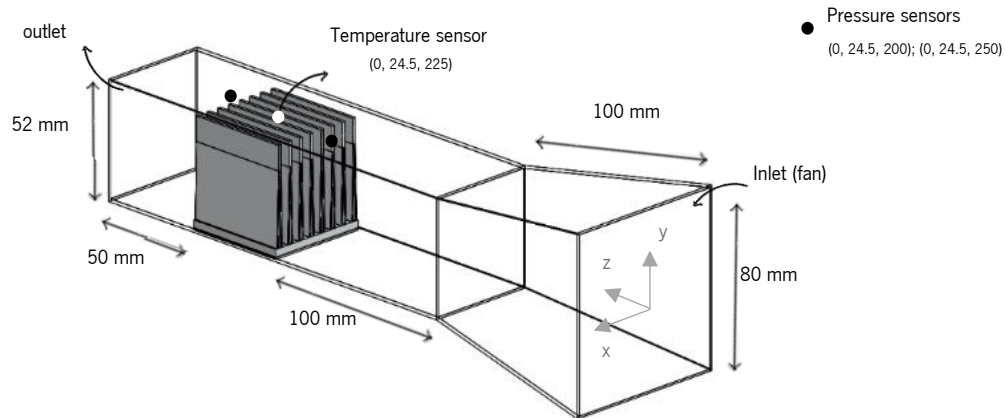


Figure 3-13. Computational domain for studying air-cooled heat sinks.

The geometry was meshed using ANSYS Meshing by applying body sizing operation and, depending on the heat sink model under study, were considered tetrahedral or hexahedral elements. Element size varied in a range between 0.4 mm and 1.2 mm and the total number of elements was the one whose results converged, with minimal computational effort, i.e., sufficient to ensure mesh independence of the simulated results.

Mesh geometry (Figure 3-14) was brought into ANSYS Fluent, where solver settings were defined. This includes defining material properties, selecting appropriate physical models, prescribing operating and boundary conditions, and providing initial values. Table 3-1 includes the main properties of the materials adopted for each component: aluminium AlSi10Mg for the heat sink and ideal air as the fluid passing through the heat sink. AlSi10Mg properties were set according to the ones calculated in Chapter 2 (without heat treatment) and the air flow was assumed incompressible with constant properties.

Table 3-1. Main properties of the materials considered for each component on air-cooled heat sinks.

Property	AlSi10Mg (Heat Sink)	Air (Fluid Domain)
Density (ρ) ($\text{kg}\cdot\text{m}^{-3}$)	2641	1.225
Specific heat (c_p) ($\text{J}\cdot\text{kg}^{-1}\cdot\text{°C}^{-1}$)	1047 ⁷	1006.43
Thermal conductivity (k) ($\text{W}\cdot\text{m}^{-1}\cdot\text{°C}^{-1}$)	165.0	0.0242
Thermal diffusivity (α) (m^2/s)	0.068	1.96×10^{-5}

⁷ Specific heat at 86 °C (Appendix 3).

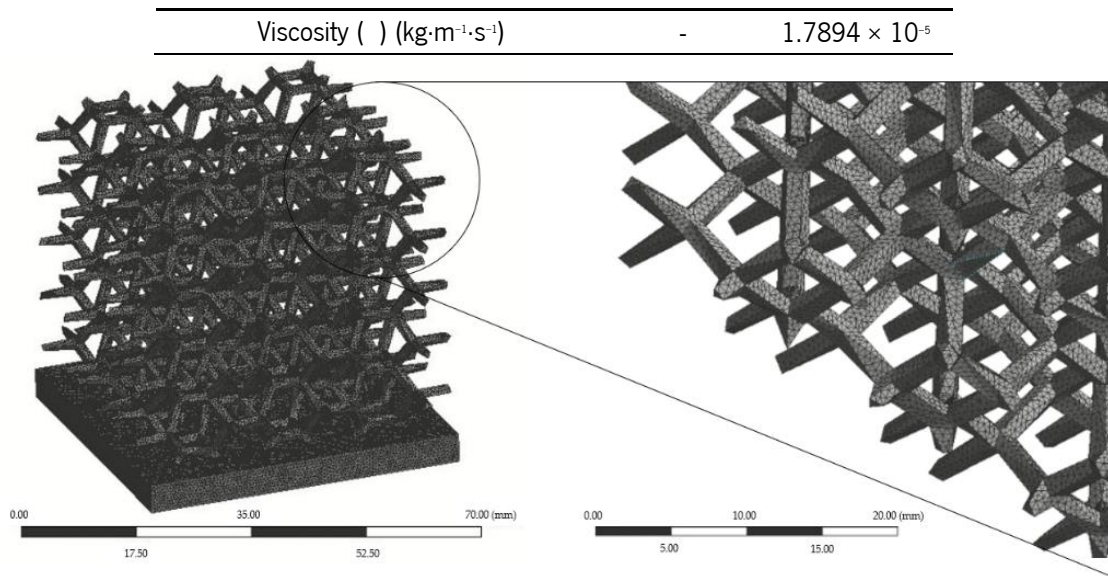


Figure 3-14. Lattice heat sink mesh.

As initial values, the system was considered at a room temperature of 20 °C. The outlet vent condition was used for the outlet boundary and the wind tunnel wall considered adiabatic. The remaining boundary conditions (heat source temperature and inlet air velocity) were established according to each specific case.

During compute solution, the discretised conservation equations are solved iteratively until convergence, i.e., when changes in solution variables from one iteration to the next are negligible (residual response less than 10^{-6}). As the most widely used engineering turbulence model for industrial applications, standard k -Epsilon viscous model was selected. The pressure-velocity coupling was achieved through the SIMPLE scheme [84] and the Least Squares Cell Based gradients were choose as the spatial discretization scheme [85].

Pressure drop across the heat sink and its temperature were reported after 15 s on the respective sensors (Figure 3-13). Considering a time step size of one second with 10 maximum iterations per time step, the 15 s were found to be a good balance between good results and computational effort (Figure 3-15) once, in most cases, the temperature reached the steady-state condition. The temperature sensor was located where, as general rule, the heat sink temperature was the minimum [86].

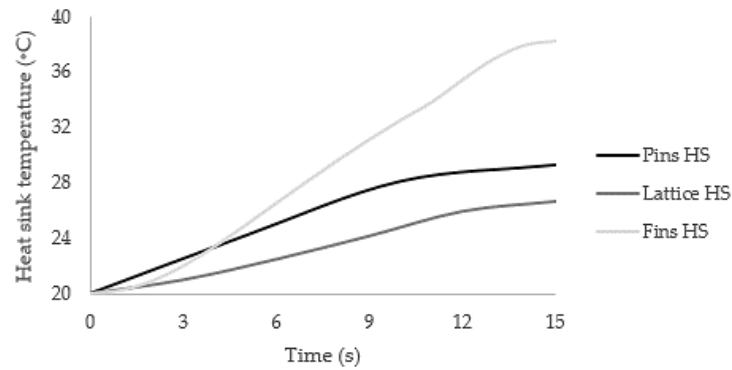


Figure 3-15. Temperature contours vs time for each type of heat sink.

The statistical design of experiments (DOE) was used to design the sets of experiments run in this work for fins and pins heat sinks, in order to optimize the main geometric parameters (pins/fins diameter/thickness and pins/fins spacing).

As boundary conditions, the temperature of the heat source (at the bottom of the heat sink) varied between 80 °C and 100 °C, with 10 °C intervals, and inlet air velocity (v) took the values 0.7 m/s, 2.1 m/s and 3.5 m/s (at 20 °C), leading to Reynolds numbers from 2500 (laminar-turbulent transition) to 12500 (very turbulent flow) according to Equation 3.4.

Equation 3-4. Reynolds number.

For fins heat sinks, DOE analyses were performed using fin thickness, fin spacing, inlet velocity, and heat source temperature as factors and pressure drop and heat sink temperature after 15 s as responses. Each factor was considered with three levels (Table 3-2) and an L9 matrix was constructed.

Table 3-2. Levels and factors for DOE matrix for fins heat sinks.

Level	Fin Thickness (mm)	Fin Spacing (mm)	Inlet Velocity (m/s)	Heat Source Temperature (°C)
1	1.5	2.0	0.7	80
2	2.5	3.5	2.1	90
3	3.5	5.0	3.5	100

For pins heat sinks, the arrangement factor (in-line or staggered) was added to compose an L18 DOE matrix. Level and factors are shown in Table 3-3.

Table 3-3. Levels and factors for DOE matrix for pins heat sinks.

Level	Pin Diameter (mm)	Pins Spacing (mm)	Inlet Velocity (m/s)	Heat Source Temperature (°C)	Arrangement
1	1.5	2.0	0.7	80	In-line (1)
2	2.5	3.5	2.1	90	Staggered (2)
3	3.5	5.0	3.5	100	-

Based on DOE results, the shape of fins or pins was varied according to some previous studies that showed good results [16, 23, 26, 41, 45–51].

For fins heat sinks (Figure 3-16), the same number of fins was considered. For pins heat sinks (Figure 3-17), the same hydraulic diameter and pin spacing was maintained. Using analysis of variance (ANOVA), the effects of variables and their interactions on each response were determined for fins and pins heat sinks. In order to confirm the advantages of additive manufacturing for thermal management components, lattice sinks with X, Hexagon, and Snow Flake (Figure 3-18) unit cells were studied. Cell size and thickness were fixed as well as boundary conditions.

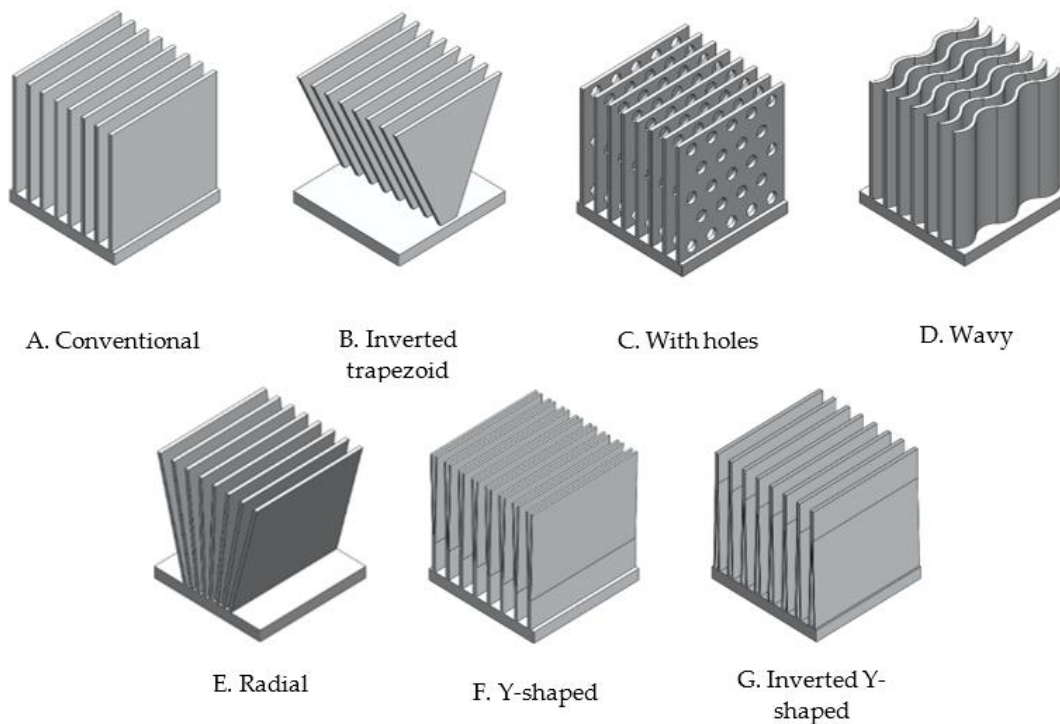


Figure 3-16. Different fins heat sink models.

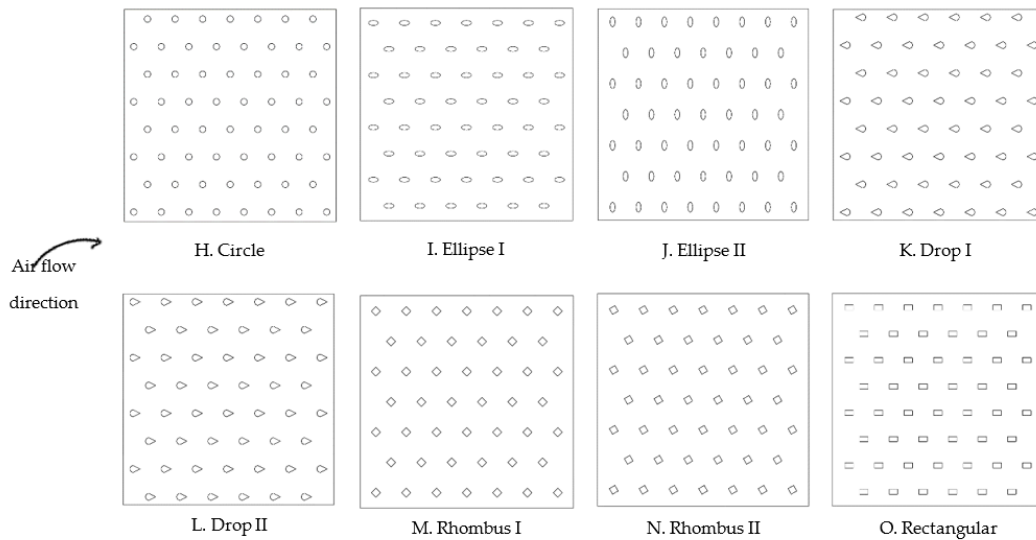


Figure 3-17. Different pins shapes under study.

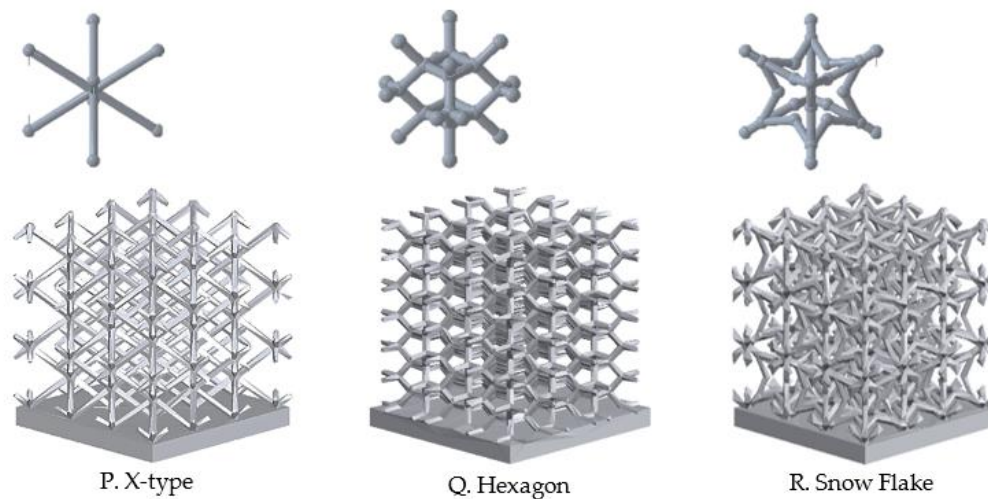


Figure 3-18. Different lattice heat sinks models.

Fins heat sinks

For fins heat sinks, it was found that, either for a lower heat sink temperature (Figure 3-19) or for a lower pressure drop (Figure 3-20), the thickness of the fins should be as small as possible. The same was not true for the spacing. On the one hand, if it is as small as possible, it increases the density of the fins and therefore causes better thermal efficiency. On the other hand, the smaller the spacing, the higher pressure drop. Being an agreement between both parameters, and since the influence is much higher for the pressure drop, the bigger fins spacing (5 mm) will be considered for further studies related to the shape of the fins.

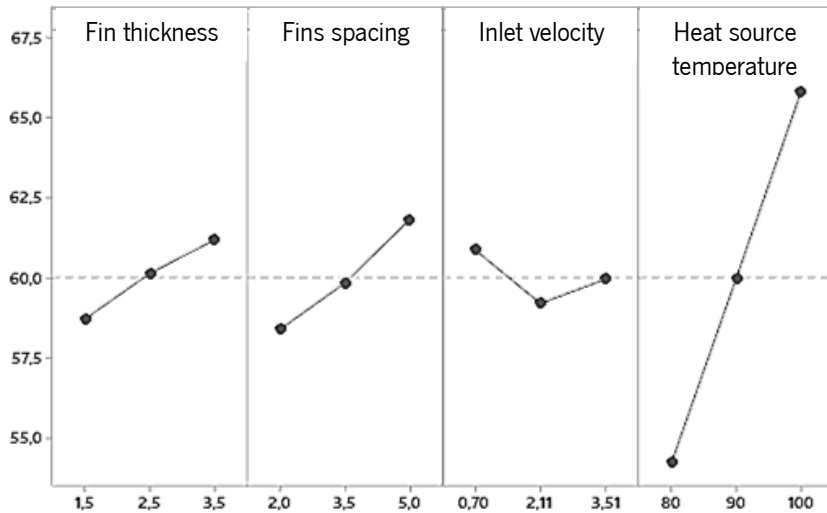


Figure 3-19. Main effects for fins heat sinks minimum temperature.

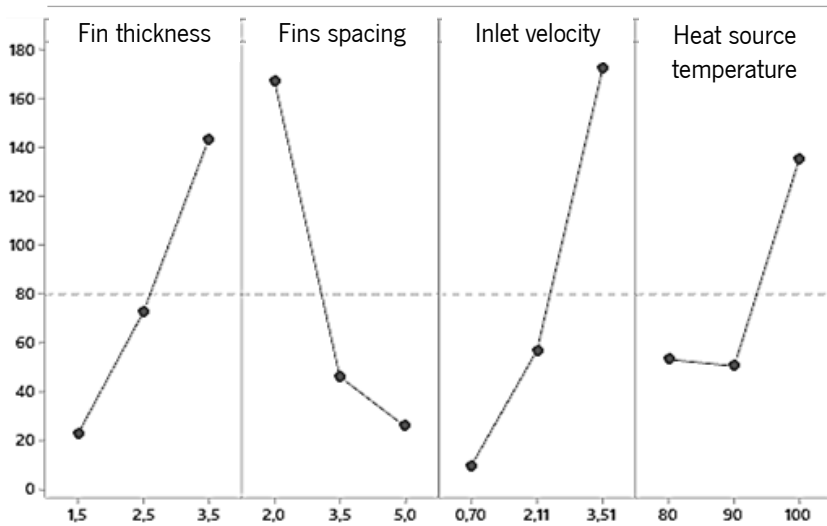


Figure 3-20. Main effects for fins heat sinks pressure drop.

Regarding boundary conditions, as expected, the effect of inlet velocity on pressure drop and heat source temperature on heat sink temperature after 15 s was linear. However, an inlet velocity of 2.11 m/s ($Re = 7500$) caused a minimum heat sink temperature and a heat source temperature of 90 °C caused a minimum pressure drop. These conclusions are related with the geometric parameters (number of fins and fins spacing), according to Tables 3-4 and 3-5, respectively.

Table 3-4. Correlation between heat sink temperature and geometrical parameters.

Simulation	Number of Fins	Heat Source Temperature (°C)	Velocity (m/s)	HS Temperature after 15 s (°C)
#1	14	80	0.7	52.2
#2	6	80	2.11	56.4
#3	8	80	3.51	54.1
#4	7	90	0.7	61.9
#5	11	90	2.11	57.7
#6	8	90	3.51	60.5
#7	7	100	0.7	68.6
#8	10	100	2.11	63.5
#9	9	100	3.51	65.3

Table 3-5. Correlation between pressure drop and DOE factors.

Simulation	Spacing (mm)	Heat Source Temperature (°C)	Velocity (m/s)	Pressure Drop (Pa)
#1	2	80	0.7	13.8
#2	3.5	90	0.7	10.5
#3	5	100	0.7	4.4
#4	5	80	2.11	40.3
#5	2	90	2.11	108.4
#6	3.5	100	2.11	22.3
#7	3.5	80	3.51	105.1
#8	5	90	3.51	32.6
#9	2	100	3.51	380.1

As boundary conditions, an inlet velocity of 2.11 m/s and a heat source temperature of 90 °C were considered for further studies with fins.

Fins shape

In all fins heat sinks variants (Figure 3-16), the same number of fins (8) and boundary parameters were considered. Results for each model are shown in Table 3-6.

Table 3-6. Temperature and pressure drop for each fin heat sink model.

Model	Total Area (cm ²)	Front Area (cm ²)	Volume (cm ³)	HS Temperature after 15 s (°C)	Pressure Drop (Pa)
A	408.9	7.7	38.6	60.6	13.4
B	260.7	7.7	27.0	40.0	30.6
C	389.4	7.7	34.2	52.4	25.1
D	397.3	20.2	35.1	53.9	52.6
E	414.5	7.7	38.6	55.2	22.4
F	682.1	7.7	38.6	52.0	31.5
G	682.1	7.7	38.6	54.5	24.5

It was found that the incorporation of fillets or chamfers did not bring any advantage, contrarily to all design variations shown in Figure 3-16 and Table 3-6. So, fins with inverted trapezoidal shape (Figure

3-16B) were considered, being an advantageous option due to its wide part exposed to ambient air [30]. Moreover, the higher the inverted trapezoid angle, the better the performance (Figure 3-21).

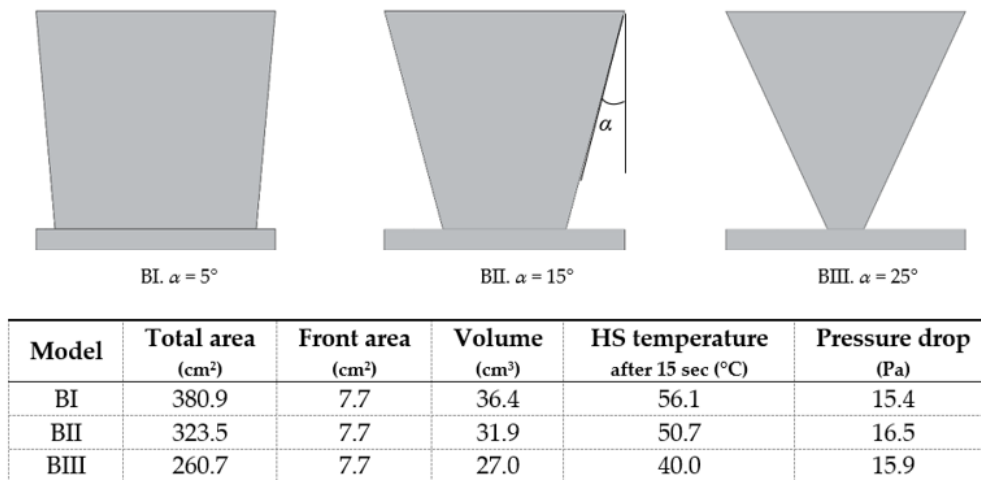


Figure 3-21. Model B variants.

The incorporation of holes in the fins (model C) has been studied by other authors [33, 34] and both agreed that it was an advantageous approach due to the higher heat transfer coefficient. Furthermore, for larger holes diameter, maintaining holes spacing (5 mm) resulted in better heat sink performance (Figure 3-22).

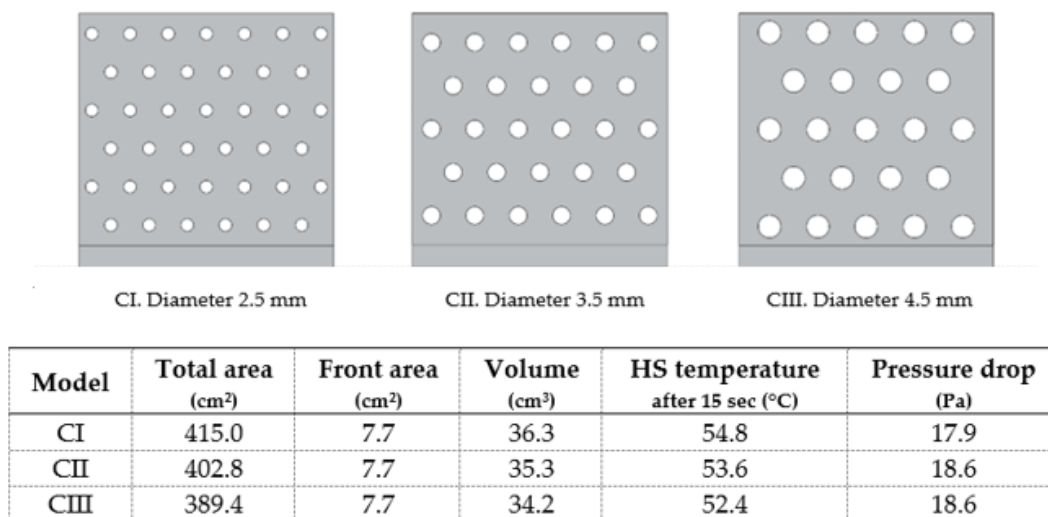
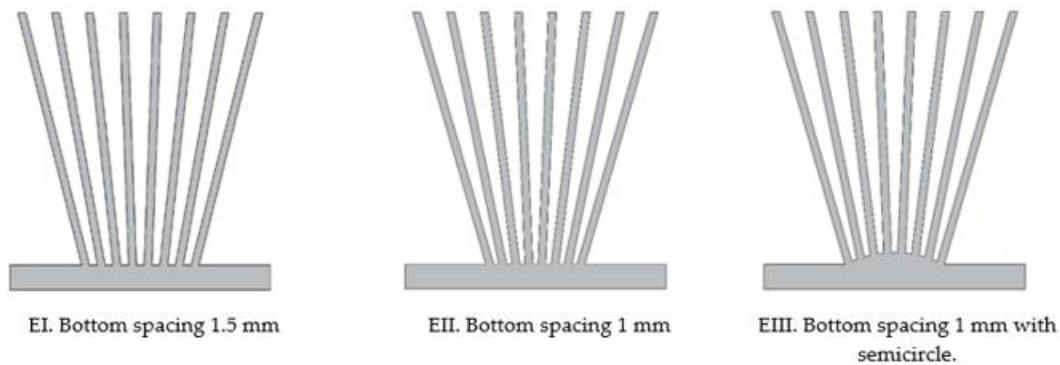


Figure 3-22. Model C variants.

Regarding model E, the lower the spacing between the fins at the bottom, keeping the top spacing equal to 5 mm, the better the heat sink performance (Figure 3-23, I and II). This happens because airflow towards radial fins tends to quicken as the gap between two consecutive fins reduces (EI to EII) [71]. These advantages of model E fins have also been confirmed experimentally by other authors [40, 87].

However, the incorporation of more material in the heat sink base (Figure 3-23, III), close to the fins, did not bring any advantage.

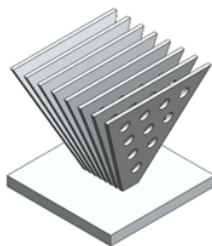


Model	Total area (cm ²)	Front area (cm ²)	Volume (cm ³)	HS temperature after 15 sec (°C)	Pressure drop (Pa)
EI	414.5	7.7	38.6	56.4	19.2
EII	414.5	7.7	38.6	55.2	22.4
EIII	406.3	7.8	39.1	56.2	22.3

Figure 3-23. Model E variants.

With this, the properties of models B, C, and E have been combined and, among the studied, the heat sink design with the best performance was attained (Figure 3-24. Best fin heat sink (among those studied).

). Following some design rules for additive manufacturing, elliptical holes were considered instead of circular ones.



Fin thickness	Heat source temperature	Inlet velocity
1.5 mm	90 °C	2.1 m/s

Total area	Front area	Volume	HS temperature	Pressure drop
255.9 cm ²	7.7 cm ²	25.1 cm ³	37.6 °C	19.8 Pa

Figure 3-24. Best fin heat sink (among those studied).

Pins heat sinks

For pins heat sinks, the arrangement factor was added: in-line or staggered pins (Figure 3-25). For staggered pins, there are two possible orientations. From orientation 1 to orientation 2, heat sink temperature increased by a maximum of 1.4 % but pressure drop decreased by about 25 %. Although the heat sink temperature after 15 s is the most pertinent response parameter, the decrease in pressure drop was much higher, causing a better performance for orientation 2 (Figure 3-25c). For this reason, the staggered arrangement was considered with orientation 2.

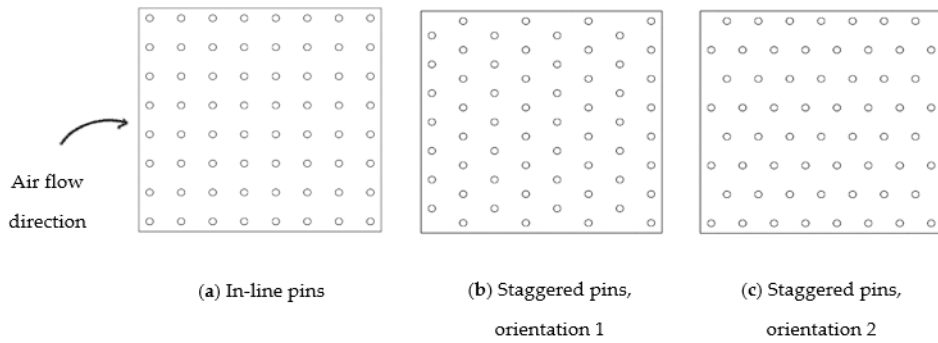


Figure 3-25. Possible pin heat sinks arrangements and orientations.

Taking this into account, it was found that, either for a lower heat sink temperature or for a lower pressure drop, the staggered arrangement (2) is more advantageous (Figure 3-26). Regarding pins diameter, for a lower heat sink temperature (Figure 3-26, top), it should be as small as possible. The same was not true for the pressure drop (Figure 3-26, bottom), where there is an ideal diameter of 2.5 mm. In agreement between both parameters, and since the heat sink temperature is the most relevant response parameter and the influence is more accentuated, the lower pins diameter (1.5 mm) will be considered for further studies related to the shape of the pins. With a smaller diameter, there is also a smaller building volume to be created by additive manufacturing.

Respecting pins spacing, if, on the one hand, there was no influence on the heat sink temperature, on the other hand, the influence on the pressure drop is quite noticeable. For this reason, the upper spacing (5 mm) was considered the best choice. These conclusions about geometric parameters agree with the fin heat sinks.

As explained for fins heat sinks, a temperature of 90 °C caused a lower pressure drop (almost irrelevant) also due to some geometrical parameters (pins spacing and heat sink front area) given in Table 3-7. For this reason, this temperature was selected for further studies with pins. Regarding the inlet velocity, its influence was linear and as expected. Therefore, a velocity of 3.51 m/s was considered because it resulted in a lower heat sink temperature.

Table 3-7. Correlation between pressure drop and geometrical parameters for an inlet air velocity of 3.51 m/s.

Arrangement	Simulation	Spacing (mm)	Front Area (mm ²)	Heat Source Temperature (°C)	Pressure Drop (Pa)
In line	#1	3.5	13.4	80	289.7
	#2	5	10.2	90	167.1
	#3	2	16.6	100	776.9
Staggered	#4	3.5	11.4	80	170.7
	#5	5	7.7	90	116.0
	#6	2	11.8	100	441.1

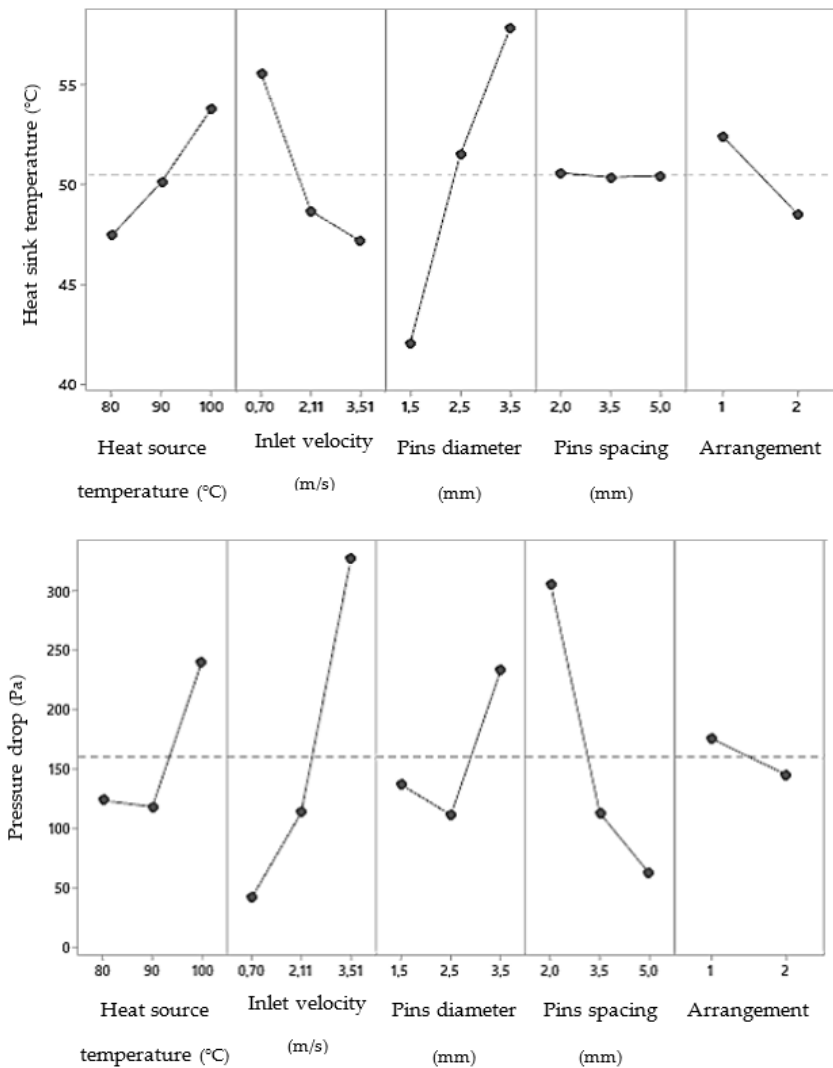


Figure 3-26. Main effects for heat sink temperature (top) and pressure drop (bottom) for pins heat sinks.

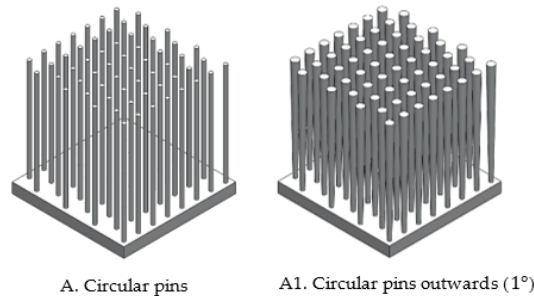
Pins shape

In all pins shapes studies (Figure 3-17), the same hydraulic diameter (1.5 mm) and pin spacing (5 mm) were maintained, as well as boundary parameters. Results are shown in Table 3-8.

Table 3-8. Temperature and pressure drop for each pin heat sink model.

Model	Nr of Pins	Total Area (cm ²)	Front Area (cm ²)	Volume (cm ³)	HS Temperature after 15 s (°C)	Pressure Drop (Pa)
H	60	162.7	7.7	16.1	36.0	116.0
I	52	165.8	6.4	16.2	38.4	57.2
J	53	168.4	9.6	16.3	38.0	203.8
K	52	178.1	8.1	16.7	39.1	60.4
L	52	178.1	8.1	16.7	42.9	95.1
M	46	159.6	9.0	16.0	50.4	96.9
N	46	159.6	9.0	16.0	44.1	91.5
O	52	185.4	6.6	16.9	49.3	56.2

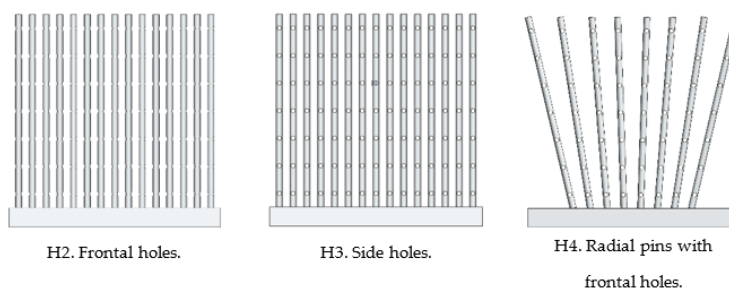
Conventional heat sinks, with circular pins, continue to be the best choice among the many options of pin shapes, even though the pressure drop is high. For these pins, considering drawing outwards (Figure 3-27), only possible to be produced by additive manufacturing, was not advantageous a higher temperature and a higher-pressure drop was obtained.



Model	Total area (cm ²)	Front area (cm ²)	Volume (cm ³)	HS temperature after 15 sec (°C)	Pressure drop (Pa)
H	162.7	7.7	16.1	36.0	116.0
H1	234.2	10.6	23.0	36.8	196.1

Figure 3-27. Comparison between circular pins (A) and circular pins outwards (A1).

Figure 3-28 shows pins heat sinks with 1 mm frontal elliptical holes (H2) and side elliptical holes (H3) as well as a radial pins heat sink also with frontal elliptical holes (H4), spaced 5 mm apart. In all cases, holes were advantageous, and the results were quite similar. For the same heat sink temperature obtained, the one with the lowest pressure drop was considered as the best option for pins heat sinks (H2).



Model	Total area (cm ²)	Front area (cm ²)	Volume (cm ³)	HS temperature after 15 sec (°C)	Pressure drop (Pa)
H	162.7	7.7	16.1	36.0	116.0
H2	173.0	7.3	15.6	29.4	61.1
H3	173.0	7.6	15.6	29.4	63.4
H4	166.0	7.3	15.4	30.1	54.2

Figure 3-28. Pins heat sinks with frontal (H2) and side (H3) holes and radial pins heat sink with frontal holes (H4).

For the case of ellipse pins (the second-best pins shape), differences were observed between maintaining the spacing (Model I) or maintaining the number of pins (Model I1), concerning the reference

heat sink (Model H). According to Table 3-9, there were no significant differences, i.e., opting for ellipse pins, the choice should be Model I once it has a smaller building volume.

Table 3-9. Temperature and pressure drop for each pin heat sink model.

Model	Nr of Pins	Total Area (cm ²)	Front Area (cm ²)	Volume (cm ³)	HS Temperature after 15 s (°C)	Pressure Drop (Pa)
H	60	162.7	7.7	16.1	36.0	116.0
I	52	165.8	6.4	16.2	38.4	57.2
I1	60	186.1	6.4	16.9	38.3	59.1
J	53	168.4	9.6	16.3	38.0	203.8

Therefore, the best option contemplated circular pins in combination with frontal holes in their structure (Figure 3-29).

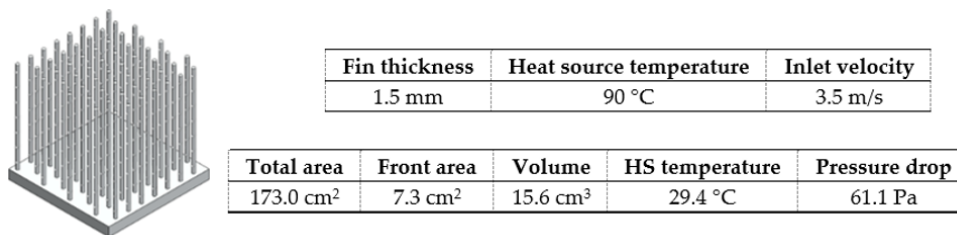


Figure 3-29. Best pin heat sink (among those studied).

Lattice heat sinks

Lattice sinks with X, Hexagon, and Snow Flake (Figure 3-18) unit cells were studied. Cell size and thickness were fixed at $15 \times 15 \times 15 \text{ mm}^3$ and 1.5 mm, respectively, as well as boundary conditions (heat source temperature of 90 °C and air inlet velocity of 3.5 m/s). The results are shown in Table 3-10.

Table 3-10. Temperature and pressure drop for each pin heat sink model.

Model	Total Area (cm ²)	Front Area (cm ²)	Volume (cm ³)	HS Temperature after 15 s (°C)	Pressure Drop (Pa)
X-type	187.9	31.3	16.8	39.2	108.1
Hexagon	243.7	41.1	19.2	26.7	161.2
Snow Flake	283.9	41.0	20.6	33.7	137.2

Among the three models studied, the heat sink with hexagon unit cell showed the lowest temperature, despite the higher pressure drop. The advantages of this unit cell in thermal management applications were also confirmed by Gu *et al.* [88].

Fins vs Pins vs Lattice heat sink

In this subchapter, it is intended to directly compare the best fins, pins, and blades heat sinks (Figure 3-30), under the same geometric and boundary parameters.

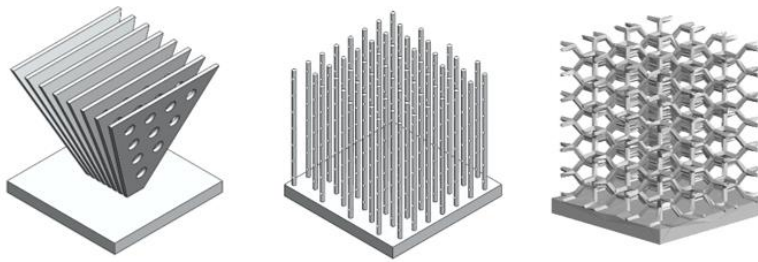


Figure 3-30. Fins, pins, and lattice heat sinks, respectively.

Table 3-11 shows that, under forced convection environments, better results were obtained for the lattice heat sink with hexagon unit cell. The pressure drop increased more than double for the same inlet velocity and Reynolds number, a consequence of the high frontal area. Even so, a decrease of about 28 % and 9 % in heat sink temperature was achieved, comparing with the best fins and pins heat sink, respectively. As inlet velocity and heat source temperature are kept constant during the experiments, the best heat sink is the one whose temperature is minimal, which, according to Equation 3-3, translates into lower thermal resistance.

Table 3-11. Direct comparison between heat sinks with fins, pins, and blades (Re = 12500).

Model	Total Area (cm ²)	Front Area (cm ²)	Volume (cm ³)	Total Area to Volume Ratio	HS Temperature after 15 s (°C)	Pressure Drop (Pa)
Fins	255.9	7.7	25.1	10.2	27.7	50.2
Pins	173.0	7.3	15.6	11.1	29.4	61.1
Lattice	243.7	41.1	19.2	12.7	26.7	161.2

Based on this study, there is a direct correlation between the total area to volume ratio and the heat sink performance. The lattice heat sink, the heat sink with the highest area to volume ratio and only possible to be produced by additive manufacturing, was considered the best option among the studied.

Experimental validation

To experimentally validate the performance of the best heat sinks obtained by CFD simulations, the three heat sinks were produced by PBF (Figure 3-31), in aluminum, considering the same parameters mentioned in previous chapter. As the thermal properties were better in the as-built condition, stress relief heat treatment was not applied to these heat sinks.



Figure 3-31. Air-cooled heat sinks produced by PBF.

Unfortunately, it was not possible to produce the pins heat sink because the perforated pins didn't have enough strength, breaking easily. With this, only heat sinks with fins and lattice structures were experimentally validated. Nevertheless, pins heat sink with 1 mm holes (spaced 5 mm) in thicker pins (diameter 2.5 mm) were evaluated through CFD simulations, considering the same boundary parameters, to realize the relevance of producing a new pin heat sink by AM. Results proven that the temperature of these heat sinks was higher than the optimized fins and lattice heat sinks (Table 3-11 and Table 3-12). For this reason, only finned and lattice heat sinks were experimentally tested.

Table 3-12. Heat sink temperature and pressure drop for pins heat sink with holes (diameter 2.5 mm).

Pins spacing (mm)	Nr of Pins	Total Area (cm ²)	Front Area (cm ²)	Volume (cm ³)	HS Temperature after 15 s (°C)	Pressure Drop (Pa)
3.5	60	278.0	11.4	23.4	41.3	188.5
5	46	221.1	10.2	16.3	44.4	77.5

The experimental testing apparatus involving a wind tunnel, a heat source, a fan and several sensors was designed (Figure 3-32). In some testing apparatuses, some fluid bypasses over the top or around the sides of the heat sink being tested. This problem is eliminated here by making the flow channel the same size as the heat sinks to be tested, in accordance with the CFD simulations (Figure 3-13). To induce fluid flow, an electronics cooling fan is used. The fan operates at 6 V on direct current (DC), with a speed of 800 rpm (i.e., 3.5 m/s). To measure the pressure drop across the heat sink, pressure taps upstream and downstream of heat sink measure the differential pressure using a differential low pressure transmitter BFT10-110 (Appendix 4). On the heat sink base, a copper block heated with two cartridge resistors was used to increase temperature, based on the voltage defined on the power supply. Four K-type thermocouples are used in each set up. One is placed in the flow of the inlet air to measure the temperature of the ambient air and another on the copper block to measure the actual heat source temperature. The other two are placed on the heat sink base and on the top of the heat sink, to measure the temperature gradient along the heat sink. All sensors data is recorded with a multichannel Multicon CMC-99 data logger.

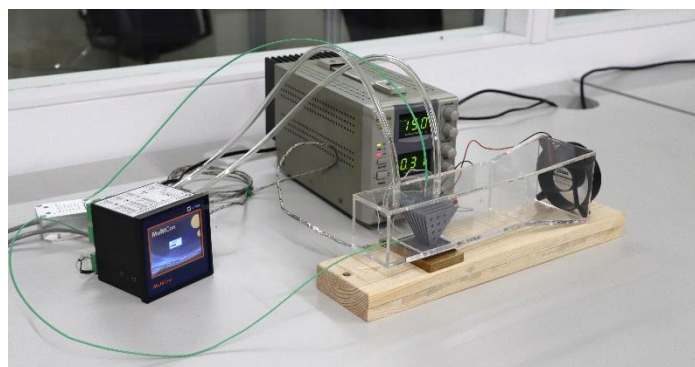


Figure 3-32. Experimental testing apparatus to evaluate heat sinks performance.

After adjusting the voltage imposed on the cartridge resistors to stabilize at a temperature of 90 °C, the heat sink to be tested is placed on the top of the cooper block and the fan is turned on. Temperatures and pressure drop were recorded for 15 seconds, in accordance with the CFD simulations. Considering the ambient temperature of around 20 °C, results are shown in Table 3-13.

Table 3-13. Air-cooled heat sinks performance: simulation vs experimental.

	HS Temperature after 15 s (°C)		Pressure Drop (Pa)	
	Simulation	Experimental	Simulation	Experimental
Fins	27.7	28.1	50.2	80.2
Lattice	26.7	26.5	161.2	97.8

Although the experimental results of the fins heat sink have a higher deviation from the simulated ones, the lattice heat sink showed a better thermal performance, albeit with a slightly higher pressure drop. Regarding the heat sink temperature after 15 seconds, there was a maximum difference of 0.5 °C (about 2 %) between simulated and experimental results.

Air-cooled heat sinks – brief summary

Smaller diameters/thicknesses and larger fins/pins spacing provided better results. For fins HS, the use of radial fins, with an inverted trapezoidal shape and with larger holes was advantageous. Regarding pins HS, the best option contemplated circular pins in combination with frontal holes in their structure. Additionally, lattice HS, only possible to be produced by additive manufacturing, was also studied. Lower temperatures were obtained with a hexagon unit cell. Lastly, a comparison between the best HS in each category showed a lower thermal resistance for lattice HS. Despite the increase of at least 38 % in pressure drop, a consequence of its frontal area, the temperature was 26 % and 56 % lower when compared to conventional pins and fins HS, respectively, and 9 % and 4 % lower when compared to the best pins and best fins of this study.

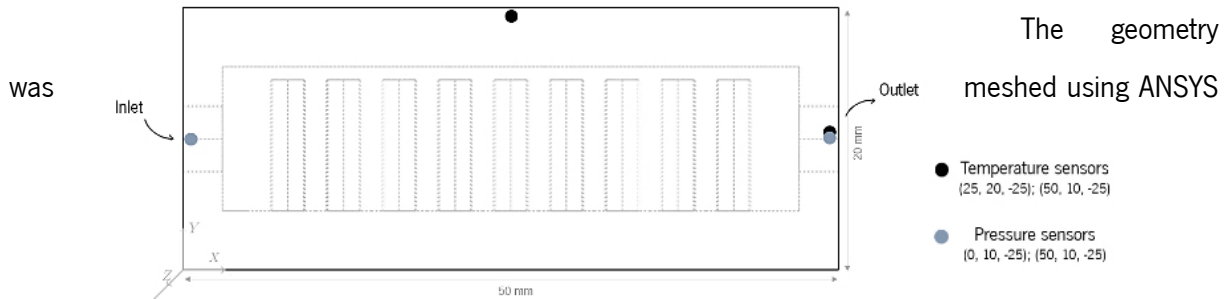
The good performance of the lattice heat sink was experimentally validated, with a deviation of only 0.5 °C between the simulations and the experimental data.

3.4.2. Water-cooled heat sinks

This subchapter shows the performance of water-cooled heat sinks with different designs, varying geometric parameters, via CFD simulations. Initially, a complete and detailed analysis of the thermal performance of various conventional heat sinks designs is taken. Afterwards, heat sinks designs are modified following some AM approaches, based on the best results of air-cooled heat sinks.

As in air-cooled heat sinks, the main goal is to reach heat sink temperatures as low as possible, minimizing thermal resistance. The computational domain (Figure 3-33) includes a microchannel heat sink (main dimensions $50 \times 50 \times 20 \text{ mm}^3$) with a 4.5 mm shell and pressure and temperature sensors.

Figure 3-33. Computational domain for studying water-cooled heat sinks.



Meshing by applying body sizing operation and, depending on the heat sink model under study, were considered tetrahedral or hexahedral elements. Element size varied in a range between 0.5 mm and 1.5 mm and the total number of elements was the one whose results converged, with minimal computational effort, i.e., enough to ensure mesh independence of the simulated results.

Mesh geometry was brought into ANSYS Fluent, where solver settings were defined. This includes defining material properties, selecting appropriate physical models, prescribing operating and boundary conditions, and providing initial values. Table 3-14 includes the main properties of the materials adopted for each component: AlSi10Mg for the heat sink and ideal water as the fluid passing inside the heat sink.

Table 3-14. Main properties of the materials considered for each component on water-cooled heat sinks.

Property	AlSi10Mg (Heat Sink)	Water (Fluid Domain)
Density ($\text{kg}\cdot\text{m}^{-3}$)	2641	998.2
Specific heat ($\text{J}\cdot\text{kg}^{-1}\cdot\text{°C}^{-1}$)	1047 [§]	4182
Thermal conductivity ($\text{W}\cdot\text{m}^{-1}\cdot\text{°C}^{-1}$)	165.0	0.6
Thermal diffusivity (m^2/s)	0.068	1.44×10^{-7}
Viscosity ($\text{kg}\cdot\text{m}^{-1}\cdot\text{s}^{-1}$)	-	1.003×10^{-3}

As initial values, the system was considered at a room temperature of 20 °C . The outlet pressure condition was used for the outlet boundary, heat source temperature was set at 90 °C and an inlet water velocity of 1.22 m/s achieves a Reynolds number of 12500. Pressure drop across the heat sink, its temperature and water outlet temperature were reported after 15 s on the respective sensors (Figure 3-33), considering a time step size of one second with 10 maximum iterations per time step. Boundary conditions and recorded data are in accordance with the CFD simulations results for air-cooled heat sinks.

[§] Specific heat at 86 °C (Appendix 3).

During compute solution, according to Standard -Epsilon viscous model, the discretised conservation equations are solved iteratively until convergence, i.e., when changes in solution variables from one iteration to the next are negligible (residual response less than 10^{-6}).

Considering the critical knowledge obtained in Chapter 3.4.1, an analysis of the influence of fins/pins thickness/diameter (Figure 3-34) and spacing (Figure 3-35) inside the microchannel was done and is reported on Table 3-15. For this purpose, pins with a diameter of 1.5 mm were not considered as their production by AM is less viable.

According to the data (Figure 3-34 and Figure 3-35), as verified in air-cooled fins heat sinks, for a lower heat sink temperature, the thickness of the fins should be as small as possible, with the bigger spacing. In the case of pins heat sinks, contrary to what was observed in air-cooled heat sinks, better results were achieved for higher pins diameter and spacing. In almost all heat sinks studied featured with fins or pins, the heat sink temperature is smaller than when a simple heat sink (i.e., without fins or pins inside) is used (orange dotted line).

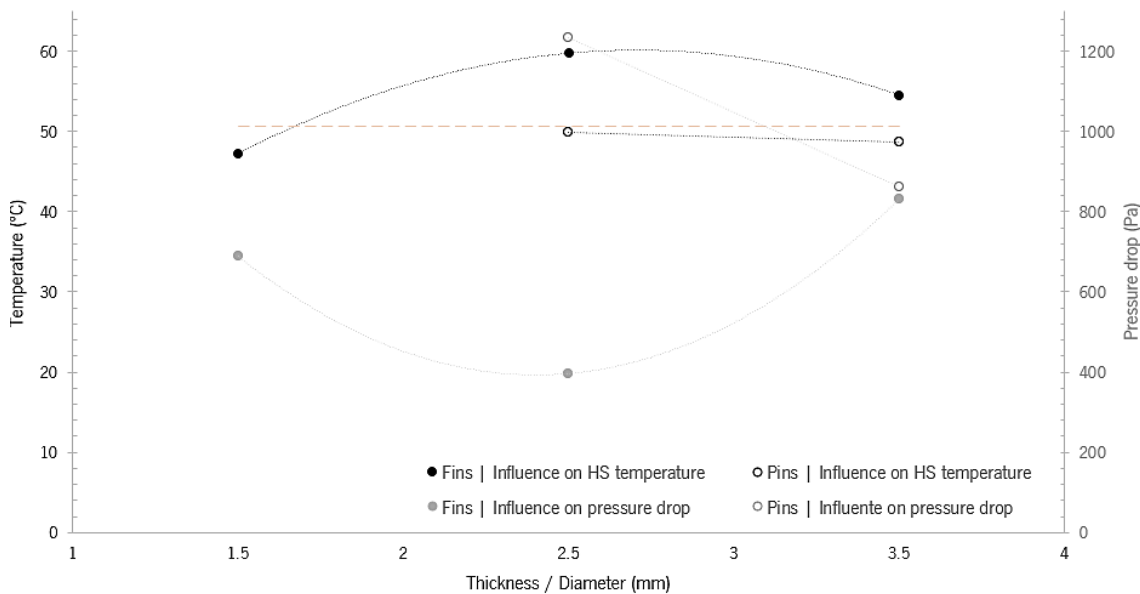


Figure 3-34. Influence of pins diameter or fins thickness on HS temperature after 15 seconds and on pressure drop.

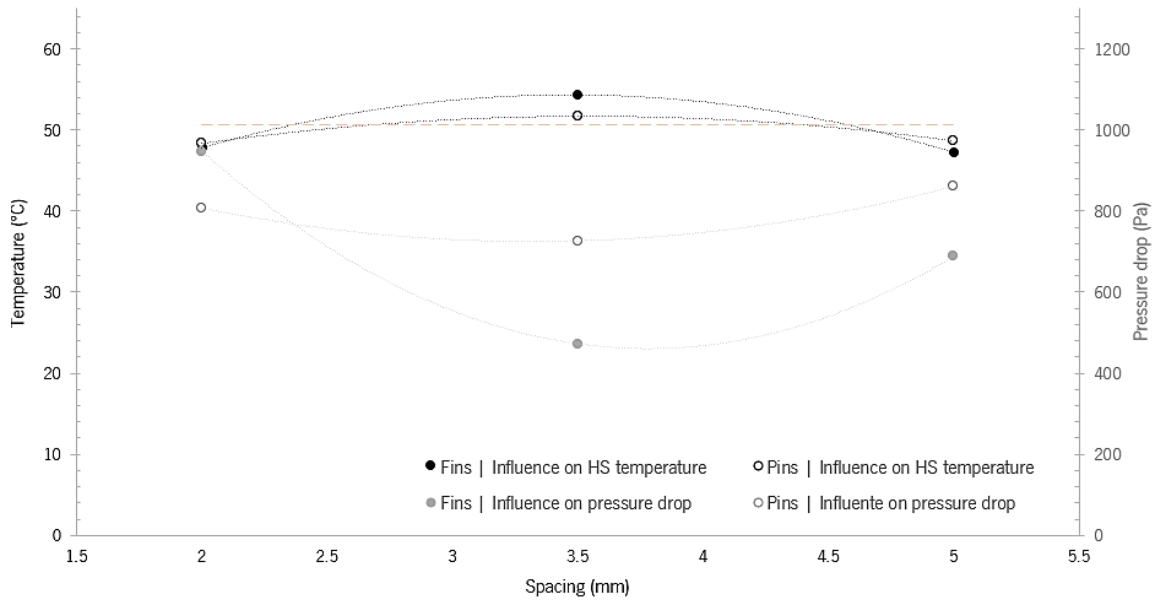


Figure 3-35. Influence of pins/fins spacing on HS temperature after 15 seconds and on pressure drop.

Table 3-15. Influence of fins/pins thickness/diameter and spacing inside the microchannel HS.

Fins microchannel HS					
	Fins thickness	Fins spacing	HS temperature after 15s	Pressure drop	Outlet water temperature
Thickness influence	1.5 mm	5 mm	47.2 °C	688.8 Pa	27.4 °C
	2.5 mm		59.8 °C	396.6 Pa	29.0 °C
	3.5 mm		54.6 °C	830.5 Pa	30.2 °C
Spacing influence	1.5 mm	2.0 mm	47.8 °C	947.7 Pa	33.9 °C
		3.5 mm	54.3 °C	472.8 Pa	26.9 °C
		5.0 mm	47.2 °C	688.8 Pa	27.4 °C

Pins microchannel HS					
	Pins diameter	Pins spacing	HS temperature after 15s	Pressure drop	Outlet water temperature
Diameter influence	2.5 mm	5 mm	49.8 °C	1232.8 Pa	28.3 °C
	3.5 mm		48.6 °C	860.8 Pa	27.6 °C
Spacing influence	3.5 mm	2.0 mm	48.3 °C	807.5 Pa	28.4 °C
		3.5 mm	51.7 °C	726.5 Pa	27.2 °C
		5.0 mm	48.6 °C	860.8 Pa	27.6 °C

After these conclusions, the same studies were done considering the best fins and pins heat sinks reported in air-cooled heat sinks (Figure 3-24 and Figure 3-29, respectively). Compared with the simplest fins or pins heat sinks (Table 3-15), there was an improvement in heat sink performance up to 9.5 %

(Figure 3-36). Hence, AM approaches mentioned in Chapter 3.4.1 are also advantageous in water-cooled heat sinks.

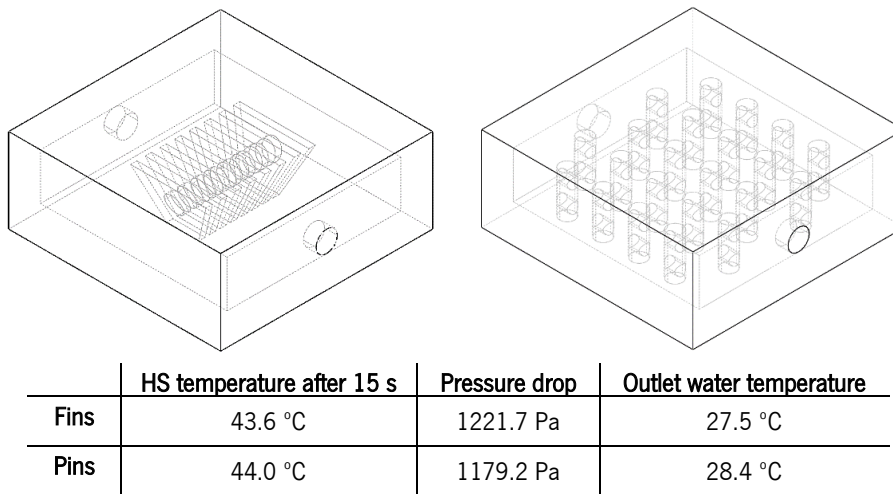
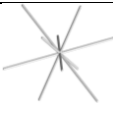

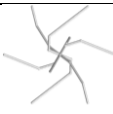




Figure 3-36. Water-cooled heat sinks based on the best air-cooled ones.

Lattice sinks with different unit cells were studied. Cell size and thickness were fixed at $15 \times 15 \times 15 \text{ mm}^3$ and 1.5 mm, respectively, in accordance with air-cooled heat sinks. The results are shown in Table 3-16. Due to software limitations, the unit cells studied for air-cooled heat sinks were not studied in this context. So, among the models studied, the heat sink with cross-pattee unit cell showed the lowest temperature. This unit cell has the higher surface area and volume.

Table 3-16. Performance of different microchannel lattice HS.

Model	HS temperature after 15s	Pressure drop	Outlet water temperature
 Star	40.8 °C	1517.4 Pa	28.1 °C
 W	40.8 °C	1321.6 Pa	26.7 °C
 3D Spider	45.3 °C	2097.0 Pa	24.2 °C
 Tetra	42.7 °C	1737.6 Pa	27.5 °C
 Cross Pattee	<u>35.4 °C</u>	<u>1578.2 Pa</u>	<u>26.1 °C</u>

Air vs water-cooled heat sinks

After the analysis of water-cooled heat sinks, in which the considered height of the heat sinks is 20 mm, a study was carried out to understand what would be the height of the lattice air-cooled heat sink (Figure 3-30) needed to reach the same temperature that was reached with water (35.4°C), considering the same Reynolds number (12500). CFD results for lattice air-cooled heat sink temperature vs height are recorded in Figure 3-37. It was found that the heat sink temperature tends to a minimum value that, according to the trend equation, is reached when the heat sink height is around 50 mm. To reach the temperature that is achieved with a 20 mm water-cooled heatsink (35.4°C), a 28.5 mm high air-cooled heat sink is required. This difference can be explained by the different thermal diffusivity values of air and water.

An important note is that, in both cases (air and water cooling), AM proved to be the best solution to produce heat sinks. Regarding the cooling method, the choice should be made according to the available volume and the cooling/performance specifications of the electronic component.

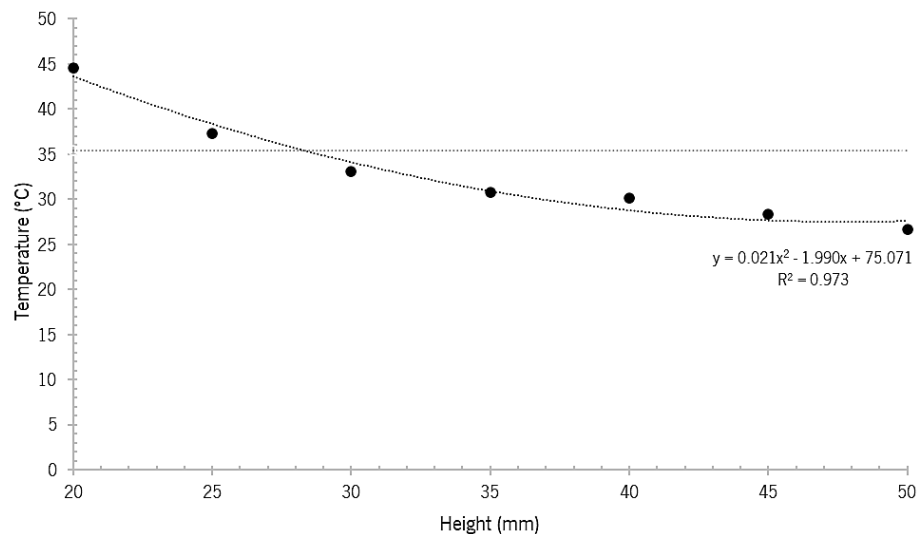
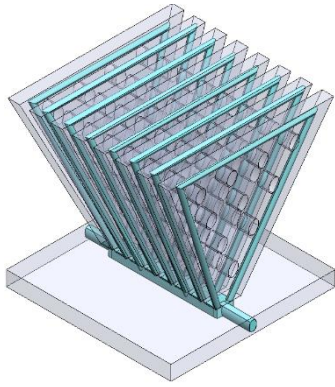


Figure 3-37. Lattice air-cooled heat sink temperature for different heights.

3.4.3. Hybrid-cooled heat sinks

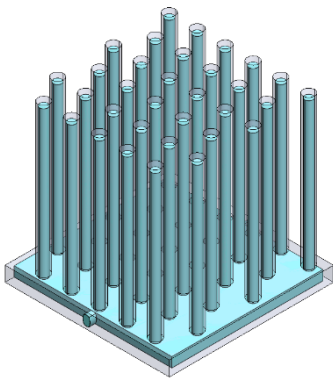
In order to optimize the results obtained in Chapter 3.4.1, water circulating in the perforated fins heat sink with thicker fins (Figure 3-38) was considered, in addition to air cooling. Despite the significant decrease in fins heat sink temperature, the air-cooled lattice heat sink (HS) continued to be advantageous.



	HS temperature after 15s
Fins air-cooled HS	36.9 °C
Fins hybrid-cooled HS	31.8 °C
Hexagon lattice air-cooled HS	26.7 °C

Figure 3-38. Hybrid-cooled fins heat sink.

A similar study considering water circulating inside the heat sink with thicker pins (Figure 3-39) was done. Considering the higher diameter for pins heat sink (i.e., 3.5 mm) with water circulating inside them, there was an improve of 0.7 °C compared to the best air-cooled heat sink model (hexagon lattice heat sink, represented on Figure 3-30). So, these gains do not compensate the incorporation of another cooling method.



	HS temperature after 15s
Pins air-cooled HS	32.4 °C
Pins hybrid-cooled HS	26.0 °C
Hexagon lattice air-cooled HS	26.7 °C

Figure 3-39. Hybrid-cooled pins heat sink.

3.5. Case study

In order apply all the knowledge acquired in Chapter 3.4, a central computer with heat sinks in aluminium was selected due to the high thermal management needs. Figure 3-40 show more detailed views of the central computer which is composed by three PCBs, three heat sinks and two cover sheets for fan and connectors protection. Aluminium heat sinks, together with convection flow created by an active fan, manage the heat dissipation.

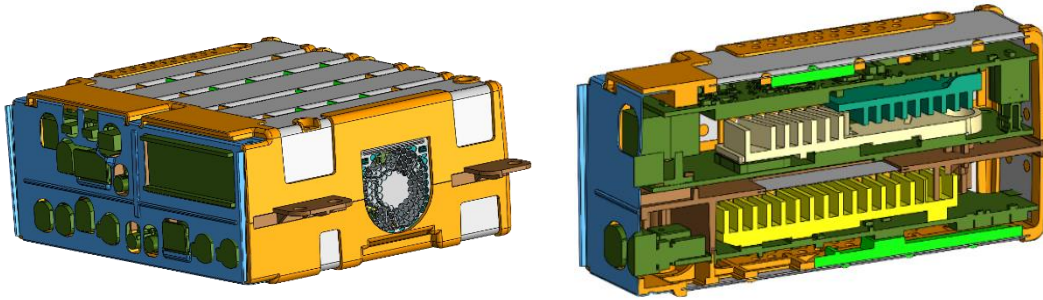


Figure 3-40. Central computer considered as case study.

The aluminium heat sink under study (Figure 3-41) has $87.5 \times 64.5 \times 11.9$ mm as main dimensions, fins with 2 mm, a weight of 71.9 g and a volume of 25.3 mm^3 . The overall dimensions of the heat sink, its holes and contact zones cannot be changed. The internal power dissipation is approximately 80 W. All components surface shall not exceed $55 \text{ }^\circ\text{C}$ at any time. In case this requirement is not fulfilled, the surrounding plastic components will be deformed. The internal fan shall have a size of mm and be operational without any restrictions from $\geq 6 \text{ V}$. The fan includes three speed-levels, controlled by software, depending on several values such as: internal component temperature, audio volume, climate control activity level and installation position in the vehicle.

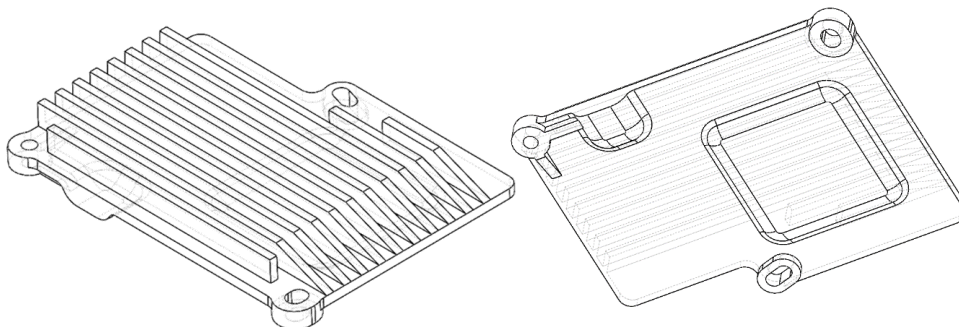


Figure 3-41. Heat sink under study.

3.5.1. Numerical simulations

To reduce the computational effort in CFD simulations, the central computer of this case study was simplified. Thus, as computational domain (

Figure 3-42), only the heat sink to be improved and the central computer housing with the fan were considered.

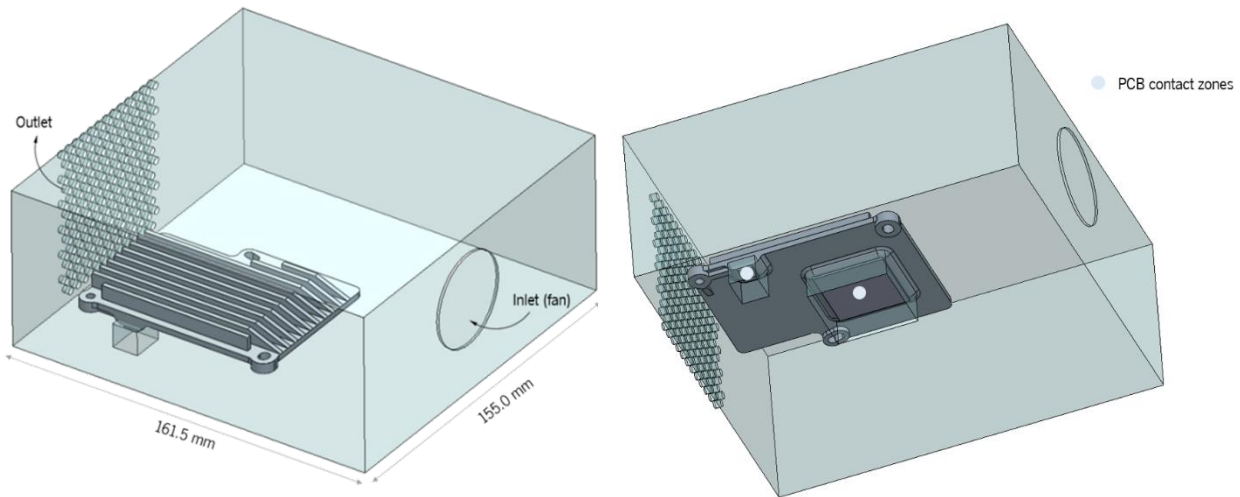


Figure 3-42. Computational domain considered for the case study.

The geometry was meshed using ANSYS Meshing by applying body sizing operation and, depending on the heat sink model under study, were considered tetrahedral or hexahedral elements. Element size varied in a range between 0.4 mm and 2.0 mm and the total number of elements was the one whose results converged, with minimal computational effort, i.e., enough to ensure mesh independence of the simulated results.

Mesh geometry (Figure 3-43) was connected into ANSYS Fluent and solver settings were defined the same as in Chapter 3.4. As initial values, the system was considered at a temperature of 28 °C, temperature at which fan is turned on. The outlet vent condition was used for the outlet boundary and the central computer housing considered adiabatic. It was defined a heat flux of 80 W in each PCB contact zone and an inlet air velocity of 5.2 m/s (1250 rpm) at 20 °C, considering the fan working at 6 V.

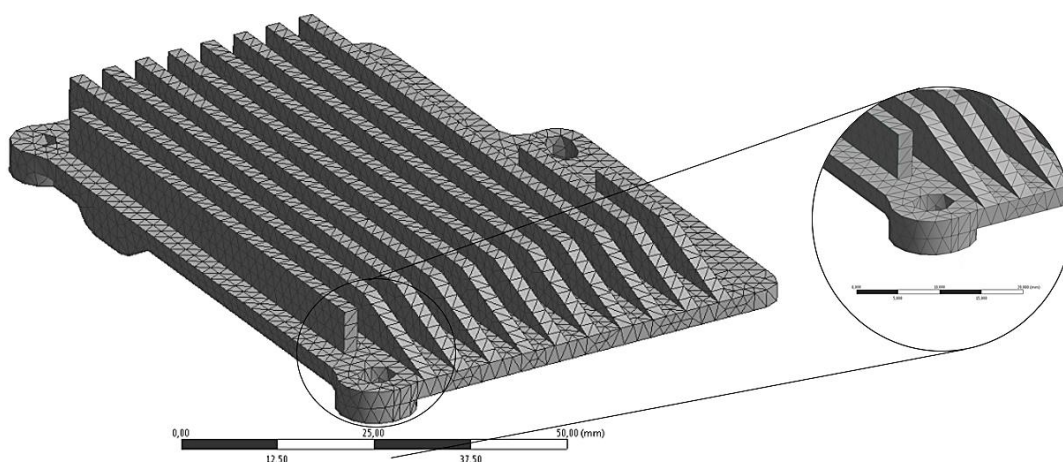


Figure 3-43. Example of a heat sink mesh considered for the case study

During compute solution, the discretised conservation equations are solved iteratively until convergence, i.e., when changes in solution variables from one iteration to the next are negligible (residual response less than 10^{-6}), considering standard ϵ -Epsilon viscous model, and time steps of one second.

The simulation is stopped when the heat sink surface temperature stabilizes, up to a maximum time of 45 seconds. During that time, the surface temperature of the hotspots, usually the nearest points to PCB contact zones (red points in Figure 3-44), was recorded.

Heat sinks design was varied according to the results obtained on Chapter 3.4, i.e., considering a reduction in thickness and the incorporation of holes (Figure 3-44, model A) and 2.5 mm pins with holes (Figure 3-44, model B), to be reliable to be produced by additive manufacturing. Also, was studied a lattice heat sink, according to the previous studies (Figure 3-44, model C). Heat sinks information is resumed in Table 3-17 and simulation results are reported in Figure 3-45 and 3.46.

As seen in the previous chapter, the lattice heat sink provided a higher area to volume ratio (Table 3-17), also resulting in lower and more uniform temperatures (Figure 3-45 and Figure 3-46). In all heat sinks studied, including the original one, surface temperature stabilizes between 45 °C and 50 °C (Figure 3-46), being below the maximum temperature imposed (55 °C). All the new heat sinks proposed are suitable to be produced by additive manufacturing and their weights are up to 29 % lower than the original one. Therefore, the implementation of AM heat sinks could improve the performance of the central computer and contribute to reduce car weight.

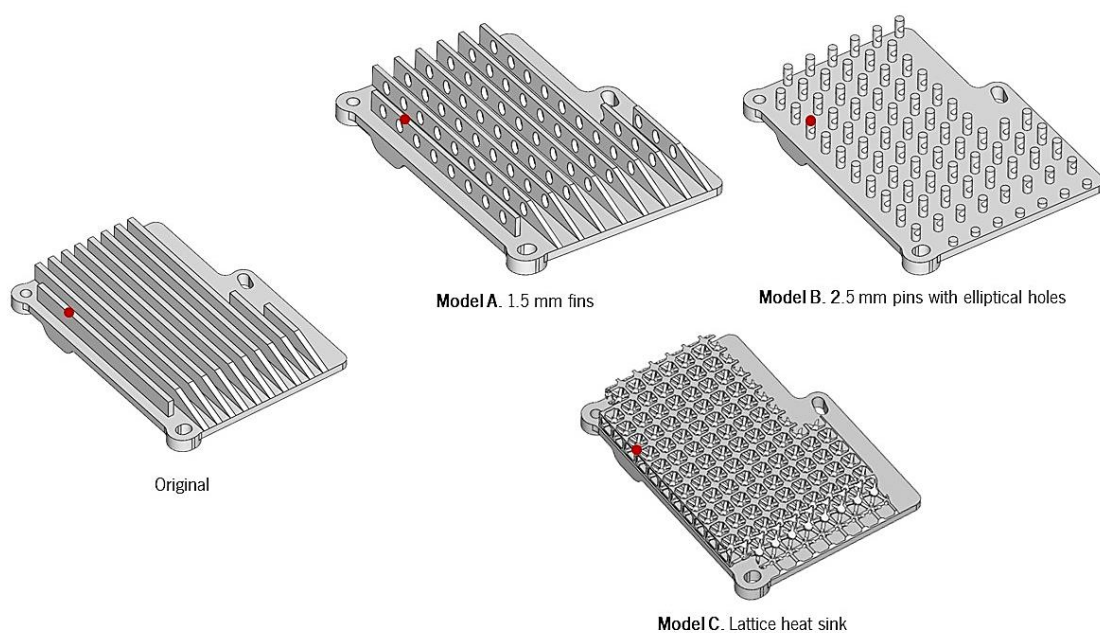


Figure 3-44. Heat sink designs considered for the case study.

Table 3-17. Geometric characteristics of the heat sink designs considered for the case study.

Model	Total area (cm ²)	Volume (cm ³)	Area to volume ratio	Weight (g)
Original	200.2	25.3	7.9	71.9
A	179.5	20.7	8.7	58.8
B	147.0	17.9	8.2	50.8
C	249.2	20.8	12.0	59.1

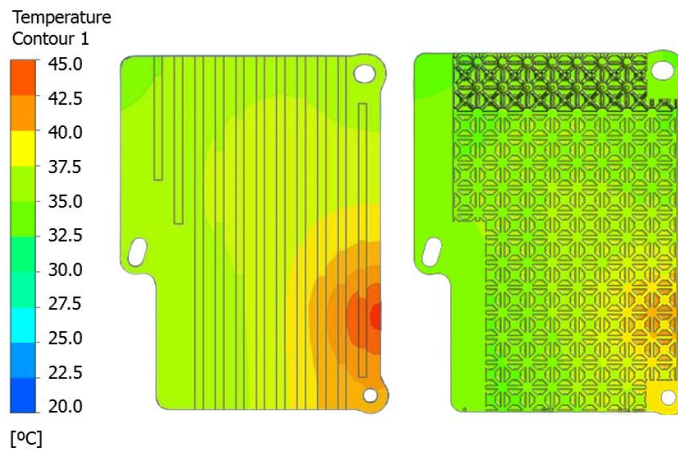


Figure 3-45. Surface temperature contours of original (left) and lattice sink (right) (reported at approximately 10 seconds).

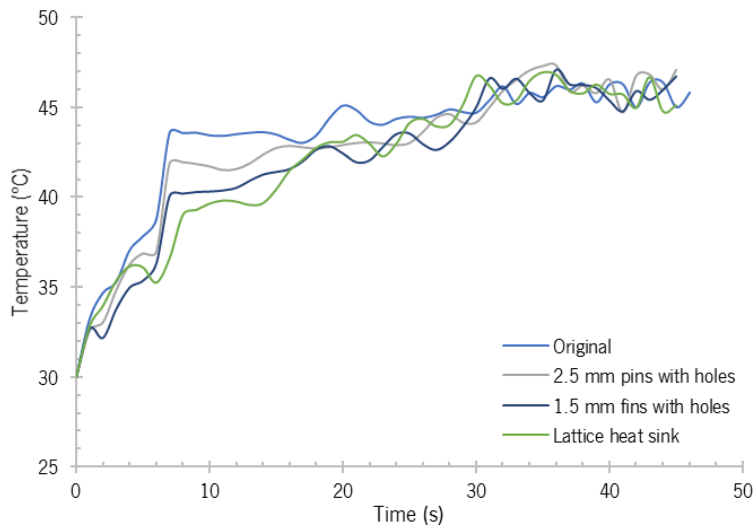


Figure 3-46. Temperature evolution recorded on the highlighted points in Figure 3-44, along 60 seconds.

3.5.2. Experimental validation

To experimentally validate the performance of AM heat sinks developed for the case study, conventional (Figure 3-47, left), lattice (Figure 3-47, middle) and hybrid lattice (Figure 3-47, right) heat sinks were produced by machining and/or with PBF, in aluminum. As in previous studies, stress relief heat treatment was not applied to PBF heat sinks.



Figure 3-47. Conventional heat sink produced by machining (left), AM heat sink produced by PBF (middle) and HM heat sink produced by machining and PBF (right).

The methodology to produce the hybrid heat sink is resumed on the flowchart of Figure 3-48. The machined half of the heat sink was attached to the building platform using four $\varnothing 4$ mm steel dowels.

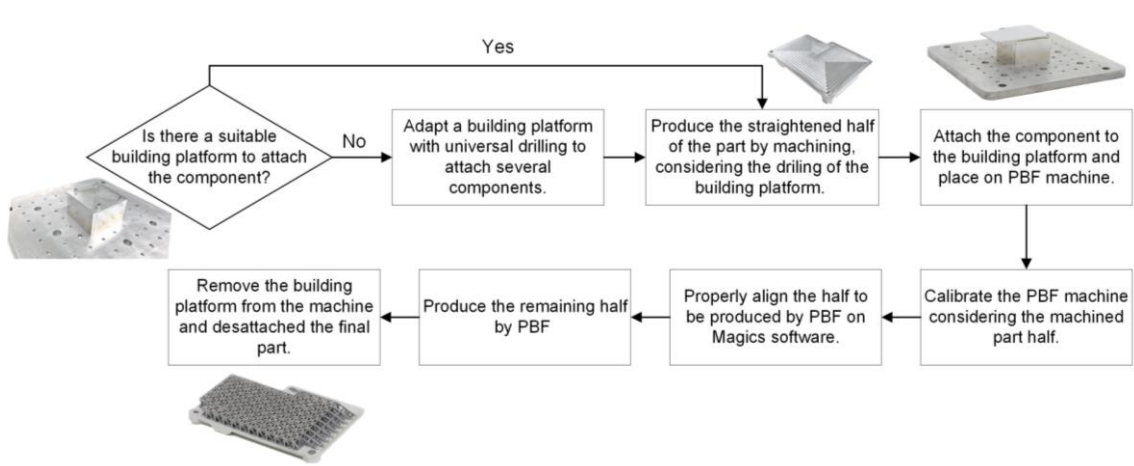


Figure 3-48. Flowchart of the production of hybrid heat sink and other hybrid parts.

Comparing to the production totally via machining or PBF, the production of hybrid heat sink was significantly faster (Table 3-18). Moreover, both in additive and hybrid heat sinks, the mass is reduced up to 12 % and 7 %.

Table 3-18. Mass and time to produce each heat sink.

	Heat sink production via		
	Machining	PBF	Machining + PBF
Production time	06h15min	07h09min	Machining: 02h15min PBF: 02h06min Total: 04h21min
Mass	70.30 g	61.45 g	65.28 g

The experimental validation was done considering the electronic enclosure described before, connected to a power supply (Figure 3-49). To simplify the system and being as close as possible to the simulations, the remaining two heat sinks were removed from the enclosure. Two K-type thermocouples were used: one is placed on the top of the heat sink (red points in Figure 3-44) and the other is placed in the smaller PCB contact zone (white point in Figure 3-42). Sensors' data were recorded with a

multichannel Multicon CMC-99 data logger for 20 seconds. On the day of the measurements, the room temperature was around 27 °C.

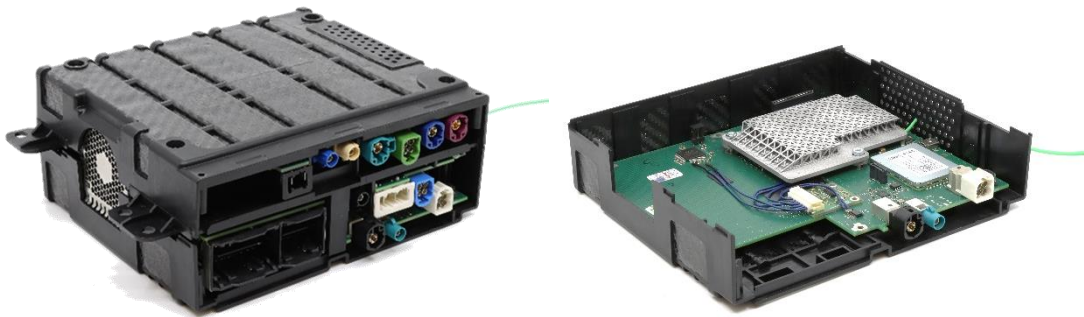


Figure 3-49. Electronic enclosure used to experimental validate the heat sinks.

However, due to the electronic enclosure prototype (Figure 3-49) limitations, it was only possible to induce 12 V of voltage, instead of the 24 V as supposed in the simulations, which corresponds to 40 W of power dissipation and the fan working at 3 V. For this reason, the numerical simulations regarding the three heat sinks had to be remade.

The results reported for the thermocouple placed on the top of each heat sink are summarized in Figure 3-50. As predicted by the simulations, the AM lattice heat sink provided lower temperatures (around 14 % lower) in the electronic enclosure, in the vicinity of the temperatures obtained for the hybrid heat sink, which were around 12 % lower, comparing to the original heat sink. In all cases, the results were relatively close to the numerical results.

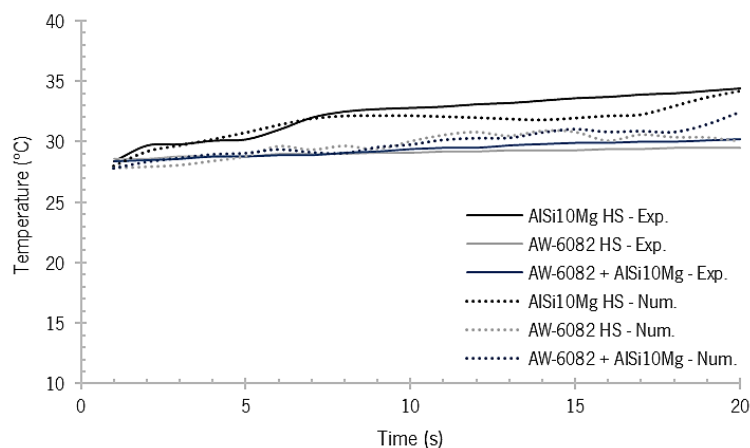


Figure 3-50. Temperature evolution on the electronic enclosure, considering each heat sink.

Moreover, the thermal resistance was calculated based on Equation 3-3 and the results reveal that, using additive manufacturing, it has been reduced to less than half (Table 3-19).

Table 3-19. Thermal resistance of each heat sink.

	Heat sink production via		
	Machining	PBF	Machining + PBF
Air temperature	27 °C		
Device temperature	34.4 °C	29.5 °C	30.2 °C
Power dissipation	40 W		
Thermal resistance	0.185 °C/W	0.063 °C/W	0.080 °C/W

3.6. Final remarks of this chapter

In this chapter, additively manufactured heat sinks were successfully evaluated through CFD simulations and validated via an experimental apparatus. The main conclusions are as follows:

- § In general, smaller diameters/thicknesses and larger fins/pins spacing with incorporation of holes provided better results than conventional fins/pins heat sinks. Additionally, performance of lattice heat sinks, only possible to be produced by additive manufacturing, was even better, providing lower temperatures and lower thermal resistance, both in the overall study (Chapter 3.4) and in the specific case study (Chapter 3.5).
- § The good performance of the lattice heat sink was experimentally validated, with a deviation of only 0.5 °C between CFD simulations and the experimental data.
- § Depending on the volume and/or performance requirements, it may be advantageous to use microchannels heat sinks, with water circulating inside them. Their performance is superior to air-cooled heat sinks.

By applying the acquired knowledge to a case study involving an automotive central computer in an action-research strategy, it was found how advantageous it is to apply AM and hybrid manufacturing (HM) with the reactive material AlSi10Mg in the production of more efficient and sustainable heat sinks. The production via HM was significantly faster than the production only via PBF, with experimental results very similar.

Answering the research question: “How much additive manufacturing improves the performance of heat sinks?”, heat sinks temperature was up to 56 % lower when compared to conventional heat sinks, and weight was reduced up to 29 %, depending on the heat sink under study and on the type of cooling method used. Considering the case study, the electronic enclosure temperatures were at least 12 % lower when PBF and hybrid heat sinks were used. This resulted in a reduction of the thermal resistance to less than half.

3.7. References

- [1] Zaharia A. Testing the Cooling Performance of a Heat Sink for Different LED Packages. *SimScale*, <https://www.simscale.com/blog/2017/03/heat-sink-led-packages/> (2018, accessed 28 October 2019).
- [2] Brindley K. *Newnes Electronics Assembly Handbook*. 1st ed. Manchester: Heinemann Newnes, 1990. Epub ahead of print 1990. DOI: <https://doi.org/10.1016/C2013-0-01084-5>.
- [3] Fowler KR, Silver CL. *Developing and Managing Embedded Systems and Products: Methods, Techniques, Tools, Processes, and Teamwork*. 1st ed. United States of America: Newnes, 2014. Epub ahead of print 2014. DOI: 10.1016/C2011-0-08758-6.
- [4] Wilson P. *The Circuit Designer's Companion*. 4th ed. United Kingdom: Elsevier Ltd., 2017.
- [5] Otake S, Tateishi Y, Gohara H, et al. Heatsink design using spiral-fins considering additive manufacturing. *2019 International Conference on Electronics Packaging (ICEP) 2019*; 175: 46–51.
- [6] Mohamad Nor NH, Ismail MH, Abu Kasim NA, et al. Magnesite effect to the alumina sintering for heat sink application. *Applied Mechanics and Materials 2014*; 465–466: 70–75.
- [7] Seo JH, Lee MY. Illuminance and heat transfer characteristics of high power LED cooling system with heat sink filled with ferrofluid. *Appl Therm Eng 2018*; 143: 438–449.
- [8] Baldry M, Timchenko V, Menictas C. Optimal design of a natural convection heat sink for small thermoelectric cooling modules. *Appl Therm Eng 2019*; 160: 114062.
- [9] Martínez-Maradiaga D, Damonte A, Manzo A, et al. Design and testing of topology optimized heat sinks for a tablet. *Int J Heat Mass Transf 2019*; 142: 118429.
- [10] Chinthavali MS, Wang ZJ. 30-kW All-SiC inverter with 3D-printed air-cooled heatsinks for plug-in and full electric vehicle applications. *Materials Science Forum 2018*; 845–848.
- [11] Bornoff R, Parry J. An additive design heatsink geometry topology identification and optimisation algorithm. *Annual IEEE Semiconductor Thermal Measurement and Management Symposium 2015*; 303–308.
- [12] Chinthavali M, Ayers C, Campbell S, et al. A 10-kW SiC inverter with a novel printed metal power module with integrated cooling using additive manufacturing. *2nd IEEE Workshop on Wide Bandgap Power Devices and Applications, WIPDA 2014 2014*; 48–54.
- [13] Collins IL, Weibel JA, Pan L, et al. Experimental Characterization of a Microchannel Heat Sink Made by Additive Manufacturing. *Proceedings of the 17th InterSociety Conference on Thermal and Thermomechanical Phenomena in Electronic Systems, ITherm 2018 2018*; 171–177.
- [14] Lazarov BS, Sigmund O, Meyer KE, et al. Experimental validation of additively manufactured optimized shapes for passive cooling. *Appl Energy 2018*; 226: 330–339.
- [15] Fasano M, Ventola L, Calignano F, et al. Passive heat transfer enhancement by 3D printed Pitot tube based heat sink. *International Communications in Heat and Mass Transfer 2016*; 74: 36–39.
- [16] Khazaka R, Martineau D, Youssef T, et al. Direct Printing of Heat Sinks, Cases and Power Connectors on Insulated Substrate Using Selective Laser Melting Techniques. *IEEE 69th Electronic Components and Technology Conference (ECTC) 2019*; 2173–2179.
- [17] Kordyban T. *Hot Air Rises and Heat Sinks: Everything You Know About Cooling Electronics Is Wrong*. ASME Press, 1998. Epub ahead of print 1998. DOI: 10.1115/1.800741.
- [18] Jiang G, Diao L, Kuang K. Introduction to Thermal Management in Microelectronics Packaging. In: *Advanced Thermal Management Materials*. New York: Springer, 2013, pp. 1–10.
- [19] Wong CM, Aziz MHBA, Ong NR, et al. Variation in heat sink shape for thermal analysis. *AIP Conf Proc*, 1885. Epub ahead of print 2017. DOI: 10.1063/1.5002487.
- [20] Abdelsalam YO, Alimohammadi S, Pelletier Q, et al. A multi-objective genetic algorithm optimisation of plate-fin heatsinks. *23rd International Workshop on Thermal Investigations of ICs and Systems 2017*; 2017-Janua: 1–6.
- [21] Jonsson H, Moshfegh B. Modeling of the Thermal and Hydraulic Performance of Plate Fin , Strip Fin , and Pin Fin Heat Sinks – Influence of Flow Bypass. 2001; 24: 142–149.
- [22] Peles Y, Koşar A, Mishra C, et al. Forced convective heat transfer across a pin fin micro heat sink. *Int J Heat Mass Transf 2005*; 48: 3615–3627.
- [23] Yang KS, Chu WH, Chen IY, et al. A comparative study of the airside performance of heat sinks having pin fin configurations. *Int J Heat Mass Transf 2007*; 50: 4661–4667.
- [24] Khan WA, Culham JR, Yovanovich MM. Optimization of pin-fin heat sinks in bypass flow using entropy generation minimization method. *Journal of Electronic Packaging, Transactions of the ASME 2008*; 130: 0310101–0310107.
- [25] Dewan A, Patro P, Khan I, et al. The effect of fin spacing and material on the performance of a heat sink with circular pin fins. *Proceedings of the Institution of Mechanical Engineers, Part A: Journal of Power and Energy 2010*; 224: 35–46.

- [26] John TJ, Mathew B, Hegab H. Parametric study on the combined thermal and hydraulic performance of single phase micro pin-fin heat sinks part I: Square and circle geometries. *International Journal of Thermal Sciences* 2010; 49: 2177–2190.
- [27] Zografos AI, Sunderland JE. Numerical simulation of natural convection from pin fin arrays. *American Society of Mechanical Engineers, Heat Transfer Division, (Publication) HTD* 1990; 157: 55–61.
- [28] Hatakeyama T, Ishizuka M, Kibushi R. Experimental study on the performance of compact heat sink for LSI packages. *Proceedings of Technical Papers - International Microsystems, Packaging, Assembly, and Circuits Technology Conference, IMPACT2000*; 193–196.
- [29] Kim DK. Thermal optimization of plate-fin heat sinks with fins of variable thickness under natural convection. *Int J Heat Mass Transf* 2012; 55: 752–761.
- [30] Charles R, Wang CC. An optimized heat dissipation fin design applicable for natural convection augmentation (IMPACT 2014). *2014 9th International Microsystems, Packaging, Assembly and Circuits Technology Conference: Challenges of Change - Shaping the Future, IMPACT 2014 - Proceedings* 2014; 61–64.
- [31] Wong KC, Indran S. Impingement heat transfer of a plate fin heat sink with fillet profile. *Int J Heat Mass Transf* 2013; 65: 1–9.
- [32] Ismail MF, Hasan MN, Ali M. Numerical simulation of turbulent heat transfer from perforated plate-fin heat sinks. *Heat and Mass Transfer/Waerme- und Stoffuebertragung* 2014; 50: 509–519.
- [33] Tijani AS, Jaffri NB. Thermal analysis of perforated pin-fins heat sink under forced convection condition. *Procedia Manuf* 2018; 24: 290–298.
- [34] Ibrahim TK, Mohammed MN, Mohammed MK, et al. Experimental study on the effect of perforations shapes on vertical heated fins performance under forced convection heat transfer. *Int J Heat Mass Transf* 2018; 118: 832–846.
- [35] Perwez A, Kumar R. Heat transfer performance investigation of the spherical dimple heat sink and inclined teardrop dimple heat sink. *Numeri Heat Transf A Appl* 2019; 76: 73–86.
- [36] Jaffal HM. The Effect of Fin Design on Thermal Performance of Heat Sink. 2017; 23: 123–146.
- [37] Hsiao C, Chang B. A study in new fin pattern of stacked fin sink for heat convection enhancement. *Proceedings of Technical Papers - International Microsystems, Packaging, Assembly, and Circuits Technology Conference, IMPACT 2011*; 404–407.
- [38] Yeh LT. Thermal performance evaluation of various heat sinks for air cooling. *InterSociety Conference on Thermal and Thermomechanical Phenomena in Electronic Systems, ITherm* 2012; 446–449.
- [39] Teeba N, Anithambigai P, Dinash K, et al. Influence of the heat sink orientation and fins arrangement on the thermal behavior of high power LED. *Proceedings of the 3rd Asia Symposium on Quality Electronic Design, ASQED 2011* 2011; 21–24.
- [40] Lin SC, Chuang FS, Chou CA. Experimental study of the heat sink assembly with oblique straight fins. *Exp Therm Fluid Sci* 2005; 29: 591–600.
- [41] Khan WA, Culham JR, Yovanovich MM. The role of fin geometry in heat sink performance. *Journal of Electronic Packaging, Transactions of the ASME* 2006; 128: 324–330.
- [42] Kou H Sen, Lee JJ, Lai CY. Thermal analysis and optimum fin length of a heat sink. *Heat Transfer Engineering* 2003; 24: 18–29.
- [43] Kou H Sen, Lee JJ, Chen CW. Optimum thermal analysis of a heat sink with various fin cross-sections by adjusting fin length and cross-section. *Heat Transfer Engineering* 2008; 29: 537–545.
- [44] Khan WA, Culham JR, Yovanovich MM. Modeling of cylindrical pin-fin heat sinks for electronic packaging. *Annual IEEE Semiconductor Thermal Measurement and Management Symposium* 2005; 125–134.
- [45] Abdel-Rehim ZS. Optimization and thermal performance assessment of pin-fin heat sinks. *Energy Sources, Part A: Recovery, Utilization and Environmental Effects* 2009; 31: 51–65.
- [46] Sahiti N, Durst F, Geremia P. Selection and optimization of pin cross-sections for electronics cooling. *Appl Therm Eng* 2007; 27: 111–119.
- [47] Zhou F, Catton I. Numerical evaluation of flow and heat transfer in plate-pin fin heat sinks with various pin cross-sections. *Numeri Heat Transf A Appl* 2011; 60: 107–128.
- [48] Gururatana S, Li X. Numerical simulation of heat sink performance with interrupted and staggered fins. *Proceedings of the ASME Summer Heat Transfer Conference 2009, HT2009* 2009; 1: 989–996.
- [49] Ho JY, Wong KK, Leong KC, et al. Convective heat transfer performance of airfoil heat sinks fabricated by selective laser melting. *International Journal of Thermal Sciences* 2017; 114: 213–228.
- [50] Xia G, Chen Z, Cheng L, et al. Micro-PIV visualization and numerical simulation of flow and heat transfer in three micro pin-fin heat sinks. *International Journal of Thermal Sciences* 2017; 119: 9–23.
- [51] Wong M, Tsopanos S, Sutcliffe CJ, et al. Selective laser melting of heat transfer devices. *Rapid Prototyp J* 2007; 13: 291–297.
- [52] Maji A, Bhanja D, Patowari PK. Effect of knurled fin surface on thermal performance of perforated fin heat sink. *J Thermophys Heat Trans* 2019; 33: 580–598.

- [53] Ramphueiphad S, Bureerat S. Synthesis of multiple cross-section pin fin heat sinks using multiobjective evolutionary algorithms. *Int J Heat Mass Transf* 2018; 118: 462–470.
- [54] Zhou F, Catton I. Numerical evaluation of flow and heat transfer in plate-pin fin heat sinks with various pin cross-sections. *Numeri Heat Transf A Appl* 2011; 60: 107–128.
- [55] Choudhary V, Kumar M, Patil AK. Experimental investigation of enhanced performance of pin fin heat sink with wings. *Appl Therm Eng* 2019; 155: 546–562.
- [56] Dede EM, Joshi SN, Zhou F. Topology Optimization, Additive Layer Manufacturing, and Experimental Testing of an Air-Cooled Heat Sink. *Journal of Mechanical Design, Transactions of the ASME*; 137. Epub ahead of print 2015. DOI: 10.1115/1.4030989.
- [57] Wits WW, Jafari D, Jeggels Y, et al. Freeform-Optimized Shapes for Natural-Convection Cooling. 2018; 2018: 1–6.
- [58] Han Y, Lu WF. A novel design method for nonuniform lattice structures based on topology optimization. *Journal of Mechanical Design, Transactions of the ASME* 2018; 140: 1–10.
- [59] Vaissier B, Pernot JP, Chougrani L, et al. Parametric design of graded truss lattice structures for enhanced thermal dissipation. *CAD Computer Aided Design* 2019; 115: 1–12.
- [60] Go JS, Kim SJ, Lim G, et al. Heat transfer enhancement using flow-induced vibration of a microfin array. *Sensors and Actuators, A: Physical* 2001; 90: 232–239.
- [61] Ikegami S, Umetani K, Hiraki E, et al. Feasibility study of fractal-fin heat sink for improving cooling performance of switching power converters. *INTELEC, International Telecommunications Energy Conference (Proceedings)*; 2018-Octob. Epub ahead of print 2019. DOI: 10.1109/INTLEEC.2018.8612377.
- [62] Bornoff R, Wilson J, Parry J. Subtractive design: A novel approach to heatsink improvement. *Annual IEEE Semiconductor Thermal Measurement and Management Symposium* 2016; 198–205.
- [63] Cho ES, Choi JW, Yoon JS, et al. Experimental study on microchannel heat sinks considering mass flow distribution with non-uniform heat flux conditions. *Int J Heat Mass Transf* 2010; 53: 2159–2168.
- [64] Chein R, Chen J. Numerical study of the inlet/outlet arrangement effect on microchannel heat sink performance. *International Journal of Thermal Sciences* 2009; 48: 1627–1638.
- [65] Sehgal SS, Krishnan M, Mohapatra SK. Effect of Flow Arrangements on Thermohydraulic Performance. 2009; 1–7.
- [66] Tang S, Zhao Y, Diao Y, et al. Effects of various inlet/outlet positions and header forms on flow distribution and thermal performance in microchannel heat sink. *Microsystem Technologies* 2018; 24: 2485–2497.
- [67] Liu Y, Luo X, Liu W, et al. Thermal performance of the multilayered honeycomb microchannel heat sink. *2009 International Conference on Energy and Environment Technology, ICEET 2009* 2009; 1: 487–490.
- [68] Lee YJ, Lee PS, Chou SK. Hotspot mitigating with obliquely finned microchannel heat sink-an experimental study. *IEEE Trans Compon Packaging Manuf Technol* 2013; 3: 1332–1341.
- [69] Hung TC, Yan WM. Effects of tapered-channel design on thermal performance of microchannel heat sink. *International Communications in Heat and Mass Transfer* 2012; 39: 1342–1347.
- [70] Hu H, Zhang J, Du X, et al. Analysis of liquid-cooled heat sink used for power electronics cooling. *J Therm Sci Eng Appl* 2011; 3: 1–9.
- [71] Xia G, Chai L, Wang H, et al. Optimum thermal design of microchannel heat sink with triangular reentrant cavities. *Appl Therm Eng* 2011; 31: 1208–1219.
- [72] Xia G, Zhai Y, Cui Z. Characteristics of entropy generation and heat transfer in a microchannel with fan-shaped reentrant cavities and internal ribs. *Sci China Technol Sci* 2013; 56: 1629–1635.
- [73] Chai L, Xia G, Zhou M, et al. Numerical simulation of fluid flow and heat transfer in a microchannel heat sink with offset fan-shaped reentrant cavities in sidewall. *International Communications in Heat and Mass Transfer* 2011; 38: 577–584.
- [74] Kuppusamy NR, Mohammed HA, Lim CW. Numerical investigation of trapezoidal grooved microchannel heat sink using nanofluids. *Thermochim Acta* 2013; 573: 39–56.
- [75] Datta A, Sharma V, Sanyal D, et al. A conjugate heat transfer analysis of performance for rectangular microchannel with trapezoidal cavities and ribs. *International Journal of Thermal Sciences* 2019; 138: 425–446.
- [76] Deldar S, Khoshvaght-Aliabadi M. Evaluation of water-cooled heat sink with complex designs of groove for application in fusion energy management. *Fusion Engineering and Design* 2019; 140: 107–116.
- [77] Hosseinpour V, Kazemeini M, Rashidi A. Developing a metamodel based upon the DOE approach for investigating the overall performance of microchannel heat sinks utilizing a variety of internal fins. *Int J Heat Mass Transf*; 149. Epub ahead of print 2020. DOI: 10.1016/j.ijheatmasstransfer.2019.119219.
- [78] Li P, Guo D, Huang X. Heat transfer enhancement, entropy generation and temperature uniformity analyses of shark-skin bionic modified microchannel heat sink. *Int J Heat Mass Transf* 2020; 146: 118846.
- [79] Al-Neama AF, Khatir Z, Kapur N, et al. An experimental and numerical investigation of chevron fin structures in serpentine minichannel heat sinks. *Int J Heat Mass Transf* 2018; 120: 1213–1228.
- [80] Al-Asadi MT, Al-damook A, Wilson MCT. Assessment of vortex generator shapes and pin fin perforations for enhancing water-based heat sink performance. *International Communications in Heat and Mass Transfer* 2018; 91: 1–10.

- [81] Collins IL, Weibel JA, Pan L, et al. A permeable-membrane microchannel heat sink made by additive manufacturing. *Int J Heat Mass Transf* 2019; 131: 1174–1183.
- [82] Tseng PH, Tsai KT, Chen AL, et al. Performance of novel liquid-cooled porous heat sink via 3-D laser additive manufacturing. *Int J Heat Mass Transf* 2019; 137: 558–564.
- [83] Ho JY, Leong KC, Wong TN. Experimental and numerical investigation of forced convection heat transfer in porous lattice structures produced by selective laser melting. *International Journal of Thermal Sciences* 2019; 137: 276–287.
- [84] Patankar S v. Calculation of the flow field. In: Phillips MA, Millman EM (eds) *Numerical Heat Transfer and Fluid Flow*. United States of America: Hemisphere Publishing Corporation, 1980, pp. 113–138.
- [85] Moukalled F, Mangani L, Darwish M. *The finite volume method in computational fluid dynamics*. Switzerland: Springer, 2016. Epub ahead of print 2016. DOI: 10.1007/978-3-319-16874-6_21.
- [86] Wu T, Ozpineci B, Ayers C. Genetic algorithm design of a 3D printed heat sink. *Conference Proceedings - IEEE Applied Power Electronics Conference and Exposition - APEC* 2016; 2016-May: 3529–3536.
- [87] Tavassoli B. Novel Heat Sink Design for Low Speed. 2000; 16–20.
- [88] Gu S, Lu TJ, Evans AG. On the design of two-dimensional cellular metals for combined heat dissipation and structural load capacity. *Int J Heat Mass Transf* 2001; 44: 2163–2175.
- [89] Shamvedi D, McCarthy OJ, O'Donoghue E, et al. 3D Metal printed heat sinks with longitudinally varying lattice structure sizes using direct metal laser sintering. *Virtual Phys Prototyp* 2018; 13: 301–310.

4. INJECTION MOULDING INSERTS

This chapter intends to answer the research questions “Which is the general behaviour of aluminium moulding inserts for injection moulding with transparent materials?” and “How much savings these approaches achieve?”. To this, different conformal cooling channels designs were evaluated via numerical simulations. The best design was applied to aluminium moulding inserts to experimentally evaluate their performance moulding amorphous and semi-crystalline parts. In the end, considering the hybrid approach studied throughout this work, it is evidenced the potential in combining the best of both methods for a faster production with less material waste.

4.1. Introduction

As a response to the needs of the market, moulds' industry integrated new technologies to reduce the time of a product development, appearing the concept of hybrid moulds (Figure 4-1). This concept consists in combining conventional mould manufacturing with additive manufacturing (AM), reducing costs and time in the production of injection moulding (IM) components. Many authors have been studied some variants and improvements of these tools and their performance, capable of producing parts with better properties than conventional manufacturing.

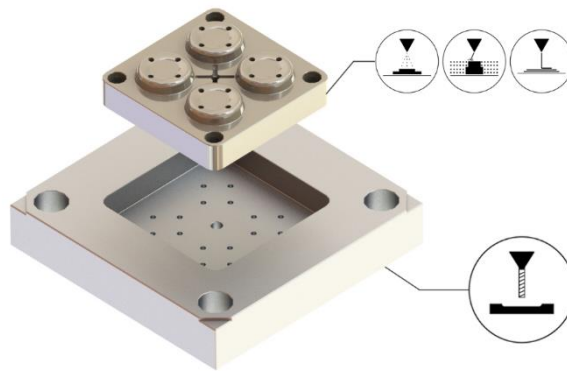


Figure 4-1. Hybrid mould concept and technologies used.

Compared to conventional moulds, hybrid moulds have interesting strengths, such as [1–3]:

- ◁ efficiency, by decreasing the volume of material used, and energy consumption, due to the possibility of being able to use the same mould structure to produce different polymeric parts;
- ◁ freedom of geometric shapes, namely in the cooling channels;
- ◁ flexibility to modify and apply a design concept to testing, such as different cooling systems for the same polymeric part.

However, it should be kept in mind that hybrid moulds concept still presents some limitations that restrict its applicability and expansion, namely [1]:

- ◁ the thermal and mechanical properties of some additive manufacturing materials available on the market are not always adequate for moulding inserts to have a life span equivalent to conventional moulds;
- ◁ the need for improvement in dimensional accuracy, surface finishing, working dimensions, as well as repeatability and reliability;
- ◁ additive manufacturing technologies still have relatively high costs to be easily implemented in the industry.

4.2. Brief review on metallic injection moulding inserts

Through the years, many AM technologies have been applied in IM inserts mainly Powder Bed Fusion (PBF), stereolithography (SLA) and Material Jetting. The metal-based technology used in this work, i.e., PBF, can create almost fully dense parts, only in one stage, if thermal treatment was not applied. However, most of the times, the use of PBF for application in injection moulds is based in tool steel and aluminium-based studies are very scarce.

Despite its lower mechanical strength, the use of aluminium moulds, with a thermal conductivity up to five times higher than a traditional steel, ensures a reduction of the cooling time, lower risk of warpage and sink marks and lower stresses with economic advantages [4–6]. Incorporating conformal cooling channels (CCC) into these moulds further enhances these advantages. Nowadays, aluminium is more discussed for simpler applications such as blow moulding [7] and extrusion dies [8, 9], or for preliminary studies about the manufacturability of internal channels, not considering the production of moulding inserts itself [10].

4.2.1. Conformal cooling channels

Injection moulding is the most used manufacturing technology for low-cost and high reliability plastic parts and comprises five main stages, by means of the application of heat and pressure: (i) plastification, (ii) injection, (iii) packing, (iv) cooling, and (v) ejection (Figure 4-2). Since the cooling phase represents a large part of the total injection cycle time (typically around 70 – 80 %), the use of this type of optimised cooling configuration can lead to significant savings (up to 50 %) that translate into increased productivity in the injection moulding process [11–13]. Moreover, with a controlled temperature distribution on the surface of the part (maintaining a constant distance from the cooling channels to the part), it is possible to prevent certain defects that can occur in the injection moulding process, such as shrinkage and warpage, ensuring the quality of the moulded parts [14, 15]. However, the field of conformal cooling channels (CCC), the focus has been mainly based on simulation work and there are few studies that consider experiments, e.g., regarding the quality of the parts [16].

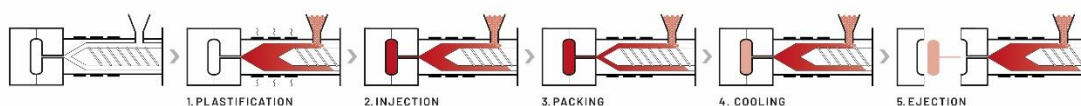


Figure 4-2. The injection moulding process.

The thermal properties of the material and the cooling channels are two key factors that determine the cooling characteristics [17]. For example, comparing injection moulding inserts with CCC with a

conventional mould in a highly thermal conductive material with straight-drilled cooling channels, e.g. copper, cycle time was similar but there were fewer residual stresses with the first one [18]. Under other conditions, moulding inserts with low thermal conductivity made from titanium alloy and with CCC had similar performance as conventional injection moulding inserts, confirming efficiency of CCC [19]. Figure 4-3 shows a comparison of straight and conformal cooling channels [20].

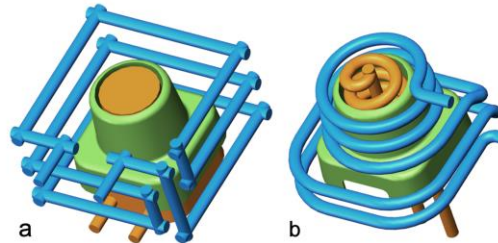


Figure 4-3. a) Straight-drilled vs b) conformal cooling channels [15].

Basic theoretical background

Injection moulding process can be described as a transient process where the heat transfer balance (Equation 4-1) occurs when the heat transfer rate from the molten polymer to the mould material by conduction (Equation 3-1) (Q_m) becomes equal to the heat transferred from the mould material to the coolant by convection (Equation 3-2) (Q_c) and ambient air (Q_e) by convection and radiation [21].

Equation 4-1. Heat transfer balance in injection moulding process.

Most of the times, the Q_e obtained is less than 5 % of Q_m , which means that, to improve the cooling performance, the aim is to maximize Q_c [22]. With this, Q_e may be considered negligible and the mould boundary adiabatic, simplifying Equation 4-1 to Equation 4-2.

Equation 4-2. Heat transfer balance in injection moulding process (simplified).

Design notes

The cross-section shape of the conformal cooling channels has influence on the heat transfer process. According to some authors, the section that offers the most efficient cooling is the one that allows a constant distance to the plastic part [23]. When considering circular shapes, the execution of water lines with a diameter greater than 8 mm should be avoided due to the need to include support structures [13]. When supports structures are not placed, surface finishing of powder-based additive manufactured internal passages tends to be poor, especially downskin surfaces (Figure 4-4, left) [24].

For this reason, some authors suggested the usage of internal supports that can suppress the collapse and warpage of internal channels, improving the manufacturability (Figure 4-4, right) [25–28]. Another suggestion is the usage of multiphase hydrodynamic flows or vibrofinishing to polish the cooling channel surface [29, 30] or the implementation of roundness prediction models [31–33].

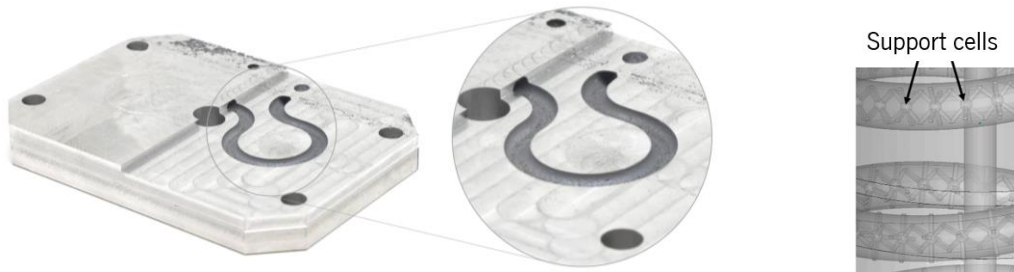


Figure 4-4. Rougher passages of cooling channels (left) and conformal cooling channels (CCC) with internal supports (adapted from [24]).

The inclusion of lattice structures is also considered for a lightweight mould, maintaining similar thermomechanical performance, and can reduce energy costs up to 13 % and mass savings in 30 % compared to a IM insert without lattice structures [34, 35].

4.2.2. Quality of mouldings

More efficient cooling promoted by CCC improves the quality of the parts obtained by injection moulding, which is evaluated according to: (i) surface appearance and (ii) shape and dimensions [36–38].

In terms of surface appearance, the quality of the mouldings depends on the surface finish of the moulding inserts [38]. The surface roughness of moulding inserts produced by PBF is defined by both the particle size of the powder and the precision and parameters of the process [37, 39, 40]. However, given the significant surface roughness, finishing operations such as polishing, machining and/or coatings must be considered [39, 41, 42].

The shape and dimensions of an injection-moulded part are also affected by warpage and shrinkage [38]. The shrinkage of mouldings can be reduced by implementing a conformal cooling system, especially when they are injected with semi-crystalline polymers, such as polypropylene (PP) [2, 3, 36, 43]. The injection process parameters also affect the shrinkage, mainly the second pressure, injection temperature and the mould temperature. Warpage is a phenomenon that is intrinsically related to non-uniform shrinkage that causes the deformation of the moulded products and the change of their geometry.

General performance of injection moulding inserts produced by additive manufacturing also depends on the nature of the injection material. That is, more abrasive materials like glass filled polymers degrade the tool more quickly than, for example, PP. Moreover, very viscous materials, which require high injection pressures or temperatures, may exceed the capabilities of the moulding inserts that have mechanical

properties inferior to those of moulding inserts made with conventional materials, e.g., maraging steel [44, 45].

4.2.3. Economic evaluation and the emerging of hybrid manufacturing

The cost evaluation of AM processes in the production of moulding inserts is not yet fully understood and always depends on the case study [46]. The decision between using additive or subtractive methods is conditioned by aspects such as the cost of raw materials and equipment, geometry and dimensions of the part [47, 48]. Some literature on this topic refers that subtractive manufacturing is the most advantageous method for larger and less complex parts [49, 50]. On the other hand, despite the constant evolution of additive processes and materials, these still present a relatively high cost. However, there are studies that demonstrate the great potential of these technologies to reduce costs and time, mainly due to the incorporation of CCC [46]. Boccardi *et al.* [51] conducted an economic feasibility study on the incorporation of AM in moulding inserts as an alternative to conventional injection moulds. Although the acquisition and operational costs of metal PBF equipment and materials are high, steel moulding inserts with conformal channels allowed a decrease in cooling time by ten seconds, compared to the conventional mould. For this reason, this industry can recover the investment if a long production series was considered [48, 52, 53].

A relevant trend in the moulds' industry in recent times is hybrid manufacturing. Hybrid manufacturing consists on produce the base of injection moulding inserts by conventional manufacturing (e.g. Computer Numerical Control (CNC)) and the moulding zone by AM, taking advantage of geometric freedom and CCC. Depending on the case study, hybrid manufacturing approaches provide lower energy consumption and costs savings up to 20 % compared to moulding inserts all produced by AM [49, 54, 55]. However, hybrid manufactured tools may have lower mechanical properties and tool life than the same tools produced by conventional machining, even though failure of the bonded regions hardly occurs during injection moulding process [54, 56].

Considering hybrid manufacturing, particular attention should be paid to the machining process (before AM) which must result in quality parallel surfaces as they serve as substrate to produce the most complex parts by AM. Substrate positioning on AM equipment must be accurate and by coordinates and it is important to calibrate the AM equipment well to ensure a more effective union between the two parts [47, 57–60].

Moreover, hybrid manufacturing processes always require careful planning that should consider the processing nature of AM (dimensional deviations, layer thickness, orientation), machining tools and part attributes (specific characteristics and tolerance requirements). This planning should also take into account

the decomposition of a part into a number of subparts (which are manufactured by AM and which are manufactured by subtractive manufacturing), the infinite number of workable process sequences for manufacturing a part and the process change time [47, 61, 62]. An algorithm developed by Homar and Pušavec [54] showed that 65 % subtractive manufacturing and 35 % AM is the ideal combination for lower cost.

4.3. Moulding inserts development

4.3.1. Part and mould structure

The test part (Figure 4-5) to be processed by the different moulding inserts was designed for monitoring thermal behaviour. With a nominal angle of 30° , it is also suitable for monitoring one of the main defects induced by non-uniform cooling, i.e., warpage.

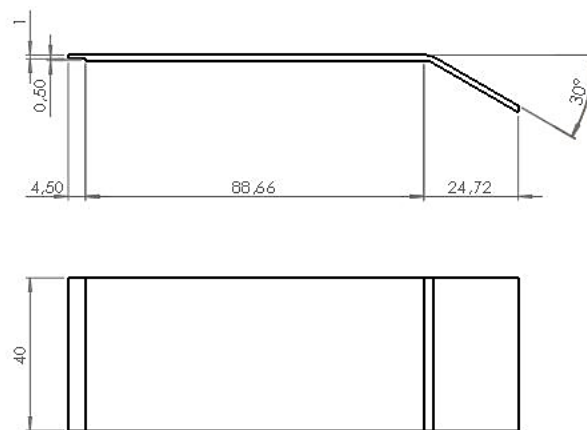


Figure 4-5. Technical drawing of the test part.

The mould structure (Figure 4-6), with main dimensions $275 \times 290 \times 238$ mm, was designed to easily receive different core and cavity moulding inserts made by conventional or additive manufacturing.

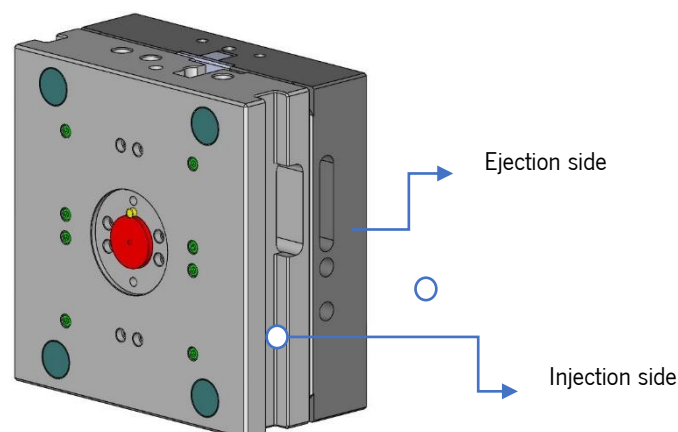


Figure 4-6. Mould structure.

With this mould structure, it is possible to produce two parts simultaneously, as shown by the initial moulding inserts (maximum dimensions: $169.9 \times 183.6 \times 60.3$ mm) (Figure 4-7, left). However, to facilitate the present study (both CAE simulations and experimental work), the moulding inserts will be reduced to half (maximum dimensions: $169.9 \times 91.8 \times 60.3$ mm). The remaining half being will remain filled with a steel block (Figure 4-7, right).

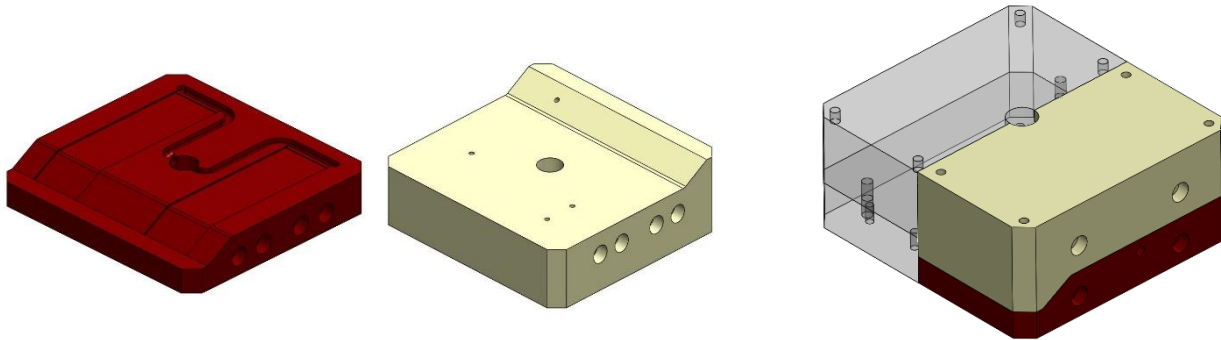


Figure 4-7. Original moulding inserts (left) and moulding inserts reduced to half (right).

The original temperature control system that removes heat from the part consists of a single U-shaped circuit in both mould halves, making the contour of the part geometry (Figure 4-8). The diameter of the machined channels is 8 mm and the selected coolant is water.

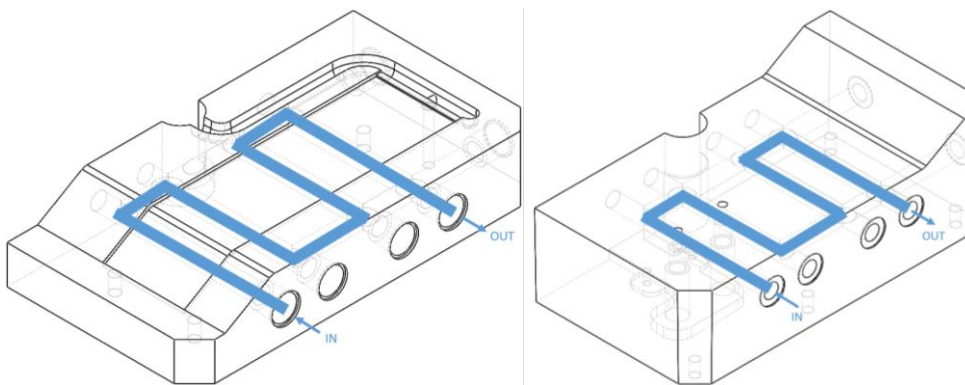


Figure 4-8. Conventional temperature control system on cavity (left) and core (right).

The ejection system consists of two cylindrical ejectors. One positioned in the central zone of the piece and the other in the feeding channels (Figure 4-9), promoting a smooth and balanced ejection of the feed system, avoiding possible warping of the parts.

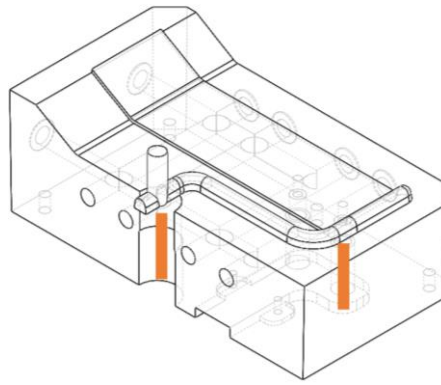


Figure 4-9. Ejection system.

4.3.2. Numerical procedure

The procedure to select the best injection moulding inserts (Figure 4-10) starts with the design of different conformal cooling channels, based on the technical-scientific knowledge acquired before. All designs are tested via Moldex3D preliminary simulations to realize the ones with the most potential to be applied to injection moulding inserts. Then, for the selected cooling systems, full injection moulding process simulations are done, considering the same cooling time. To the final CCC configuration, the pressure curves are acquired and then considered for mechanical simulations via ANSYS Static Structural to check if the maximum strength is below the compressive yield strength reported on previous chapter (Table 2-13). If yes, the moulding inserts to be produced by additive manufacturing can be topology optimized to reduce the mass and the material needed, and increase producing speed, without compromising the structural performance.

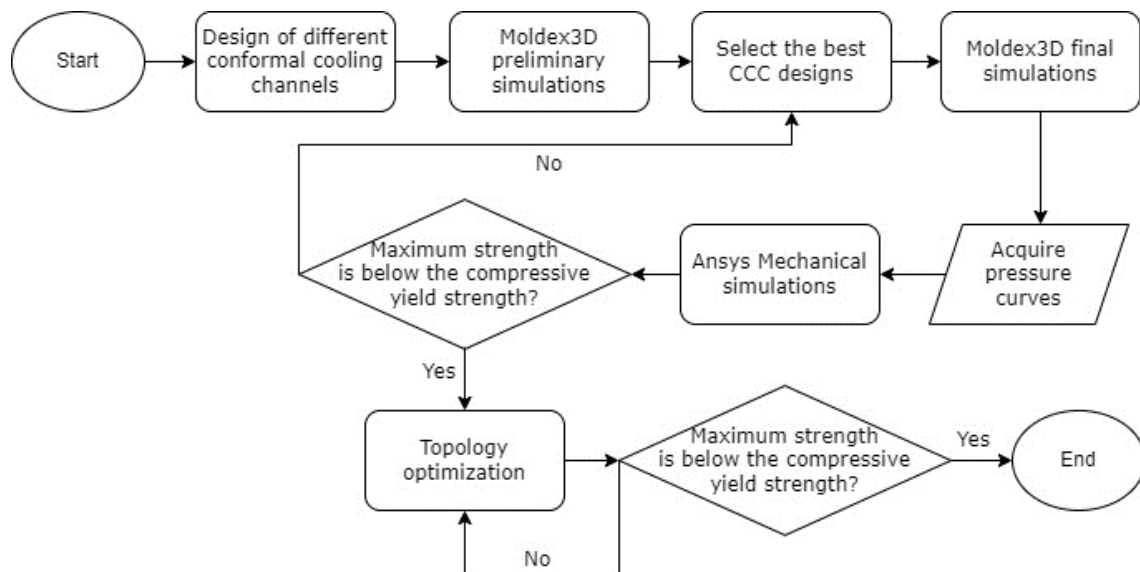


Figure 4-10. Procedure to select the best injection moulding inserts.

Materials properties

As injection materials, two different materials were considered: an amorphous polystyrene (PS) 165N/L da Styrolution (Appendix 5) and a semicrystalline PP 579S da Sabic (Appendix 6), whose main properties are summarized in Table 4.1. A semi-crystalline material was chosen because the degree of crystallinity and molecular weight affect the properties of a polymer and, under controlled cooling conditions, it is possible to maximise the volume of crystallites and hence the degree of crystallinity.

Table 4-1. Injection materials main properties.

Property	PS 165N/L (Styrolution)	PP 579S (Sabic)
Tensile Stress at Yield, 23 °C	52 MPa	37 MPa
Tensile Strain at Yield, 23 °C	2 %	8 %
Tensile Modulus	3.3 GPa	1.8 GPa
Hardness (Rockwell)	62	113
Density	1040 kg/cm ³	905 kg/cm ³

The moulding inserts materials used in the simulations were aluminium alloy AW-6082 (for conventional straight-drilled cooling channels) and AlSi10Mg for conformal cooling channels. The properties of the materials used were set according to Chapter 2, and are shown in Table 4.2. As thermal properties were similar with and without the stress relief heat treatment (HT), but the compressive properties were improved by 7.5 % after heat treatment, the stress relief heat treatment was considered in this application.

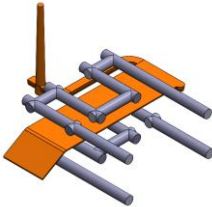
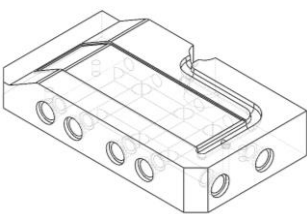
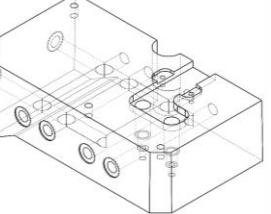
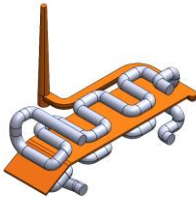
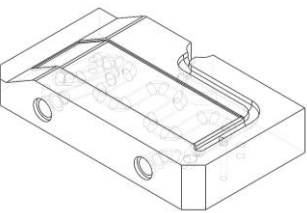
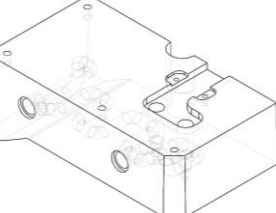
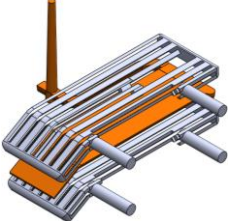
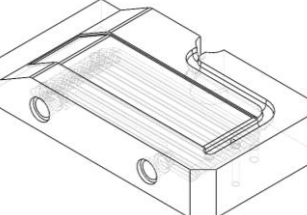
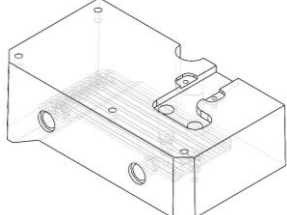
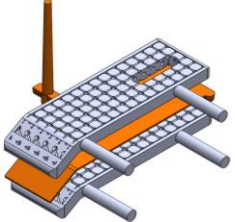
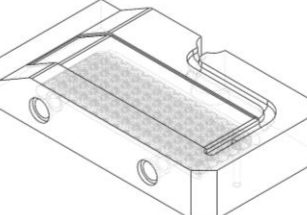
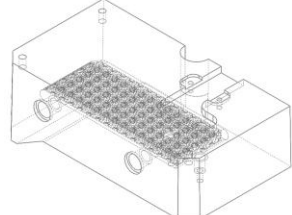
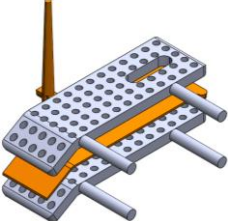
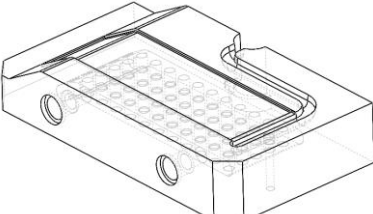
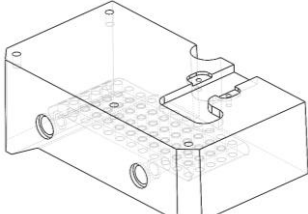
Table 4-2. Moulding inserts materials main properties.

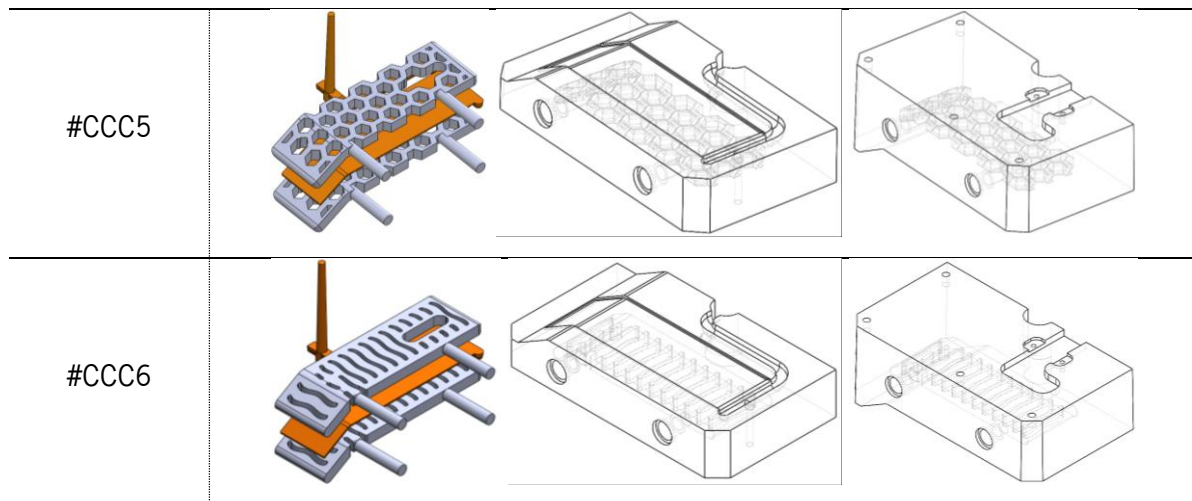
Property	AW-6082	AlSi10Mg (with HT)	
Density	2.757 g/cm ³	2.645 g/cm ³	
Heat capacity (at 40 °C)	794.2 J/g°C	980.7 J/g°C	
Thermal conductivity	133.17 W/m°C	165.9 W/m°C	
Thermal expansion coefficient	22.09×10 ⁻⁶ °C ⁻¹	25.85×10 ⁻⁶ °C ⁻¹	
Tensile efforts	Young's modulus	83.7 GPa	64.9 GPa
	Yield strength at 0.2%	182.7 MPa	111.5 MPa
	Elongation at yield	0.62 %	0.30 %
	Ultimate tensile strength	422.0 MPa	322.3 MPa
	Elongation at break	4.99 %	3.29 %
Compressive efforts	Compressive modulus	19.1 GPa	14.3 GPa
	Yield strength 0.2%	328.5 MPa	252.2 MPa
	Elongation at yield	2.06 %	2.43 %

Conformal cooling system design

The conformal cooling channels (CCC) geometries that were analysed were designed in the computer-aided design (CAD) software Solidworks. In conventional geometry, the cooling channels with a diameter of 8 mm are between 18 mm and 31 mm away from the part. Otherwise, for all conformal cooling channels designs, this distance is constantly equal to 18 mm. In all cases, the geometries were exported in STEP (Standard for the Exchange of Product Data), which is a neutral file format, and imported into Moldex3D. The analysed CAD geometries are shown in Table 4-3, where grey volumes correspond to water.

Table 4-3. Conformal cooling channels studied.

Name	Geometry		
Conventional (Ø 8 mm)			
#CCC1 (Ø 8 mm)			
#CCC2			
#CCC3			
#CCC4			



Geometry #1 represents the most usual conformal cooling channel geometry. Then, conformal cooling channels from #2 to #6 were created based on a bain-marie concept, where almost the whole geometry of the part is covered by water (Figure 4-11) [64]. Geometry #2 is based on a distributor and collector channel; Geometry #3 considers the lattice structures studied on the previous chapter (Figure 3-44); Geometry #4 includes pins to induce turbulence of the coolant uniformly through the cooling channel [63]; Geometry #5 is based on honeycomb structures; and Geometry #6 considers wavy blades.

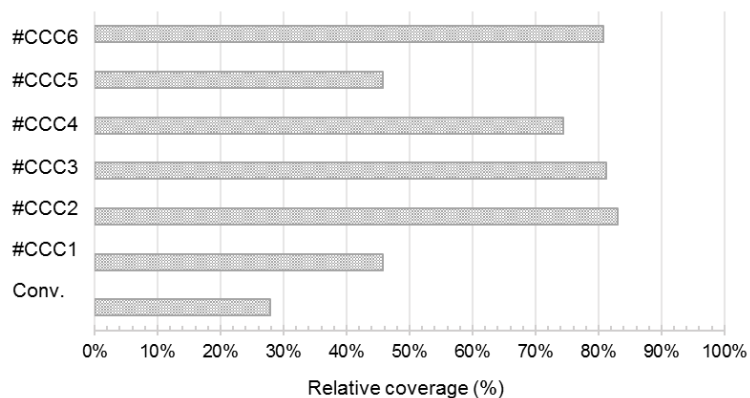


Figure 4-11. Relative coverage of the part with each conformal cooling channels designed.

4.3.3. Evaluation of thermal behaviour

To evaluate the thermal behaviour of the different cooling designs, Moldex3D software was used. In a first stage, filling and packing analysis were done, considering mesh elements of 2 mm, according to the mesh study done for standard moulding inserts and presented in Figure 4-12. Mesh elements of 2 mm make a total number of approximately 21000 mesh elements.

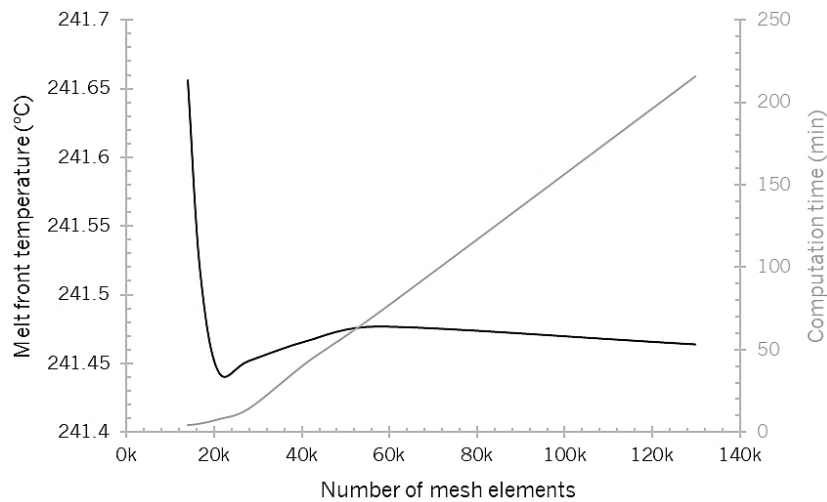


Figure 4-12. Number of mesh elements in the part as a function of melt front temperature and computation time for conventional moulding inserts.

The standard finite element method (FEM) model of the analysed moulding part together with the cooling channel systems is shown in Figure 4-13. Polymeric materials for planned simulations were selected from Moldex3D database: PP 579S from Sabic and GPPS 165H from Styrolution. Mould materials were selected depending on the designed cooling channels, i.e, AW-6082 for conventional cooling channels and AISi10Mg for conformal cooling channels, considering the main properties referred in Table 4-2.

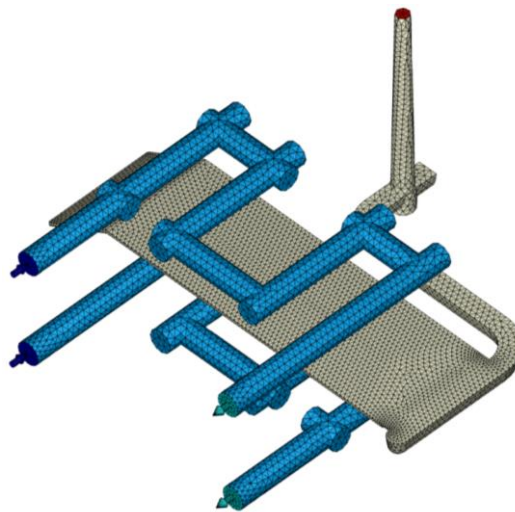


Figure 4-13. FEM model of the part and designed cooling channels with inlets and outlets for simulation in Moldex3D.

In the injection moulding simulation, the Modified Cross Models were used as viscosity model of the analysed materials. For PP 579S, Equations 4-3 and 4-4 were considered, where η is the apparent viscosity, η_0 the lower Newtonian viscosity, $\dot{\gamma}$ the shear rate, T the temperature, P the pressure and material constants have the values $n = 0.341$, $\eta_0 = 227000$ Pa, $B = 0.0145$ Pa.sec, $T_0 = 5210$ K and $D = 0$ P⁻¹.

Equation 4-3. Apparent viscosity according to Modified Cross Model.

$$\eta_a = \eta_0 \left(\frac{\dot{\gamma}}{D_1} \right)^{n-1} \left(1 + \frac{D_2}{\dot{\gamma}} \right)^{-1} \left(1 + \frac{D_3}{P} \right)^{-1}$$

Equation 4-4. Lower Newtonian viscosity for PP 579S, according to Modified Cross Model.

$$\eta_0 = A_1 \left(\frac{D_1}{\dot{\gamma}} \right)^{A_2} \left(1 + \frac{D_3}{P} \right)^{-1}$$

For GPPS 165H, Equations 4-3, 4-5 and 4-6 were considered, where η_a is the apparent viscosity, η_0 the lower Newtonian viscosity, $\dot{\gamma}$ the shear rate, T the temperature, P the pressure and material constants have the values $n=0.18542$, $\eta_0=36027$ Pa, $D_1=2.11096 \times 10^{12}$ Pa.sec, $D_2=373.15$ K, $D_3=0$ K/Pa, $A_1=28.3127$ and $A_2=51.6$ K.

Equation 4-5. Lower Newtonian viscosity for GPPS 165H, according to Modified Cross Model.

$$\eta_0 = A_1 \left(\frac{D_1}{\dot{\gamma}} \right)^{A_2} \left(1 + \frac{D_3}{P} \right)^{-1}$$

Equation 4-6. Calculation of material constants for GPPS 165H.

and

In Table 4-4, the basic process parameters selected in accordance with the recommendations of the producers of the polymeric materials are presented. Up to 98 %, the part was filled at a constant flow rate. Then, the packing pressure was set in three steps for both materials (Figure 4-14).

Table 4-4. Basic process parameters used in the injection analysis.

Processing parameter	PP 579S	GPPS 165H
Maximum injection pressure	140 MPa	250 MPa
Injection temperature	240 °C	230 °C
Mould temperature		40 °C
Eject temperature	90 °C	84 °C
Injection time		0.75 s
VP switch-over by volume		98 %
Packing time		4.73 s

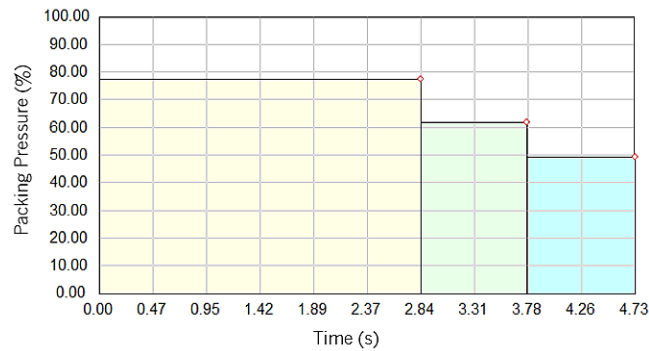


Figure 4-14. Multistep setting of the packing pressure profile.

To global analyse the performance of the different cooling channels designed, average packing temperature was recorded (Figure 4-15). Results showed that, for both amorphous and semicrystalline polymers, the average temperature after packing (5.5 seconds) was up to 4.7 % lower for conformal cooling channels #2.

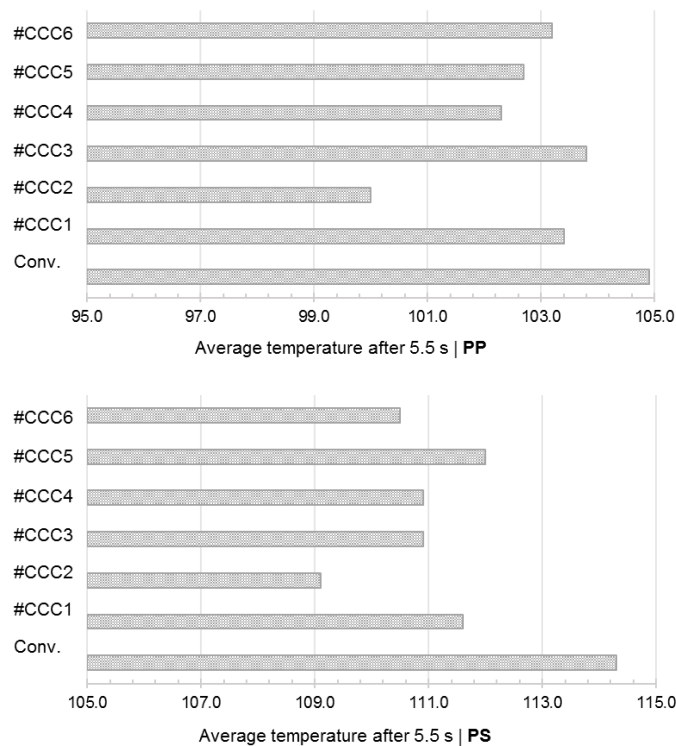


Figure 4-15. Average temperature after packing for each cooling channels.

For this reason, considering these cooling channels, the mechanical strength of the moulding inserts was evaluated using ANSYS Mechanical.

4.3.4. Mechanical simulations

Considering the results of the injection moulding process simulations, filling pressure curves obtained in Moldex3D (Figure 4-16) were imported in Ansys Mechanical to evaluate the structural performance of the AlSi10Mg moulding inserts with the stress relief heat treatment. As the pressure when moulding PS is

higher, this curve was considered for the mechanical simulations. The part was supported in the way that is closest to the real situation of a mould in the injection moulding machine. The constraints and loads applied to the numerical models are shown in Figure 4-17. All degrees of freedom were constrained, so the constrained faces do not allow any translational or rotational motion.

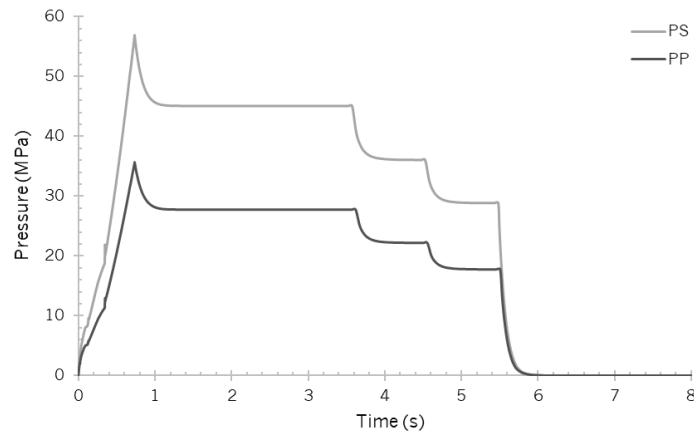


Figure 4-16. Filling pressure curves obtained in Moldex3D.

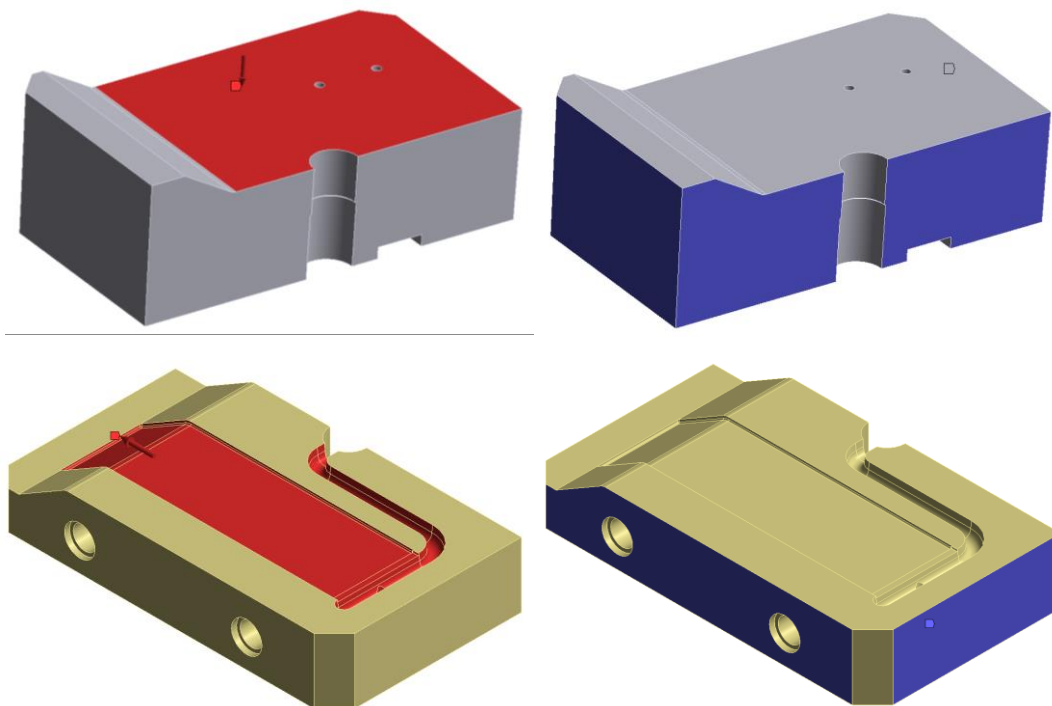


Figure 4-17. Pressure applied on the injection moulding inserts (left) and fixed faces (right).

Contours were obtained to assess the distribution of stresses and displacements. The aim of mechanical simulations is to apply topology optimization fundamentals, by reducing material on the points of lowest stresses, within the available volume. Figure 4-18 (left) shows graphic results in terms of equivalent stresses according to Von-Mises criterion. The contours show highest von-Mises stresses close

to the centre of the areas of load application, in the conformal cooling channels. While the contour might not present clear gradients of results, it is important to note that von-Mises stresses are equivalent stresses, which are calculated according to the principal stresses. The relationships between the principal stresses might originate results whose contours are non-trivial, such in this case.

Figure 4-18 (right) shows graphical results in terms of total displacement. The contour shows higher deflections in the place of load application, which is also a place with higher distance to the constrained areas. In general, there is a deflection gradient caused by the distance to the areas of load application.

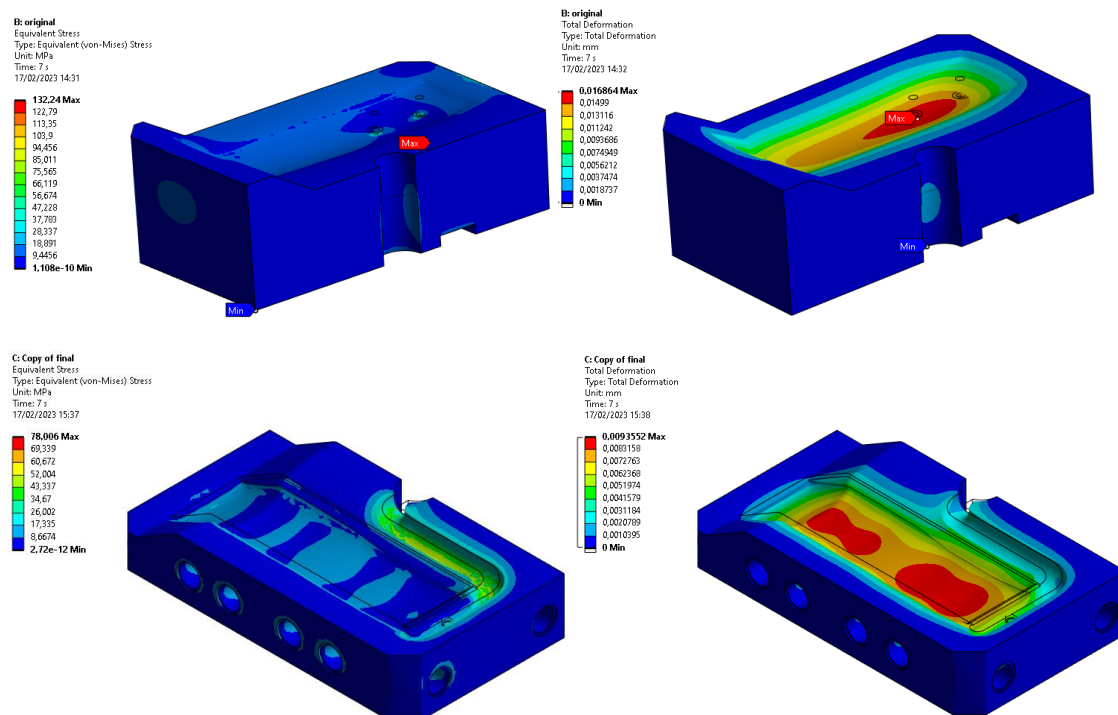


Figure 4-18. Stress and displacement of core (top) and cavity (bottom) with conformal cooling channels.

The main purpose of studying geometries with conformal cooling channels are the advantages from the thermal point of view, namely a reduction in the cooling time, as well as of the warpage. Nevertheless, the structural behaviour must be good enough to withstand the pressure during the injection moulding process.

Taking these results into account, the inclusion of cellular structures was considered in the injection moulding inserts with conformal cooling channels, to be produced by PBF. Periodical cell rib/strut length (L), diameter (D) and angle (θ) were designed to be, respectively, 2 mm, 0.6 mm and -30° (Figure 4-19). Considering the adopted cell/strut angle (i.e. -30°), it is expected that the lattices display auxetic behaviour (i.e. negative Poisson's ratio) once they have been proven to highlight hinging deformation mechanisms, relatively to flexure and axial deformation mechanism [59]. Moreover, due to their cellular nature, they will also lead to a reduction in mass.

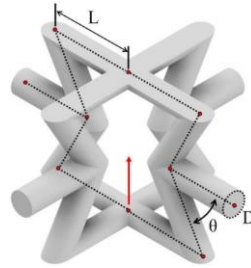


Figure 4-19. Unitary periodic auxetic cell with printing direction highlighted by red arrow, used to mass and volume optimizations [59].

In this sense, some auxetic unit cells arrays were incorporated around the injection moulding inserts, considering the available volume (Figure 4-20).

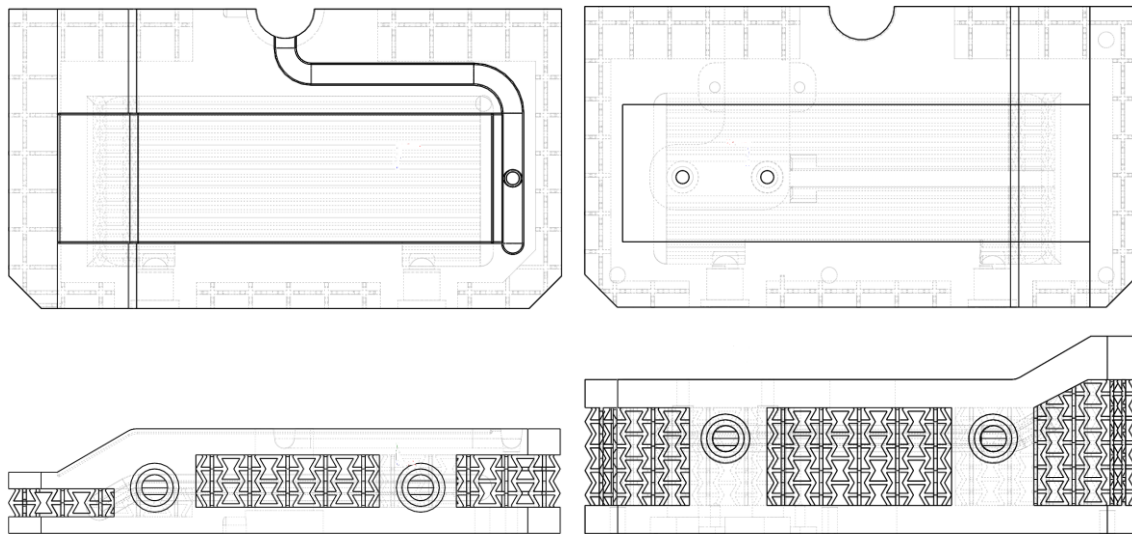


Figure 4-20. Injection moulding inserts with conformal cooling channels and auxetic structures.

Numerical mechanical simulations were also done for these optimized injection moulding inserts and considering the same boundary conditions. The results, resumed in Figure 4-21 and Table 4-5, showed a similar or even better mechanical performance for these lighter moulding inserts. Weight and volume were reduced at least 15 %, with lower von-Mises stresses. Core displacement was the same while in the cavity increased only three thousandths of a millimetre.

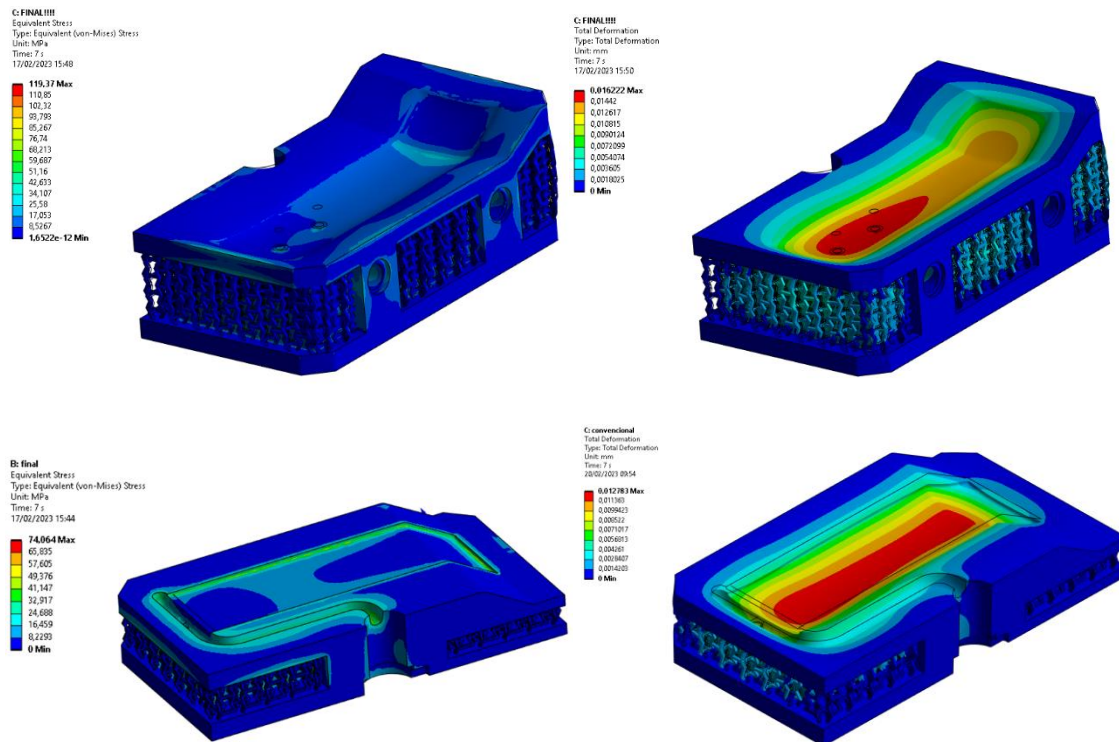


Figure 4-21. Stress and deformation of optimized core (top) and cavity (bottom) with conformal cooling channels.

Table 4-5. Results of weight/volume optimization of moulding inserts with conformal cooling channels.

		Weight	Volume	Maximum pressure
Core	Original	1955 g	709 cm ³	132 MPa
	Optimized	1542 g	583 cm ³	119 MPa
	<u>Reduction</u>	≈ 21 %	≈ 18 %	≈ 10 %
Cavity	Original	1175 g	445 cm ³	78 MPa
	Optimized	995 g	377 cm ³	74 MPa
	<u>Reduction</u>	≈ 15 %	≈ 15 %	≈ 5 %

As, in both moulding inserts, the compressive stress is less than half of the one reported in the experimental characterizations (Table 2-13), these mass and volume optimizations were considered effective for the next steps.

4.3.5. Injection moulding process simulations

To complete the analysis of the different injection moulding inserts developed, fully process injection moulding simulations were done, considering the same parameters presented in Table 4-4 and Figure 4-14. The cooling time was adjusted for conventional cooling channels and is the one for which the frozen layer ratio of the part is higher than 50 % and the average temperature throughout the thickness in practically the entire part and feed system is below the freezing temperature, i.e., 110 °C for PP and 104

°C for PS (Figure 4-22). This results in a cooling time of 17 seconds for PP 579S and 20 seconds for GPPS 165H.

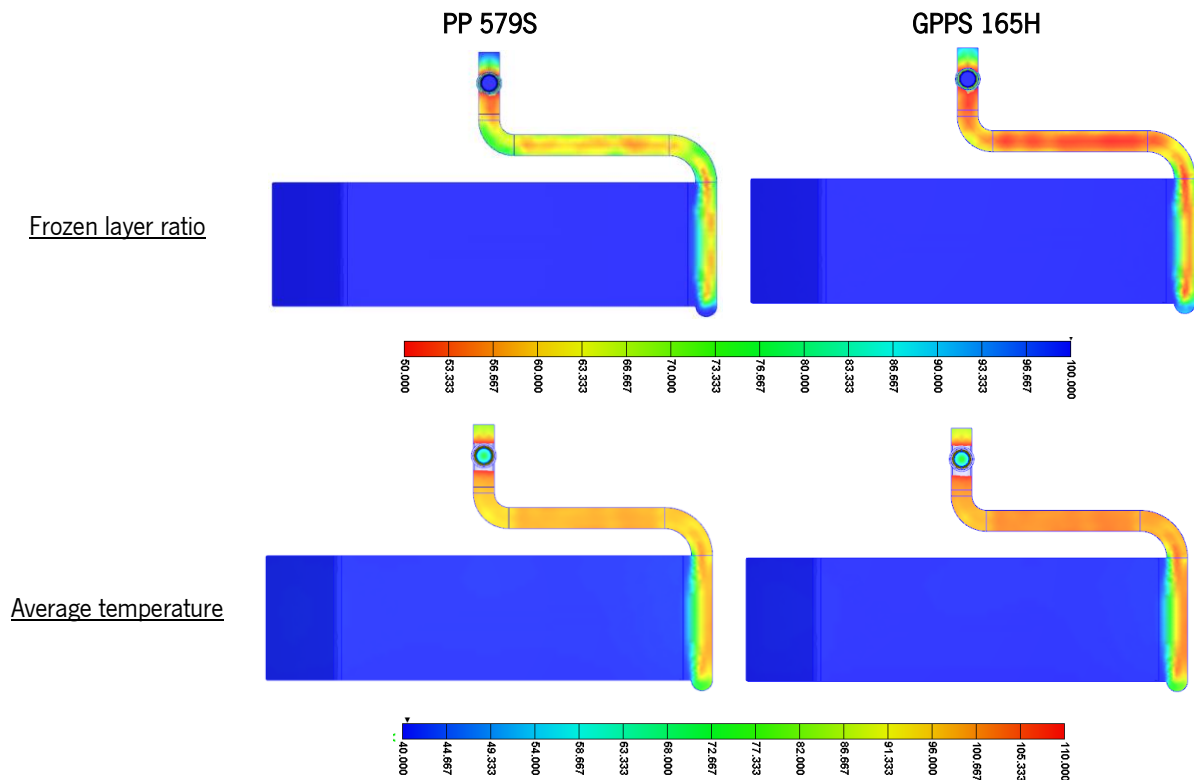


Figure 4-22. Frozen layer ratio and average temperature considering the defined cooling time.

Figure 4-23 shows the numerical simulation results of part temperature difference of injection moulding inserts with straight-drilled and conformal cooling channels. In straight-drilled cooling channels, sharp turns at the connection of two adjacent straight-drilled channels impede the coolant mobility, leading to a sudden pressure drop that weakens the cooling capacity downstream and further enhances the uneven cooling [60]. Considering the same cooling time, the highest temperature of the part surface is much lower and more uniform using conformal cooling channels.

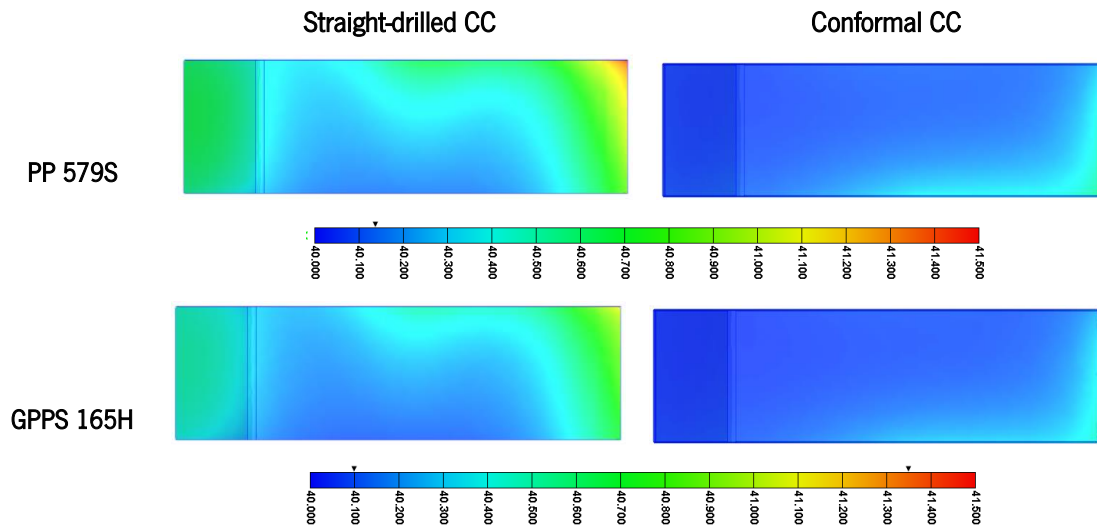


Figure 4-23. Numerical simulation results of part surface temperature at the end of the cooling.

The influence of conformal cooling channels can also be notorious in the cavity surface average temperature evolution considering two injection cycles (Figure 4-24). Using AISi10Mg and conformal cooling channels, moulding inserts average temperature can be reduced in about 3 % or 2 %, depending on polymer crystallinity. That is, the more crystalline the material, the more pronounced this reduction.

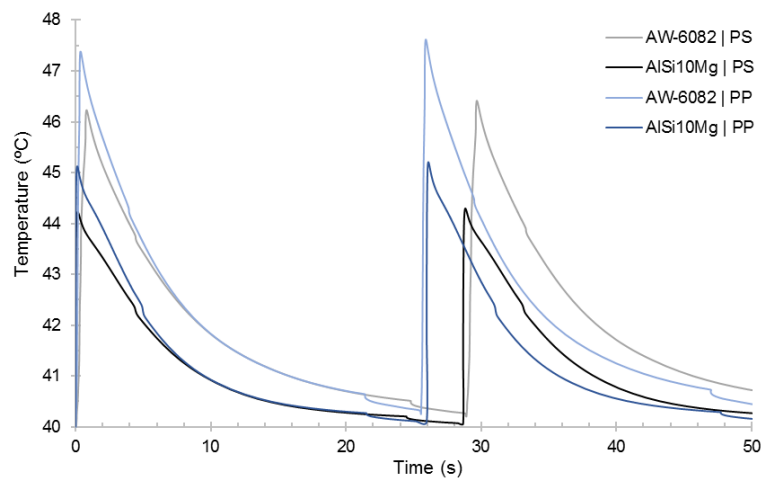


Figure 4-24. Cavity surface average temperature moulding PP 579S and GPPS 165H.

The thermal and pressure gradient are the most important parameters deciding the shrinkage and warpage [61]. As expected, the shrinkage was higher for semicrystalline polymer. Although, in both cases, the shrinkage decreased with conformal cooling channels, which is consequence of thermal and pressure histories inside the mould (Figure 4-25).

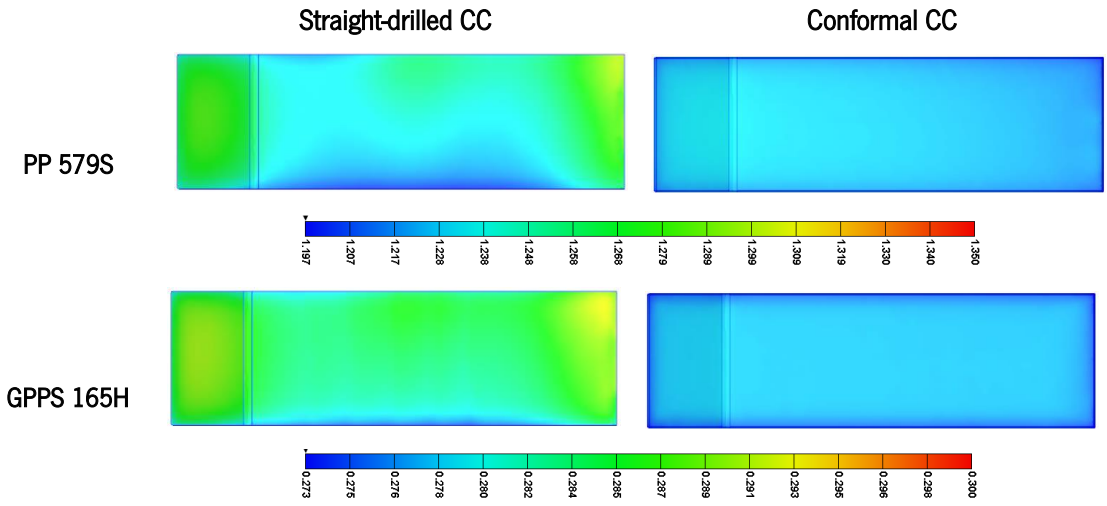


Figure 4-25. Numerical simulation of volumetric shrinkage at the end of the injection cycle.

Figure 4-26 shows the numerical simulation results of total displacements in total directions. The more anisotropic shrinkage resulted in greater warpage in the part produced with the moulding inserts with conventional cooling channels and even greater in the semicrystalline polymer. In GPPS 165H parts, there are no significant different between both cooling methods.

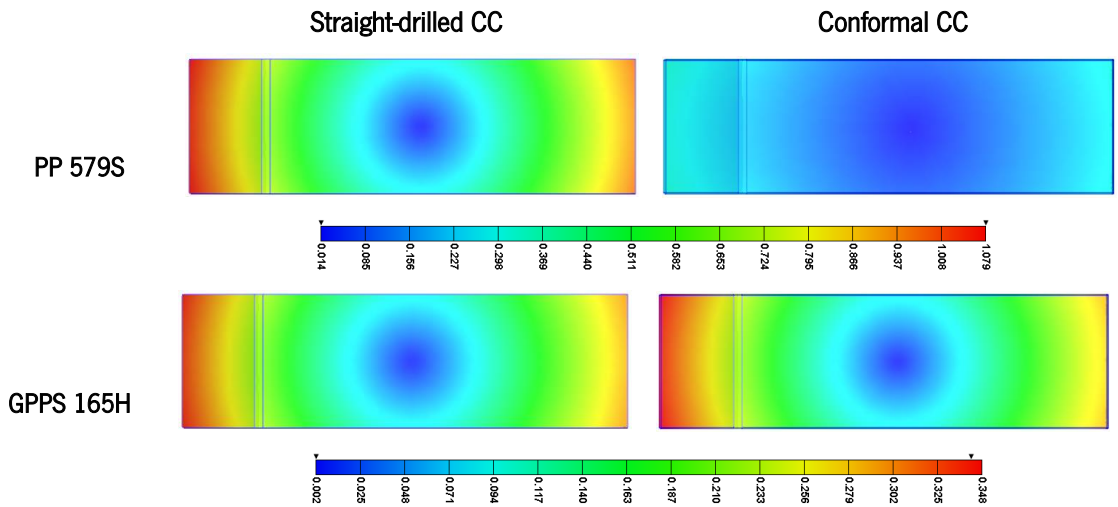


Figure 4-26. Numerical simulation of total displacements at the end of the injection cycle.

4.3.6. Production of moulding inserts

The production of conventional moulding inserts by machining, i.e., subtractive manufacturing, was done considering the aluminium alloy AW-6082 and a CNC DMU 50 machine (Figure 4-27). The production of optimized moulding inserts with conformal cooling channels by powder bed fusion (PBF) was done considering the aluminium alloy AlSi10Mg. In this case, the injection moulding inserts were manufactured upright with the lowest possible built height for time efficiency and the minimum amount of support structures. It was considered a layer thickness of 50 μm , according to a parallel study reported in

Appendix 7. All external surfaces were manufactured with an oversize between 0.5 mm and 1 mm (according to Chapter 2.4.4) to enable post-processing (Figure 4-28). This includes machining of as-built surfaces and hand threading of the holes for water inlet and outlet and sensors (Figure 4-29, right).



Figure 4-27. Injection moulding inserts produced by subtractive manufacturing with straight-drilled cooling channels.

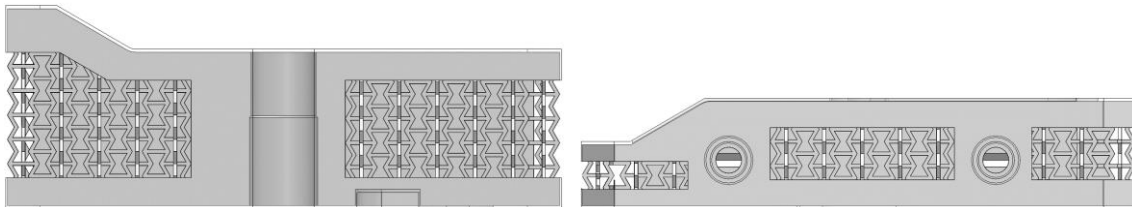


Figure 4-28. Schematic images of oversized moulding inserts to be produced by additive manufacturing.



Figure 4-29. Injection moulding inserts produced by additive manufacturing before (left) and after (right) surface finishing (via machining).

However, even after finishing operations, the surface of the moulding inserts produced by additive manufacturing showed some porosity (Figure 4-30). Given the round shape of the pores, this porosity, visible on both the core and the cavity, could be due to overheating caused by a relatively high energy density in the sintering process. Nevertheless, cavity surface roughness means that the contact area between the polymer and the cavity wall increases, which can result in a better contact situation, increasing the heat transfer coefficient, i.e., thermal transfer ability of the interface between the polymer melt and the aluminium wall [24, 69]

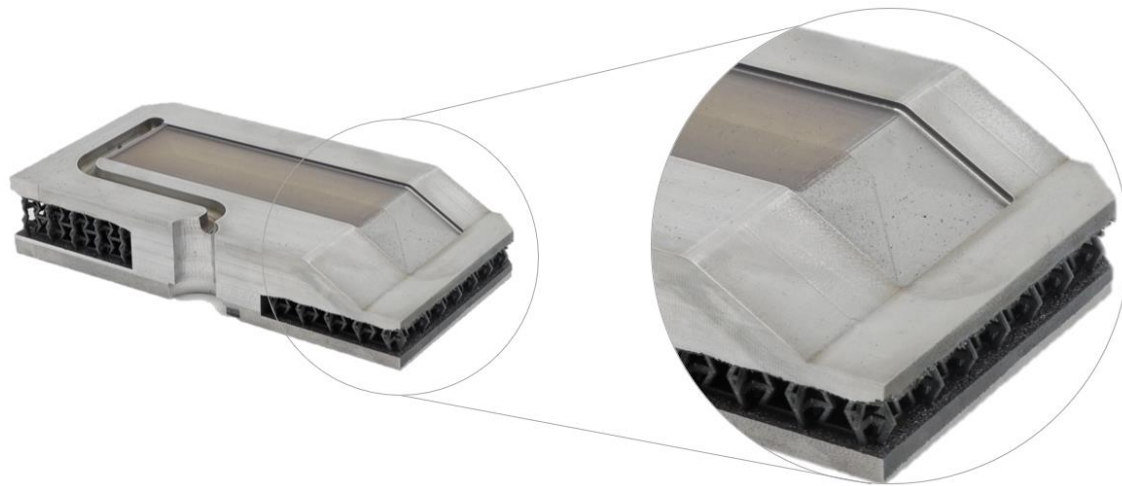


Figure 4-30. Detailed view of porous surface on the cavity produced by PBF, after machining.

Regardless of that, a resume of material and time consuming in the production of conventional moulding inserts (by subtractive manufacturing) and with conformal cooling channels (by additive manufacturing) is presented in Table 4-6.

Table 4-6. Summary of material and time consuming in the production of conventional moulding inserts (by subtractive manufacturing) and with conformal cooling channels (by additive manufacturing).

	<u>Subtractive manufacturing</u>			<u>Additive manufacturing</u>		
	Core	Cavity	Total	Core	Cavity	Total
Spent material (g)	4200	2400	6600	2002	1168	3170
Pre-production time (hh:mm)	02:40	04:20	07:00	00:15	00:15	00:30
Production time (hh:mm)	07:45	07:25	15:10	59:52 ⁹		
Finishing operations time (hh:mm)	02:55	00:50	03:45	05:40	09:35	15:15
Total time (hh:mm)	13:20	12:35	25:55	05:55	09:50	75:37
Final weight (g)	1895	1142	3037	1590	995	2585
Material waste (%) ¹⁰	55 %	52 %	54 %	21 %	15 %	18 %

From the analysis of the Table 4-6, it is important to note that, although the production time is higher for the moulding inserts produced by additive manufacturing, the time when the operator is needed is less than 16 hours, which corresponds to pre- and post-production operations. In the case of subtractive manufacturing, the operator time is higher, being close to the production time.

In the end, by using the moulding inserts produced by additive manufacturing, the material spent was reduced by more than 50 % and the final weight by about 15 %, resulting in a much lower material wastage.

⁹ Considering the production of the two injection moulding inserts simultaneously.

¹⁰ Based on the spent material and the final weight of the moulding inserts.

4.4. Injection moulding

For the experimental trials, the injection machine used was an Engel 200V/45, equipped with a Ø30 screw diameter and a clamping force of 450 kN. The initial injection moulding parameters for both moulding inserts and injection materials were based on Moldex3D simulations (Table 4-4). Only adjustments had to be made to the cushion to get completely full and compliant parts. The cooling time was 17 seconds for PP parts and 20 seconds for GPPS parts.

After the stabilization of the process, 20 shots of parts were produced in each material and moulding inserts and the pressure and temperature curves were acquired with the respective sensors (Figure 4-31) (Priamus 6001B1.0 and Type-K thermocouple) and data acquisition systems. Experimental temperature measurements also revealed differences in the average temperature recorded with the thermocouple, which is resumed in Table 4-7. Using additively manufactured moulding inserts, the reduction in average temperature is more evident for the semi-crystalline polymer, as predicted in the simulations (Figure 4-24). Experimental temperature vs time evolution along ten injection cycles is presented in Appendix 8.

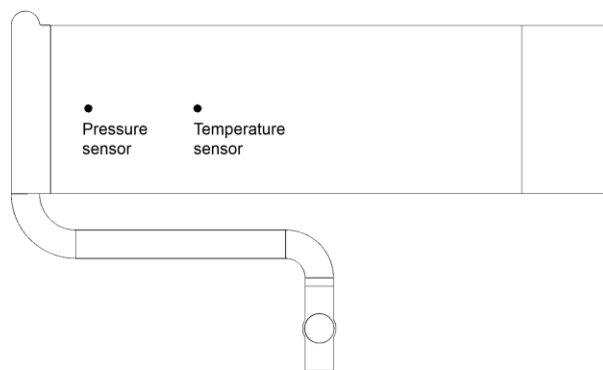


Figure 4-31. Location of pressure and temperature sensors on the surface of the part.

Table 4-7. Recorded average temperature for each moulding inserts and polymers, considering 10 shots.

	PP 579S	GPPS 165H
<u>AW-6082</u>	46.3 °C	44.5 °C
<u>AlSi10Mg</u>	44.0 °C	44.4 °C
	- 4.8 %	- 0.3 %

Figure 4-32 resumes the data acquired with the pressure sensor, for both materials. One reason to the difference between numerical simulation and experiment might be due to the true injection response being slower [63].

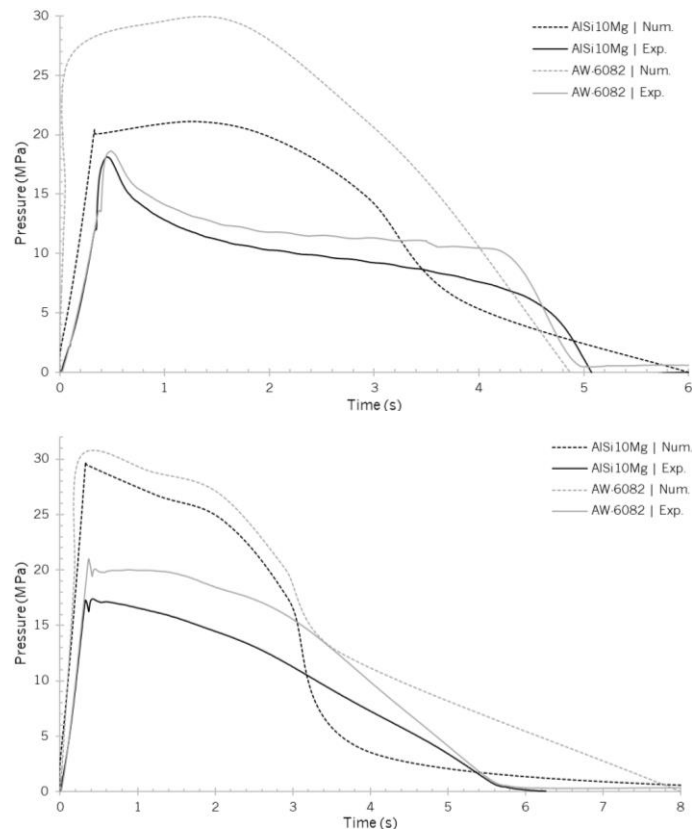


Figure 4-32. Cavity pressure curves for PP (up) and PS (bottom).

4.5. Parts analysis

After the production of the mouldings, it was verified that their appearance reflected the surface finishing of the moulding inserts (Figure 4-30). That is, the parts produced with the AISi10Mg injection moulding inserts replicated the roughness and porosity of cavity and core. These defects were especially visible in the amorphous parts (Figure 4-33).

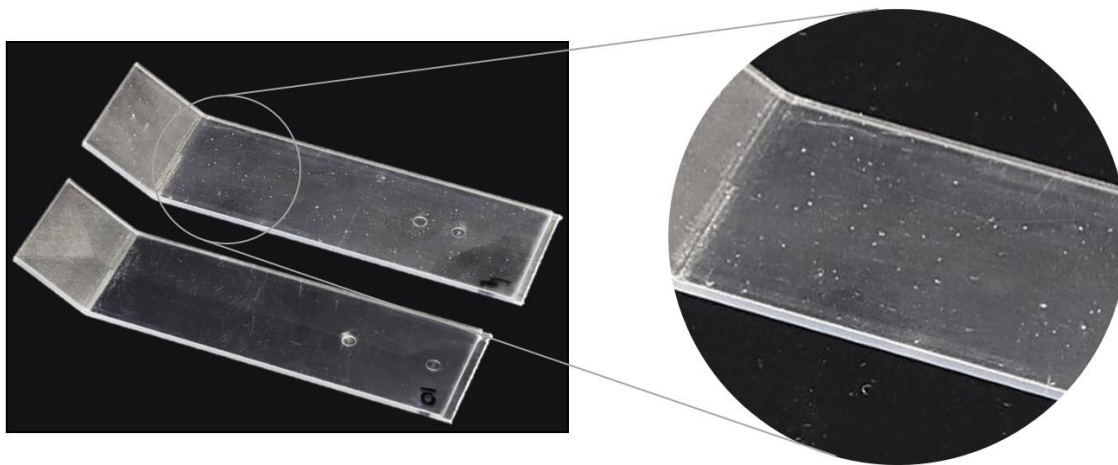


Figure 4-33. Surface appearance of the GPPS 165H mouldings, produced with the additive (top) and conventional (bottom) moulding inserts.

Nevertheless, both PP 579S and GPPS 165H parts were evaluated regarding tab angle, relative crystallinity (for semi crystalline material) and haze (amorphous material), although haze results are predictably worse for the moulding inserts with conformal cooling channels.

4.5.1. Warpage

The first criterion in which the conformal cooled mould was compared with the conventional cooled mould is the degree of parts warpage. The tab angle of five injection moulded specimens were measured with a 3D scanner (resolution: 117 μm) in combination with measuring software. The resulting measurements on the side of the core, as well as actual angle of the moulding inserts, are listed in Table 4-8. Remaining measurements are presented in Appendix 9.

Table 4-8. Average tab angle of injection moulded specimens, considering five measurements on the side of the core, and comparison with the predicted tab angle predicted by the simulations.

	Moulding inserts		PP 579S		GPPS 165H	
	Nominal	Actual	Predicted	Actual	Predicted	Actual
<u>AW-6082</u>	30.00	$30.00^\circ \pm 0.01^\circ$	30.14	$31.17^\circ \pm 0.27^\circ$	30.03	$30.34^\circ \pm 0.15^\circ$
<u>AlSi10Mg</u>	30.00	$29.98^\circ \pm 0.01^\circ$	30.12	$31.05^\circ \pm 0.25^\circ$	30.02	$30.30^\circ \pm 0.33^\circ$

Although the difference is not as significant as expected, probably due to the visible surface defects in the mould produced by additive manufacturing (Figure 4-30) or the roughness on CCC surface (Figure 4-4), there were improvements in terms of plastic parts angle. Naturally, these improvements were more significant in the parts produced with the semi-crystalline polymer, being practically negligible in the parts produced with the amorphous polymer (Figure 4-34). Furthermore, as the angle measurement process is based on a point cloud, if the surface finishing of the additively manufactured moulding inserts were fully compliant, the improvements in warpage would be even more relevant and the noted angle for these moulding inserts would be even closer to the nominal one.

Comparing predicted and actual warpage, the warpage predicted by Moldex3D was always below the real warpage, reaching deviations of around 3 % for semi crystalline mouldings and 1 % for amorphous mouldings. Curiously, in all cases, numerical-experimental deviations are lower for moulding inserts with conformal cooling channels compared to moulding inserts with straight-drilled cooling channels.

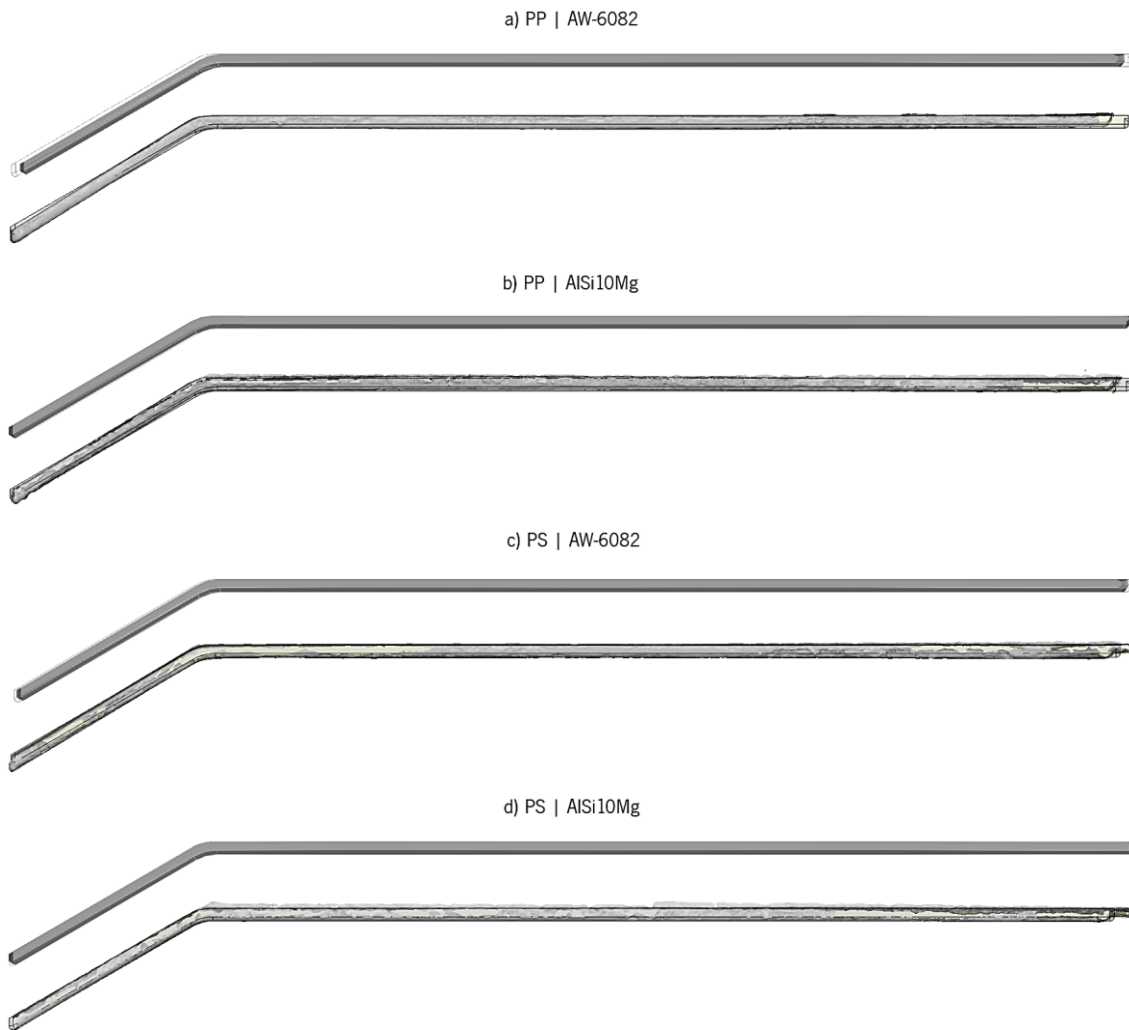


Figure 4-34. Warpage of the mouldings (predicted – top; actual – bottom).

4.5.2. Relative crystallinity

Cooling rate proved to have a significantly stronger influence on crystallinity of polymers. In this sense, relative crystallinity was measured using Differential Scanning Calorimetry (DSC), based on the heat required to melt the semicrystalline polymer, i.e., PP 579S. The heat associated with fusion is reported as percent crystallinity by normalizing the observed heat of fusion to that of a 100 % crystalline sample of the same polymer. According to TA Instruments [64], this value is equal to 207 J/g for PP.

In this work, three samples of PP moulded with each injection moulding inserts, with a mass around 10 mg, were analysed over a temperature range from 30 °C to 200 °C, considering a heating rate of 10 °C/min. Figure 4-35 shows DSC curve for one PP sample, moulded with each moulding inserts. Netzsch Proteus software was used to calculate the enthalpy of fusion for each sample. The results are summarized in Table 4-9.

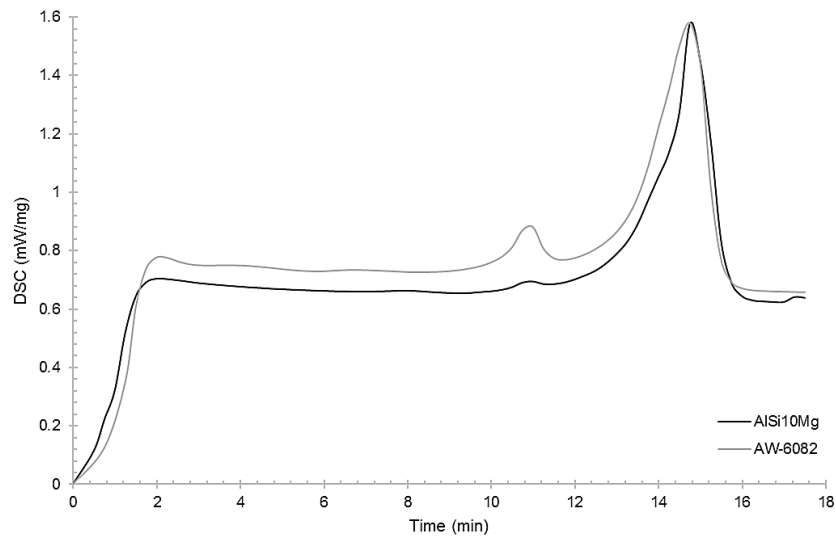


Figure 4-35. DSC curve for PP 579S parts moulded with AISi10Mg (conformal cooled) and AW-6082 (straight-drilled cooled) moulding inserts.

Table 4-9. DSC characterization of PP 579S samples.

	Melt onset temperature ¹¹	Melt peak temperature	Enthalpy	Crystallinity
<u>AW-6082</u>	155.8 ± 3.1 °C	169.3 ± 0.6 °C	90.7 ± 1.5 J/g	43.8 ± 0.7 %
<u>AISi10Mg</u>	160.6 ± 2.5 °C	170.1 ± 0.6 °C	82.2 ± 5.8 J/g	39.7 ± 2.8 %

Results revealed a decrease in PP 579S crystallinity when additively manufactured moulding inserts were used. The conformal cooling channels increase the cooling rate, decreasing the melt crystallization temperature and the amount of polymer that crystallizes from the molten state. In other words, when a semi-crystalline material is slowly cooled down, the amount of crystallized chains ratio reaches to the ultimate crystallinity and equivalently the relative crystallinity would be 100 % [65, 66]. Lower crystallinities may be beneficial especially in the case of using propylene with clarifying agents. Moreover, the better cooling efficiency also had effects in increasing both melt onset and peak temperatures.

4.5.3. Haze

In amorphous polymers, with no structural ordering of the chains, the largest ordered region corresponds to the carbon-carbon bond; as this dimension is much smaller than the wavelength of visible light, these polymers are usually transparent. Furthermore, more transparent parts made with amorphous polymers can be obtained by quickly cooling the molten to below the glass transition temperature. This can be done taking advantage of conformal cooling channels [67].

¹¹ Onset temperature is defined as the temperature at which the heat that is released by a reaction can no longer be completely removed from the reaction vessel.

In this sense, the evaluation of specific light-transmitting properties of the planar section of amorphous parts was done using a hazemeter. According to ASTM D-1003 [68], haze is the scattering of light by a specimen responsible for the reduction in contrast of objects viewed through it, i.e., reduction in transparency. In other words, haze can be defined as the percentage of the total transmitted light that is scattered from the incident beam by an angle greater than 2.5° .

The instrument used for measurements was Hazemeter XL-211 Hazegard and detected haze for GPPS 165H parts moulded with the moulding inserts with straight-drilled cooling channels was $20.16 \pm 0.08 \%$ while for the parts moulded with conformal cooling channels was $32.65 \pm 0.13 \%$. The increase in haze for the parts produced with the moulding inserts produced by additive manufacturing is explained by its porosity (Figure 4-30 and Figure 4-33) and, therefore, is not a measure of a better or worse temperature control system.

4.6. Final remarks of this chapter

In this chapter, different moulding inserts with temperature control systems were developed, taking into consideration some design conclusions obtained in the previous chapter. Among six designs of conformal cooling channels, the one that showed the most promising results was the one based on the distributor concept. Considering the pressures imposed during the injection moulding process with both materials (semicrystalline homopolymer PP and amorphous GPPS), the moulding inserts with the chosen cooling channels were mechanically validated after topology optimization for mass reduction. Some improvements were foreseen in the quality of the moulded parts considering the moulding inserts produced by additive manufacturing in AlSi10Mg with conformal cooling channels, in comparison with conventional moulding inserts with straight-drilled cooling channels in AW-6082.

Therefore, both types of moulding inserts were produced: with straight-drilled cooling channels via machining and with conformal cooling channels via powder-bed fusion, in AW-6082 and AlSi10Mg, respectively. The use of additive manufacturing allowed material waste savings of about 36 %, even considering the subsequent finishing of these moulding inserts by machining. However, some porosity was visible in them, which inevitably influenced the surface quality of the moulded parts.

Considering the same injection moulding parameters, predicted in Moldex3D simulations, the mouldings obtained with the additively manufactured moulding inserts revealed a reduction in warpage, with this reduction being more significant for the PP mouldings. Moreover, these parts also had less crystallinity because of the better cooling efficiency. However, the results regarding haze were not as expected due the surface porosity of AlSi10Mg moulding inserts.

The hypothesis of considering hybrid manufacturing to produce the conformal cooled injection moulding inserts, combining a machined base plate with the more complex part produced by additive manufacturing, could be advantageous in terms of material and time savings (Figure 4-36 and Table 4-10). Overall, considering the data of Table 4-6, production by hybrid manufacturing could be 12% faster than production exclusively by additive manufacturing and waste 17% less material than exclusive production by machining.

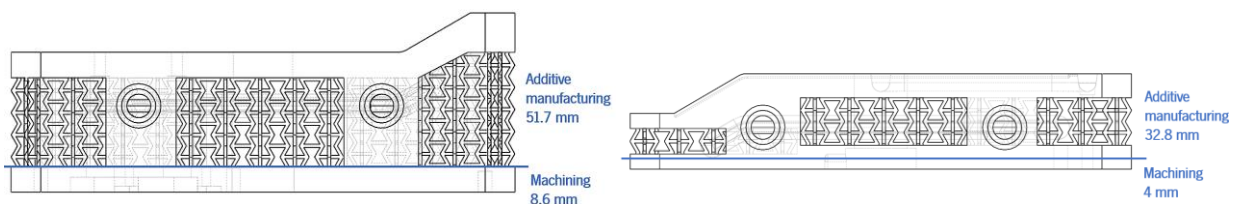


Figure 4-36. Hypothesis of hybrid manufacturing to produce injection moulding inserts.

Table 4-10. Forecast of material and time consuming, if a hybrid production of the moulding inserts was considered.

	Hybrid manufacturing				Total
	Subtractive manufacturing		Additive manufacturing		
	Core	Cavity	Core	Cavity	
Spent material (g)	1008	1008	1428	888	4332
Pre-production time (hh:mm)	00:25	00:20	00:20	00:20	01:25
Production time (hh:mm)	01:00	00:50	46:50		48:40
Finishing operations time (hh:mm)	00:30	00:30	05:40	09:35	16:15
Total time (hh:mm)	01:55	01:40	06:00	09:55	66:20
Final weight (g)	391	186	1322	847	2746
Material waste (%) ¹²	61 %	82 %	7 %	5 %	37 %

Answering the research question: “Which is the general behaviour of aluminium moulding inserts for injection moulding with transparent materials?” and “How much savings these approaches achieve?”, AlSi10Mg moulding inserts with temperature control system with conformal cooling channels showed potential in the production of transparent GPPS parts, although the porosity verified after surface finishing by machining has compromised the quality in terms of haze of the mouldings. Considering the hybrid approach studied throughout this work, the best of both methods can be combined: 12 % faster production maintaining parts complexity characteristic of additive manufacturing (i.e., conformal cooling channels), with 17 % less material waste, compared with subtractive manufacturing.

¹² Based on the spent material and the final weight of the moulding inserts.

4.7. References

- [1] Combrinck J, Booyesen GJ, Van der Walt JG, et al. Limited Run Production Using Alumide Tooling for the Plastic Injection Moulding Process. *The South African Journal of Industrial Engineering* 2012; 23: 131–146.
- [2] Martinho PG, Bártolo PJ, Pouzada AS. Hybrid moulds: Effect of the moulding blocks on the morphology and dimensional properties. *Rapid Prototyp J* 2009; 15: 71–82.
- [3] Pouzada AS. Hybrid moulds: A case of integration of alternative materials and rapid prototyping for tooling. *Virtual Phys Prototyp* 2009; 4: 195–202.
- [4] Gatto A, Bassoli E, Iuliano L. Performance Optimization in Machining of Aluminium Alloys for Moulds Production: HSM and EDM. In: Kvačakaj T, Bidulský R (eds) *Aluminium Alloys, Theory and Applications*. Rijeka, Croatia: InTech, 2011, pp. 355–376.
- [5] Amorim FL, Weingaertner WL. Influence of duty factor on the die-sinking Electrical Discharge Machining of high-strength aluminum alloy under rough machining. *Journal of the Brazilian Society of Mechanical Sciences* 2002; 24: 194–199.
- [6] Peças P, Ribeiro I, Folgado R, et al. A Life Cycle Engineering model for technology selection: a case study on plastic injection moulds for low production volumes. *J Clean Prod* 2009; 17: 846–856.
- [7] Kai-Fu Liew, Hsin-Shu Peng, Te-Ming Jou, et al. Investigation on the Establishment and Analyses of Conformal Cooling Channel Design for Blow Mold. In: *Proceedings of IEEE International Conference on Applied System Innovation*. 2018, pp. 1236–1239.
- [8] Reggiani B, Todaro I. Investigation on the design of a novel selective laser melted insert for extrusion dies with conformal cooling channels. *International Journal of Advanced Manufacturing Technology* 2019; 104: 815–830.
- [9] Özsoy K. Examining mechanical properties of profiles manufactured aluminium extrusion dies using powder bed fusion. *Measurement (Lond)*; 177. Epub ahead of print 1 June 2021. DOI: 10.1016/j.measurement.2021.109266.
- [10] Kolb T, Mahr A, Huber F, et al. Qualification of channels produced by laser powder bed fusion: Analysis of cleaning methods, flow rate and melt pool monitoring data. *Addit Manuf* 2019; 25: 430–436.
- [11] Hsu FH, Wang K, Huang CT, et al. Investigation on conformal cooling system design in injection molding. *Advances in Production Engineering & Management* 2013; 8: 107–115.
- [12] Vojnová E. The benefits of a conforming cooling systems the molds in injection moulding process. In: *Procedia Engineering*. Elsevier Ltd, 2016, pp. 535–543.
- [13] Kovács JG, Szabó F, Kovács NK, et al. Thermal simulations and measurements for rapid tool inserts in injection molding applications. *Appl Therm Eng* 2015; 85: 44–51.
- [14] Minguella-Canela J, Morales Planas S, de Medina Iglesias VC, et al. Quantitative analysis of the effects of incorporating laser powder bed fusion manufactured conformal cooling inserts in steel moulds over four types of defects of a commercially produced injected part. *Journal of Materials Research and Technology* 2023; 23: 5423–5439.
- [15] Feng S, Kamat AM, Pei Y. Design and fabrication of conformal cooling channels in molds: Review and progress updates. *Int J Heat Mass Transf* 2021; 171: 121082.
- [16] Shinde MS, Ashtankar KM. Additive manufacturing-assisted conformal cooling channels in mold manufacturing processes. *Advances in Mechanical Engineering* 2017; 9: 1–14.
- [17] Ahn DG. Applications of laser assisted metal rapid tooling process to manufacture of molding & forming tools - state of the art. *International Journal of Precision Engineering and Manufacturing* 2011; 12: 925–938.
- [18] Luboš B, Jozef D. Conformal Cooling of the Injection Moulds. *Applied Mechanics and Materials* 2013; 308: 127–132.
- [19] Borg A, Rochman A. Design, manufacture and testing of titanium EBM insert for injection molding. *High Value Manufacturing: Advanced Research in Virtual and Rapid Prototyping* 2013; 373–378.
- [20] Pereira AB, Pontes AJ, Silva CS, et al. Comparação de tempo e custo entre moldes convencionais e híbridos para injeção de dissipadores de calor. *O Molde*, 137, 2023, pp. 66–71.
- [21] Zhou H, Li D. Mold cooling simulation of the pressing process in TV panel production. *Simul Model Pract Theory* 2005; 13: 273–285.
- [22] Au KM, Yu KM. Variable Distance Adjustment for Conformal Cooling Channel Design in Rapid in Rapid Tool. *J Manuf Sci Eng* 2014; 136: 044501.
- [23] Liu C, Cai Z, Dai Y, et al. Experimental comparison of the flow rate and cooling performance of internal cooling channels fabricated via selective laser melting and conventional drilling process. *International Journal of Advanced Manufacturing Technology* 2018; 96: 2757–2767.
- [24] Tan C, Wang D, Ma W, et al. Design and additive manufacturing of novel conformal cooling molds. *Mater Des*; 196. Epub ahead of print 1 November 2020. DOI: 10.1016/j.matdes.2020.109147.
- [25] Brooks H, Brigden K. Design of conformal cooling layers with self-supporting lattices for additively manufactured tooling. *Addit Manuf* 2016; 11: 16–22.

- [26] Kanbur BB, Zhou Y, Shen S, et al. Metal Additive Manufacturing of Plastic Injection Molds with Conformal Cooling Channels. *Polymers (Basel)*; 14. Epub ahead of print 1 February 2022. DOI: 10.3390/polym14030424.
- [27] Oh SH, Ha JW, Park K. Adaptive Conformal Cooling of Injection Molds Using Additively Manufactured TPMS Structures. *Polymers (Basel)*; 14. Epub ahead of print 1 January 2022. DOI: 10.3390/polym14010181.
- [28] Nagalingam AP, Santhanam V, Dacheppally NKG, et al. Multiphase hydrodynamic flow characterization for surface finishing the laser powder bed fused AlSi10Mg conformal cooling channels. *J Manuf Process* 2021; 68: 277–292.
- [29] Hamidi M, Falzetti A, Redaelli A, et al. Finishing of internal and external surfaces produced by Powder Bed Fusion. In: *Joint Special Interest Group meeting between euspen and ASPE Dimensional Accuracy and Surface Finish in Additive Manufacturing, KU Leuven, BE*, www.euspen.eu (2017).
- [30] Klingaa CG, Mohanty S, Hattel JH. Realistic design of laser powder bed fusion channels. *Rapid Prototyp J* 2020; 26: 1827–1836.
- [31] Kamat AM, Pei Y. An analytical method to predict and compensate for residual stress-induced deformation in overhanging regions of internal channels fabricated using powder bed fusion. *Addit Manuf*; 29. Epub ahead of print 1 October 2019. DOI: 10.1016/j.addma.2019.100796.
- [32] Feng S, Chen S, Kamat AM, et al. Investigation on shape deviation of horizontal interior circular channels fabricated by laser powder bed fusion. *Addit Manuf*; 36. Epub ahead of print 1 December 2020. DOI: 10.1016/j.addma.2020.101585.
- [33] Koresawa H, Tanaka K, Narahara H. Low-energy injection molding process by a mold with permeability fabricated by additive manufacturing. *International Journal of Automation Technology* 2016; 10: 101–105.
- [34] Wu T, Liu K, Tovar A. Multiphase Thermomechanical Topology Optimization of Functionally Graded Lattice Injection Molds. *Proceedings of the ASME 2016 International Design Engineering Technical Conferences and Computers and Information in Engineering Conference* 2016; 1–10.
- [35] Kampker A, Triebs J, Kawollek S, et al. Direct polymer additive tooling – effect of additive manufactured polymer tools on part material properties for injection moulding. *Rapid Prototyp J* 2019; 25: 1575–1584.
- [36] León-Cabezas MA, Martínez-García A, Varela-Gandía FJ. Innovative advances in additive manufactured moulds for short plastic injection series. *Procedia Manuf* 2017; 13: 732–737.
- [37] Silva EC, Sampaio AM, Pontes AJ. Estudo de materiais de manufatura aditiva para aplicação em moldes de injeção híbridos. *O Molde: Revista da CEFAMOL Associação Nacional da Indústria de Moldes*, 2019, pp. 58–69.
- [38] Mendible GA, Rulander JA, Johnston SP. Comparative study of rapid and conventional tooling for plastics injection molding. *Rapid Prototyp J* 2017; 23: 344–352.
- [39] Redwood B, Schöffner F, Garret B. *The 3D Printing Handbook - Technologies, design and applications*. 1st ed. Amsterdam: 3D Hubs, 2018.
- [40] Bagalkot A, Pons D, Clucas D, et al. A methodology for setting the injection moulding process parameters for polymer rapid tooling inserts. *Rapid Prototyp J* 2019; 25: 1493–1505.
- [41] Noble J, Walczak K, Dornfeld D. Rapid tooling injection molded prototypes: A case study in artificial photosynthesis technology. *Procedia CIRP* 2014; 14: 251–256.
- [42] Michaeli W, Lindner F. Influence of mould materials on the morphological and mechanical properties of injection-moulded prototypes. *Macromol Mater Eng* 2001; 286: 232–236.
- [43] Krikorian G. A practical comparison of rapid prototyping and tooling options. *Wescon/96* 1995; 1–5.
- [44] Rodríguez J. Use of Additive Manufacturing (AM) to Fabricate Injection Molding Inserts. *14th LACCEI International Multi-Conference for Engineering, Education, and Technology: "Engineering Innovations for Global Sustainability"*. Epub ahead of print 2016. DOI: 10.18687/laccei2016.1.1.345.
- [45] Lozano AB, Álvarez SH, Isaza CV, et al. Analysis and Advances in Additive Manufacturing as a New Technology to Make Polymer Injection Molds for World-Class Production Systems. *Polymers*; 14. Epub ahead of print 1 May 2022. DOI: 10.3390/polym14091646.
- [46] Manogharan G, Wysk RA, Harrysson OLA. Additive manufacturing-integrated hybrid manufacturing and subtractive processes: Economic model and analysis. *Int J Comput Integr Manuf* 2016; 29: 473–488.
- [47] Tosello G, Charalambis A, Kerbache L, et al. Value chain and production cost optimization by integrating additive manufacturing in injection molding process chain. *International Journal of Advanced Manufacturing Technology*. Epub ahead of print 2018. DOI: 10.1007/s00170-018-2762-7.
- [48] Booysen G, de Beer D, Truscott M, et al. Combining additive fabrication and conventional machining technologies to develop a hybrid tooling approach. *21st International DAAAM Symposium* 2010; 21: 1563–1564.
- [49] Ilyas I, Taylor C, Dalgarno K, et al. Design and manufacture of injection mould tool inserts produced using indirect SLS and machining processes. *Rapid Prototyp J* 2010; 16: 429–440.
- [50] Boccardi G, Junior M, Costa A. Manufatura aditiva aplicada na fabricação de insertos para moldes de injeção termoplásticos. *Scientia Cum Industria* 2019; 7: 76–82.
- [51] Huang R, Riddle ME, Graziano D, et al. Environmental and Economic Implications of Distributed Additive Manufacturing: The Case of Injection Mold Tooling. *J Ind Ecol* 2017; 21: S130–S143.

- [52] van As B, Combrinck J, Booyesen GJ, et al. Direct metal laser sintering, using conformal cooling, for high volume production tooling. *South African Journal of Industrial Engineering* 2017; 28: 170–182.
- [53] Ahn DG, Kim HW. Study on the manufacture of a thermal management mould with three different materials using a direct metal tooling rapid tooling process. *Proc Inst Mech Eng B J Eng Manuf* 2010; 224: 385–402.
- [54] Homar D, Čerče L, Kopač J. Cooling simulation of conformal cooling injection mould insert produced by hybrid manufacturing. *Tehnicki vjesnik - Technical Gazette* 2017; 24: 981–986.
- [55] Zhu Z, Dhokia VG, Nassehi A, et al. A review of hybrid manufacturing processes - State of the art and future perspectives. *Int J Comput Integr Manuf* 2013; 26: 596–615.
- [56] Kirchheim A, Katrodiya Y, Zumofen L, et al. Dynamic conformal cooling improves injection molding: Hybrid molds manufactured by laser powder bed fusion. *International Journal of Advanced Manufacturing Technology* 2021; 114: 107–116.
- [57] Boivie K, Karlsen R, Ystgaard P. The concept of hybrid manufacturing for high performance parts. *South African Journal of Industrial Engineering* 2012; 23: 106–115.
- [58] Biondani F, Bissacco G, Tang PT, et al. Additive Manufacturing of Mould Inserts with Mirror-like Surfaces. *Procedia CIRP* 2018; 68: 369–374.
- [59] Cortina M, Arrizubieta JI, Calleja A, et al. Case study to illustrate the potential of conformal cooling channels for hot stamping dies manufactured using hybrid process of laser metal deposition (LMD) and milling. *Metals (Basel)*; 8. Epub ahead of print 2018. DOI: 10.3390/met8020102.
- [60] Joshi A, Anand S. Geometric Complexity Based Process Selection for Hybrid Manufacturing. *Procedia Manuf* 2017; 10: 578–589.
- [61] Strong D, Sirichakwal I, Manogharan GP, et al. Current state and potential of additive - Hybrid manufacturing for metal parts. *Rapid Prototyp J* 2017; 23: 577–588.
- [62] Heogh W, Yeon SM, Kang DS, et al. The design and additive manufacturing of an eco-friendly mold utilized for high productivity based on conformal cooling optimization. *Mater Des*; 222. Epub ahead of print 1 October 2022. DOI: 10.1016/j.matdes.2022.111088.
- [63] Rahim SZA, Sharif S, Zain AM, et al. Improving the Quality and Productivity of Molded Parts with a New Design of Conformal Cooling Channels for the Injection Molding Process. *Advances in Polymer Technology*; 35. Epub ahead of print 1 March 2016. DOI: 10.1002/adv.21524.
- [64] Arman S, Lazoglu I. A comprehensive review of injection mold cooling by using conformal cooling channels and thermally enhanced molds. *The International Journal of Advanced Manufacturing Technology*. Epub ahead of print 3 June 2023. DOI: 10.1007/s00170-023-11593-w.
- [65] Carneiro VH, Puga H, Meireles J. Positive, zero and negative Poisson's ratio non-stochastic metallic cellular solids: Dependence between static and dynamic mechanical properties. *Compos Struct*; 226. Epub ahead of print 15 October 2019. DOI: 10.1016/j.compstruct.2019.111239.
- [66] Saifullah ABM, Masood SH. Finite Element Thermal Analysis of Conformal Cooling Channels in Injection Moulding. In: *5 th Australasian Congress on Applied Mechanics, ACAM. 2007.*
- [67] Kurt M, Saban Kamber O, Kaynak Y, et al. Experimental investigation of plastic injection molding: Assessment of the effects of cavity pressure and mold temperature on the quality of the final products. *Mater Des* 2009; 30: 3217–3224.
- [68] Liu Y, Gehde M. Evaluation of heat transfer coefficient between polymer and cavity wall for improving cooling and crystallinity results in injection molding simulation. *Appl Therm Eng* 2015; 80: 238–246.
- [69] Huang CT, Hsu YH, Chen BS. Investigation on the internal mechanism of the deviation between numerical simulation and experiments in injection molding product development. *Polym Test* 2019; 75: 327–336.
- [70] Blaine RL. *Polymer Heats of Fusion*. 2002.
- [71] Makhoulouf A, Satha H, Frihi D, et al. Optimization of the crystallinity of polypropylene/submicronic-talc composites: The role of filler ratio and cooling rate. *Express Polym Lett* 2016; 10: 237–247.
- [72] Hu Y, Liao Y, Zheng Y, et al. Influence of Cooling Rate on Crystallization Behavior of Semi-Crystalline Polypropylene: Experiments and Mathematical Modeling. *Polymers (Basel)*; 14. Epub ahead of print 1 September 2022. DOI: 10.3390/polym14173646.
- [73] Lin Y, Bilotti E, Bastiaansen CWM, et al. Transparent semi-crystalline polymeric materials and their nanocomposites: A review. *Polymer Engineering and Science* 2020; 60: 2351–2376.
- [74] ASTM International. *ASTM D 1003: Standard Test Method for Haze and Luminous Transmittance of Transparent Plastics*. 2000.

5. CONCLUDING REMARKS

In this chapter the final considerations and main conclusions of the present thesis are summarized, as well as some proposals for future developments.

5.1. Main conclusions

This research project was focused on answering the research:

How much additive manufacturing contributes to improve the performance of thermal management components?

To that, it was divided in four subordinate questions whose answers are summarized in this chapter.

How much hybrid manufacturing, i.e. combining subtractive and additive technologies, contributes to the production of optimal aluminium parts?

With hybrid manufacturing, it was possible to produce parts with up to 34 % better thermal performance (i.e., higher thermal diffusivity) and 27 % higher than those of AlSi10Mg in terms of compressive response. In addition, according to the case study presented, metallic PBF technologies could have a significant role in the building of a circular economy.

How much AM improves the performance of heat sinks? How close are CAE simulations to real measurements in predicting thermal management?

With AM, heat sinks temperature was up to 56 % lower when compared to conventional heat sinks, and weight was reduced up to 29 %, depending on the heat sink under study and on the type of cooling method used. Considering the case study, the thermal resistance was reduced to less than half. Regarding the second part of this research question, the deviation between CAE simulations and real measurements was, in the worst-case scenario, 2 %.

Which is the general behaviour of aluminium moulding inserts for injection moulding with transparent materials?

AlSi10Mg moulding inserts with temperature control system with conformal cooling channels showed potential in the production of transparent GPPS parts, although the porosity verified after surface finishing by machining has compromised the quality in terms of haze of the mouldings.

How much savings these approaches achieve?

With the hybrid approach studied throughout this work, the best of both methods can be combined. Comparing to the production totally via machining or PBF, the production of hybrid heat sink was at least 31 % faster. Moreover, both in additive and hybrid heat sinks, the mass is reduced up to 12 % and 7 %. Regarding second thermal management application, i.e., injection moulding inserts, forecasts point to 12

% faster production maintaining parts complexity (i.e., conformal cooling channels), with 17 % less material waste, compared with subtractive manufacturing.

5.2. Future research directions

Based on the results and experience gained throughout this work, it would be interesting to pursue the following studies:

- § To analyse the performance of heat sinks as a function of a constant incrementation of area to volume ratio. The goal is to understand if there is an optimum ratio value for a certain thermal management specification.
- § Kicking from the best shape of conformal cooling channels (#CCC2), optimise the cross-section and/or blades' spacing to achieve an optimal cooling system.
- § To improve the surface finishing of the moulding inserts produced by PBF. This can be achieved by applying coatings or by optimising the parameters of the additive manufacturing process.
- § Injection moulding of reinforced polymers to evaluate the wear of aluminium inserts.
- § To produce the hybrid moulding inserts developed at the end of Chapter 4.

APPENDIXES

In following section is presented in the form of annexes all the additional for this thesis.

Appendix 1 – AlSi10Mg datasheet

CONCEPTLASER

a GE Additive company

CL 30AL / CL 31AL Aluminium alloys

Aluminium alloy (powder), chemical composition
 CL 30AL according to DIN EN 1706 AlSi12(a),
 CL 31AL according to DIN EN 1706 AlSi10Mg(b)

With an appropriate approval* CL 30AL and CL 31AL can be used for production of lightweight components in the field of automotive and aerospace industries.

13
Al
 26,982

CHEMICAL COMPOSITION

Component	CL 30AL Indicative value (%)	CL 31AL Indicative value (%)
Si	10,5 – 13,5	9,0 – 11,0
Mg	0 – 0,05	0,20 – 0,45
Fe	0 – 0,55	0 – 0,55
Mn	0 – 0,35	0 – 0,45
Ti	0 – 0,15	0 – 0,15
Cu	0 – 0,05	0 – 0,10
Zn	0 – 0,10	0 – 0,10
C	0 – 0,05	0 – 0,05
Ni	0 – 0,05	0 – 0,05
Pb	0 – 0,05	0 – 0,05
Sn	0 – 0,05	0 – 0,05
Al	Balance	Balance

000217 | Subject to technical changes.
 Information is provided for informational purposes only.
 Metallurgical: Concept Laser GmbH
 Airwork: laser@concept-laser.de

RANGE OF APPLICATION

With an appropriate approval* CL 30AL and CL 31AL can be used for production of lightweight prototypes, unique or series production parts in the field of automotive and aerospace industries with high mechanical and dynamic load.

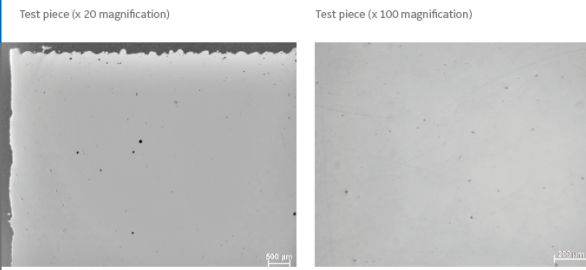
TECHNICAL DATA AFTER RECOMMENDED HEAT TREATMENT

	90° (horizontal)	45° (polar angle)	0° (upright)
Yield Strength $R_{p0,2}^1$	211 ± 4 N/mm ²	215 ± 3 N/mm ²	205 ± 3 N/mm ²
Tensile Strength R_m^1	329 ± 4 N/mm ²	346 ± 3 N/mm ²	344 ± 2 N/mm ²
Elongation A^1	9 ± 1 %	7 ± 1 %	6 ± 1 %
Young's Modulus E^2	approx. 75 · 10 ³ N/mm ²	approx. 75 · 10 ³ N/mm ²	approx. 75 · 10 ³ N/mm ²
Thermal Conductivity λ^2	120 - 180 W/mK	120 - 180 W/mK	120 - 180 W/mK
Coefficient of thermal Expansion (at rt) ²	20 · 10 ⁻⁶ K ⁻¹	20 · 10 ⁻⁶ K ⁻¹	20 · 10 ⁻⁶ K ⁻¹

¹ Tensile test according to DIN EN 50125 at 20°C
² specification according to the material manufacturer's data sheet

CL 30AL CL 31AL Aluminium alloy

MICROSECTION



STRESS RELIEF HEAT TREATMENT

Stress relief annealing: Heat up in 1 hour to 240°C. Maintain temperature for 6 hours. Allow the components to cool down in the oven to 100°C. Afterwards allow the component cooling down at ambient atmosphere.

MICROSTRUCTURE

Components made from aluminium alloys CL 30AL and CL 31AL display a homogeneous, dense structure after they are manufactured by means of the metal laser melting process LaserCUSING®.

All of the specified figures are approximate figures. The figures which are provided are not binding and do not constitute a warranty. The information provided on this material is therefore not binding and is not deemed to be certified.
 * The approval is branch-specific and/or application-specific and it must be approved by Concept Laser GmbH. Approval of materials by Concept Laser GmbH is not available.

Concept Laser GmbH
 An der Zehn 8
 D 95215 Lichtenfels

T: +49 (0) 95 71 1679 200
 F: +49 (0) 95 71 1679 299
 info@concept-laser.de



www.concept-laser.de

www.concept-laser.de

Appendix 2 – AW-6082 datasheet



ESPECIFICAÇÕES – ALU 6082

Marca: ALU 6082

Nº de Material: 6082

Perfis:

Estado de Fornecimento: Tratado T6

Aplicações: Trata-se de uma liga que apresenta excelentes características mecânicas e boa resistência à corrosão. Reage bem à anodização. É largamente usada em elementos estruturais de construção civil (andaimos, estruturas ferroviárias), elementos de máquinas, eletrodomésticos, peças de alta precisão e aplicações na construção naval.

Categoria: ALUMÍNIOS

1-Normas

EuroNorma EN	EN AW
AlSiMgMn	6082 T6

2-Composição Química % (valores médios)

Al	Si	Mg	Mn	Fe	Outros
Resto	0,70-1,30	0,60-1,20	0,40-1,0	≤0,50	≤0,60

3-Características Mecânicas

ρ (kg/dm ³)	Rm (N/mm ²)	Rp _{0,2} (N/mm ²)	A5 %	Dureza HB
2,70	205-310	110-260	8-12	65-95

4- Características Físicas

C.Térmica W/m.K	C.Eletr m/Ω.mm ²	Exp.Térmica 10 ⁻⁶ /K
170-220	26	23,4

Appendix 3 – Specific heat capacity (raw data)

Baseline		Sapphire			AW-6082			AlSi10Mg As-built		
mass (g)	(-)	mass (g)	30.78		Mass (g)	19.5		Mass (g)	16.36	
Temp. (°C)	DSC (mW)	Temp. (°C)	DSC (mW)	Cp (J/gK)	Temp. (°C)	Fluxo (mW)	Cp (J/gK)	Temp. (°C)	DSC (mW)	Cp (J/gK)
26.77216	1.06879	27.01979	6.12949	0.7792	26.28046	3.64276	0.730953	26.98766	3.85593	0.92223
36.37232	1.06422	36.60679	5.91628	0.7999	36.81132	3.64729	0.778379	36.5884	3.72419	0.947336
46.93249	1.05636	47.15248	5.78561	0.8194	46.38483	3.62309	0.809953	47.14921	3.66896	0.977631
56.53265	1.04673	56.73947	5.72214	0.838	56.91569	3.60496	0.833336	56.74995	3.62746	0.999479
67.09282	1.03642	66.32647	5.67338	0.8556	66.4892	3.58374	0.853099	66.35068	3.58629	1.017559
76.69298	1.02744	76.87216	5.6299	0.8721	77.02007	3.56417	0.871481	76.91149	3.54348	1.032716
86.29314	1.0176	86.45916	5.59944	0.8878	86.59358	3.55191	0.888928	86.51223	3.50857	1.046613
96.85331	1.0123	97.00485	5.57645	0.9027	97.12444	3.54832	0.906656	97.07304	3.47802	1.059261
106.45347	1.00978	106.59185	5.55982	0.9168	106.69795	3.54657	0.923116	106.67378	3.44847	1.069857
117.01364	1.00632	117.13754	5.55217	0.9302	116.27146	3.55201	0.939338	116.27451	3.42921	1.080919
126.6138	1.00316	126.72454	5.55024	0.9429	126.80232	3.57171	0.957776	126.83533	3.40754	1.089131
136.21396	1.0012	136.31153	5.54553	0.955	136.37584	3.60771	0.980677	136.43606	3.38954	1.098213
146.77413	1.0001	146.85722	5.55899	0.9666	146.9067	3.66657	1.00634	146.99687	3.37501	1.104107
156.37429	0.9972	156.44422	5.5592	0.9775	156.48021	3.68182	1.021883	156.59761	3.35612	1.110267
166.93446	0.9962	166.98991	5.564	0.9876	167.01107	3.67635	1.030018	167.15842	3.34513	1.117101
176.53462	0.99675	176.57691	5.575	0.9975	176.58458	3.69065	1.042329	176.75916	3.34255	1.125204
187.09479	0.99531	187.1226	5.578	1.0074	187.11544	3.67748	1.048354	186.35989	3.32887	1.131112
196.69495	0.99627	196.7096	5.5856	1.0164	196.68896	3.62089	1.040026	196.9207	3.31662	1.135471

AISI10Mg HT			AW-6082/AISI10Mg AB			AW-6082/AISI10Mg HT		
mass (g)	18.23		Mass (g)	42.1		Mass (g)	43.52	
Temp. (°C)	DSC (mW)	Cp (J/gK)	Temp. (°C)	Fluxo (mW)	Cp (J/gK)	Temp. (°C)	DSC (mW)	Cp (J/gK)
26.88347	4.37319	0.94	26.72461	6.542761	0.68	26.08807	6.090189	0.58
36.47795	4.2359	0.966974	36.32897	7.219729	0.713665	36.63384	6.40832	0.612789
47.03187	4.15823	0.994345	46.89376	6.954078	0.720067	46.22091	6.325197	0.633579
56.62634	4.10074	1.013981	56.49811	6.854301	0.733897	56.76669	6.260352	0.648431
66.22082	4.04713	1.030524	66.10247	6.806728	0.750505	66.35375	6.216397	0.663052
76.77474	4.00151	1.046578	76.66726	6.725896	0.761732	76.89953	6.184627	0.677577
86.36921	3.96204	1.060648	86.27161	6.616857	0.767024	86.4866	6.167219	0.691576
96.92313	3.92801	1.073594	96.8364	6.640854	0.785952	96.07366	6.161997	0.705483
106.5176	3.89612	1.084746	106.4408	6.67706	0.804981	106.6194	6.163738	0.718849
117.07153	3.87118	1.095062	116.0451	6.633697	0.812561	116.2065	6.172877	0.731444
126.666	3.84975	1.104252	126.6099	6.576862	0.816882	126.7523	6.189414	0.743675
136.26047	3.83186	1.114171	136.2143	6.535604	0.822873	136.3394	6.210304	0.756402
146.81439	3.81208	1.119167	146.779	6.494346	0.825606	146.8851	6.235546	0.766841
156.40887	3.79758	1.12744	156.3834	6.45393	0.829689	156.4722	6.263834	0.778977
166.96279	3.78626	1.134714	166.9482	6.414777	0.832457	166.0593	6.294733	0.790225
176.55726	3.77428	1.140208	176.5525	6.462771	0.845422	176.605	6.377856	0.807091
187.11118	3.76387	1.147731	186.1569	6.442984	0.85074	186.1921	6.439219	0.822501
196.70566	3.75186	1.152719	196.7217	6.428249	0.855212	196.7379	6.480998	0.834097

Appendix 4 – Pressure transmitter BFT10-110



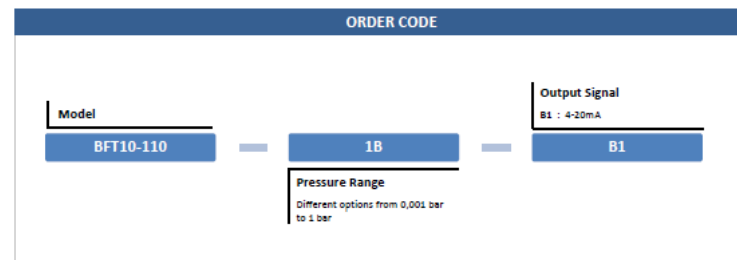
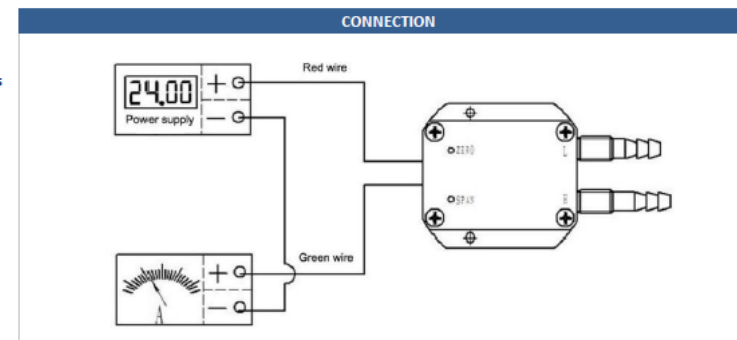
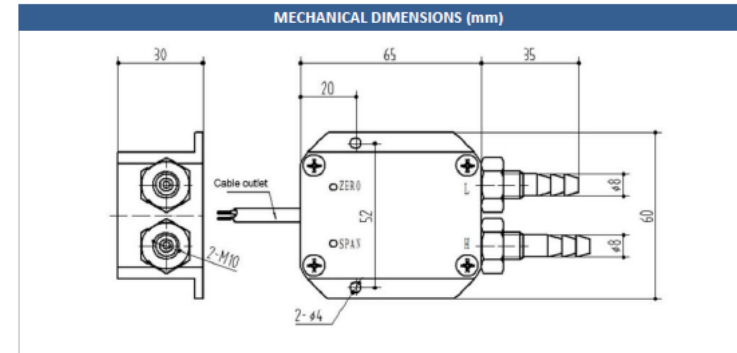
PRESSURE TRANSMITTER "Differential Pressure Transmitter for Low Pressure" BFT10-110



- $\phi 8$ agnail connection, easy to install
- Measuring tiny gas differential pressure value
- Firm and well-sealed aluminium alloy housing
- The zero point and full span of the product can be adjusted externally
- With the short circuit protection and reverse polarity protection
- Full range compensation for zero and sensitivity temperature
- Strong anti-interference capacity, stability performance

BFT10-110 Differential Pressure Transmitter is assembled by OEM piezoresistive silicon differential pressure sensor, and the housing is the aluminium alloy structure; the pressure connection is M10 thread & agnail structure, and can be directly installed on the measuring piping or connected through the press-leading tube; it is easy to install and use, and widely applies in the air supply for boiler, underground ventilation and other electricity and mining industries, as well as the process control field of automated pressure detection for the super clean workshop.

TECHNICAL FEATURES	
Pressure range	0~0,0025bar...0,001bar...1bar
Pressure reference	Differential pressure
Supply & output	4~20mA (16~36V)
Operating temp.	-10°C ... +60°C
Medium temp.	-10°C ... +60°C
Storage temp.	-40°C ... +125°C
Zero temp. coefficient	±2.5%FS (@0°C~50°C)
Sensitivity temp. coefficient	±3%FS (@0°C~50°C)
Overpressure	200%FS
Mechanical vibration	20G (20~5000Hz)
Shock	100g (11ms) 0.001bar, 0.0025bar: ±3%FS
Comprehensive accuracy	0.005bar, 0.01bar, 0.02bar: ±2%FS
	0.05bar, 0.07bar, 0.1bar: ±1.5%FS
	0.1bar~1bar: ±0.5%FS
Insulation	≥200MΩ/250VDC
Response time	≤1ms (Up to 90%FS)
Long-term stability	±0.2%FS/year
Protection	IP65
Service life	≥10×10 ⁸ pressure cycles
Material	Stainless steel or aluminium alloy for Housing
Medium compatibility	All kinds of media compatible with the stainless steel or aluminium alloy



Atek Sensor Technologies

Tuzla KOSB Organize Sanayi Bolgesi Melek Aras Bulvarı, No:67 34956 Tuzla-Istanbul / TURKEY

Tel: +90 216 399 44 04 Fax: +90 216 399 44 02
www.ateksensor.com info@ateksensor.com

DS-BFT.004 Rev No:0 2

Appendix 5 – Styrolution PS 165N/L

INEOS
STYROLUTION

Styrolution PS 165N/L General Purpose Polystyrene (GPPS)

TECHNICAL
DATASHEET

DESCRIPTION

Styrolution PS 165N/L is a high molecular weight, good flowing grade, often blended with high impact extrusion grades.

FEATURES

- High molecular weight
- Good flow characteristics
- Appropriate for blending with HIPS
- UL 94 HB (Antwerp only)

APPLICATIONS

- Transparent parts for refrigerators
- Blending with HIPS for thermoformed cups

Property, Test Condition	Standard	Unit	Values
Rheological Properties			
Melt Volume Rate, 200 °C/5 kg	ISO 1133	cm ³ /10 min	3.4
Mechanical Properties			
Tensile Stress at Yield, 23 °C	ISO 527	MPa	52
Tensile Strain at Break, 23 °C	ISO 527	%	2
Tensile Modulus	ISO 527	MPa	3300
Tensile Creep Modulus (1000h)	ISO 899	MPa	2600
Tensile Creep Modulus (1h)	ISO 899	MPa	3300
Flexural Strength, 23 °C	ISO 178	MPa	86
Flexural Modulus, 23 °C	ISO 178	MPa	1650
Hardness, Rockwell	ISO 2039-2	R scale	62
Hardness, Ball Indentation	ISO 2039-1	MPa	150
Thermal Properties			
Vicat Softening Temperature VST/B/50 (50N, 50 °C/h)	ISO 306	°C	89
Vicat Softening Temperature, B/1 (120 °C/h, 10N)	ASTM D 1525	°C	97
Heat Deflection Temperature A; (annealed 4 h/80 °C; 1.8 MPa)	ISO 75	°C	76
Heat Deflection Temperature B; (annealed 4 h/80 °C; 0.45 MPa)	ISO 75	°C	84
Coefficient of Linear Thermal Expansion	ISO 11359	10 ⁻⁶ /°C	80

INEOS
STYROLUTION

Styrolution PS 165N/L General Purpose Polystyrene (GPPS)

TECHNICAL
DATASHEET

Property, Test Condition	Standard	Unit	Values
Thermal Conductivity	DIN 52612-1	W/(m K)	0.17
Electrical Properties			
Dielectric Constant (100 Hz)	IEC 62631-2-1	-	2.5
Dissipation Factor (100 Hz)	IEC 62631-2-1	10 ⁻⁴	0.9
Dissipation Factor (1 MHz)	IEC 62631-2-1	10 ⁻⁴	0.7
Volume Resistivity	IEC 62631-3-1	Ohm*m	>10 ¹⁶
Surface Resistivity	IEC 62631-3-1	Ohm	>10 ¹⁴
Optical Properties			
Refractive Index, Sodium D Line	ISO 489	-	1.56
Light Transmission at 550 nm	ASTM D 1003	%	89
Haze	ASTM D 1003	%	2
Other Properties			
Density	ISO 1183	kg/m ³	1040
Processing			
Melt Temperature Range	ISO 294	°C	180 - 280
Mold Temperature Range	ISO 294	°C	40
Injection Velocity	ISO 294	mm/s	200

Typical values for uncolored products
Please note that all processing data stated are only indicative and may vary depending on the individual processing complexities.
Please consult our local sales or technical representatives for details.

SUPPLY FORM

Styrolution PS 165N/L can be supplied in two versions, without or with an external additive for improving pneumatic conveying. "L" as a suffix to the grade designation characterises the version with this agent, i.e. Styrolution PS 165L. Styrolution PS 165N/L is supplied as cylindrical or lens shaped pellets, packed in 25 kg bags or bulk.

PROCESSING

Styrolution PS 165N/L can be injection molded at temperatures between 180 and 280°C, and recommended mold temperatures between 10 and 60 °C. Extrusion temperatures should not exceed 240 °C.

Appendix 6 – SABIC PP 579S



SABIC® PP 579S

PP homopolymer for Injection moulding

Description:

This grade has been specially developed for use in thin-walled, antistatic containers. The material has outstanding flow properties and a high stiffness, enabling high production rates. Special characteristics are low tendency for warpage, high lot to lot consistency, good contact transparency and high gloss. It is formulated with a combined processing and antistatic additive package.

Health, Safety and Food Contact regulations:

Material Safety Data Sheets (MSDS) and Product Safety declarations are available on our Internet site <http://www.SABIC-europe.com>

The product mentioned herein is in particular not tested and therefore not validated for use in pharmaceutical/ medical applications.

This grade material is UL registered under File E111275 (www.ul.com)

IMDS ID: 7172624

Typical values		Revision 20121203	
Properties	Unit (SI)	Values	Test methods
Polymer properties			
Melt flow rate (MFR) at 230 °C and 2.16 kg	g/10 min	47	ASTM D 1238
Density	kg/m ³	905	ASTM D 792
Formulation			
Anti static agent	-	Yes	-
Nucleating agent	-	No	-
Mechanical properties			
Tensile test			
stress at yield	¹⁾ MPa	37	ASTM D 638
strain at yield	¹⁾ %	8	
secant modulus at 1% elongation	²⁾ MPa	1800	
Izod Impact notched at 23 °C	J/m	25	ASTM D 256A
Rockwell hardness R-scale	-	113	ASTM D 785
Thermal properties			
Heat deflection temperature			
at 1.80 MPa (HDT/A)	°C	60	ASTM D 648
at 0.45 MPa (HDT/B)	°C	95	
Vicat softening temperature			
at 10 N (VST/A)	°C	153	ASTM D 1525
at 50 N (VST/B)	°C	95	

1) Speed of testing: 50 mm/min
2) Speed of testing: 1 mm/min
3) Temperature rate: 120°C/h

SABIC® PP 579S

PP homopolymer for Injection moulding

Quality:

SABIC Europe is fully certified in accordance with the internationally accepted quality standard ISO9001.

Storage and handling:

Avoid prolonged storage in open sunlight, high temperatures (<-50 °C) and /or high humidity as this could well speed up alteration and consequently loss of quality of the material and /or its packaging. Keep material completely dry for good processing.

Disclaimer. The information contained herein may include typical properties of our products or their typical performances when used in certain typical applications. Actual properties of our products, in particular when used in conjunction with any third party material(s) or for any non-typical applications, may differ from typical properties.

It is the customer's responsibility to inspect and test our product(s) in order to satisfy itself as to the suitability of the product(s) for its and its customers particular purposes. The customer is responsible for the appropriate, safe and legal use, processing and handling of all product(s) purchased from us.

Nothing herein is intended to be nor shall it constitute a warranty whatsoever, in particular, warranty of merchantability or fitness for a particular purpose.

SABIC Europe as referred to herein means any legal entity belonging to the SABIC Europe group of companies.

Appendix 7 – Tailoring the mechanical properties of lattices fabricated by powder bed fusion by changing the deposition layer thickness

V.H. Carneiro^{1,2,*}, E.C. Silva^{3,4}, I. Gomes⁵, I. Duarte^{6,7}, H. Puga⁵, A.M. Sampaio^{3,4,8} and A.J. Pontes^{3,4}

¹ Department of Engineering, Universidade de Trás-os-Montes e Alto Douro, Quinta de Prados, 5001-801 Vila Real - Portugal

² METRICs, University of Minho, Campus de Azurém, 4800-058 Guimarães, Portugal.

³ IPC – Institute of Polymers and Composites, Department of Polymer Engineering, University of Minho, Campus de Azurém, 4800-058 Guimarães, Portugal.

⁴ DONE Lab – Advanced Manufacturing of Polymers and Tools, University of Minho, Campus de Azurém, 4800-058 Guimarães, Portugal.

⁵ CMEMS-UMinho, University of Minho, Campus de Azurém, 4800-058 Guimarães, Portugal.

⁶ Department of Mechanical Engineering, Centre for Mechanical Technology and Automation (TEMA), University of Aveiro, 3810-193 Aveiro, Portugal

⁷ LASI - Intelligent Systems Associate Laboratory, Portugal

⁸ Lab2PT, School of Architecture, University of Minho, Campus de Azurém, 4800-058 Guimarães, Portugal

Abstract

Aluminium alloy cellular solids are attractive due to their high strength to weight ratio, being suitable for applications where a combination of high strength and low density is crucial. The current developments on additive manufacturing technologies, e.g. powder bed fusion, allow a profitable route to manufacture these cellular solids. This study explores using the deposition layer thickness in non-stochastic additively manufactured cellular lattices as a variable to modify their macroscopic mechanical properties, correlating these results with the unitary cell macrostructural dimensions and microstructural details. It is shown that increasing the layer thickness leads to cellular ribs with shorter lengths and larger diameters (i.e. reduces bending moment while the second moment of area increases) which promote an increase in apparent elastic modulus. However, large deposition layers reduce the Al matrix hardness by impairing dislocation pinning and reduces the macroscopic lattice collapse strength. Results show an impressive range of macroscopic mechanical properties ($E^* = 387$ MPa to 612 MPa and $Pf^* = 8.8$ MPa to 12.9 MPa) may be selected by simply changing the deposition layer thickness (25 μ m to 80 μ m). A novel diagram was devised to allow the mechanical property tailoring for these lattices.

Keywords: Additive Manufacturing; Cellular lattices; AlSi10Mg; Deposition layer thickness.

1. Introduction

Cellular lattices are characterized by a solid porous phase that is surrounded by a fluid phase [1,2]. While they may be composed by open and closed topologies, these materials present high specific mechanical properties due to their reduced relative density [3]. These materials are useful in a wide range

of applications [4,5], where metallic solid fractions seem to be suitable when load - bearing properties are required. Currently, these materials in many load bearing applications in transportation, medical and other industries [6].

In recent years there has been significant research on non-stochastic lattice topologies. The use of periodic unitary cellular lattices in a matrix configuration has been shown as effective for mechanical property tailoring purposes [7]. Numerous researchers have reported periodic cellular lattice topologies that are able to display tailored static and dynamic mechanical properties [8], including counterintuitive properties such as negative Poisson's ratios [9], impact/explosion absorption [10], vibration mitigation [11], etc.

The fundamental bottleneck for the widespread application of non-stochastic metallic cellular lattices is their manufacturing. While stochastic metallic cellular solids and foams are frequently produced by foaming or powder metallurgy [12,13], these methods are not suited to produce non- stochastic topologies. Complex non-stochastic metallic cellular lattices are manufactured by investment casting [14] or additive manufacturing [15]. Frequently, the process for the investment casting includes the additive manufacturing of the polymer sacrifice model to produce a ceramic mold [16]. Indeed, metal-based additive manufacturing techniques allow a more direct route to produce non-stochastic metallic cellular lattices.

Current reports on metal-based additive manufacturing frequently focus on the lattice topology [17,18], i.e. manufacturing parameters are kept constant and the studied final mechanical properties are only dependent on the cell topology [19]. However, it is widely known that the manufacturing parameter in metal-based additive manufacturing processes has a significant impact in the mechanical properties and dimensional characteristics of printed components [20,21].

Considering that the mechanical behavior of cellular solids depends on the unitary cell topology (i.e. macroscopic dimensions and defects) and base material properties (i.e. microstructural morphology), it is expected it that additive manufacturing parameters are highly relevant to the final macroscopic mechanical properties. Weidmann *et al* [22] studied the optimization of powder bed fusion parameters such laser as scan power, speed and hatching in the macroscopic mechanical properties of in-plane honeycomb lattices. Gülcan *et al* [23] studied the effect of laser power, hatch and building orientation on the mechanical behavior of powder bed fusion CoCrMo lattices. M. Alaña *et al* [24] characterized the fatigue response of powder bed fusion Ti6Al4V lattices, showing that it is dependent on cell topology, base material properties and lattice relative density. S.H. Ahmadi *et al* [25] also detailed the effect of cellular topology on the mechanical fatigue of Co-Cr lattices. Additionally, M. Galati *et al* [26] showed that

the processing parameters in powder bed fusion Ti6Al4V lattices significantly affects their dimensional accuracy.

Here, we explore using different deposition layer thicknesses in AlSi10Mg non-stochastic cellular lattices manufactured by powder bed fusion to tailor their macroscopic mechanical properties. These results are correlated with the unitary cell metrological analysis by X-ray computed microtomography (μCT) and -Al matrix microhardness (i.e. macroscopical and microscopical aspects) in lattices manufactured using different deposition layer thicknesses.

2. Methodology

2.1 Lattice design and manufacturing

The AlSi10Mg lattices (Fig.1 (a)) that were designed with a three-dimensional inverted honeycomb topology to study the hypothesis tailoring their macroscopic mechanical properties by changing the thickness of powder bed fusion layers.

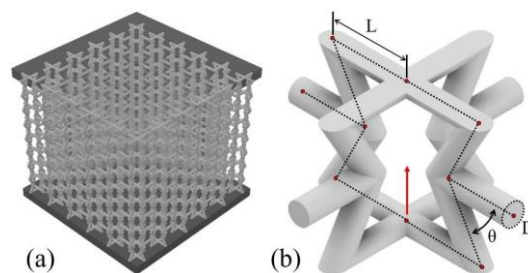


Fig.1. CAD model: (a) auxetic lattice with transparent top and bottom plates; and (b) unitary periodic auxetic cell with printing direction highlighted by red arrow.

According to Fig.1 (b), the inverted honeycomb periodical cells were designed to display a rib/strut length (L), diameter (D) and angle (θ) with, respectively, 2 mm, 0.6 mm and 30° . The periodic cells were assembled into a $9 \times 9 \times 8$ matrix configuration and 2 mm plates were added to their tops and bottoms. The adopted cell/strut angle (i.e. -30°) was selected to promote auxetic behavior (i.e. negative Poisson's ratio) that has previously been shown to increase rib hinge stiffness [27] and potentially magnify the effect of changing the deposition layer thickness.

The AlSi10Mg lattice structures were fabricated with an array of deposition layer thicknesses (25, 35, 50, 65 and 80 μm) using a powder bed fusion equipment (Concept Laser M2 Cusing, supplied by GE, USA). The manufacturing process parameters were set according to the recommendation of the supplier: laser power, scanning speed, hatch spacing and spot size were, respectively, 370 W, 1400 mm/s, 90 μm and 60 μm . To avoid the influence of residual thermal stress, the building platform is heated at 200 $^\circ C$ during the entire production. The built orientation was set along the z-direction, as highlighted by the red arrow in Fig. 1 (b).

2.2 X-ray computed microtomography (μ CT)

X-ray computed microtomography (μ CT) scanning was performed using a Bruker SkyScan 1275 CT scanner (Bruker μ CT, Kontich, Belgium) controlled with an X-ray beam with penetrative X-rays of 76 kV and 131 μ A, in high resolution mode (voxel size 21 μ m, 41 ms of exposure time, 10 of frame averaging, 0.20 deg of rotation step, 1 mm Al filter and 360° of rotation). The X-ray detector of this μ CT scanner is an 3MP (1944x1536 pixels) active pixel CMOS flat panel. NRecon (v.1.7.3.1 software, Bruker, Kontich, Belgium) software was used to reconstruct cross-section slices from acquired μ CT angular projections through the AlSi10Mg lattice structures. The reconstructed μ CT images were used for volume rendering of tomographic data, creating 2D and 3D models using DataViewer (v1.6.0.0. 64 bit, Bruker, Kontich, Belgium) and CTVOX (v.3.3.0 r1403 software, Bruker, Kontich, Belgium).

2.3 Microstructural analysis

Microhardness Vickers testing (Shimadzu HMV-2, Kyoto, Japan) was performed in polished samples by indentation the vertical (i.e. inclined) ribs. Indentations (0.5 kgf load for 10 s) were performed in the perpendicular direction to the deposited layers and only one indentation was performed by rib given their 0.6 mm diameter. A total of 10 indentations (i.e. 10 individual ribs) were tested per sample and 3 samples were tested for each specimen type. To prevent rib deformation under the indenter load, the samples were previously impregnated in resin before being grinded and polished.

2.4 Uniaxial compression

The manufactured lattices (3 for each specimen type, i.e. deposition layer thickness) were assembled between two hardened steel plates to perform uniaxial compression using an INSTRON 8874 universal testing equipment (Norwood, USA) with a 25kN load-cell. A 0.05 mm/s displacement rate in compression was imposed in the top plate while the instant load-displacement values were used as reference to determine the apparent stress-strain curve of the samples.

3. Results and discussion

Fig.2 shows an example X-Ray CT reconstructed unitary cellular unit, highlighting the rib length and diameter. While the inspection of the reconstructed cellular units for each specimen type suggests that there are no significant differences to the dimensions and morphology between the samples, the reconstructed data allowed a detailed metrological analysis using the open-source image analysis software Fiji [28].

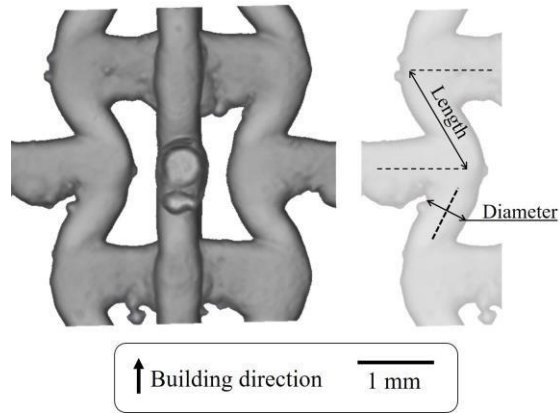


Fig.2. Detail of an X-ray CT reconstructed cellular unit (example extracted from a sample manufactured with a 50 μm deposition layer thickness).

The results of the metrological analysis are presented in Fig.3, in which the fundamental aspects of the cells, i.e. rib length and diameter (see Fig.2) are analyzed. Indeed, according to the data in Fig. 3, it may be observed that the true length (L, 1.83 mm to 1.76 mm) of the ribs and struts tends to decrease as the deposition layer thickness (T) increases. In terms of rib diameter, however, the metrological analysis shows that this dimension tends to increase their diameter (0.60 mm to 0.61 mm) as the deposition layer thickness is increased. These changes are highlighted by the very good correlation with the linear regressions established in Fig.3. Considering dimensions of the CAD model (L and D, respectively, 2 mm and 0.6 mm – see Fig.1), the results show that the samples dimensions tend to deviate from the designed model as the deposition layer thickness increases. In fact, the loss of accuracy by increasing the deposition layer thickness has already been reported for aluminum alloys [29], as this impairs the discretization of the CAD model. These results also determine that the samples display an $8.4\pm 0.3\%$ specific density.

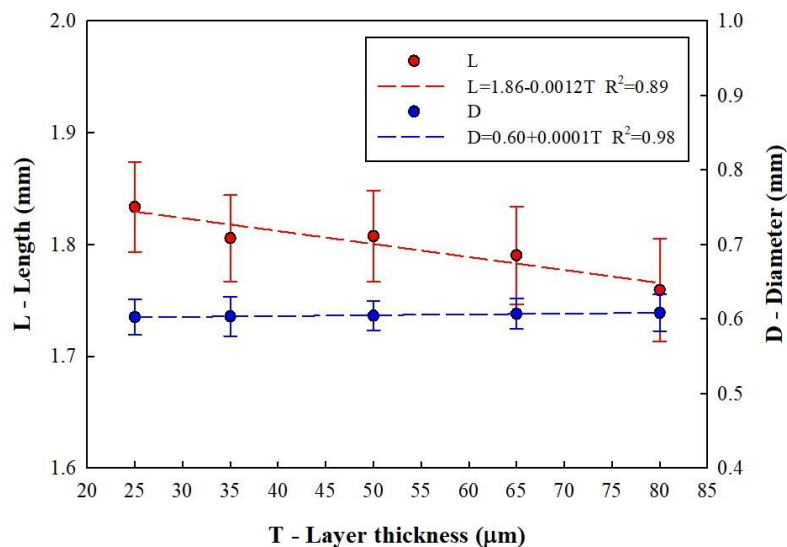


Fig.3. Metrological analysis by X-Ray CT detailing the impact of layer thickness on the true length and diameter of the ribs/struts.

While the topology of the cellular lattices is known to significantly influence their mechanical properties, it is essential to determine if different deposition layer thicknesses generate statistically different samples. Fig.4 shows the comparison of the rib/strut length and diameter of the different samples using a non-parametric one-way A-NOVA on Ranks Kruskal-Wallis statistical analysis. As expected, these results show the dimensions of samples with similar deposition layer thickness are not statistically different. However, there are statistically significant differences between the length of the rib/struts in the samples that were manufactured with very dissimilar deposition layer thicknesses (e.g. 25 μm vs 80 μm). The statistical analysis shows that there seems to be no significant differences in the rib/strut dimensions in samples that were manufactured in the range of 25 μm to 50 μm .

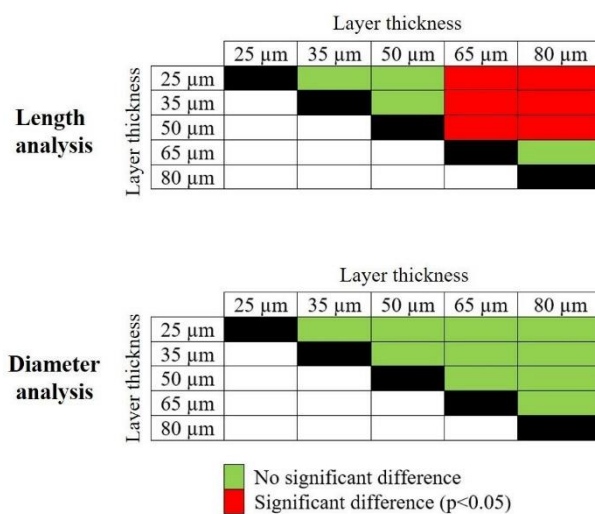


Fig.4. Statistical analysis to the metrological data obtained by X-Ray CT.

While the topology of the cellular lattices has a significant impact in their mechanical properties, it is known that these are also considerably dependent on the base material properties (i.e. microstructural aspects) [30]. Fig.5 shows a reduction in hardness with increased deposition layer thickness. Indeed, it is well established that the increase in microhardness in these alloys is related with higher dislocation pinning [31,32] and, consequently, an increase in yield strength is expected.

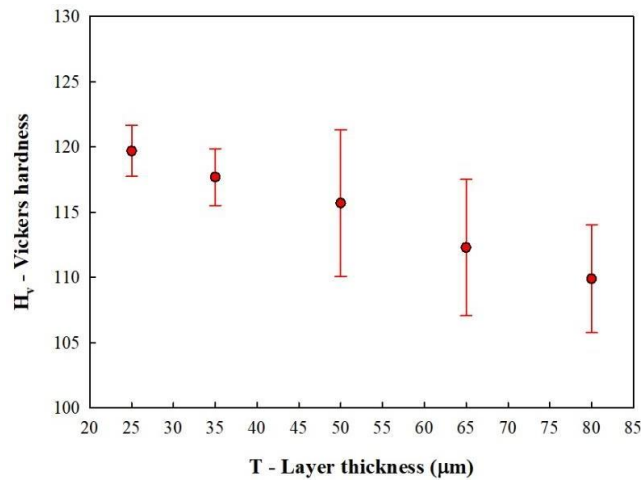


Fig.5. Vickers microhardness of the lattice samples manufactured with different deposition layer thickness.

This correlation between the macrostructural (i.e. cell topology - Figs.3 and 4) and microstructural (i.e. hardness - Fig.5) aspects of the manufactured samples shows that they significantly impact the mechanical properties of the lattices, as highlighted with their apparent stress-strain curves in compression (Fig.6).

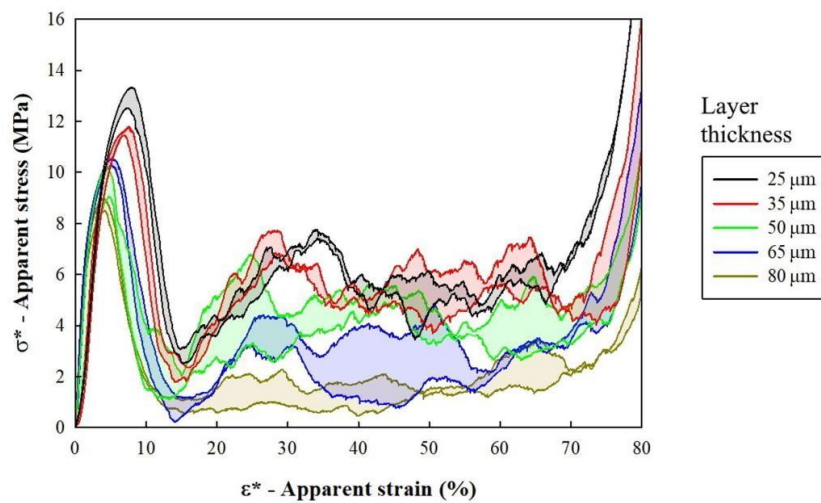


Fig.6. Compression apparent stress-strain curves of the samples, comprising the minimum and maximum apparent stress values that were monitored during the testing of 3 specimens for each sample type.

The results in Fig.6 show the typical mechanical behavior of a lattice material in compression as highlighted in Fig.7: an initial linear elastic domain (Fig.7 (a)), followed by their plastic collapse after elastic instability failure (Fig.7 (b)), compression plateau (Fig.7 (c)) and densification (Fig.7 (d)). Results show the plateau occurs at higher stress values for lower deposition layer thicknesses, however, this is not true for their plastic collapse strength (σ_{pl}^*). Even though there a clear trend for samples with lower depositions layer thickness to display higher plastic collapse strength, this trend is not observed when comparing samples with 50 µm and 65 µm.

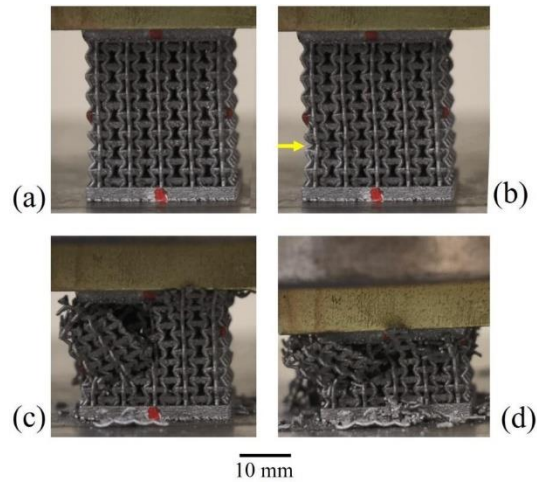


Fig.7. Detail of a mechanical deformation during the compression testing (in the case, 25 mm sample): (a) initial linear elastic region at $\epsilon = 0.01$; (b) after its plastic collapse at $\epsilon = 0.08$, where the collapse region is highlighted; (c) in the region of the plateau at $\epsilon = 0.40$; and (d) at the initial densification stage at $\epsilon = 0.70$.

Even though, the collapse mechanism was the same across the specimens, the apparent stress- strain curves in Fig.5, highlight that the samples that were manufactured with different deposition layer thickness display dissimilar mechanical properties. These results were detailed by analyzing the mechanical properties that are most commonly used for static structural applications, namely their Apparent modulus (E^* , i.e. normalized stiffness) and Plastic collapse strength (σ_{pl}^* , i.e. normalized strength), as shown in Figs. 8 and 9.

Fig.8 shows that the stiffness (i.e. Apparent modulus) tends to increase to a plateau as the deposition layer thickness is increased, as highlighted by its non-linear regression fit ($R^2=0.78$) with an exponential rise to maximum function. The samples that have been manufactured with a 50 mm deposition layer thickness do not follow this trend, as they present values that are similar to those observed for samples with 25 mm and 35 mm. While this may initially seem surprising, these values are proposed to be determined by the rib length, as Fig.4 shows that the rib length/diameter in samples with 25 mm to 50 mm are not statistically different.

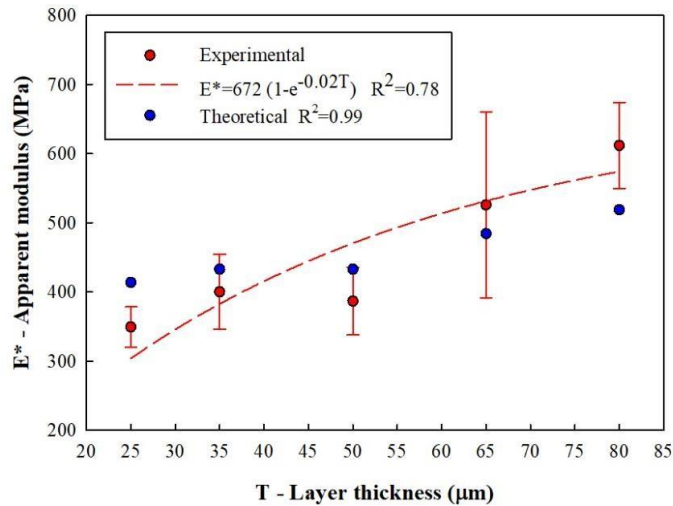


Fig.8. Influence of the deposition layer thickness (T) in the Apparent modulus (E^*).

Indeed, by the input of the monitored rib length/diameters in a theoretical model that has been designed to predict the elastic properties of this type of lattice [27], it may be observed that these present an excellent fit ($R^2 = 0.99$) to the experimental data. It may be established that the stiffness (i.e. Apparent modulus) of the samples is mainly dependent on the cell topology and, consequently, on the influence of the deposition layer thickness on the rib length and diameter. According to the experimental results non-linear regression, it is suggested that as the layer thickness is increased, the Apparent modulus tends to a stable value of 672 MPa.

Fig.9 shows that higher deposition layer thicknesses (T) tend to lower the Collapse strength (σ_{PI}^*). According to these results, it is shown that the Collapse strength dependence to the deposition layer thickness is described by an exponential decay function ($R^2 = 0.95$). These results highlight that the selected deposition layer thickness impacts the macroscopic strength due to microstructural hardness (Fig.5). A reduction in hardness effectively decreases the intrinsic strength in the γ -Al matrix and precipitation strengthening. According to the non-linear regression of experimental results, it is suggested that as the layer thickness is increased, the Collapse strength tends to an 8.74 MPa stable value.

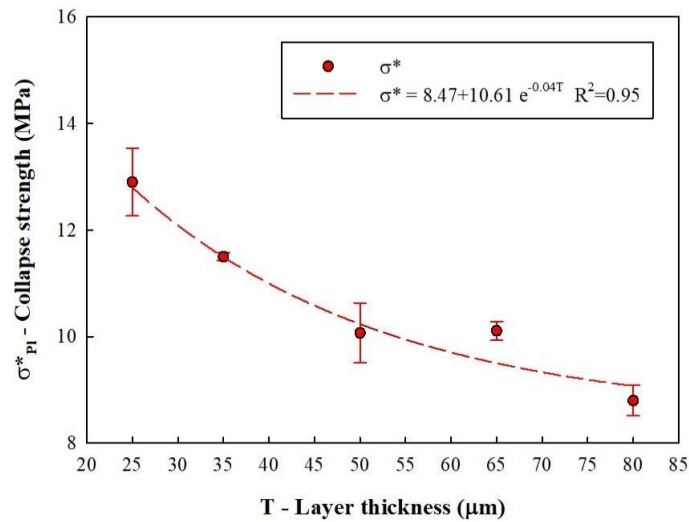


Fig.9. Influence of the deposition layer thickness (T) in the Collapse strength (σ^*_{PI}).

4. Tailoring the mechanical properties based on the deposition layer thickness

Considering the experimental results that have been portrayed in Section 3, a graphical representation was devised to correlate the Deposition layer thickness (T) and the macroscopic stiffness (i.e. E^* , Apparent modulus) and strength (i.e. σ^*_{PI} , Collapse strength).

Fig.10 presents a compilation of the results from Figs. 8 and 9 into a single chart, which is here referred to as a T - E^* - σ^*_{PI} diagram. It may be also understood, that a graphical representation with this configuration could also be applied to other manufacturing parameters and lattice topologies.

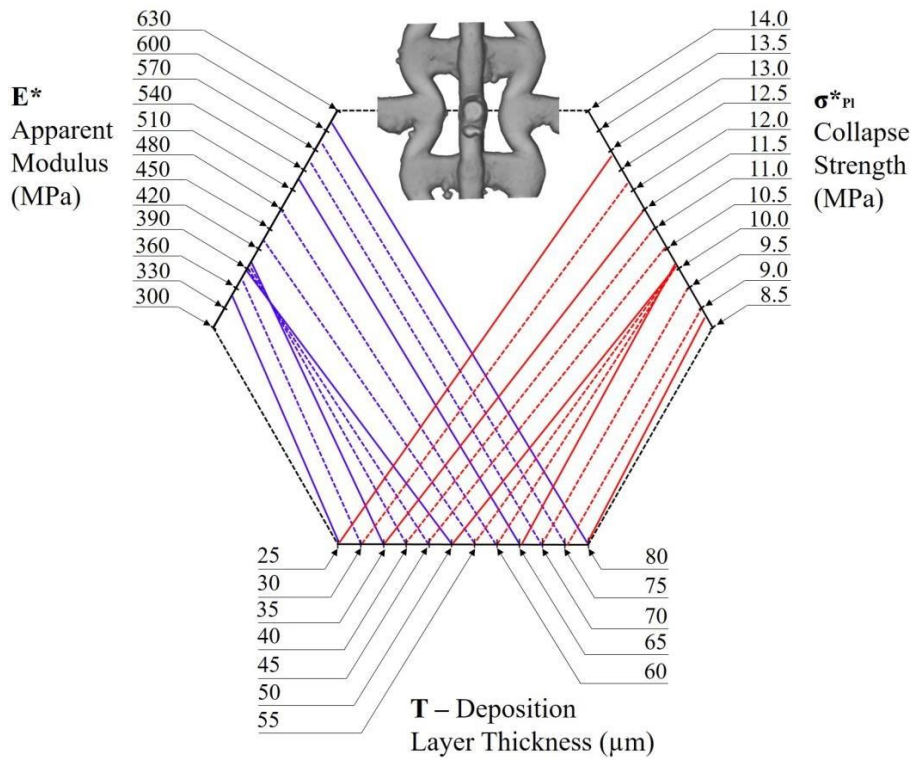


Fig.10. Graphical representation of the resultant T - E^* - σ^*_{PI} diagram (Note: solid and - - - dashed lines represent, respectively, experimental and extrapolated results).

Indeed, the diagram shown in Fig.10 is suggested as a simple and quick route for designers and manufacturers to predict and tailor the fundamental macroscopic mechanical properties of this topology. The practical use of this diagram is relevant in two approaches:

- i. Selecting Deposition layer thickness: user selects a given deposition layer thickness (T) from the bottom horizontal axis and follows the respective (blue and red, respectively E^* and PI^*) lines to the lateral axis to determine the estimated mechanical property. For example, if $T = 25 \text{ }\mu\text{m}$ is selected, the diagram in Fig.10 predicts that the lattice displays $E^* = 349.5 \text{ MPa}$ and $PI^* = 12.9 \text{ MPa}$ macroscopic properties;
- ii. Selecting Mechanical property: user selects a given mechanical property (either E^* and PI^*) and follows the line(s) to the respective (or range of) deposition layer thickness(es) (T). From this point, it is possible to estimate the other macroscopic mechanical property. For examples, if $PI^* \sim 10.1 \text{ MPa}$ is desired, Fig.10 shows that a range to $T = 50 \text{ }\mu\text{m}$ to $T = 65 \text{ }\mu\text{m}$ may be selected. Here the user has the chance of selecting $E^* = 387 \text{ MPa}$ to 526 MPa , depending on the selected value for the Deposition layer thickness (T).

5. Conclusions

This paper presents a route to tailor the macroscopic mechanical properties of powder bed fusion AlSi10Mg lattices by changing the deposition layer thickness. An experimental approach was used to couple macro-scale (X-ray CT) and micro-scale (Vickers microhardness) analysis to the apparent stress-strain behavior of auxetic lattices fabricated with different layer thicknesses. The following conclusions were drawn:

- i. Fabricating samples with different deposition layer thickness impacts the overall mechanical properties of lattices. This is correlated with macro- and microscopical changes, respectively, variations in the topological aspects of the periodic cells and hardness of the β -Al matrix;
- ii. Increasing the deposition layer thickness decreases the length and increases the diameter of the periodical cell ribs. Consequently, the stiffness (i.e. Apparent modulus) of the lattices increases with the increase of deposition layer thickness. These differences are only statistically relevant for wider layer thickness gradients (e.g. while comparing samples manufactured with $35 \text{ }\mu\text{m}$ layers and those manufactured with $65 \text{ }\mu\text{m}$ layers);
- iii. The collapse strength of the lattices is reduced as the deposition layer thickness is increased. Experimental results show that there is a significant reduction in the β -Al hardness as the layer thickness increases. Therefore, there is a reduction in dislocation pinning and, consequently, the

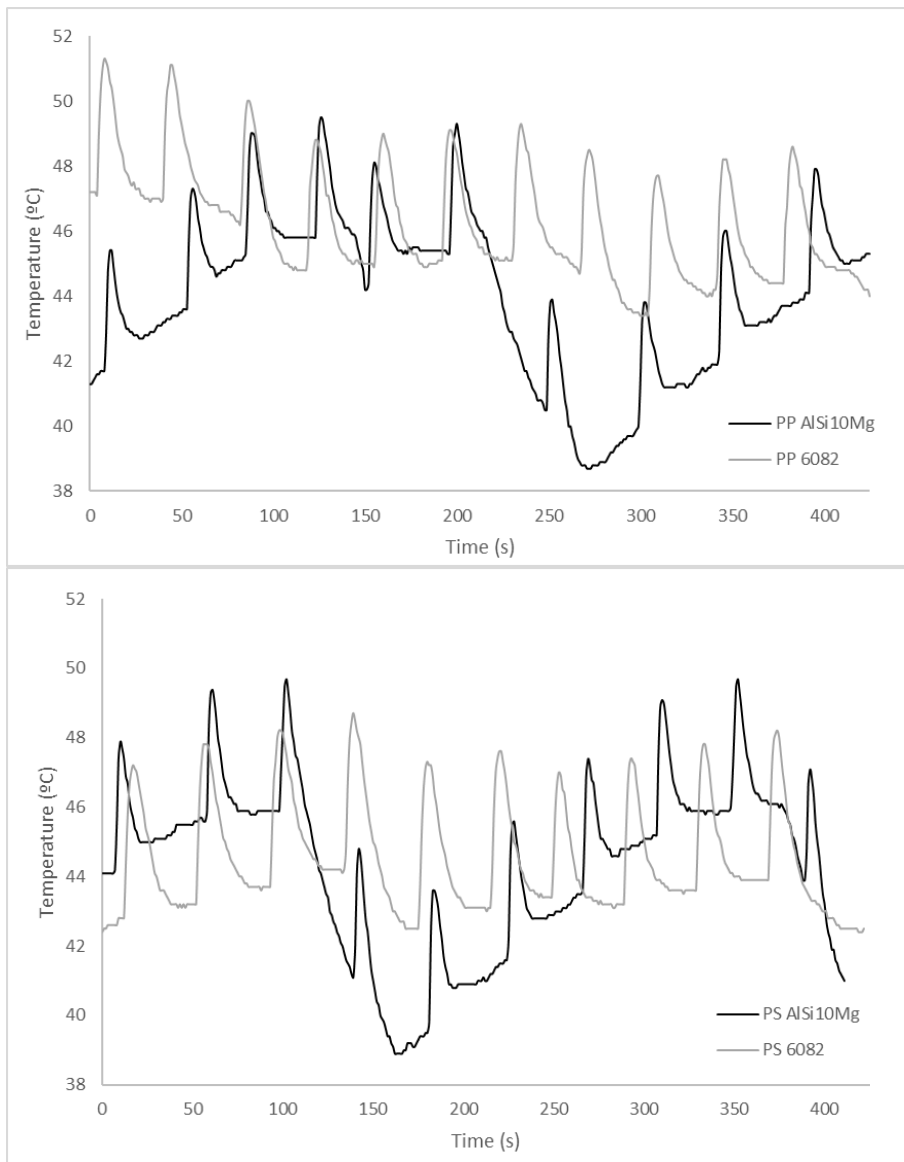
- yield strength of the Al matrix is decreased. This effectively lowers the collapse strength of the lattices for samples fabricated with a higher deposition layer thickness;
- iv. The same AlSi10Mg lattices topology may display a wide range of macroscopic mechanical properties ($E^* = 387 \text{ MPa}$ to 612 MPa and $PI^* = 8.8 \text{ MPa}$ to 12.9 MPa), just by changing the deposition layer thickness ($25 \text{ }\mu\text{m}$ to $80 \text{ }\mu\text{m}$) in a powder bed fusion process. A diagram was devised to correlate these mechanical properties and manufacturing parameters, allowing novel route to predict and guide the design and manufacturing of these cellular solids.

References

- [1] Ashby MF, Evans T, Fleck NA, Hutchinson J, Wadley H, Gibson L. Metal foams: a design guide. Elsevier; 2000.
- [2] Gibson LJ, Ashby MF. Cellular Solids: Structure and Properties. 2nd ed. Cambridge: Cambridge University Press; 1997.
- [3] Benedetti M, du Plessis A, Ritchie RO, Dallago M, Razavi SMJ, Berto F. Architected cellular materials: A review on their mechanical properties towards fatigue-tolerant design and fabrication. *Materials Science and Engineering: R: Reports* 2021;144:100606.
- [4] Carneiro VH, Puga H, Meireles J. Positive, zero and negative Poisson's ratio non-stochastic metallic cellular solids: Dependence between static and dynamic mechanical properties. *Composite Structures* 2019;226:111239.
- [5] Silva EC, Sampaio AM, Pontes AJ. Evaluation of Active Heat Sinks Design under Forced Convection—Effect of Geometric and Boundary Parameters. *Materials* 2021;14.
- [6] du Plessis A, Razavi SMJ, Benedetti M, Murchio S, Leary M, Watson M, et al. Properties and applications of additively manufactured metallic cellular materials: A review. *Progress in Materials Science* 2022;125:100918.
- [7] Carneiro VH, Puga H. Enhanced mechanical properties in cellular solids using axisymmetric configurations. *Composite Structures* 2021;255:112972.
- [8] Jia Z, Liu F, Jiang X, Wang L. Engineering lattice metamaterials for extreme property, programmability, and multifunctionality. *Journal of Applied Physics* 2020;127:150901.
- [9] Valle R, Pincheira G, Tuninetti V. Design of an auxetic cellular structure with different elastic properties in its three orthogonal directions. *Proceedings of the Institution of Mechanical Engineers, Part L: Journal of Materials: Design and Applications* 2021;235:1341–50.
- [10] Chen X, Ji Q, Wei J, Tan H, Yu J, Zhang P, et al. Light-weight shell-lattice metamaterials for mechanical shock absorption. *International Journal of Mechanical Sciences* 2020;169:105288.
- [11] Jiang W, Yin G, Xie L, Yin M. Multifunctional 3D lattice metamaterials for vibration mitigation and energy absorption. *International Journal of Mechanical Sciences* 2022;233:107678.
- [12] Duarte I, Vesenjak M, Vide MJ. Automated Continuous Production Line of Parts Made of Metallic Foams. *Metals* 2019;9.
- [13] Banhart J. Manufacture, characterisation and application of cellular metals and metal foams. *Progress in Materials Science* 2001;46:559–632.
- [14] Carneiro VH, Rawson SD, Puga H. , Withers PJ. Macro-, meso- and microstructural characterization of metallic lattice structures manufactured by additive manufacturing assisted investment casting. *Scientific Reports* 2021;11:4974.
- [15] Gebhardt U, Gustmann T, Giebler L, Hirsch F, Hufenbach JK, Kästner M. Additively manufactured AlSi10Mg lattices – Potential and limits of modelling as-designed structures. *Materials & Design* 2022;220:110796.
- [16] Carneiro VH, Rawson SD, Puga H, Meireles J, Withers PJ. Additive manufacturing assisted investment casting: A low-cost method to fabricate periodic metallic cellular lattices. *Additive Manufacturing* 2020;33:101085.
- [17] Babamiri BB, Barnes B, Soltani-Tehrani A, Shamsaei N, Hazeli K. Designing additively manufactured lattice structures based on deformation mechanisms. *Additive Manufacturing* 2021;46:102143.
- [18] Park S-Y, Kim K-S, AlMangour B, Grzesiak D, Lee K-A. Compressive deformation behavior and energy absorption characteristic of additively manufactured sheet CoCrMo triply periodic minimal surface lattices. *Journal of Materials Research and Technology* 2022;18:171–84.
- [19] Riva L, Ginestra PS, Ceretti E. Mechanical characterization and properties of laser-based powder bed-fused lattice structures: a review. *The International Journal of Advanced Manufacturing Technology* 2021;113:649–71.
- [20] Zhao L, Song L, Santos Macias JG, Zhu Y, Huang M, Simar A, et al. Review on the correlation between microstructure and mechanical performance for laser powder bed fusion AlSi10Mg. *Additive Manufacturing* 2022;56:102914.

- [21] Krishnan M, Atzeni E, Canali R, Calignano F, Manfredi D, Ambrosio EP, et al. On the effect of process parameters on properties of AlSi10Mg parts produced by DMLS. *Rapid Prototyping Journal* 2014;20:449–58.
- [22] Weidmann J, Großmann A, Mittelstedt C. Laser powder bed fusion manufacturing of aluminum honeycomb structures: Theory and testing. *International Journal of Mechanical Sciences* 2020;180:105639.
- [23] Gülcan O, Simsek U, Cokgunlu O, Özdemir M, Şendur P, Yapici GG. Effect of Build Parameters on the Compressive Behavior of Additive Manufactured CoCrMo Lattice Parts Based on Experimental Design. *Metals* 2022;12.
- [24] Alaña M, Cutolo A, Ruiz de Galarreta S, Van Hooreweder B. Influence of relative density on quasi-static and fatigue failure of lattice structures in Ti6Al4V produced by laser powder bed fusion. *Scientific Reports* 2021;11:19314.
- [25] Ahmadi SM, Hedayati R, Li Y, Lietaert K, Tümer N, Fatemi A, et al. Fatigue performance of additively manufactured meta-biomaterials: The effects of topology and material type. *Acta Biomaterialia* 2018;65:292–304.
- [26] Galati M, Giordano M, Iuliano L. Process-aware optimisation of lattice structure by electron beam powder bed fusion. *Progress in Additive Manufacturing* 2022.
- [27] Carneiro VH. On the elastic properties of three-dimensional honeycomb lattices. *Composites Communications* 2020;17:14–7.
- [28] Rueden CT, Schindelin J, Hiner MC, DeZonia BE, Walter AE, Arena ET, et al. ImageJ2: ImageJ for the next generation of scientific image data. *BMC Bioinformatics* 2017;18:529.
- [29] Aboulkhair NT, Simonelli M, Parry L, Ashcroft I, Tuck C, Hague R. 3D printing of Aluminium alloys: Additive Manufacturing of Aluminium alloys using selective laser melting. *Progress in Materials Science* 2019;106:100578.
- [30] Liu M, Takata N, Suzuki A, Kobashi M. Development of gradient microstructure in the lattice structure of AlSi10Mg alloy fabricated by selective laser melting. *Journal of Materials Science & Technology* 2020;36:106–17.
- [31] Colley LJ, Wells MA, Poole WJ. Microstructure–yield strength models for heat treatment of Al–Si–Mg casting alloys II: modelling microstructure and yield strength evolution. *Null* 2014;53:138–50.
- [32] Granato A, Lücker K. Theory of Mechanical Damping Due to Dislocations. *Journal of Applied Physics* 1956;27:583–93.

Appendix 8 – Temperature vs time evolution during injection moulding



Appendix 9 – Average tab angle of injection moulded specimens

		Moulding inserts		PP 579S		GPPS 165H	
		Nominal	Actual	Predicted	Actual	Predicted	Actual
<u>AW-6082</u>	Core	30.00	$30.00^\circ \pm 0.01^\circ$	30.14	$31.17^\circ \pm 0.27^\circ$	30.03	$30.34^\circ \pm 0.15^\circ$
	Cavity		$30.01^\circ \pm 0.01^\circ$	30.12	$31.07^\circ \pm 0.18^\circ$	29.96	$30.19^\circ \pm 0.18^\circ$
<u>AlSi10Mg</u>	Core	30.00	$29.98^\circ \pm 0.01^\circ$	30.12	$31.05^\circ \pm 0.25^\circ$	30.02	$30.30^\circ \pm 0.33^\circ$
	Cavity		$30.03^\circ \pm 0.05^\circ$	30.11	$30.90^\circ \pm 0.53^\circ$	29.99	$30.18^\circ \pm 0.43^\circ$